CENTER FOR RADAR ASTRONOMY

Stanford Electronics Laboratories
Stanford University, CA 94305-4055

VOYAGER RADIO OCCULTATION BY THE URANIAN RINGS: STRUCTURE, DYNAMICS, AND PARTICLE SIZES

IN-91-CR

Donna Leigh Gresh

February, 1990

19912

p.231

Scientific Report No. D845-1990-1

Prepared under
JPL contracts 953618 and 957887
NASA contract NAGW1210

VOYAGER RADIO OCCULTATION BY THE URANIAN RINGS: STRUCTURE, DYNAMICS, AND PARTICLE SIZES

By

Donna Leigh Gresh

February, 1990

Scientific Report No. D845-1990-1

Prepared under
JPL contracts 953618 and 957887, and NASA contract NAGW1210

Center for Radar Astronomy
Stanford Electronics Laboratories
Stanford University, CA 94305-4055

This report constitutes a Ph.D. dissertation submitted to Stanford University. The research was supported by the Voyager Project Office at the Jet Propulsion Laboratory, the NASA Uranus Data Analysis Program, and a National Science Foundation Graduate Fellowship.

Abstract

Diffraction of Voyager 2's 3.6 and 13 cm wavelength (λ) microwaves by the Uranian rings is removed through an inverse Fresnel transform filtering procedure that accommodates the significant eccentricity of the rings. Resulting 50 m resolution profiles at two observation longitudes: (i) reveal remarkably detailed and longitudinally varying structure, (ii) provide eccentricity gradient profiles of Rings α, β, and ϵ which bring into question current theoretical models for observed rigid precession, and (iii) suggest that two possible unseen satellites, with semimajor axes 42901 km and 47166 km, may confine some of the very sharp edges observed via resonant interactions.

The observed invariance of integrated opacity as ring width changes implies that Rings α, γ, δ, and ϵ are not monolayers and that the thickness of Ring ϵ may vary in inverse proportion to its width. Near periapse Ring ϵ must be $\gtrsim$ 10 layers thick. A comparison of measurements of differential opacity $\Delta\tau \equiv \tau(3.6\text{ cm}) - \tau(13\text{ cm})$ and differential phase delay $\Delta\phi_c \equiv \phi_c(13\text{ cm}) - \frac{3}{11}\phi_c(3.6\text{ cm})$ with a "classical" noninteracting particles model implies: (i) for the five innermost rings, the measured $\Delta\phi_c/\tau(3.6\text{ cm})$ and $\Delta\tau$ are inconsistent ($\sim$ 40–75$\times10^{-3}$ cycles/unit optical depth and $\simeq 0$, respectively), and (ii) for Ring ϵ, an inverse power law size distribution with exponent $q \sim 2.75$, minimum size cutoff $\lesssim$ 2 cm, and maximum size cutoff $\gtrsim$ 1.5 m matches $\Delta\tau$ and $\Delta\phi_c$. Assuming an ice-like density 1 g-cm^{-3}, this implies a surface mass density $\sigma \gtrsim$ 50 g-cm^{-2} and a ring thickness $h \gtrsim$ a few meters. If the possibly anomalous $\Delta\phi_c$ is disregarded, the effective particle radius may be $\gtrsim$ 70 cm independent of q, implying that $\sigma \gtrsim$ 80 g-cm^{-2} and $h \gtrsim$ 30 m.

The anomalously large $\Delta\phi_c$ of the inner rings does not appear to be due to coherent interactions between ring particles. Exact computations for extinction by 2–5 spheres show that: (i) when particles are large ($a/\lambda \gtrsim 1$), geometric shadowing is a good model for the interactions, and for an isolated pair, shadowing persists to separation $d \sim 10a^2/\lambda$, (ii) averaged over all orientations, coherent interaction between pairs of spheres of arbitrary size is negligible when $d \gtrsim 5a$, corresponding to volume fraction $< 1\%$, and (iii) generally, coherent interactions decrease $\Delta\phi_c$ relative to the noninteracting case.

A "pairwise" approximation which includes coherent interactions between pairs of spheres but neglects higher-order interactions agrees to within a few percent with the exact computations for three spheres except when particles are arranged in endfire configuration. It predicts that, for a monolayer distribution of large particles, τ *decreases* with increasing packing fraction f in a manner consistent with the shadowing model, whereas for small particles $(a/\lambda \ll 1)$ τ *increases* with increasing f.

Acknowledgments

It has been a great privilege to work on the Voyager project. Being among the first visitors, albeit somewhat vicarious, to the planets Uranus and Neptune was the opportunity of a lifetime. I have been very fortunate to have been able to work with my colleagues at the Center for Radar Astronomy at Stanford. Above all, I am indebted to my principal advisor, Len Tyler, Principal Investigator of the Voyager Radio Science experiment, whose guidance, mentorship, and inspiration have contributed immensely to my development as a scientist. In addition, his leadership, tenacity, and dedication have made the Voyager Radio Science experiment a great success. The high quality of the data analyzed here can be attributed to his unrelenting refusal to accept anything less than was technically possible to achieve. I have benefited from countless discussions with my associate advisor, Essam Marouf, whose enormous enthusiasm and careful attention to detail make him a wonderful role model for any scientist. He contributed to this work, not only by lending both his great scientific insight and his seemingly bottomless supply of valuable and relevant reference material, but also by spending long hours reading numerous drafts of this dissertation, and improving it greatly each time.

I would also like to thank Paul Rosen, who has been my friend and office-mate and who in general has made being involved with the Voyager project lots of fun. He revealed to me many of the secrets of radio occultation data processing and analysis. Eric Gurrola has been a great addition to Durand 211, and has been a friendly and helpful office-mate. Dick Simpson was involved in most of the original and much of the ongoing computer programming which turned the original hundreds of magnetic tapes into real scientific data. His careful nurturing of the Data General computer kept the data processing on track. Von Eshleman, original principal investigator for Voyager Radio Science, has been a leader in the use of the technique of radio occultation to study the solar system, and was a welcome member of my oral defense committee. Our secretaries Hazel Rand and Sara Zientek warmly and efficiently kept the Voyager crew organized.

I also am indebted to Kirk Fuller, who generously handed over to me the product of his own Ph.D. dissertation work: a program to compute the scattering behavior of two to five spheres. He was always very helpful when I had questions.

I would like to thank Anthony Siegman for pleasantly serving as the third member of my reading committee, and my Ph.D. oral defense chairperson, Teresa Meng, whose friendliness made a stressful occasion quite a bit more bearable.

Many friends at Stanford have been of great support to me, and have made my 6^+ years in graduate school very pleasant. In particular, I thank Nick Babchuk, Arman Bernardi, Phil Chou, Andy Comly, Sumire Kobayashi, Carol Mann-Comly, Lois Ogilby, Sandy Smith Pitner, and Maura Sullivan for friendship and fun.

With seemingly infinite patience, my husband-to-be, Jeff Kephart, put up with what was certainly the most stressful year-and-a-half of my graduate student career, including my oral defense and finishing the final version of this dissertation. He even read it, carefully. He contributed to this work through his careful questions and great physical intuition. Much more importantly, I treasure his honesty, sincerity, curiosity, and love of life. Every day, he reminds me of the magic and wonder of this universe.

Finally, I thank my parents Philip and Maija Gresh, and my brother, David Gresh. Their confidence in me, and their unconditional support during stressful times, was a great boost during the difficult periods in my graduate studies. They have given me a loving home, even from 3000 miles away, and, with love and affection, I dedicate this work to them.

Acknowledgment is made to Academic Press, Inc., for permission granted to reprint, in Chapters 2, 3, 4, and Appendix A, portions of "Voyager Radio Occultation by Uranus' Rings. I: Observational Results" by Gresh *et al.* (1989); Figures 3–21 and 26, and Tables 1–4, 7, and 11: Copyright ©1989 by Academic Press, Inc.

Contents

List of Tables

List of Figures

List of Symbols

The following mathematical symbols and abreviations are used in the text. In some cases, the same symbol is used for more than one quantity.

a	semimajor axis (Chapters 2 and 3)
a	radius of sphere (Chapters 4 and 5)
a_0	reference size for power law size distribution
a_{min}, a_{max}	lower and upper size cutoffs of a power law size distribution
a_n, b_n, c_n, d_n	Mie coefficients of the expansion of the scattered and internal fields
${}^l a_{mn}$, ${}^l b_{mn}$	expansion coefficients in two-sphere theory for the lth sphere
a_r	semimajor axis of particle orbit
a_s	semimajor axis of a satellite
a'	variable of integration
$\nabla a'$	two-dimensional gradient of a'
A	area
$A^{(1)}$	area of one particle
$A^{(1)}_{\text{eff}}$	"effective" area of one particle, given shadowing
$A^{mn}_{m\nu}$, $B^{mn}_{m\nu}$	translation coefficients
B	ring opening angle
$BGYM$	modified Born-Green-Yvon formulation for $g(r)$
C	contour of integration
C_α	= 2.49, as defined in Marouf *et al.* (1986)
C_{ext}	extinction cross section
d	distance between centers of two spheres

dB	Decibel; $10\log_{10}$ [signal power / reference power]
$\mathbf{d}$	vector connecting the centers of two spheres
dl	thickness of a ring layer
$d\mathbf{r_i}$	element of area around $\mathbf{r_i}$
D	distance of Voyager from ring plane intercept point
e	eccentricity
e_s	eccentricity of a satellite
$\hat{\mathbf{e}}_{\parallel}$, $\hat{\mathbf{e}}_{\perp}$	unit vectors defining polarization directions
E	total electric field
E_i, E_s	incident and scattered electric fields
E_{ps}, E_{qs}	scattered electric field in p and q polarizations
E_{pi}, E_{qi}	incident electric field in p and q polarizations
$< E_{ps} >, < E_{qs} >$	average of electric field over all possible pair orientations
$E_{\parallel i}$	parallel electric field component of the incident wave
$E_{\perp i}$	perpendicular electric field component of the incident wave
$E_{\parallel s}$	parallel electric field component of the scattered wave
$E_{\perp s}$	perpendicular electric field component of the scattered wave
E_0	field strength in the absence of rings
E_c	complex field strength of coherent received signal
F	Fresnel scale
f	packing fraction, $= \rho/\pi a^2$
f_0	radio frequency
g_i	cross-sectional area of the ith sphere
$g^{(n)}$	n-sphere correlation function
$g^{(2)}(r) = g(r)$	the pair correlation function
g_1, g_2, g_3	first three terms in virial expansion for $g(r)$
G	gravitational constant (Chapters 3 and 4)
G	total cross-sectional area of a cluster of spheres (Ch. 5)
i	inclination
I	intensity
I_i	incident intensity
$\mathrm{Im}\{\cdot\}$	imaginary part of the quantity inside the braces

IER	inner eccentric resonance
J_2	dynamical oblateness of the planet (Uranus)
k	wavenumber $2\pi/\lambda$
$\mathbf{k}$	wave vector
l	total thickness of a ring
m	number of azimuthal wavelengths for a resonance (Ch. 3)
m	relative refractive index (Chs. 4 and 5)
M	mass of the planet (Uranus)
n	mean motion of a ring particle (Chapter 3)
n	area, or columnar, density of particles (Chapters 4 and 5)
n_0	coefficient of power law size distribution
n_s	mean motion of a satellite
$n(a)$	size distribution of particles
n_v	volume density
N	number of layers (Chapter 4)
N	number of spheres or disks (Chapter 5)
${}^{l}\mathbf{N}_{mn}^{(3)}$, ${}^{l}\mathbf{M}_{mn}^{(3)}$	vector spherical harmonics in coordinates centered on lth scatterer
NASA	National Aeronautics and Space Administration
OER	outer eccentric resonance
p, q	labels for two orthogonal polarization directions
$p^{(n)}(\mathbf{r_1}, ..., \mathbf{r_n})$	joint probability density of n disks located at $d\mathbf{r_1}$, etc.
P	observation point
P_N	noise power
P_S	signal power
P_{Mie}	(imaginary) extinction efficiency of a sphere using Mie theory
$P^{(2)}$	exact imaginary extinction efficiency for two spheres
$P^{(2)}_{\mathrm{n.i.}}$	non-interacting imaginary extinction efficiency for two spheres
$P^{(N)}$	exact imaginary extinction efficiency of N spheres
$P^{(N)}_{\mathrm{n.i.}}$	imaginary extinction efficiency of N spheres assuming non-interaction
$< P^{(2)} >$	average imaginary extinction efficiency over all orientations
PAG	particle-accumulation-group (defined by Rosen, 1989)
PPS	Photopolarimeter (Voyager occultation experiment, $\lambda = 0.27\mu\mathrm{m}$)

q	eccentricity gradient defined as $a\,de/da$ (Chapter 3)
q	power law index (Chapter 4)
Q_{Mie}	real extinction efficiency for a sphere using Mie theory
$Q^{(2)}$	exact real extinction efficiency for two spheres
$Q^{(2)}_{\mathrm{n.i.}}$	non-interacting real extinction efficiency for two spheres
$\hat{Q}^{(2)}_{\mathrm{asym}}$	perturbation to real extinction efficiency as computed from $\hat{S}^{(2)}_{\mathrm{asym}}$
$Q^{(N)}$	exact real extinction efficiency of N spheres
$Q^{(N)}_{\mathrm{n.i.}}$	real extinction efficiency of N spheres assuming non-interaction
$< Q^{(2)} >$	average real extinction efficiency over all orientations
r	distance from scatterer to the observation point (Ch. 4)
r	distance between particles, normalized by particle diameter (Ch. 5)
$\mathbf{r_1}, \ldots, \mathbf{r_n}$	particle positions relative to origin (Ch. 5)
$\mathbf{r_i}$	position of a particle
$\mathbf{r}_l$	vector position of lth sphere
R_e	eccentric resonance location
R	radius of the planet (Uranus)
R	radial limit of integration (Chapter 5)
$\mathrm{Re}\{\cdot\}$	real part of the quantity inside the braces
$\overline{R}_c$	vector from the planet to the spacecraft
S	amplitude scattering matrix
$S(\theta)$	scattering amplitude in the θ (near-forward) direction
$S(0)$	scattering amplitude in the forward direction
$S_{\parallel}$, $S_{\perp}$, S_3, S_4	components of the scattering matrix S
$S^{(2)}$	exact forward scattering amplitude for two spheres
$S^{(2)}_{\mathrm{asym}}$	approximation of $S^{(2)}$
$\hat{S}^{(2)}_{\mathrm{asym}}$	approximation to $S^{(2)} - S^{(2)}_{\mathrm{n.i.}}$
$S^{(1)}(\beta)$	scattering amplitude of an isolated sphere at angle β
$S_{\perp}(\beta)$, $S_{\parallel}(\beta)$	Mie solution for scattering amplitude at angle β
$S^{(N)}$	exact forward scattering amplitude of N spheres
$S^{(N)}_{\mathrm{n.i.}}$	non-interacting forward scattering amplitude
$< S_{q,p}(0) >$	average of forward scattering amplitude over all possible orientations
S_{pert}	perturbed forward scattering amplitude

SF	shadow fraction; $1 - SF \sim Q^{(2)}/Q^{(2)}_{\text{n.i.}}$ (simple shadowing model)
SNR	signal-to-noise ratio
SNR_0	free-space signal-to-noise ratio in a 1 Hz bandwidth
$T(\rho, \phi)$	actual transmittance at ring plane radius ρ and azimuth ϕ
$\hat{T}(\rho, \phi)$	observed transmittance at ring plane radius ρ and azimuth ϕ
$\mathbf{u}_0$	the projection of $\mathbf{k}$ onto the monolayer
UVS	Ultraviolet Spectrometer (Voyager occultation experiment, $\lambda = 0.11\mu$m)
v	velocity of ring particle
W	ring width
(x, y)	position in the observation plane
z	projection of vector r onto the direction of the original ray
α	angle between forward direction and line connecting two spheres
α, δ	right ascension and declination of the rotational pole of Uranus (Ch. 3)
α_r, δ_r	right ascension and declination of the normal to a given ring plane
β	angle from forward direction
γ_p	polarization of incident wave ($\gamma = 0$ is $\|$, $\gamma = \pi/2$ is $\perp$)
γ	angular coordinate in the plane of the monolayer
$\delta[\cdot]$	Dirac delta function
$\Delta\tau$	differential opacity, defined as $\tau(3.6 \text{ cm}) - \tau(13 \text{ cm})$
$< \Delta\tau >$	average differential opacity, defined as $\int \Delta\tau/W$
$\Delta\phi_c$	differential phase delay defined as $\phi_c(13 \text{ cm}) - \frac{3}{11}\phi_c(3.6 \text{ cm})$
$< \Delta\phi_c >$	average differential phase delay, defined $\frac{1}{W} \int [\phi_c(13 \text{ cm}) - \frac{3}{11}\phi_c(3.6 \text{ cm})]$
θ	scattering angle
θ_p	angle from orbit periapsis
κ	epicyclic frequency of a ring particle
κ_s	epicyclic frequency of a satellite
λ	radio wavelength
μ_0	ring opening projection $\sin(B)$
ρ	material density of ring particles (Chapter 4)
ρ	number of particles per unit area, $= N/A$ (Chapter 5)
(ρ, ϕ)	coordinates in the ring plane (Ch. 3)
(ρ_s, ϕ_s)	stationary phase point

σ	standard deviation
σ	surface mass density of a ring (Chapter 4)
σ_τ	standard deviation in measured optical depth
σ_{ϕ_c}	standard deviation in measured phase delay
Σ_i	integrated optical depth up to the ith point
τ	normal optical depth
τ_e	peak opacity reached near a ring edge
$\tau_{\mathrm{n.i.}}$	optical depth of assumed non-coherently-interacting monolayer
τ_{TH}	threshold opacity (defined in Appendix A)
τ_U, τ_L	upper and lower limits of 70% confidence interval for τ
ϕ	orientation of two spheres in plane orthogonal to $\mathbf{k}$
ϕ_c	coherent phase; positive ϕ_c indicates phase retardation
$\phi(r)$	potential function (Ch. 5)
ψ	phase factor in diffraction reconstruction
ω	location of the line of apsides of an eccentric orbit
Ω	ascending node of Uranus' equator on the Earth's mean equator

Chapter 1

Introduction

Voyager 2's brief encounter with Uranus on January 24, 1986 resulted in an enormous increase in our knowledge over that which had been accumulated during the 205 years since William Herschel's discovery of this distant blue planet. Its two-billion mile distance from Earth renders it too faint to be visible with the naked eye (except under good seeing conditions), and has made the collection of information about Uranus from Earth-based measurement very difficult. Our first close-up look through the eyes and ears of Voyager has provided much information which we never could have suspected, much less obtained, before.

This work describes the results of one of the many experiments on board Voyager, the "radio occultation" experiment, in which two coherent radio signals at wavelengths of approximately 3.6 and 13 cm were transmitted from Voyager through the Uranian rings toward Earth. As the signals passed through the rings, they were reduced in amplitude, shifted in phase, and diffracted. Two hours and 45 minutes later, the perturbed signals were received on Earth at three antennas in Australia. The total time that Voyager spent behind the rings and planet was just over three hours; the analysis of this data has so far taken over three years, and the observations presented here will undoubtedly result in even more analysis time as theoreticians incorporate these results into their models of the Uranian rings.

1.1 Rings of the Gaseous Giants

Until about a decade ago, it was thought that planetary rings were a rare occurrence. Saturn had been known to have an extended ring system since the early days of telescopic observation, but it was not until March, 1977, during the observation of a star passing behind Uranus (stellar occultation), that it was discovered that a second planet in the solar system possessed rings (*v.*, *e.g.*, Elliot *et al.*, 1977). Soon afterward, Voyager 1 discovered tenuous rings around Jupiter (Owen *et al.*, 1979), confirming an earlier proposal by Acuña and Ness (1976) that the low energetic-particle fluxes measured by Pioneer 10 inwards of Amalthea's orbit were due to an undiscovered ring or a satellite. Stellar occultations later revealed what appeared to be a set of incomplete arc rings around Neptune (Hubbard *et al.*, 1986). The recent encounter of Voyager 2 with Neptune in August, 1989 showed that these rings extend around the entire circumference of the orbit, but appear clumpy in nature. Thus we have now found that rings exist around each of the gaseous giants. The characteristics of the ring systems differ greatly, however. For the following discussion, a schematic of the four known ring systems is shown, to scale, in Figure 1.

Saturn has the most extended ring system, with the three main rings (Rings A, B, and C) spanning a distance of almost 70,000 km, most of which is occupied by ring material. Recent Earth-based and Voyager observations have discovered four additional, mostly tenuous, rings named D, E, F, and G. The particles in Saturn's rings decrease in number density in approximately inverse cubic proportion to their sizes over the millimeter to several meter size range (Marouf *et al.*, 1983; Zebker *et al.*, 1985). Their typical normal optical depth[1] at microwave wavelengths is in the range of 0.1 to about 1 or 2 (Tyler *et al.*, 1983).

In contrast, the nine main Uranian rings are narrow, dense, and sharp-edged. Although spread over a region approximately 10,000 km wide, about 99% of this region is essentially empty, with optical depth $< 10^{-4}$. The microwave optical depths of the main rings range from ~ 0.5 to values approaching 6 or 7 (Gresh *et al.*, 1989), the largest values observed in any ring system. Particle sizes that dominate the optical depth are relatively large ($\gtrsim$ 1 m) if it is assumed that the size distribution is Saturn-like, but could be smaller ($\gtrsim$ 10 cm) if the distribution is less steep than an inverse cubic power law.

Jupiter's ring system is composed of a "main band", a "halo", and a "gossamer" ring (Showalter *et al.*, 1985; Showalter *et al.*, 1987). The main band extends over a radial distance of about 7000 km. It contains a component of micron-sized particles with an optical depth at visual wavelengths of only a few $\times 10^{-6}$. A component of macroscopic bodies also exists, and contributes a similar amount to the optical depth. The halo, internal to the main ring, extends over approximately 30,000 km

---

[1] Optical depth is a logarithmic measure of attenuation of a signal by ring material. The intensity of a signal passing through the ring in a direction perpendicular to the ring plane is attenuated by $e^{-\tau}$, where τ is the normal optical depth.

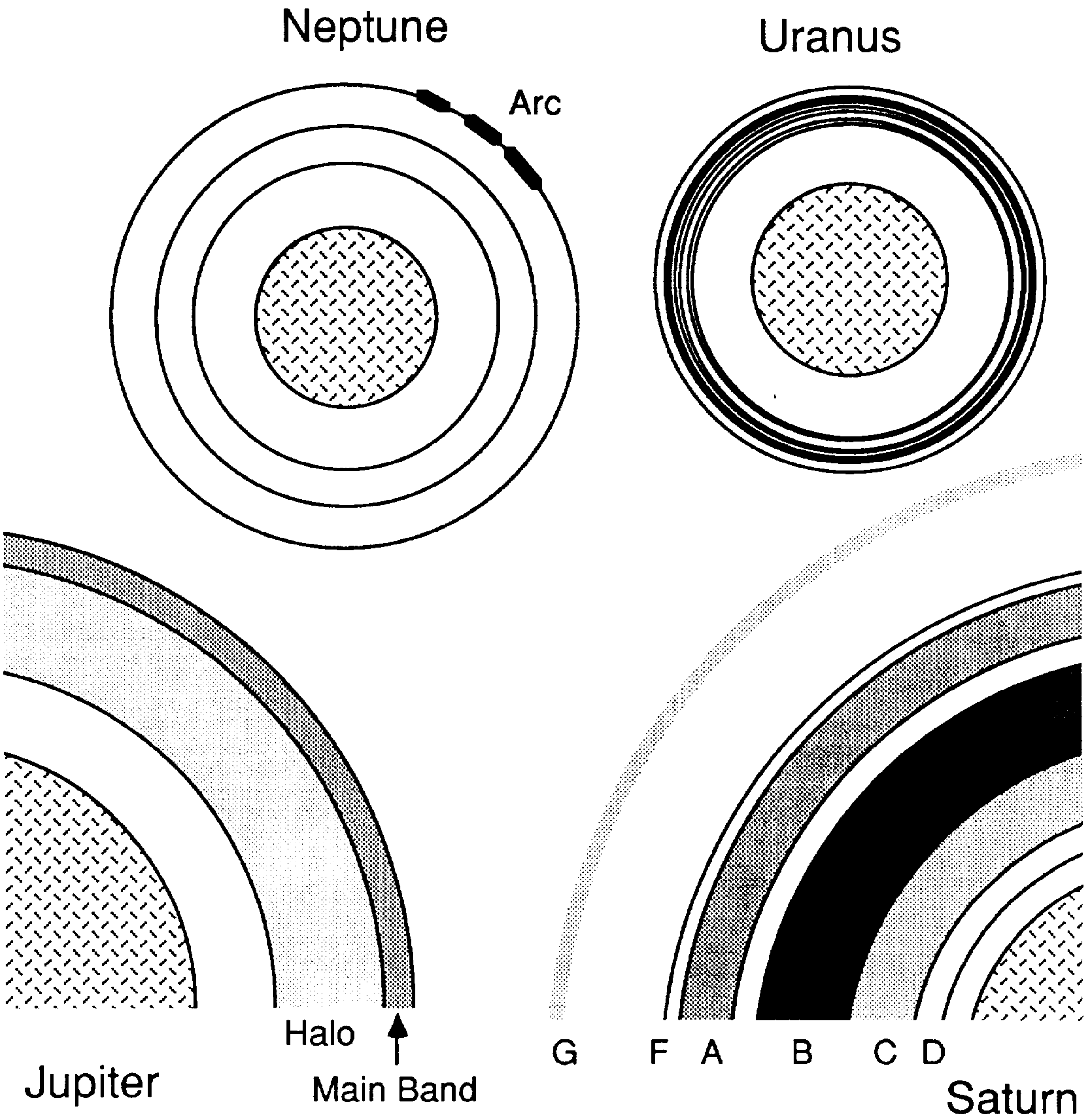

FIG. 1: Schematic of the four ring systems of the gaseous giants. Planets and rings are to scale. Not shown are the gossamer ring of Jupiter, which extends outward beyond the main band, and Saturn's Ring E, which extends from ~ 3 to ~ 8 Saturn radii.

radially and up to 20,000 km in vertical thickness, and a so-called "gossamer" ring extends outward from the main component, and appears to be composed of micron-sized grains.

Finally, Voyager 2 found Neptune to have rings at radii of approximately 42,000 km, 52,300 km, and 62,900 km, with additional tenuous material distributed throughout the ring region (Smith *et al.*, 1989). The ring at 62,900 km is composed of a low optical depth component which extends around the entire circumference of the orbit, and a clumpy component with higher optical depth of ~ 0.1, which extends, in three distinct pieces, over about 30°. This ring "arc" appears to be the feature responsible for most pre-Voyager Earth-based observations (Nicholson *et al.*, 1989; Smith *et al.*, 1989). Preliminary analysis indicates that the Neptunian rings contain a significant fraction of dust.

The search for reasons for these dramatic differences in morphology, extent, and particle properties among the four known ring systems has become a fruitful area of research over the last decade or so. Each planetary system is composed of a large central body, a number of smaller massive bodies (satellites) and a collection of even smaller ring particles. By far the dominant force shaping the rings is gravity; however, in some cases, electromagnetic interactions between small charged particles are significant (Grün *et al.*, 1984). Bodies are constrained to obey Newton's laws of motion (relativistic effects are completely negligible), and inelastic collisions between ring particles can serve as a sink of kinetic energy. This simple set of interactions has somehow led to apparently different sorts of ring systems around Jupiter, Saturn, Uranus, and Neptune. A better understanding of what brings about this complexity and variability may shed light on the evolution of other gravitational systems, such as our solar system as a whole and our galaxy.

1.2 Radio Occultation Studies of the Rings of Jupiter and Saturn

Theoretical foundation for the study of planetary rings through the technique of radio occultation was developed initially within the context of the anticipated Voyager occultation by Saturn's rings (Marouf, 1975; Marouf *et al.*, 1982). Experimental investigation began somewhat inauspiciously with the non-detection of Jupiter's tenuous ring in the Voyager 1 radio occultation data. The fact that the ring was not observed was used to place bounds on its optical depth and particle size distribution (Tyler *et al.*, 1981). Experimental study of rings through radio occultation truly began with the successful occultation of Voyager 1 by Saturn's rings in 1980 (Tyler *et al.*, 1981; Marouf *et al.*, 1982; Marouf and Tyler, 1982; Tyler *et al.*, 1983). Using data from that experiment, a high resolution map of Saturn's rings was produced (Marouf *et al.*, 1986; Rosen, 1989), ring particle sizes were inferred (Marouf *et al.*, 1983; Zebker *et al.*, 1983; Zebker *et al.*, 1985) and limits were placed on the vertical extent of the rings (Marouf and Tyler, 1982; Zebker and Tyler, 1984). By comparing features in the radio and ultraviolet spectrometer occultations, the orientation of Saturn's pole was refined (Simpson *et al.*, 1983).

Waves in Saturn's rings induced by the gravitational perturbations of moons have also been an active area of research. Analysis of wave-like features in the radio occultation data observed in the Encke Gap (Marouf *et al.*, 1986; Showalter *et al.*, 1986), and the Cassini division (Marouf and Tyler, 1986), pointed to the possible existence of satellites embedded within the ring system. Analysis of bending waves forced by Saturn's satellite Mimas allowed local ring properties such as surface mass density and viscosity to be inferred (Gresh *et al.*, 1986). Recently, a previously unidentified wave feature in Saturn's Ring C was identified as a nodal bending wave due to vertical forcing by Titan, and is the first such feature ever observed (Rosen and Lissauer, 1988). An exhaustive analysis of density and bending waves in Saturn's rings (Rosen, 1989) characterized surface mass densities in many regions of the rings and pointed out differences in ring morphology based on the strength of the gravitational perturbation there.

1.3 Overview of the Uranian Rings

The Uranian ring system has in the 12 years since its discovery contributed more than its share of puzzles to ring science. Before the Voyager 2 encounter with the planet in 1986, numerous stellar occultations of the rings were observed from Earth, and nine narrow rings were discovered and named (for a pre-Voyager review, see Elliot and Nicholson, 1984). The pre-Voyager rings span the distance from ~40,000 km to ~50,000 km from the center of Uranus, and are named, from the innermost out, Rings 6, 5, 4, α, β, η, γ, δ, and ϵ. Ring ϵ, which on the average spans a distance of approximately 60 km, is the widest of the Uranian rings, and contains most of the mass of the ring system. The remaining eight rings vary in average width from about 1 to 10 km. Voyager added much new information which could not have been obtained from the ground. From images taken by cameras on-board Voyager, a ring was discovered between Rings δ and ϵ, and an extended sheet of low optical depth material throughout the ring system was found (Smith *et al.*, 1986). Occultation experiments also observed the rings. Two stars, σ-Sagittarii and β-Persei, passed behind the rings as viewed from Voyager, and the attenuation of the starlight was observed at two wavelengths (0.27μm and 0.11μm) (Lane *et al.*, 1986; Holberg *et al.*, 1987). In addition, the Voyager 2 encounter provided the first occultation by the Uranian rings at microwave wavelengths (Tyler *et al.*, 1986; Gresh *et al.*, 1989). Detailed ring profiles at six distinct longitudes were obtained for the first time from these occultations.

Since their discovery, two major surprises have characterized the Uranian rings. The first is their extreme narrowness. Random collisions within the ring would be expected to widen the ring indefinitely. Following their discovery, Goldreich and Tremaine (1979a) hypothesized that so-called "shepherd" satellites could exert a torque on the ring particles to prevent their radial spreading. This theory was dramatically supported by the discovery in 1980 of two shepherd satellites orbiting just inside and outside of Saturn's narrow Ring F (Smith *et al.*, 1981). It was expected that a number of shepherd satellites would be found similarly bracketing the narrow Uranian rings.

The second major surprise was the discovery that many of the rings are both eccentric and inclined to the equatorial plane (Elliot *et al.*, 1977; French *et al.*, 1982). Ring ϵ is by far the most eccentric ring yet observed in the solar system, with an eccentricity of $\sim 1\%$. Prior to these observations, it had been believed that planetary rings would always be approximately circular, because the precession rate of a satellite (such as a ring particle) around an oblate planet is a function of the semimajor axis of the orbit. Therefore, ring particles in an eccentric orbit would precess faster than neighboring particles slightly further from the planet. The resulting collisions would tend to circularize the ring. The observation of clearly eccentric rings resulted in a scramble to find a mechanism which could counteract the differential precession. Not long after the discovery of the Uranian rings, Goldreich and Tremaine (1979b) developed a theory whereby self-gravity between the ring particles supplied the necessary force to balance the differential precession.

The encounter of Voyager 2 with Uranus presented a great opportunity to test out the theories of ring dynamics presented to deal with the Uranian rings from afar. As it turned out, the rings were not quite so well-behaved when viewed close-up. The ring-shepherding theory for confinement fared relatively well with the discovery of shepherd satellites on each side of Ring ϵ. However, no other shepherd satellites larger than $\sim$ 10 km in radius were observed, leaving most of the rings without an obvious source of confinement. For lack of competitors, self-gravity remains the leading contender for explaining locked precession, but several serious difficulties with ring masses and the evolution of profile shape with longitude around the planet were brought to light by results of the Voyager encounter, and by no means may the problem be considered solved.

1.4 Radio Occultation of the Uranian Rings

The subject of the present work is the analysis of the Voyager radio occultation observations of the Uranian rings. The issues discussed above relating to the dynamics of the Uranian rings are one area open to investigation through analysis of the detailed ring profiles obtained from the radio occultation data; an equally important area of research is the study of particle sizes and properties. We have briefly discussed above the differences in particle sizes in the Jovian, Saturnian, Uranian, and Neptunian ring systems. Strict bounds on particle sizes are necessary for any quantitative analysis of the causes of particle size differences. For Uranus, the radio occultation data is the best source for such quantitative information, due to the high signal-to-noise ratio of the measurements, the dual wavelength nature of the experiment, and the wavelength match to particle sizes exceeding ~ 1 cm. Thus ring profiles and their relation to dynamics, and dual-wavelength observations and their implications for particle sizes are the two cornerstones of the research topics addressed in this work.

The following chapters are organized as follows. Chapter 2 contains a description of the radio occultation experiment, including relevant aspects of the occultation geometry, characteristics of the radio system, and a description of the observables of the experiment. This chapter also discusses the sequence of data reduction steps necessary to produce the final data set. The original data must be corrected for frequency drift and antenna gain variability and then converted from samples in time to samples in radial distance from the planet center.

Chapter 3 begins with a description of the final stage of data reduction, in which the data are processed to compensate for the effects of diffraction through an inverse Fresnel filtering operation. For the Uranian rings, it was necessary to extend the diffraction-reconstruction procedures developed for Saturn's rings (Marouf *et al.*, 1986) to allow for reconstruction of elliptical rings. We present the high resolution (50 m) profiles of the nine Uranian rings, and discuss the implications for ring structure and its variation with observation longitude. We then use the high-resolution profiles to investigate two dynamical problems. A method for determining eccentricity gradients of three Uranian rings is developed, and results are compared to the self-gravity predictions, leading to the conclusion that this theory for uniform precession is not entirely correct. Locations for possible unseen shepherd moons are inferred from the radial location of observed abrupt ring edges.

Chapter 4 presents a collective analysis of the 3.6 and 13 cm wavelength observations, including dual-wavelength estimates of integrated optical depths and phase delay for all nine rings. These measurements may be used to constrain the microscopic properties of the rings—that is, ring thickness and particle sizes, assuming a model for the interaction of radio waves with rings. We begin with a summary of Mie theory for scattering by a single homogeneous, spherical, dielectric particle and illustrate how individual particles of different size and refractive index affect the incident wave. Then we describe three models for scattering by ensembles of such particles: the monolayer model, in which all the ring particles lie in a plane, the many-particle-thick model, in which the ring is many particle diameters in vertical extent, and a third model, developed by Zebker *et al.* (1985), which is a hybrid of these two. Each of these models assumes that the scattering behavior of a particle in the ensemble is not coherently affected by the presence of other particles nearby. We use these models along with the measurements to investigate the implications for ring thickness and discuss the interpretation of the radio occultation measurements in light of the standard theories for determining ring particle sizes. Finally, we discuss some problems in the analysis of the dual-wavelength data, such as possible non-sphericity of the particles and possible coherent interactions between neighboring particles.

Chapter 5 deals with the issue of coherent interparticle interactions. An analytical theory for analyzing the scattering behavior of two spherical particles is described, and representative computations that illustrate coherent coupling effects as a function of particle size and separation are presented. In the second part of the chapter, a "pairwise approximation" is developed for extending the two particle results to an ensemble of particles, and its validity is checked against exact computations for finite clusters of spheres. The pairwise approximation is then used to investigate the problem of extinction by a monolayer of particles as a function of increasing packing fraction and results are compared to the standard non-interacting models. Implications for the interpretation of the Uranian ring measurements are also discussed.

Finally, Chapter 6 summarizes the conclusions that can be drawn about the Uranian rings through use of the radio occultation measurements. Important open questions and directions for future work are discussed.

Appendix A consolidates the equations for noise power, and consequently uncertainty intervals, as a function of radial resolution. For completeness, Appendix B presents dual-wavelength profiles of rings not specifically discussed in Chapter 4. Appendix C details the procedures we use to construct an eccentricity gradient profile from the observations.

1.5 Contributions

Specific contributions of this research are as follows:

1. Extension of the diffraction-reconstruction procedures initially developed for circular rings (Marouf *et al.*, 1986) to eccentric rings, allowing high resolution (50 m) reconstruction of Uranian rings (Gresh *et al.*, 1989), and characterization of salient features of these profiles.
2. Development of procedures to determine eccentricity gradients of Uranian Rings α, β, and ϵ based solely on the radio occultation observations. The findings bring into question current theoretical models for observed rigid precession of these rings.
3. Identification of two possible unseen shepherd satellites, each responsible for simultaneously confining three or more sharp ring edges.
4. Analysis of dual-wavelength observations of all nine rings and comparison with the predictions of theoretical models. Placement of bounds on the particle size distributions which are consistent with the radio measurements of Ring ϵ.
5. Placement of constraints on vertical ring structure and physical ring thickness and formulation of a new model of Ring ϵ in which ring thickness may vary with azimuth in inverse proportion to ring width.
6. Analysis of the problem of coherent extinction by a pair of identical spheres and characterization of the results as a function of particle size, particle separation, and pair orientation relative to the incident wave.
7. Development of the pairwise approximation for calculating coherent extinction by an ensemble of identical particles. Application to the problem of coherent extinction by a closely packed monolayer distribution of particles and characterization of the results as a function of packing fraction and incidence angle.
8. Analysis of bending waves in Saturn's rings, leading to estimates of wave height profile, surface mass density, and viscosity in Ring A wave regions. (This analysis is not discussed in this work; see Gresh *et al.* (1986) for details.)

Chapter 2

Description of the Experiment and Data Reduction Procedures

Before interpretation of the data may begin, it is necessary to describe the salient characteristics of the experiment itself. This chapter discusses the relevant aspects of the occultation geometry, the observables of the experiment, and the data processing procedures. Much of the discussion to follow was originally presented in Gresh *et al.* (1989).

2.1 Occultation Geometry

Figure 2 shows the geometry of the Voyager occultation by the Uranian ring system. Note that at the time of the Voyager encounter the mean ring plane was almost orthogonal to the radio path (ring opening angle $B = 81.5°$). Figure 2 also shows that the occultation track resulted in two complete profiles of the ring system, separated ~141–149° in longitude. Overall, the geometry for the Uranian ring occultation was highly favorable for this experiment (See Table 1 for relevant geometric parameters). First, the radial velocity of the occultation ray in the ring plane was a relatively slow 8.2 km-sec^{-1} at both ingress and egress. A slow intercept velocity allows longer integration time per unit distance in the ring plane, and therefore yields a better signal-to-noise ratio. Second, because the rings were almost fully open, the radio path length through the rings was not increased significantly by projection effects, resulting in high signal levels even in large optical depth regions, although this also resulted in a reduced sensitivity to optically thin portions of the rings. The

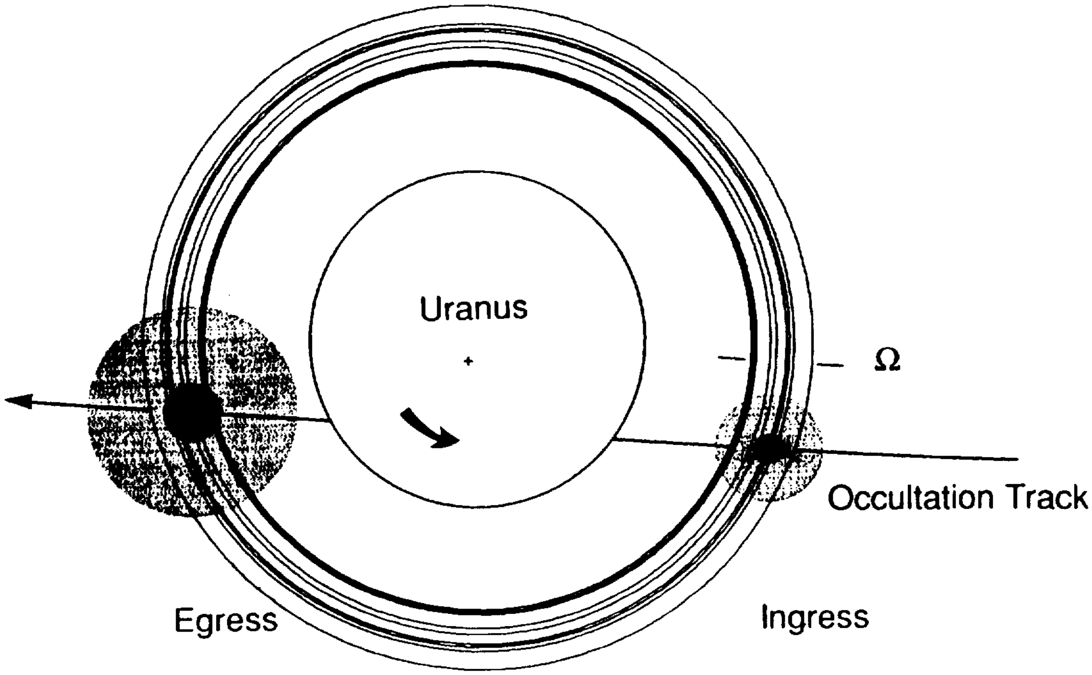

FIG. 2: View from Earth of Voyager radio occultation geometry. The spacecraft passed behind the rings and planet as viewed from Earth, resulting in two complete sets of ring occultations. The grey circles represent the null-to-null antenna beam "footprint" at the ring plane, with the inner and outer circles representing the 3.6 and 13 cm signals, respectively. The ascending node of Uranus' equator on the Earth's mean equator of 1950.0 is a convenient reference for longitude, and is denoted by Ω.

large ring opening was fortuitous, given the particularly large optical depths of the Uranian rings. Finally, the Fresnel scale at Uranus was 1.6–2.3 km at wavelength $\lambda = 3.6$ cm, allowing high spatial resolution in the reconstruction of initially diffraction-limited observations. This combination of conditions has allowed reconstruction of ring optical depth profiles with acceptable noise levels to resolutions as fine as 50 m; the reconstruction has been performed at even finer resolution (20 m) for study of selected features.

2.2 Radio System Configuration

The radio occultation experiment used the Ultra-Stable Oscillator on board Voyager as a reference frequency standard for the emitted radio signal (typical short term stability $\simeq 2$–5×10^{-12} over 1 sec; Eshleman *et al.*, 1977). Two harmonically-related, right-circularly-polarized signals at wavelengths of

Assumed pole of Uranus[a]	α: 76.5969°	δ: 15.1117°
Angle of ring opening, B	81.5°	
Location of Receiving antenna (Canberra, Australia)	lat: -35.22092°	long: -148.98128°
Frequency and Wavelength	$f_0 = 8420430456.1$ Hz, $\lambda = 3.560$ cm (X-Band) $f_0 = 2296481033.5$ Hz, $\lambda = 13.054$ cm (S-Band)	
	Ingress	Egress
Elevation angle of receiving antenna	77–75°	59–55°
Light-time, Voyager 2 to Earth (sec)	9890.7	9890.5
Azimuth[b] (deg)	344.6–341.1	199.7–196.0
Radial Velocity (km-sec^{-2})	(–) 8.2–8.1	8.2–8.3
Distance[c] (10^5 km)	1.4–1.6	2.8–2.9
Fresnel Scale F^d (km)		
$\lambda = 3.560$ cm	1.6–1.7	2.2–2.3
$\lambda = 13.054$ cm	3.0–3.2	4.3–4.4

TABLE 1: Selected geometric and operating parameters (Additional details may be found in Table 1 of Gresh *et al.*, 1989).

[a]: Right ascension, α, and declination δ are from French *et al.* (1988).

[b]: Measured in the direction of particle motion (prograde) in the ring plane from the ascending node of the ring on the Earth's mean equator of 1950.0 to the occultation track.

[c]: Distance from the spacecraft to the equatorial plane along the line-of-sight.

[d]: Defined by Eq. (6) of Marouf *et al.* (1986).

approximately 3.6 and 13 cm were transmitted simultaneously. The co-polarized signal components were received on Earth at three stations. Both the 3.6 and 13 cm signals were received at the 64 m NASA Deep Space Network antenna in Canberra, Australia. In addition, the 13 cm signal was received at a 34 m antenna in Canberra, and the 3.6 cm signal was received at the Parkes Radio Astronomy Observatory 64 m antenna, also in Australia. Results presented here use the data from the 64 m Canberra antenna exclusively except where otherwise noted. The free-space signal-to-noise ratios in a 1 Hz bandwidth (SNR_0) for these signals were approximately 46 and 32 dB for the 3.6 and 13 cm data, respectively[1]. On the ground, the station frequency reference sources were atomic clocks, so the spacecraft source is the limiting element for frequency stability.

2.3 Observables

The received signal can be decomposed into coherent and scattered components. The coherent signal is the coherent sum of the transmitted sinusoidal wave and the individual scattered waves for particles very close to the line of sight. The result is a wave which, relative to the original wave, is reduced in amplitude and delayed or advanced in phase by its interaction with ring material. The scattered signal is the incoherent superposition of all waves scattered in the direction of the Earth by ring particles illuminated by the spacecraft antenna.

Both the amplitude and the relative phase of the coherent signal are measured accurately by this experiment. The radio occultation experiment measures E_c, which is the complex field strength of the coherent received signal. After correction for diffraction effects, the normal optical depth τ and coherent phase ϕ_c may be calculated from

$$E_c/E_0 = X_R + iX_I = \exp[-\tau/2\mu_0 + i\phi_c]$$

where $\mu_0 = \sin(B)$ is the ring opening projection, E_0 is the value of the field strength in the absence of rings and (X_R, X_I) is the normalized complex signal amplitude. Thus optical depth τ is a measure of the reduction in signal amplitude by the ring, while ϕ_c represents the change from the phase of the signal in free space; a positive value indicates phase retardation, a negative value phase advance.

Additive noise limitations on measurements of τ and ϕ_c can be estimated from results in Appendix A. At 1 km resolution, for example, $\mathrm{SNR}_0 = 46$ dB implies a 1-σ detection threshold of $\tau \simeq 0.02$ and $\phi_c \simeq 3.5 \times 10^{-3}$ cycles. It also implies a SNR of better than 10 dB for rings of

---

[1] SNR in dB is defined as $10\log_{10}(P_S/P_N)$, where P_S is the signal power and P_N is the noise power in a specified bandwidth.

opacity $\tau \leq 6$. The availability of such a broad dynamic range for measurement of τ has proven indispensable for observing both the tenuous and optically thick features that typify several of the Uranian rings.

Waves scattered by a ring can be distinguished from the coherent wave by a shift in frequency of the scattered signals. This frequency change is a Doppler effect introduced by the relative motion of the spacecraft and the ring particles. In cases where the spacecraft orbit is otherwise largely unconstrained, as was the case for the Voyager 1 ring occultation at Saturn, it is possible to optimize the geometry so that ring particles at a constant radius from the center of the planet scatter at approximately the same Doppler shift. This facilitates detection by concentrating the signal scattered by any individual ring feature into a narrow portion of the spectrum (Marouf *et al.*, 1982; Marouf *et al.*, 1983). In the Saturn occultation experiment, the observed scattered signal was used to infer the shape of the forward diffraction lobe of the rings large particles, which allowed, through direct inversion, recovery of the rings' particle size distribution (Marouf *et al.*, 1983; Zebker *et al.*, 1985).

No such trajectory optimization took place at Uranus, as flyby conditions were constrained by the gravity assist required to encounter Neptune; consequently, the signal from an individual ring was spread into a large bandwidth ($\simeq$ 3 kHz). Furthermore, because the Uranian rings are physically narrow, the surface area available for scattering is small. For these reasons, the scattered signal was expected to be approximately 20 dB below the noise level. Surprisingly, a strong "anomalous" scattered signal was actually observed in the neighborhood of Ring ϵ. This signal component is not discussed further in this work (see, however, Tyler *et al.*, 1986; Gresh *et al.*, 1989).

2.4 Reduction of Observations

The radio signals which are received on the ground must go through a series of processing stages to prepare them for analysis. These stages include the removal of non-ring-related frequency variations, correction for antenna pointing errors, conversion from samples equally spaced in time to samples equally spaced in distance from Uranus, and most importantly, reconstruction of the initially diffraction-limited profiles of the rings.

The analog signals received at the Earth stations were first heterodyned to baseband frequency, sampled, and quantized for recording on magnetic tape. Original data bandwidths of 25 kHz and 40 kHz for the Canberra and Parkes data, respectively, are much larger than the spectral width containing information relevant to diffraction reconstruction procedures, so several stages of filtering were undertaken to reduce the bandwidth.

Frequency offsets due to Doppler shifts from the relative motion of the Earth and spacecraft and special and general relativistic effects in the gravitational fields of Uranus and the Sun were removed to a level of approximately 0.1 Hz by digitally "steering" (that is, compensating) the data (Tyler *et al.*, 1983; Tyler, 1987). Correction for the effects just listed is referred to as first-order steering. Remaining residual drifts, presumably caused by reference oscillator instabilities, the medium through which the signals propagate (which includes the interplanetary medium and Earth's atmosphere), and residual errors in the spacecraft trajectory, are removed in two more stages of steering. In the first of these, a polynomial is fit to the phase in clear regions between the rings and the polynomial is subtracted from the signal phase. This is termed second-order steering. The slowly varying component of the residual frequency error can be removed in a final stage, third-order steering, by taking advantage of the sparse nature of the Uranian rings to estimate the residual long term ($\gtrsim$ 3 sec) phase variations and eliminate them. This is accomplished empirically by dividing the data by a unit-magnitude low-pass filtered version of itself, the filtering chosen so that ring-related frequency changes are not affected. The residual phase fluctuations after filtering behave like a zero mean random process with peak value not exceeding about 10 millicycles. Because we are able to remove essentially all the effects of the interplanetary medium and the reference frequency instabilities, very high resolution diffraction correction is possible (see Figure 11, Marouf *et al.*, 1986). Note that amplitude variations, such as might be caused by a broad tenuous ring, are not affected by this procedure. Given the phase-steered data set, further reduction in bandwidth may take place, depending on the desired radial resolution of the final data set and on the geometrical mapping of time sampling to radius sampling.

While the original data are sampled uniformly in time, efficient reconstruction of the diffraction-limited profile requires that the data samples be spaced uniformly in radial distance from the planet in the ring plane. An interpolation step is required to change from time to radius sampling. Before this step, we apply a continuously-varying anti-aliasing filter to the data to ensure that the interpolation stage does not anywhere undersample the data.

Uncertainties in orientation of the ring plane translate directly into uncertainties in the radial location assigned to a given time sample. However, as the incidence direction for the radio occultation geometry at Uranus was almost orthogonal to the mean ring plane, the intersection radius in this experiment is relatively insensitive to small errors in pole direction. In particular, the ingress geometry is highly insensitive to overall changes in pole direction, thereby allowing calculation of an extremely accurate radial scale. French *et al.* (1988) estimate the 1-σ uncertainty in the right-ascension (α) and declination (δ) of the pole to be 0.06 mrad, which implies a maximum error in radial location for our data from this source of less than 300 m. As a result, the primary source of uncertainty in the radial scale is due to timing uncertainty in Voyager's trajectory.

Presently, there is no formal *a posteriori* estimate of the uncertainty in the Voyager trajectory solution. There are strong indications that the level of error is a few kilometers, or perhaps 1–2 km 1-σ. First, *a priori* estimates indicate that, given the quantity and quality of tracking data obtained, the uncertainties would be of the order of 1 km (Van Allen *et al.*, 1982). Examination of the Doppler tracking residuals indicates that the solution obtained is of the quality expected, so the *a priori* estimates are believed to be valid (Gray, 1988). Second, the atmospheric occultation of Uranus, which took place in the interval between the two periods of ring occultation, is consistent with a trajectory uncertainty of a few kilometers (Lindal *et al.*, 1987). Finally, combining the radio occultation with Earth-based stellar occultations and Voyager PPS[2] and UVS[3] stellar occultations results in a solution for ring particle orbits which is consistent at the level of approximately 1 km (French *et al.*, 1988). On the basis of these considerations we adopt an uncertainty of 1 km (1-σ) as the probable uncertainty in the radial location of the rings as derived for the data here.

Errors in radial scale resulting from the assumption that the rings lie in the equatorial plane can amount to several kilometers (French, 1987). Several of the rings are known to exhibit small but significant inclination with respect to the mean plane (French *et al.*, 1982; Smith *et al.*, 1986; French *et al.*, 1988); that is, individual ring planes are each defined by a slightly different normal. In the data considered here, each ring was processed individually using the pole orientation appropriate for that ring; the right ascension α_r and declination δ_r of individual ring normals (or poles) used are given in Table 2. Errors in the radial scale due to uncertainty in the orientation of the line of nodes and in the inclination of the ring imply errors of 150 m or less, even for the most inclined rings. Also included in Table 2 are the semimajor axis a and eccentricity e for each ring as given in French *et al.* (1988); these are used in the reconstruction of the diffraction-limited observations as described below.

A final step in the preliminary data reduction corrected the signal amplitude for fluctuations introduced by known variations in pointing of the spacecraft and ground antennas. The spacecraft pointing was reconstructed by the Voyager Spacecraft Team at the Jet Propulsion Laboratory, while the ground pointing was calculated through modeling by personnel of the Deep Space Network.

---

[2] Photopolarimeter, $\lambda = 0.27\mu$m

[3] Ultraviolet Spectrometer, $\lambda = 0.11\mu$m

				Ingress		Egress	
Ring	a (km)	$e \times 10^3$	i (deg)	$\alpha_r{}^b$ (deg)	$\delta_r{}^b$ (deg)	α_r (deg)	δ_r (deg)
6	41837.15	1.013	0.0616	76.6587	15.0964	76.6586	15.0961
5	42234.82	1.899	0.0536	76.5426	15.1004	76.5426	15.1007
4	42570.91	1.059	0.0323	76.5764	15.0862	76.5763	15.0863
α	44718.45	0.761	0.0152	76.5940	15.1266	76.5941	15.1267
β	45661.03	0.442	0.0051	76.5937	15.1158	76.5937	15.1158
η	47175.91	(0.004)	0.0011	76.5980	15.1116	76.5980	15.1116
γ	47626.87	0.109	0.0015	76.5964	15.1103	76.5964	15.1103
δ	48300.12	0.004	0.0011	76.5958	15.1118	76.5958	15.1118
ϵ	51149.32	7.936	0.0002	76.5970	15.1119	76.5970	15.1119

Table 2: Elements of Keplerian ring orbits used in processing[a]

[a]: Adapted from Table XIV of French *et al.* (1988). (a, e, and i denote, respectively, semimajor axis, eccentricity, and inclination).
[b]: Because of varying inclination of individual rings, profile reconstruction with accurate radial scale requires specification of a different ring plane normal (or pole) for each ring. α_r and δ_r denote right ascension and declination of individual poles used in processing.

Both systematic and random signal fluctuations persist in the corrected data, most likely due to unmodeled errors in ground antenna pointing. The random fluctuations have characteristic spatial scales of ~500–5000 km (time scale ~ 1–10 minutes) and maximum fluctuations in optical depth $\tau \simeq 0.05$ (~ 0.2 dB signal power). The magnitude of the fluctuations is comparable to the fluctuations due to signal-to-noise limitations at 1 km resolution, and their persistence over relatively long periods of time degrades our ability to detect very broad ($\gtrsim$500 km wide) tenuous rings; they are much less significant for the detection of narrower tenuous features ($\lesssim$ 100 km wide), as demonstrated below.

2.5 Discussion

The experimental conditions and the data processing procedures for preliminary processing of the raw radio data have been described above. The next two chapters will detail the way in which the raw data are further processed and analyzed to infer a wide range of structural, dynamical, and physical properties of the rings. Conceptually, this work is divided fairly neatly into two areas, and the following two chapters follow this natural division.

Chapter 3 is concerned with the overall structure and dynamics of the Uranian rings. In order to accomplish this study, it is necessary to have high resolution profiles with which to work. First we describe the diffraction-correction procedures, particularly the alterations which were made to standard procedures to allow high resolution reconstruction of the significantly eccentric Uranian rings. The result of this reconstruction is a set of high resolution (50 m) profiles which serve as the basis of further study of ring structure and dynamics in the ensuing sections of the chapter.

Chapter 4 is concerned with the ways in which the radio occultation data may be applied to determine the "microscopic" properties of the Uranian rings. In that chapter we present dual-wavelength optical depth and phase delay profiles, and show how they can be used to infer physical properties of the rings, such as ring thickness and particle size distributions.

Chapter 3

High-Resolution Profiles and Implications for Structure and Dynamics

In Chapter 2 we briefly described the experimental conditions and the data reduction procedures. The result of this preliminary processing of the data is a diffraction-limited set of amplitude and phase measurements. The resolution is on the order of the Fresnel scale—a few kilometers for the geometry at Uranus (see Table 1). Since eight of the Uranian rings are only a few to several kilometers wide, this would seriously limit our ability to study the structure and dynamics of these rings. However, preservation of phase information in this experiment allows for reconstruction of the diffraction-limited observations to achieve resolutions much finer than the Fresnel scale.

In this chapter we briefly review the diffraction-correction procedures, which were initially developed for the locally almost-circular Saturnian rings (Marouf *et al.*, 1986), and describe the changes made to the procedures in order to reconstruct the significantly elliptical Uranian rings. Then, we present the reconstructed high-resolution profiles and describe qualitatively the appearance of the rings, and the variation in ring structure between the two observation azimuths. In addition, we present quantitative measures of ring location, ring width, and edge sharpness.

The reconstructed radio occultation profiles have implications for dynamical problems associated with the rings. As discussed briefly in Chapter 1, the significant eccentricity of many of the Uranian rings presented theoreticians with a problem: How can the eccentricity of a ring be maintained despite differential precession of individual streamlines around an oblate planet? In Section 3.5, we derive an eccentricity gradient from the two observed ring profiles, and compare it to that implied by the current leading theory for maintaining uniform ring precession, finding significant discrepancies.

A second problem which may be addressed with the aid of the high resolution profiles is the issue of ring confinement. Voyager 2 observed two shepherd satellites bracketing Ring ϵ. It is clear that these satellites are associated with the confinement of this ring, and most likely also confine the outer edges of Rings γ and δ (Porco and Goldreich, 1987). However, the failure of Voyager to detect any other shepherd satellites leaves the confinement of most of the ring edges unexplained, despite the fact that many of these edges are sharp, indicative of a confinement mechanism at work. In Section 3.6 we discuss the results of a search for possible locations of satellites too small to be seen by the Voyager cameras.

3.1 Reconstruction of Diffraction-Limited Observations

The original procedures for diffraction reconstruction were developed by Marouf *et al.* (1986) for the Saturnian rings. The preservation of the phase of the diffracted wave allows removal of diffraction effects, resulting in radial resolution much finer than the Fresnel scale. This has been crucial in studying many dynamical problems in both Saturn's and Uranus' rings. Following Marouf *et al.* (1986), we begin with a summary description of the procedure for circular rings, and then indicate the modifications necessary for the eccentric Uranian rings.

Voyager transmitted a nearly pure monochromatic wave which passed through the rings and was later received on Earth. In the absence of noise, one observes a profile of transmittance $\hat{T}(\rho_0, \phi_0)$, where (ρ_0, ϕ_0) is the radius and azimuthal position angle with respect to the planet of the ring intercept point (see Figure 1 in Marouf *et al.* for geometry). The ring intercept point is the intersection of the ray from Voyager to Earth with the ring plane, and may be calculated from knowledge of the positions of Voyager, Uranus, and Earth as described in Rosen (1989), Appendix B. The transmittance $\hat{T}$ is the normalized amplitude and phase of the diffracted received signal. What we wish to find is the actual ring transmittance T, which would be the amplitude and phase of the wave observed just beyond the ring plane. $\hat{T}$ and T are related through Huygens' principle as:

$$\hat{T}(\overline{\rho}_0) = \hat{T}(\rho_0, \phi_0) = \frac{\mu_0}{i\lambda} \int_0^{2\pi} \int_0^{\infty} \frac{T(\rho, \phi) e^{i\psi(\rho_0, \phi_0; \rho, \phi)}}{|\overline{R}_c - \overline{\rho}|} \rho \, d\rho \, d\phi, \qquad (1)$$

where $\mu_0 = \sin(B)$, B is the ring opening, λ is the observation wavelength, $\overline{R}_c$ is the vector from the planet to the spacecraft, and the phase ψ is given by

$$\psi(\rho_0, \phi_0; \rho, \phi) = kD\left[\sqrt{1+2\xi+\eta} - (1+\xi)\right],$$

where

$$\xi = \cos B(\rho_0 \cos\phi_0 - \rho\cos\phi)$$

$$\eta = [\rho_o^2 + \rho^2 - 2\rho\rho_0\cos(\phi - \phi_0)]/D^2,$$

$D = |\overline{R}_c - \overline{\rho}_0|$ and $k = 2\pi/\lambda$.

Under the assumption of azimuthal symmetry, $T(\rho, \phi) = T(\rho)$, and Eq. 1 simplifies to

$$\hat{T}(\rho_0, \phi_0) = \frac{\mu_0}{i\lambda}\int_0^\infty d\rho\,\rho\,T(\rho)\int_0^{2\pi}\frac{e^{i\psi(\rho_0,\phi_0;\rho,\phi)}}{|\overline{R}_c - \overline{\rho}|}d\phi. \tag{2}$$

The ϕ integral may be evaluated by the stationary phase method (Marouf *et al.*, 1986). The resulting one-dimensional integral may then be inverted, and as a result $T(\rho)$ may be determined. In reality, one recovers the normalized complex amplitude $X \equiv X_R + iX_I = T + n$, where n is the additive noise contribution.

The improvement achieved from such reconstruction is best illustrated by an example. Figure 3 shows both measured and reconstructed (resolution = 50 m) opacity and phase shift profiles of Ring δ at egress. Disregarding the phase information, the nearly symmetric diffraction-limited τ profile is highly suggestive of a classical diffraction pattern of an opaque narrow strip, a model usually used to interpret Earth-based observations of the rings (*v.*, *e.g.*, French *et al.*, 1988). With the phase information considered, however, the reconstruction reveals a highly asymmetric ring profile with significant structure across its $\simeq$ 3 km width.

The reconstruction procedures described above assume the rings to be at least locally circularly symmetric, with the center of the circle coincident with the center of the planet. This assumption was approximately met for the Saturnian rings for which these procedures were developed, but does not hold for at least six of the Uranian rings (6, 5, 4, α, β, and ϵ), all of which exhibit small but measurable eccentricity ($e \sim 5 \times 10^{-4}$ to 8×10^{-3}; French *et al.*, 1988). Eccentricities of this order affect profile reconstruction at resolutions $\lesssim$ 200 m; characteristic signs of poor "focussing" include overshoots of free-space signal levels or ringing near some sharp edges.

The significant eccentricity of the Uranian rings prompted us to modify the diffraction-reconstruction procedures to allow the highest possible resolution reconstruction of the ring profiles. All of the

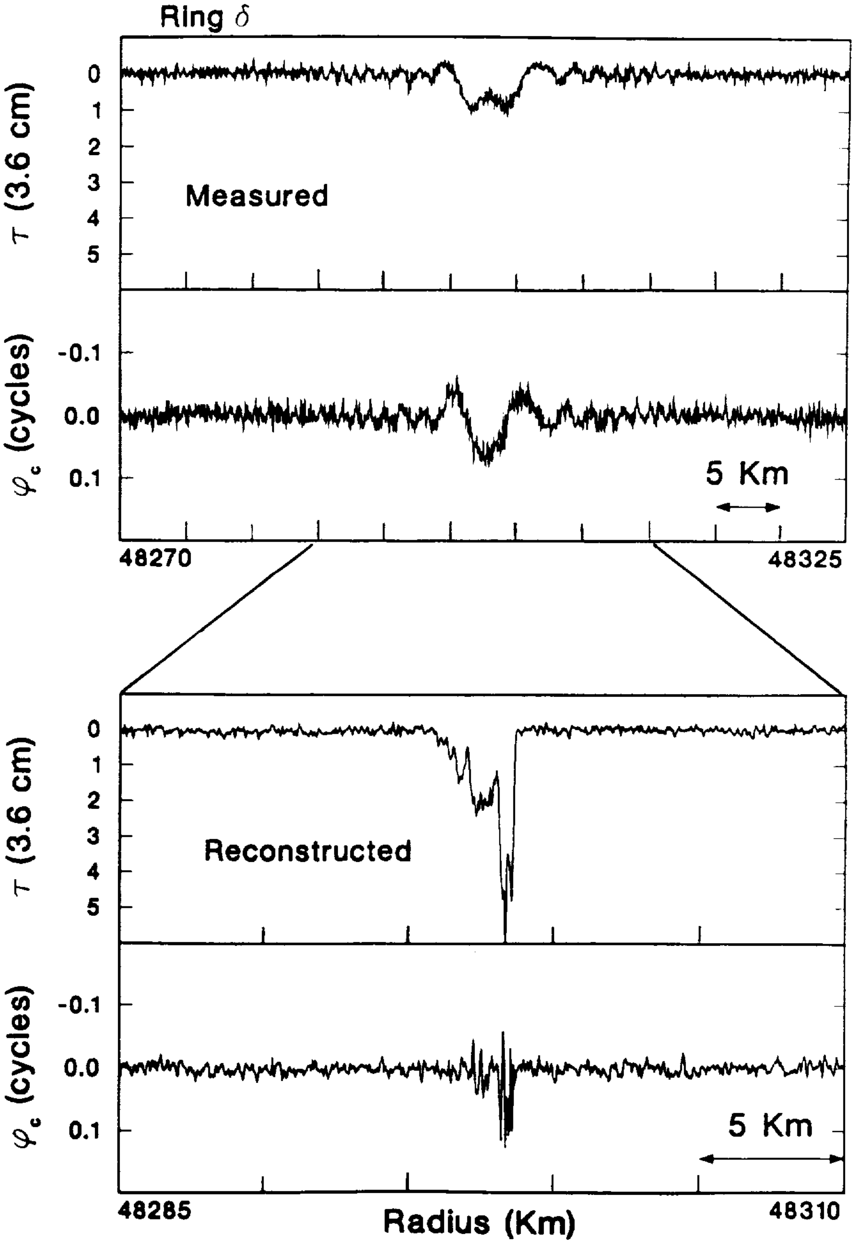

FIG. 3: Diffraction reconstruction of Ring δ egress profile. Top two panels are the initial diffraction-limited optical depth and phase profiles; bottom panels are the corresponding profiles reconstructed at 50 m resolution. Note the marked asymmetry of the reconstructed opacity profile despite an apparently symmetric opacity diffraction pattern.

profiles discussed in this work have been reconstructed using the eccentric ring algorithm. The modifications are as follows: Consider a ring for which T is constant not along a fixed radius as for a circular ring, but rather along some set of contours $\rho = f(\phi)$. In particular, we consider elliptical contours of the form

$$\rho = a(1-e^2)/(1+e\cos(\phi-\omega)), \tag{3}$$

assumed to be parameterized by the semimajor axis a. The eccentricity e and angle of periapse ω are assumed constant; $\phi - \omega$ denotes the true anomaly[1].

Note that in Eq. 3 every point (ρ, ϕ) in the ring plane is associated with a unique ellipse. Therefore, the transmittance $T(\rho, \phi)$ may be written as

$$T(\rho,\phi) = T(a) = \int_{-\infty}^{\infty} \delta[a-a']T(a')da', \tag{4}$$

where $\delta[\cdot]$ is the Dirac delta function and the lower limit of the integral is for mathematical convenience. Substituting Eq. 4 in Eq. 1, one obtains

$$\hat{T}(\rho_0,\phi_0) = \frac{\mu_0}{i\lambda}\int_{-\infty}^{\infty} da'T(a')\left[\int_0^{2\pi}\int_0^{\infty}\delta[a-a']\frac{e^{i\psi(\rho_0,\phi_0;\rho,\phi)}}{|\bar{R}_c-\bar{\rho}|}\rho\, d\rho\, d\phi\right].$$

The δ-function in the integrand may be used to reduce the double integral over ρ and ϕ to a single integral along the contour C along which (ρ, ϕ) satisfies Eq. 3 for $a = a'$. The result is

$$\hat{T}(\rho_0,\phi_0) = \frac{\mu_0}{i\lambda}\int_{-\infty}^{+\infty} da'T(a')\int_C \frac{e^{i\psi(\rho_0,\phi_0;\rho,\phi)}}{|\bar{R}_c-\bar{\rho}|}\frac{dl}{|\nabla a'(\rho,\phi)|}, \tag{5}$$

where dl is an element of length along C and $\nabla a'$ denotes the two-dimensional gradient of a' with respect to ρ and ϕ.

To evaluate the integral along C, we use the method of stationary phase to search along the contour C for the pair (ρ_s, ϕ_s) such that

$$\left.\frac{d\psi}{d\phi}\right|_{\phi_s} = \left.\left(\frac{\partial\psi}{\partial\phi}+\frac{\partial\psi}{\partial\rho}\frac{\partial\rho}{\partial\phi}\right)\right|_{\phi_s} = 0. \tag{6}$$

Neglecting the effect of eccentricity on $d^2\psi/d\phi^2$ at $\phi = \phi_s$, we obtain

---

[1] True anomaly is the angular distance in the orbit plane from periapsis, measured in the direction of motion. Periapsis is the point on the orbit closest to the planet. For future reference, apoapsis is the point on the orbit farthest from the planet.

$$\hat{T}(\rho_0,\phi_0) \simeq \frac{1-i1}{2F} \int\limits_{-\infty}^{\infty} T(\rho')e^{i\psi(\rho_0,\phi_0;\rho_s,\phi_s)}d\rho', \qquad (7)$$

where we have replaced a' by the radius ρ' at which the contour C intersects the occultation track and F denotes the Fresnel scale defined by Eq. 6 of Marouf *et al.* (1986). Eq. 7 differs from the corresponding equation for a circular ring (Eq. 5 of Marouf *et al.*, 1986) only in the different stationary phase point, hence procedures previously developed to reconstruct T from observed $\hat{T}$ can also be used here.

To illustrate, Figure 4a shows a simulated diffraction pattern generated using Voyager's occultation geometry and assuming an opaque, elliptical, knife-edge that has eccentricity and radial location coincident with the outer edge of Ring ϵ at ingress. Figure 4b shows a 20 m resolution reconstructed profile of the "data" in Figure 4a, assuming the incorrect, circular-ring model. The reconstruction greatly sharpens the diffraction-limited edge, but a slow rise followed by oscillations is noticable at a much finer scale. The substantial improvement in the reconstructed profile when the correct, elliptical-ring model is used is clearly evident in Figure 4c, where a "clean" transition occurs over the (20 m) extent of a resolution element (note the expansion of scale of Figures 4b and 4c). In comparison, Figure 5 shows the results of applying these reconstruction models to actual observations. Similar improvement is also evident in Figure 5c. A small but persistent residual overshoot in Figure 5c indicates that unmodeled perturbations in the assumed Keplerian ellipse model of the outer edge of Ring ϵ may persist.

3.2 High Resolution Profiles

Above, we have described the way in which the raw radio occultation data have been processed to remove the effects of diffraction and significantly improve the radial resolution of the data. This step was critical in order to proceed with analysis of the structure and dynamics of the rings, as almost all of the structure was masked by diffraction. Due to approximately 14 dB higher signal-to-noise ratio of the 3.6 cm data relative to the 13 cm data, this analysis was performed only for the shorter wavelength. However, as we shall see in Chapter 4, the 13 cm data are useful in constraining particle sizes in the rings.

Global profiles of the entire Uranian ring system as observed at 3.6 cm wavelength are presented in Figure 6. The nine pre-Voyager rings are visible at both ingress and egress. In addition, we detect the tenuous companions of Rings η and δ. No other ring features are detectable in the radio data

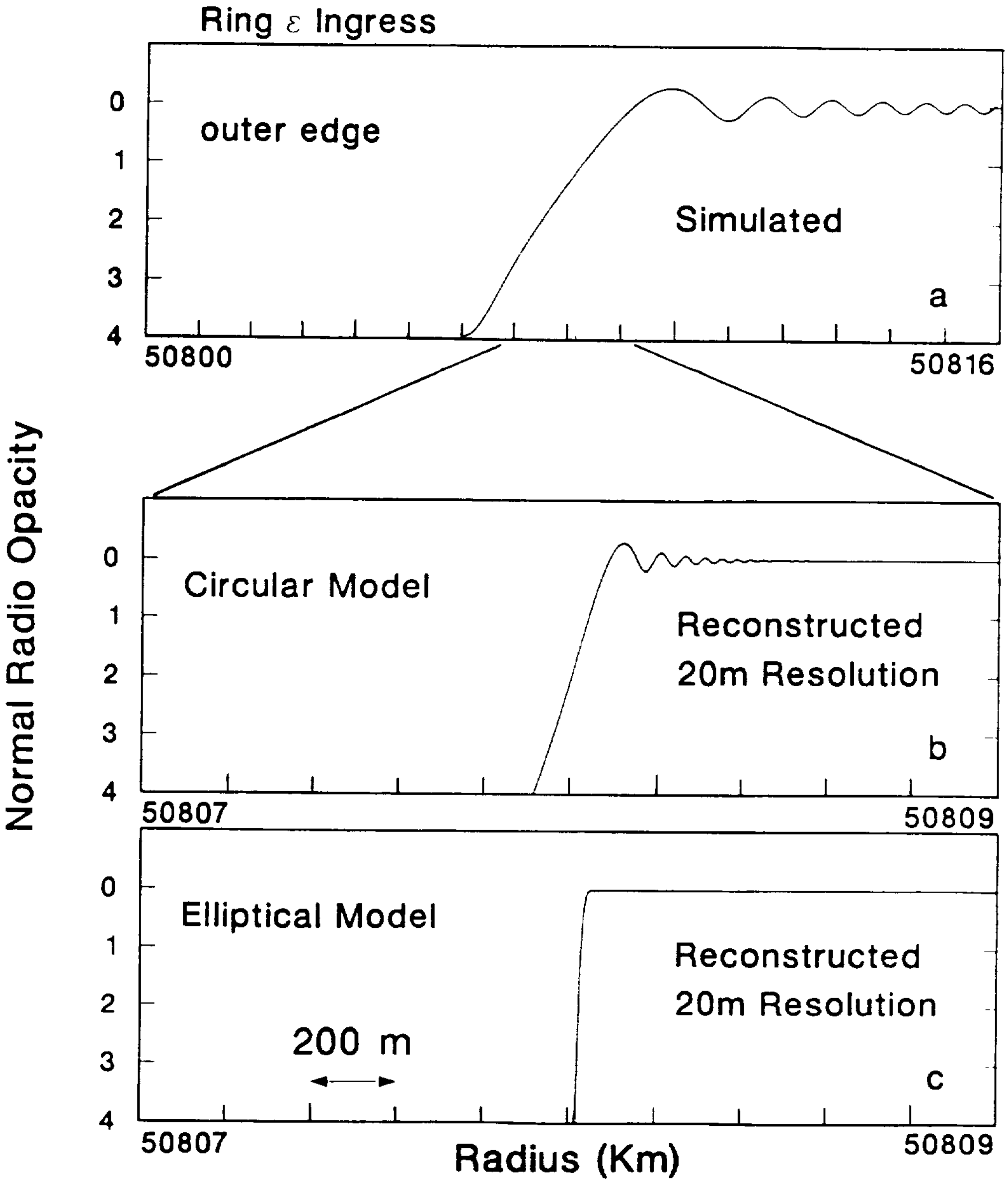

FIG. 4: Reconstruction of simulated diffraction by an elliptical, opaque knife-edged ring. The simulated edge has the same eccentricity, semi-major axis and true anomaly as the outer edge of Ring ϵ as observed by the radio experiment at ingress. Profile (a) is the simulated observed diffraction pattern. Profile (b) has been reconstructed using a circular-ring model, while profile (c) is reconstructed using an algorithm that incorporates ring ellipticity (Appendix B). Note the "clean" transition to free space signal level in the latter case. The two reconstructed profiles (b, c) were processed to a resolution of 20 m. Note expansion of scale in two lower panels.

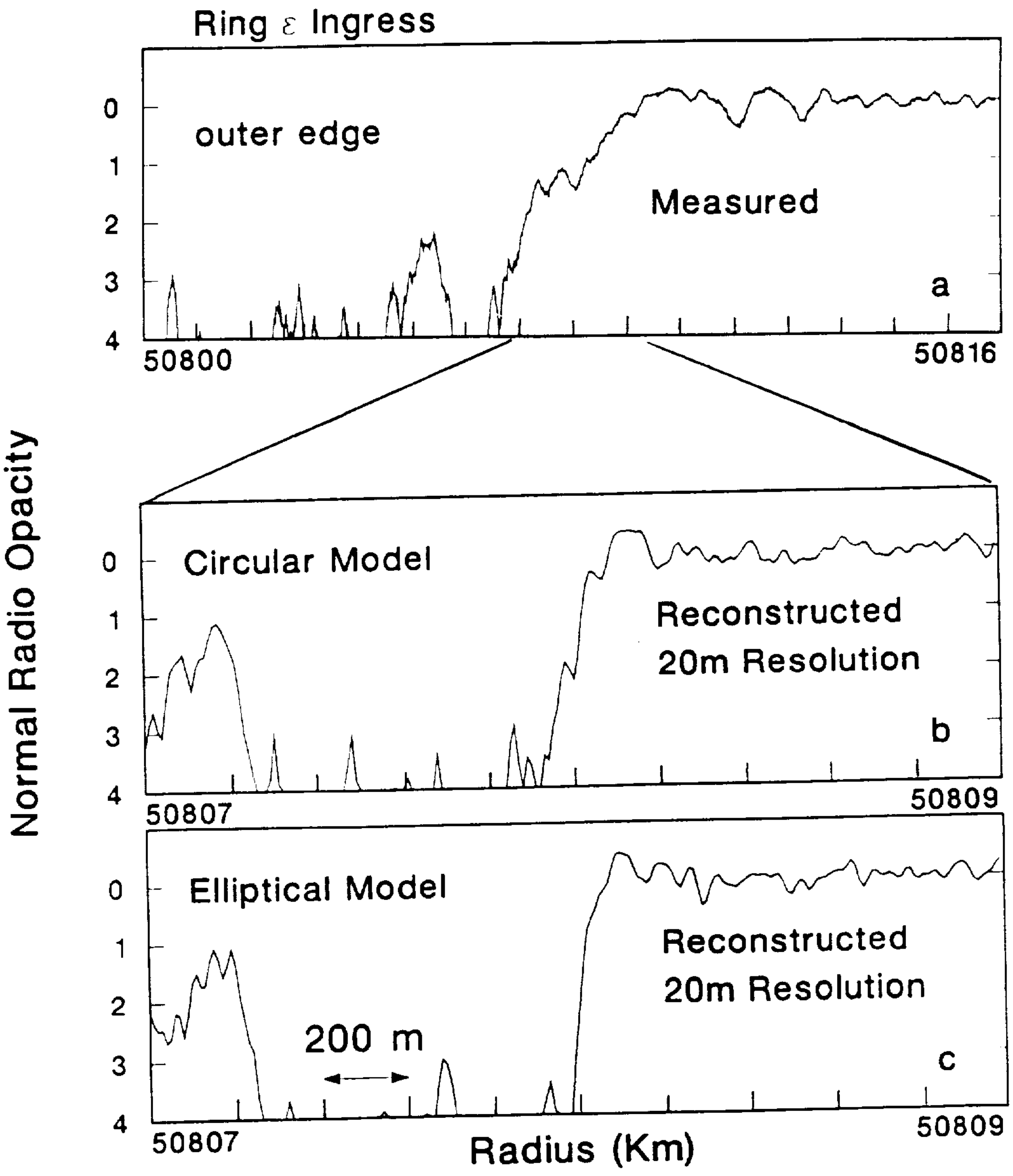

FIG. 5: Reconstruction of outer edge of Ring ϵ at ingress. All panels are identical in scale and contents to those shown in Figure 4, except actual observed data are used here. The reconstructed profiles (b, c) in Figure 4 and this figure show that significant improvement in edge sharpness is achieved when an elliptical ring model is used instead of a circular one.

within the limitations of baseline fluctuations and noise. Figures 7–18 show the radio opacity profiles (optical depth profiles at 3.6 cm wavelength) of the nine rings. The heavy line in these figures is the 50 m resolution profile, and, except for Figures 17 and 18, the lighter line is the 200 m resolution profile, for which the noise is significantly reduced. For Ring ϵ, the 200 m resolution profiles are shown separately, in Figure 19.

The high resolution profiles reveal a ring system of remarkable morphological variability which may be divided into three main groups. Group 1 includes the three outer rings (γ, δ, and ϵ), which are characterized by ring features of unusually large values of optical depth ($\tau > 3$). The most extreme member of this group is Ring γ, which has very sharp edges despite an optical depth at egress exceeding ~ 6 and a width of only ~ 1.6 km. Rings γ and ϵ share the distinction of being the only two rings in the system that exhibit very sharp inner and outer edges at both observation azimuths. The outer edge of Ring δ is also sharp, while the inner edge is significantly different in character, falling almost exponentially towards $\tau = 0$ at both radio observation azimuths. Ring δ is distinguished by the only clearly regular structure observable in the ring system, appearing in the egress profile (Figure 16) as wave-like fluctuations superposed on the graded inner edge of the ring. The fluctuations are marginally detectable in the ingress profile. Significant radial structure characterizes the Ring ϵ egress profile; however, no evidence for wave-like structures is immediately apparent.

The diffraction reconstruction algorithm for Ring γ at egress has incorporated a canting angle of approximately -0.1° from the nominal ellipse. This angle was chosen empirically as discussed in more detail in Gresh *et al.* (1989) to remove obvious "ringing" observed near the edges of this ring. This canting may be indicative of a perturbation of the ring edge by the shepherding satellite Ophelia, or it may be a result of the viscous instability of the ring which results in a "breathing" inward and outward motion as discussed by French *et al.* (1988).

Group 2 includes Rings α and β. Both are relatively broad and are characterized by diffuse edges, at least at one observation azimuth. Among the nine rings, Ring β has the most diffuse edges, the smallest overall opacity, and the least distinct radial structure. The Ring α ingress profile exhibits a diffuse inner edge, with a distinct tenuous feature of opacity $\tau \simeq 0.25$ and width $\simeq 3.5$ km. Remarkably, the inner feature in the egress profile is completely different in nature, appearing as a nearly detached, relatively dense, and very narrow feature. At this azimuth, both edges of Ring α are relatively sharp, and significant structure is apparent across the ring.

Group 3 includes the three innermost rings, Rings 6, 5, and 4. All three are characterized by widths of ~2–3 kilometers, which are small compared to Groups 1 and 2, and moderate optical depths of order 1–2, which are small compared to Group 1. They all possess an abrupt outer, quasi-exponential inner edge.

Ring η is somewhat of a puzzle. It is the most "circular" ring among the nine observed. By location it belongs to Group 1, and shares the circularity property with two other nearly circular members, Rings γ and δ. It also shares with Ring δ the distinction of being one of only two rings that possess detectable broad tenuous companions (see below). Yet morphologically its ~1.5 km width, its near unit opacity, and its edge behavior suggest strong similarities to Group 3 rings (6, 5, and 4). However, while its edge behavior is morphologically similar to Rings 6, 5, 4, and also δ, it is exactly reversed. Indeed, Ring η is the only ring among the nine observed that exhibits a sharp *inner* edge and diffuse, apparently exponentially shaped *outer* edge. Perhaps Ring η deserves a group all by itself, Group 4!

Regardless of designation, significant changes in profile morphology with azimuth are observed for almost all rings. Five of the six known elliptical rings were occulted by Voyager once close to periapse. This is remarkable, given the chance nature of such events. In three of these five cases (α, β, and ϵ), the near-periapse profiles are narrower and have higher opacity. While significant longitudinal changes are also evident for the other two rings (6 and 5), the morphology does not appear to be strongly correlated with true anomaly. Ring 4 was occulted at almost exactly ±71° from periapse. The observed profile morphology is indeed similar in overall behavior, nonetheless differences in width and optical depth between the two profiles are evident. The morphology is very similar to that observed for Ring 5 at 8° from periapse, again pointing to the fact that profile morphology of Rings 6, 5, and 4 is probably not strongly correlated with true anomaly.

The three nearly circular rings (η, γ, and δ) also show significant differences with azimuth. Despite nearly constant width and overall opacity, a striking change in the morphology of Ring η is evident. Rings γ and δ, on the other hand, behave very much like Ring ϵ, varying in opacity roughly in inverse proportion to width without significant change in overall morphology. While the near-periapse Ring δ profile is indeed more narrow, this is not the case for Ring γ, where the narrow dense profile is observed 147° from periapse.

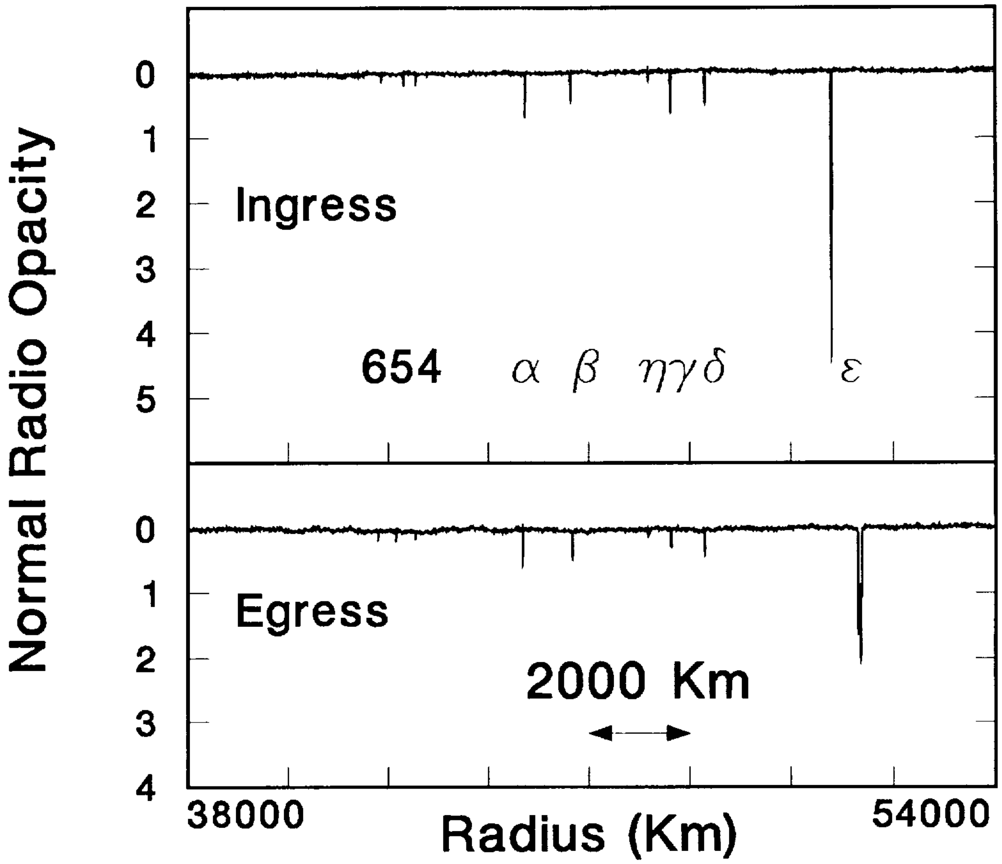

FIG. 6: Global ring system profile at 3.6 cm wavelength at 10 km resolution. The nine pre-Voyager rings are visible at both ingress and egress. Note the increase in ≃ 1000 km scale free space noise level for the egress profile relative to ingress. This is due to degradation in spacecraft antenna pointing accuracy after ~4 hours, during which the spacecraft attitude was controlled by onboard gyros. Note also the evident eccentricity of Ring ϵ.

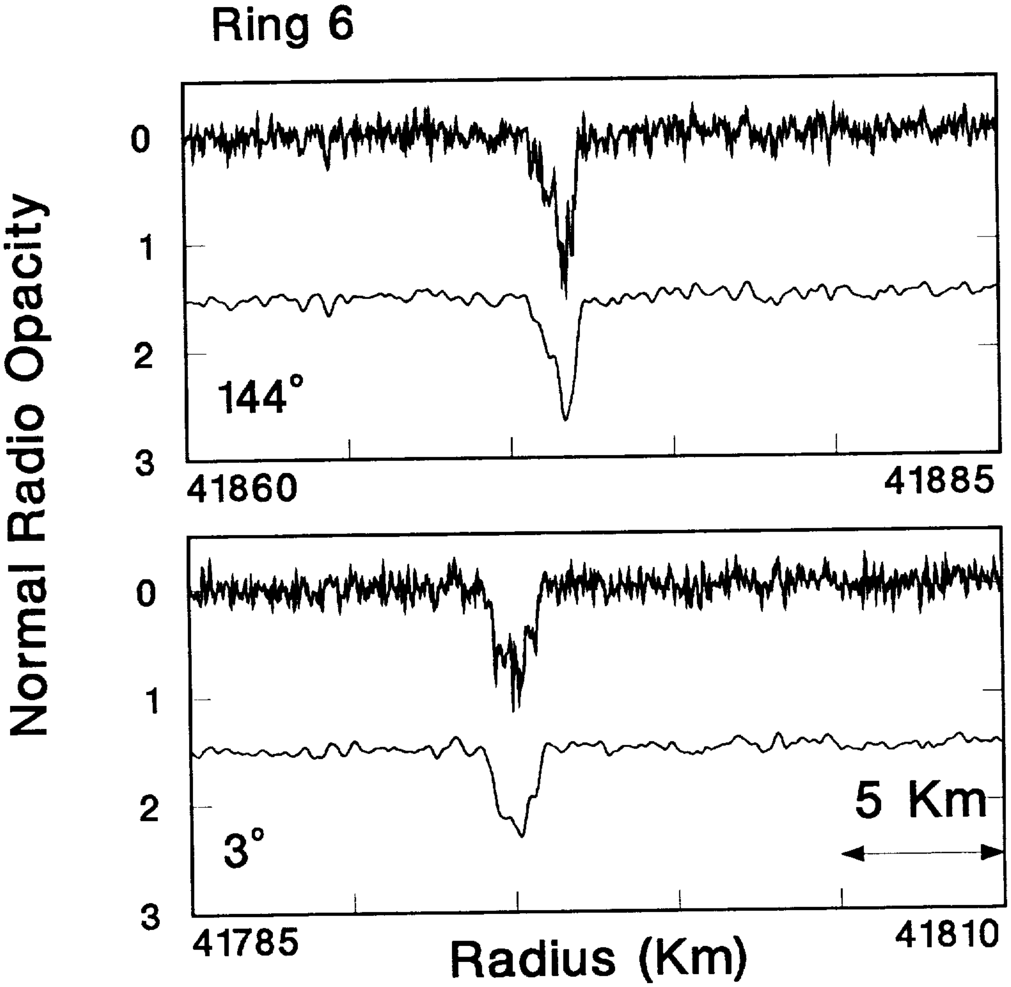

FIG. 7: Opacity profile of Ring 6 observed at 3.6 cm wavelength. Indicated angles correspond to true anomalies of assumed Keplerian streamline model at location of radio observations. Ingress and egress profiles are located in top and bottom panels, respectively. Resolution is 50 m. The second (smoother) curve in each panel is a 200 m resolution profile, offset in (radius in km, opacity) by (0,1.5). Uncertainty intervals for this profile, as well as others to follow, are given in Table 11 of Appendix A; for example, the free space standard deviation of optical depth σ_τ is 0.09 at 50 m resolution.

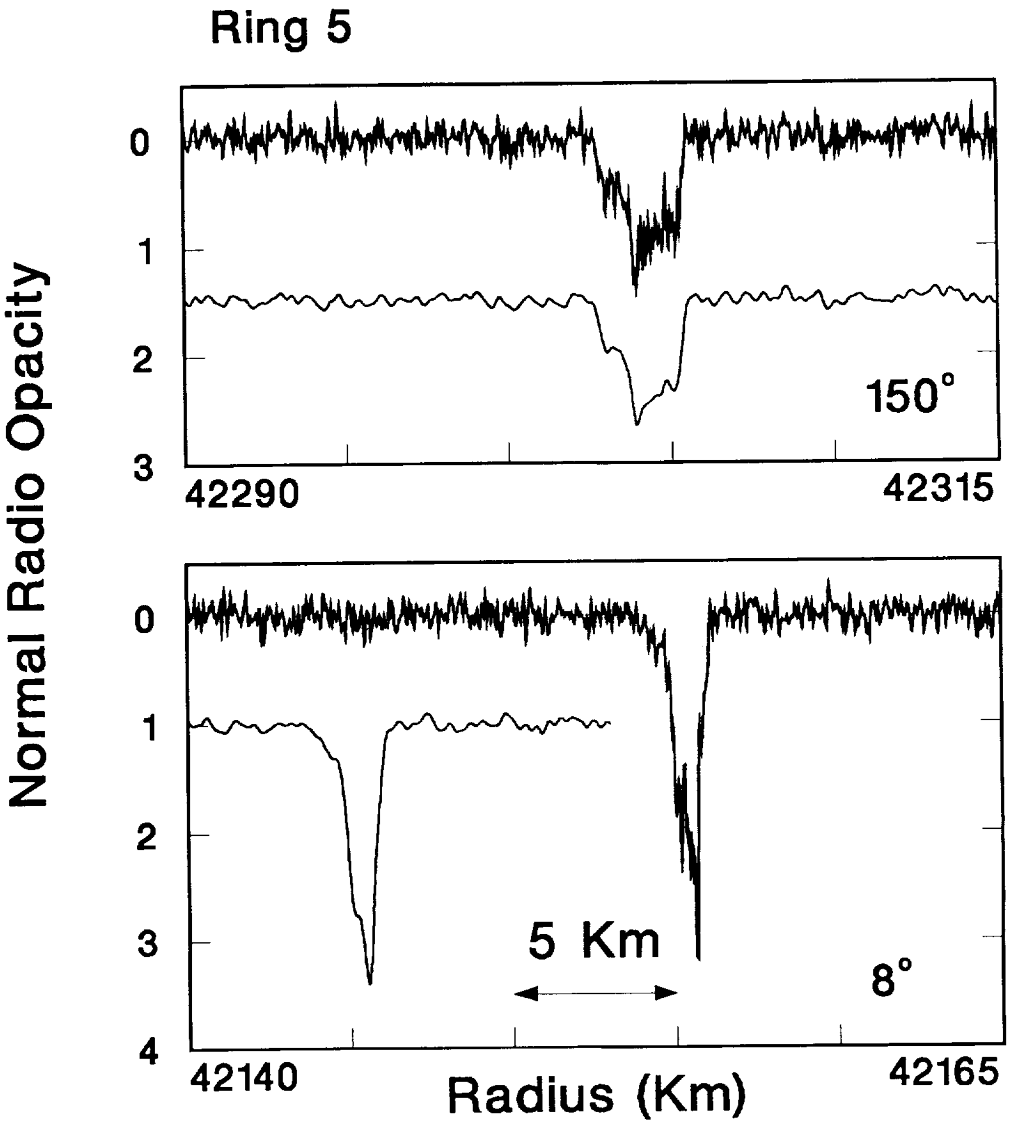

FIG. 8: Opacity profile of Ring 5. See caption of Figure 7 for details; offset is (0,1.5) and (-10,1) for the top and bottom panels, respectively. Note the significant change of profile morphology with observation longitude and the relatively large opacity level reached at 8° true anomaly.

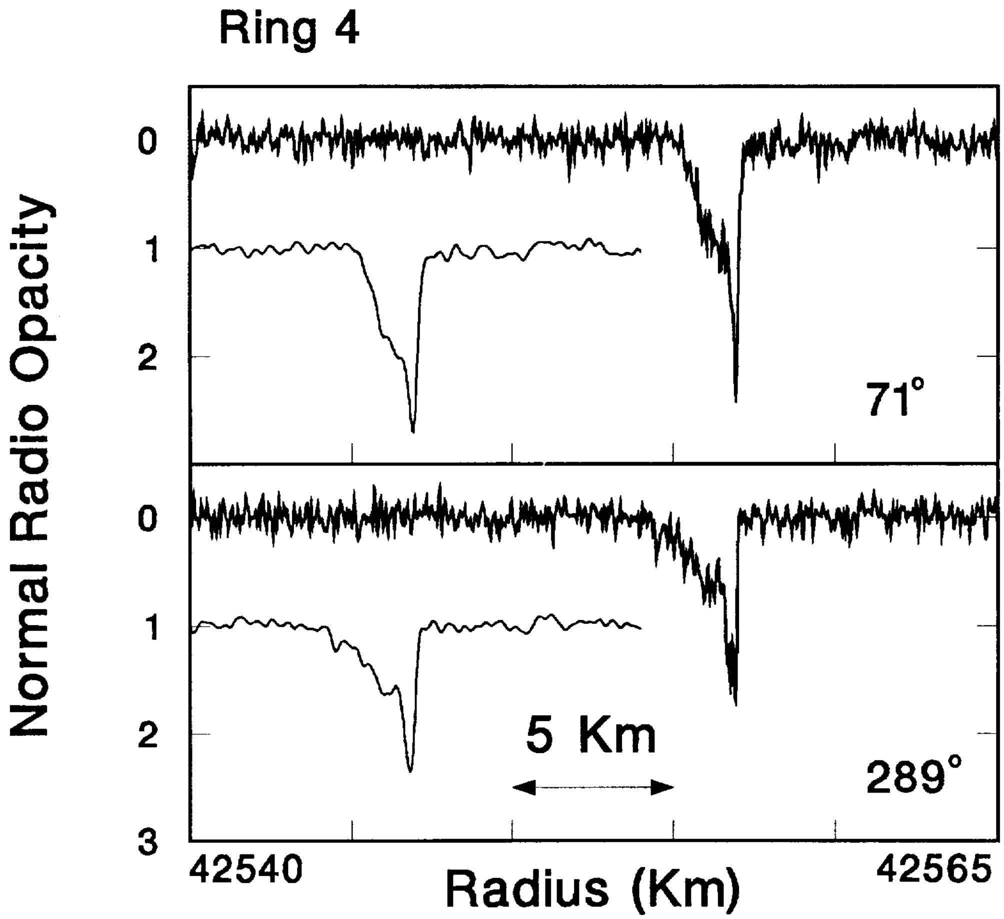

FIG. 9: Opacity profile of Ring 4. See caption of Figure 7 for details; offset is (-10,1). A pattern of sharp outer edge, diffuse quasi-exponentially shaped inner edge characterizes the profile at both observation longitudes (~ ±71° true anomaly). Similar morphology is also apparent for Ring 5 at 8° (Figure 8) and Ring 6 at 144° (Figure 7), indicating little correlation of this particular edge morphology with location from periapse.

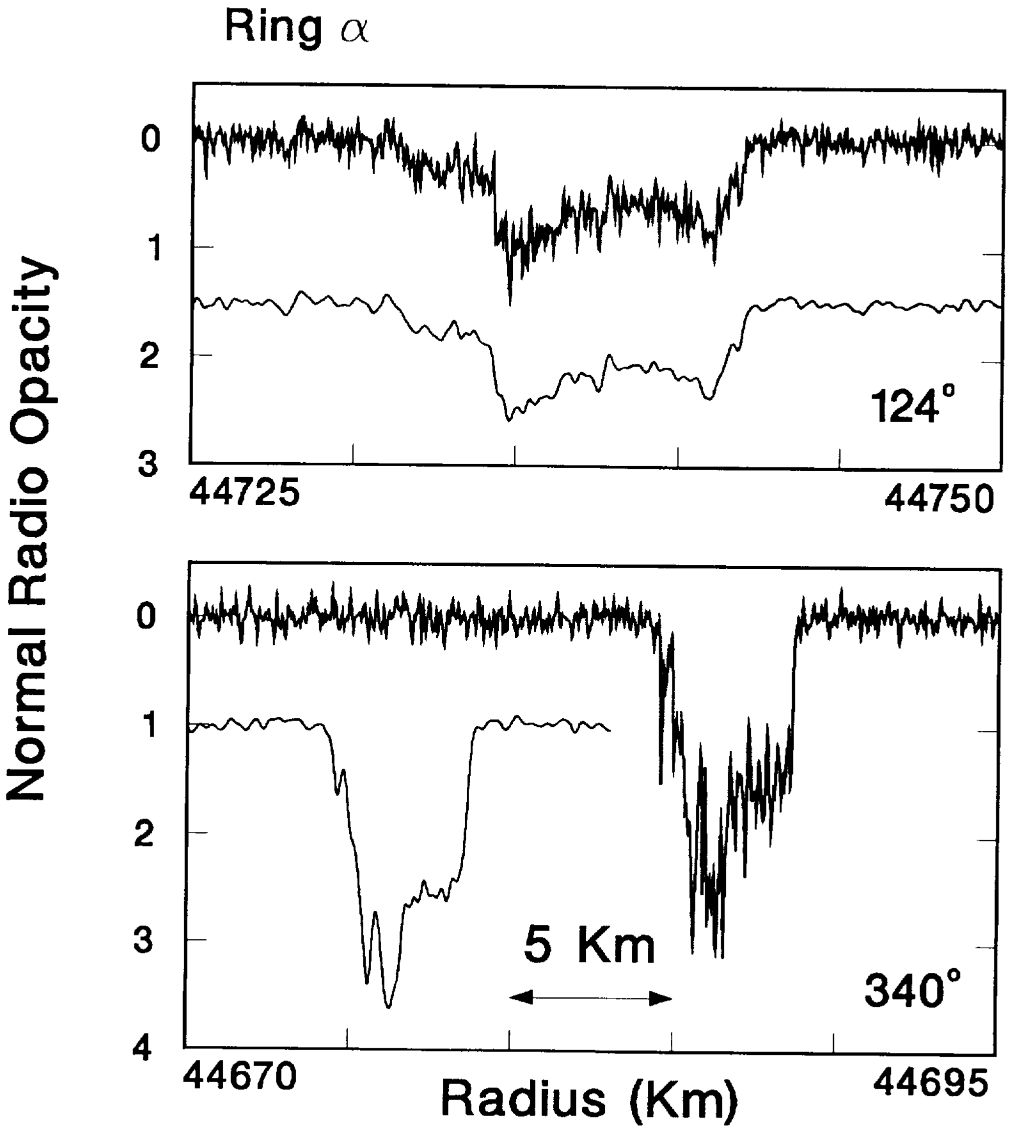

FIG. 10: Opacity profile of Ring α. See caption of Figure 7 for details; offset is (0,1.5) and (-10,1) for upper and lower panels, respectively. Note in particular the relatively diffuse edges at 124° evolving into sharp edges at 340°, and the interior broad and relatively tenuous feature at 124°, partly evolving into a very narrow, dense, and nearly detached feature at 340°.

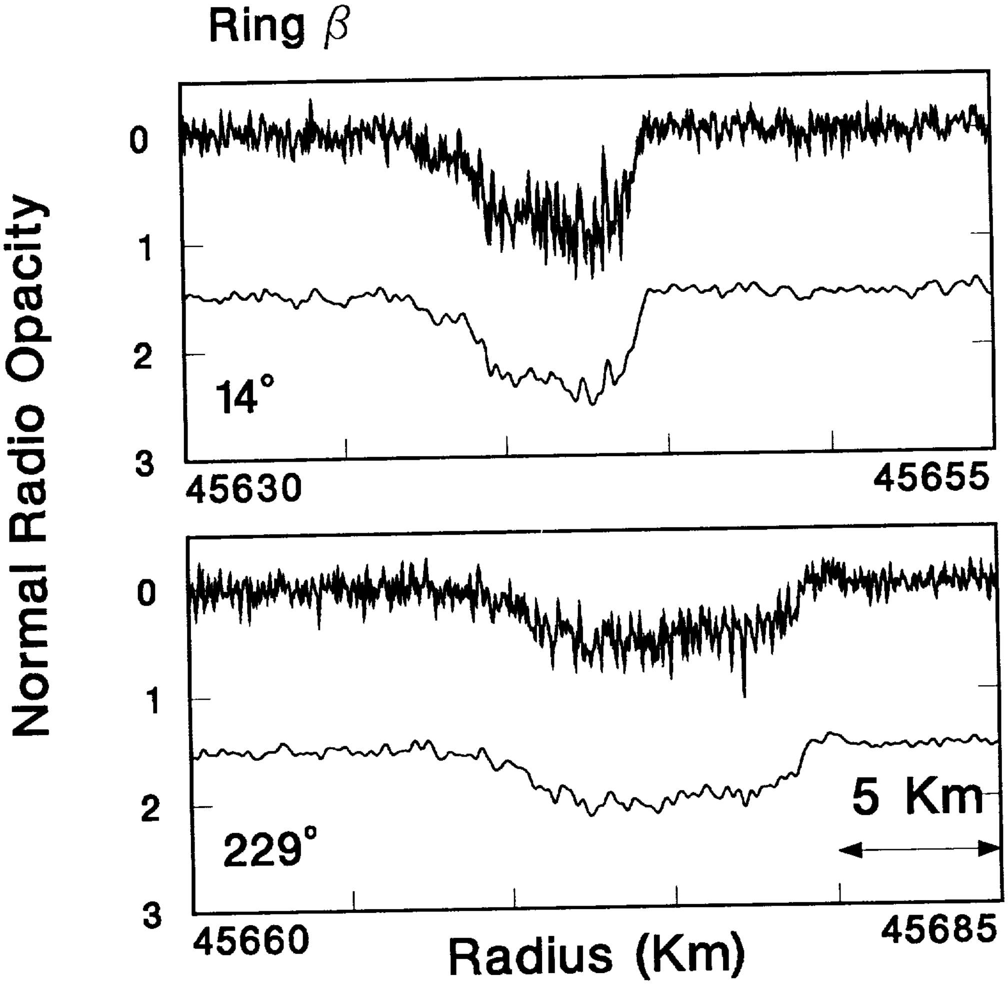

FIG. 11: Opacity profile of Ring β. See caption of Figure 7 for details; offset is (0,1.5). Ring β has the most diffuse edges, the least opacity, and least prominent radial structure of the Uranian rings. A notably more diffuse inner edge is apparent at both observation longitudes.

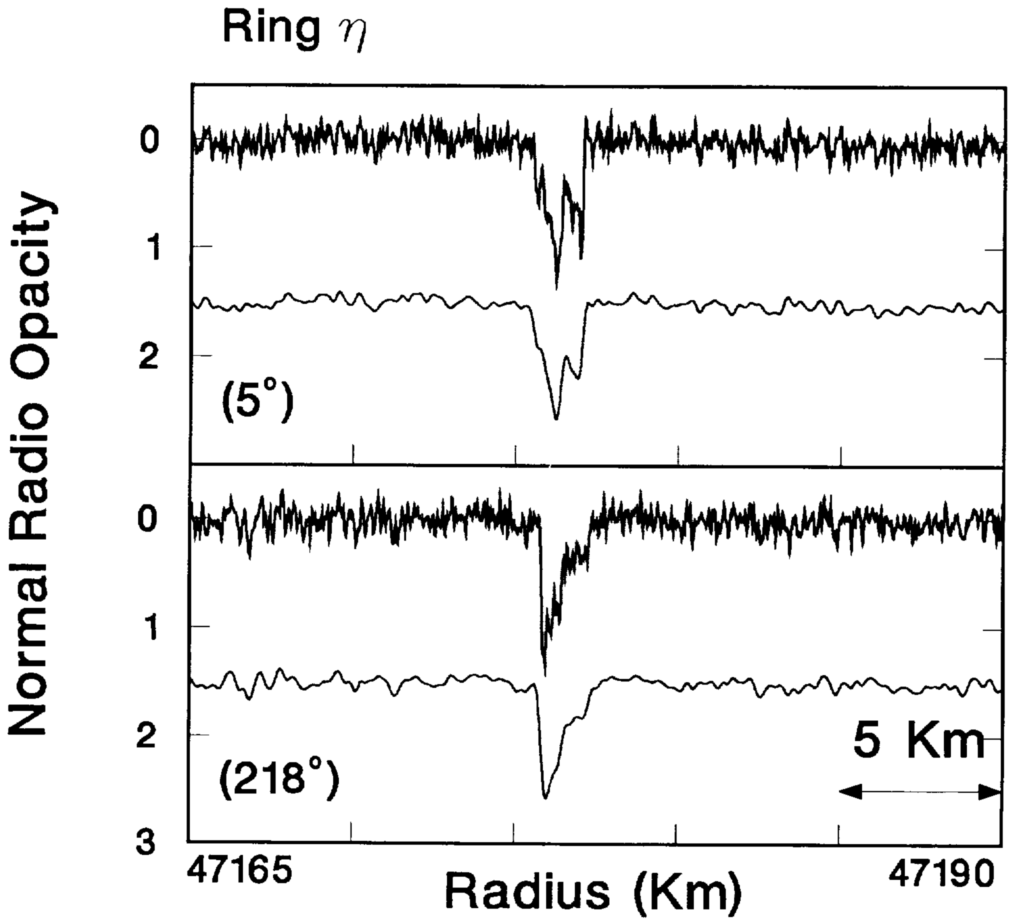

FIG. 12: Opacity profile of Ring η. See caption of Figure 7 for details; offset is (0,1.5). This ring is almost circular (note the radius scale above); true anomalies in parentheses indicate large uncertainties in location of periapse. Edge behavior at 218° is opposite to the characteristic sharp outer edge–diffuse inner edge observed for several other rings. Not apparent in the profiles here is a tenuous companion exterior to the ring, shown separately in Figure 20.

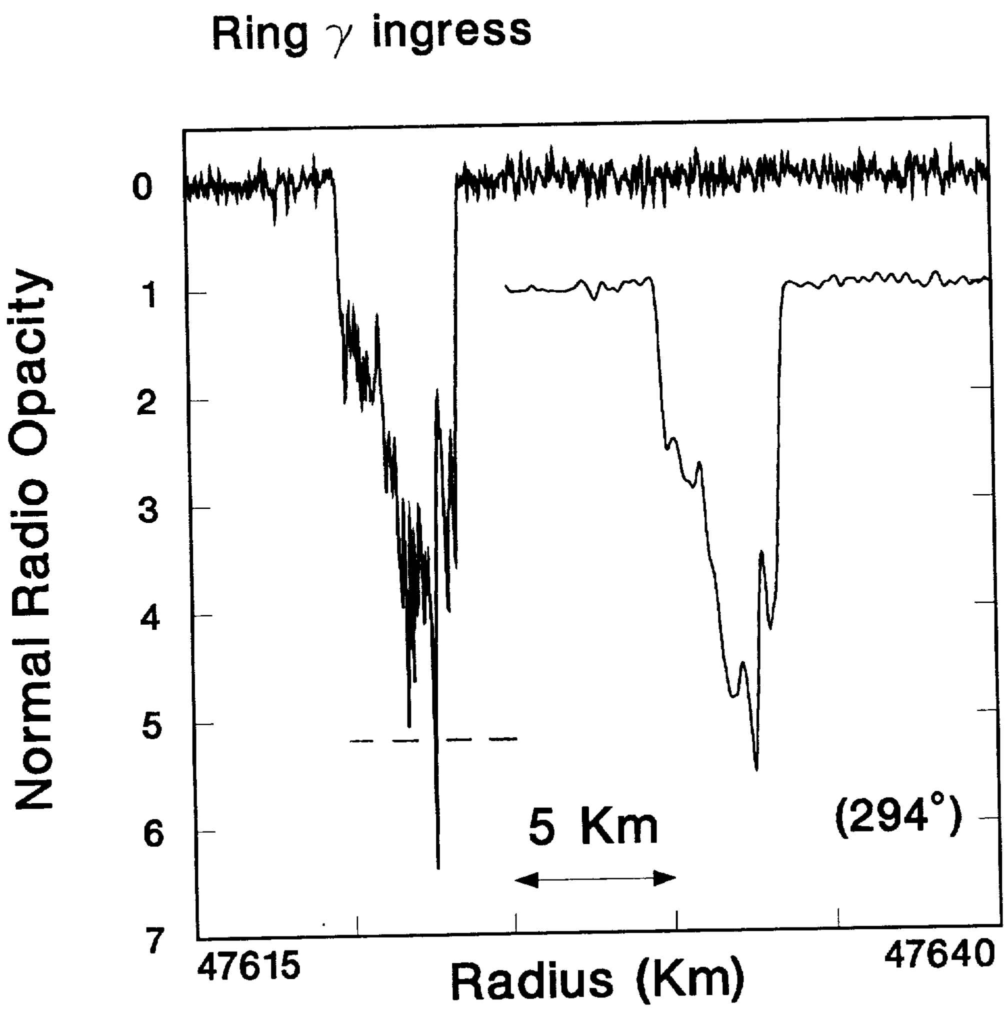

FIG. 13: Opacity profile of Ring γ (ingress). See caption of Figure 7 for details; offset is (10,1). The horizontal dashed line identifies the threshold opacity level τ_{TH} ($\tau \geq \tau_{TH}$ indicates noise limited measurement; see Appendix A). Ring γ is one of two Uranian rings (the other is Ring ϵ) whose overall morphology is reminiscent of narrow ringlets in Saturn's rings, for which extremely sharp inner and outer edges are a common feature. Unusually high opacity here is unmatched by any known feature in Saturn's rings. True anomaly in parentheses indicates nearly circular orbit and high uncertainty in periapse location.

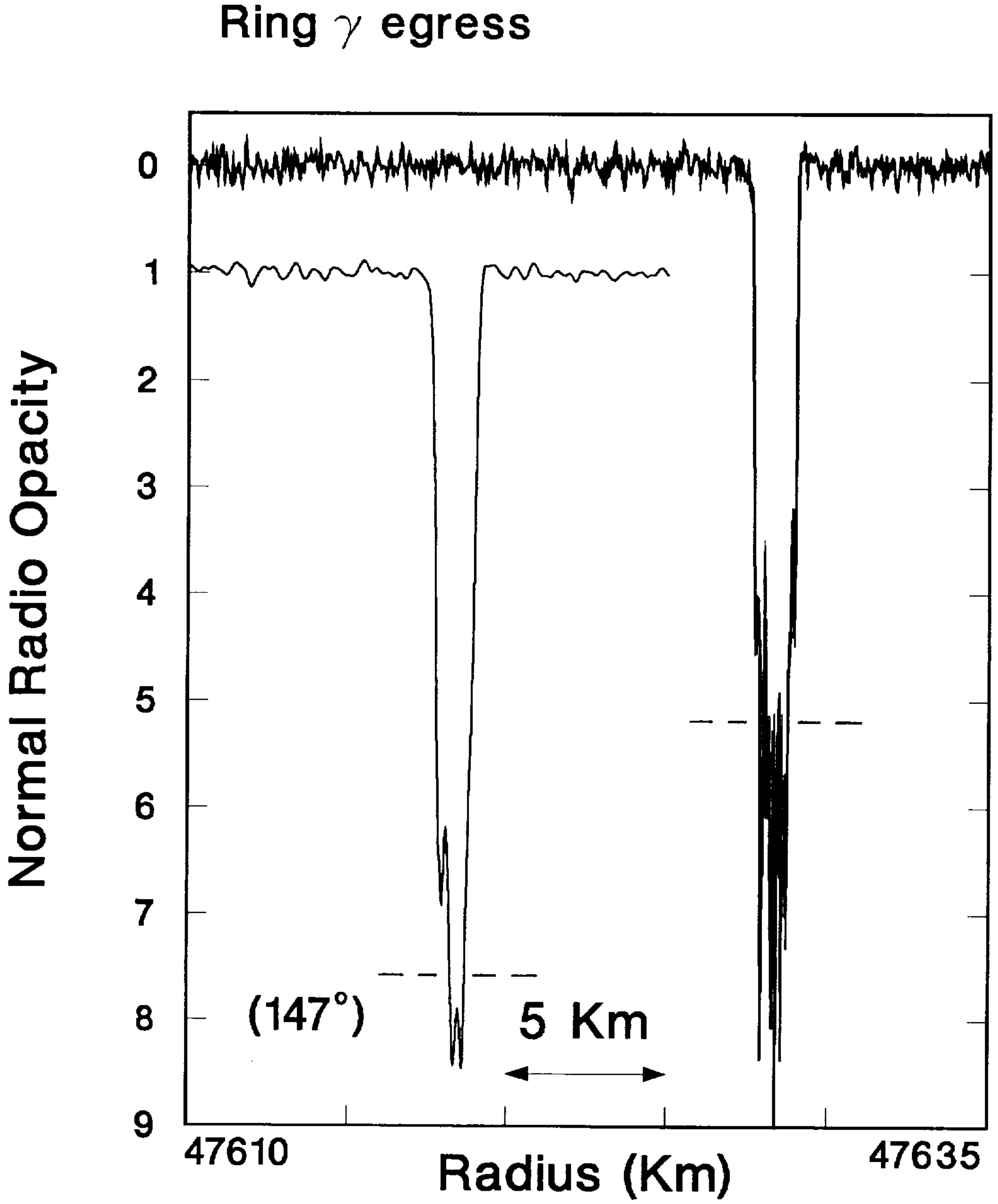

FIG. 14: Opacity profile of Ring γ (egress). See captions of Figures 7 and 13 for details; offset is (-10,1). As discussed in the text, the reconstruction algorithm for this profile incorporates a canting angle of $-0.107°$. Note that extremely sharp edges are maintained despite an optical depth exceeding $\sim$ 6 over a width of about 1.6 km at this longitude. The thickest part of the ring has opacity exceeding the threshold level at 200 m resolution ($\tau_{TH} \simeq 6.6$).

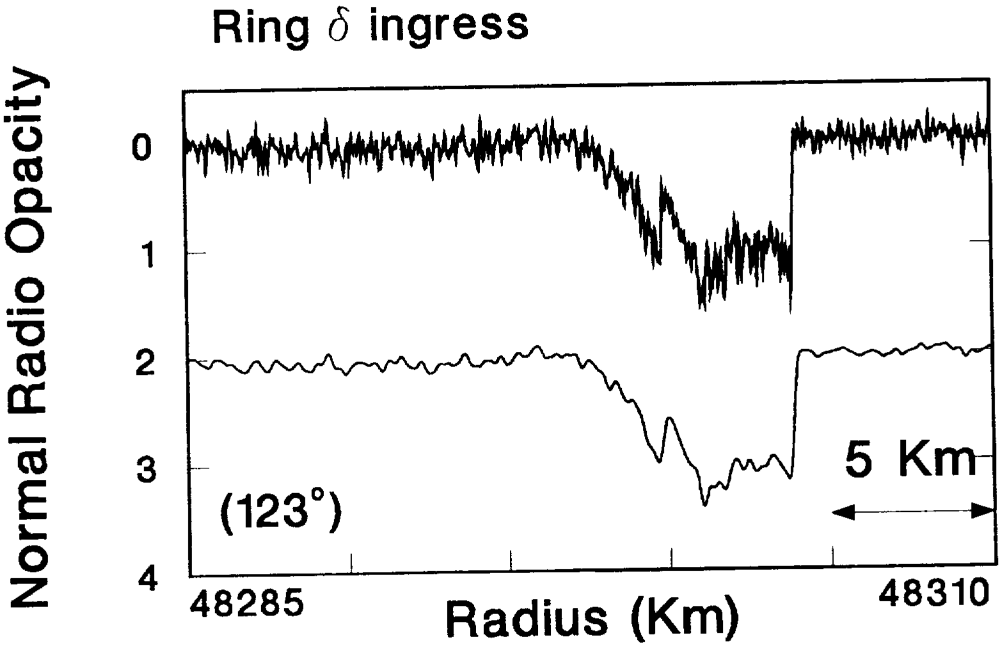

FIG. 15: Opacity profile of Ring δ (ingress). See caption of Figure 7 for details; offset is (0,2). Despite its much larger width, Ring δ shares with Rings 6, 5, and 4 their distinct sharp-outer diffuse-inner edge characteristics. A tenuous companion interior to the inner edge, shown separately in Figure 21, is distinguishable in the profile. Ring δ is nearly circular, so its periapse location is uncertain; true anomaly in parentheses indicates this fact.

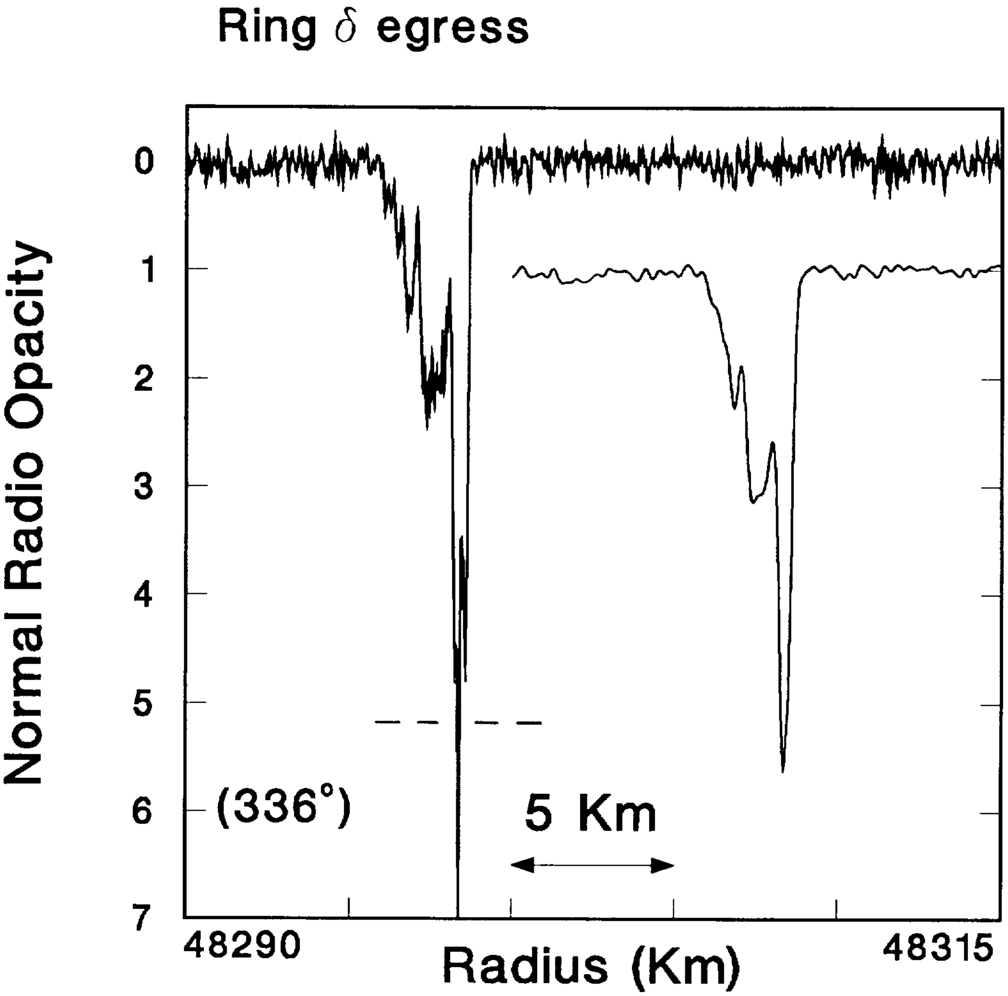

FIG. 16: Opacity profile of Ring δ (egress). See captions of Figures 7 and 15 for details; offset is (10,1). Comparison with the ingress profile (Figure 15) shows significant changes with observation azimuth. Note in particular the wave-like fluctuations superposed on the tapered inner edge, perhaps the wake of a near-by satellite or a density (or bending) wave driven by a resonance with a more distant satellite. In the latter case, the fluctuations should also be present in the ingress profile, a marginal case at best considering the profiles in Figure 15.

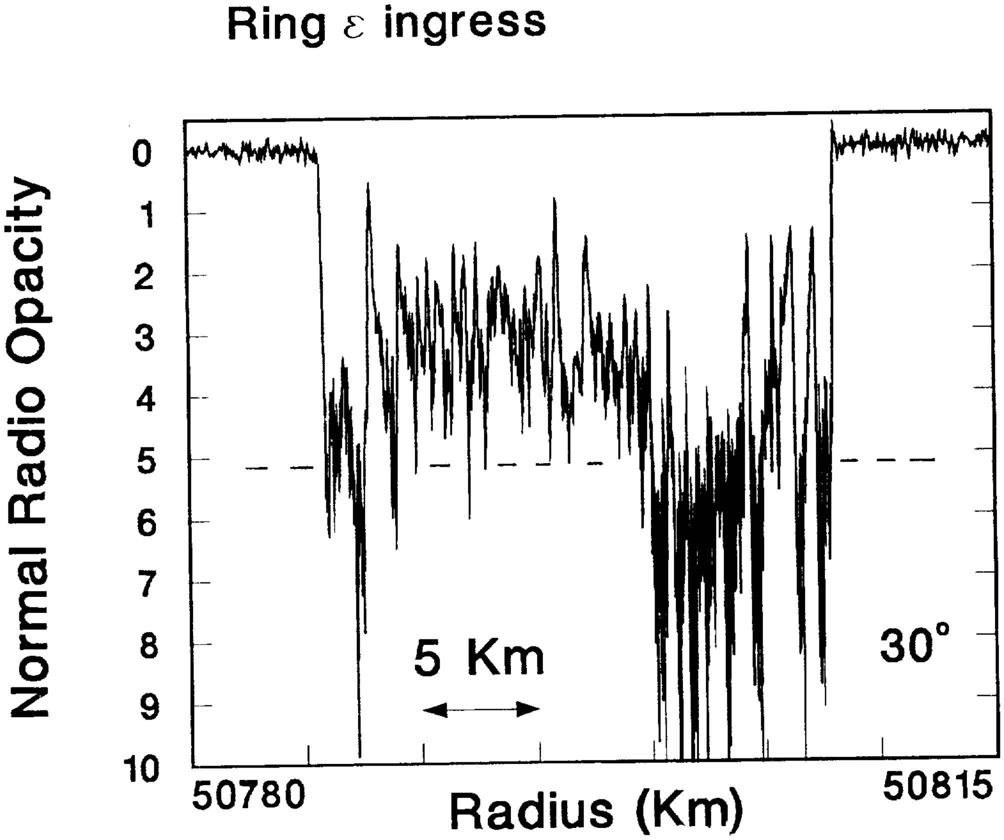

FIG. 17: Opacity profile of Ring ϵ (ingress) observed at 3.6 cm wavelength. Resolution is 50 m. At 30° from periapse, the ring width is $\simeq$ 22.4 km, close to the ring's minimum width ($\simeq$ 18 km). A dense outer core superposed on a relatively less dense ($\tau \sim 3$) background characterizes the overall morphology of the ring. Significant small-scale structure within the background medium is present. Both the dense core and opacity enhancements near the edges fall below the threshold level $\tau_{TH} \simeq 5.2$ (horizontal dashed line) and are noise limited. Note that both the vertical and horizontal scales here are more compressed compared to all previous profiles.

See following page.

FIG. 18: Opacity profile of Ring ϵ (egress). See also caption of Figure 17. The radius and opacity scales for this figure differ from those of previous profiles. The outer core is only moderately dense at this longitude, so $\tau < \tau_{TH} \simeq 5.2$ everywhere. A small, but noticable, free-space level overshoot is evident at the edges (see also Figure 17) and is probably caused by as yet unmodeled perturbations in the Keplerian ring orbit model used to remove diffraction.

3.3 Tenuous Ring Companions

Low optical depth companions to Rings η and δ (*v.*, *e.g.*, Elliot and Nicholson, 1984) are observed in the 3.6 cm data (Figures 21 and 20). Table 3 gives the estimated locations and widths of these companion rings. The width of the Ring η companion is $\sim$ 55 km and its mean optical depth is $\simeq$ 0.03, while the corresponding quantities for Ring δ are about 10 km and 0.06, respectively. It appears that both of the companion rings are roughly circular with no obvious differences between the ingress and egress profiles. Note in particular that the position of the companion to Ring δ remains fixed as the shape and width of the main ring change significantly. Therefore the behavior of the companion ring appears to be controlled separately from that of the main core.

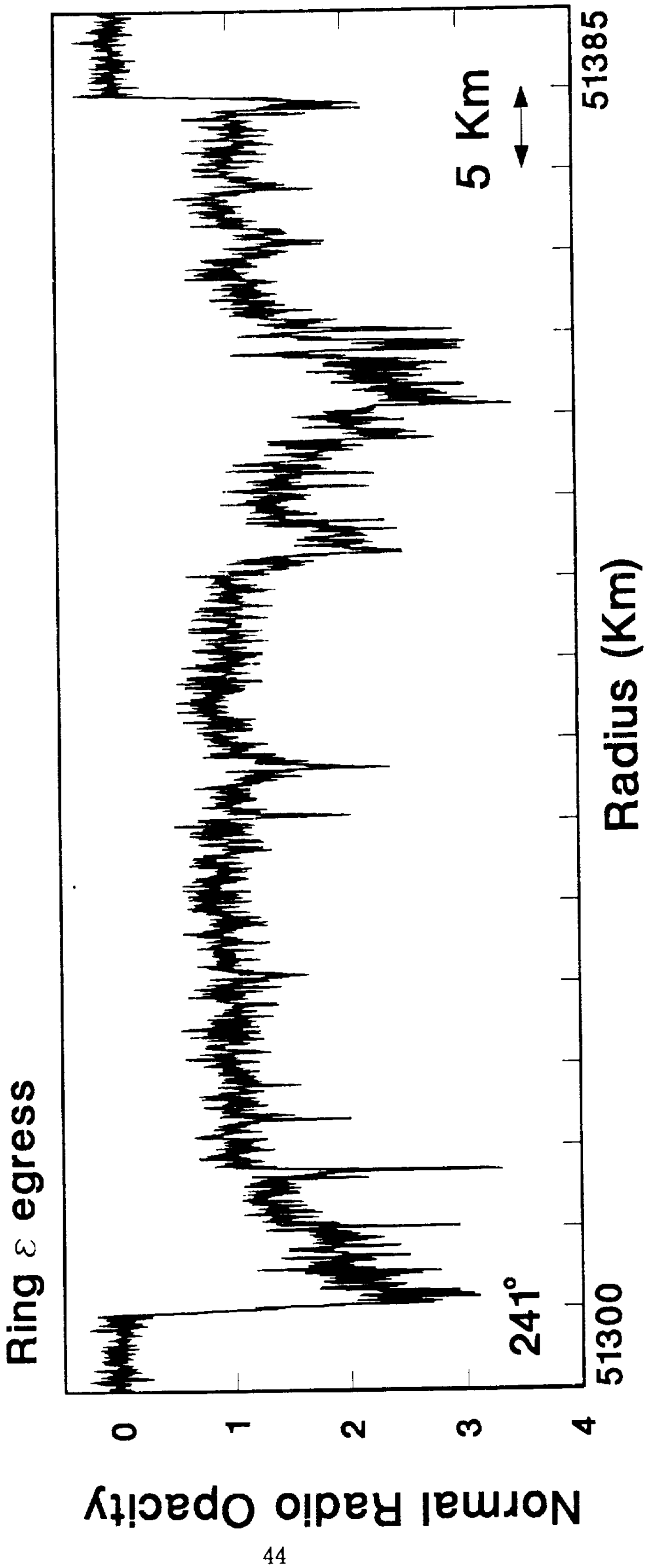
Ring ε egress
241°
5 Km
Normal Radio Opacity
0
1
2
3
4
51300
51385
Radius (Km)

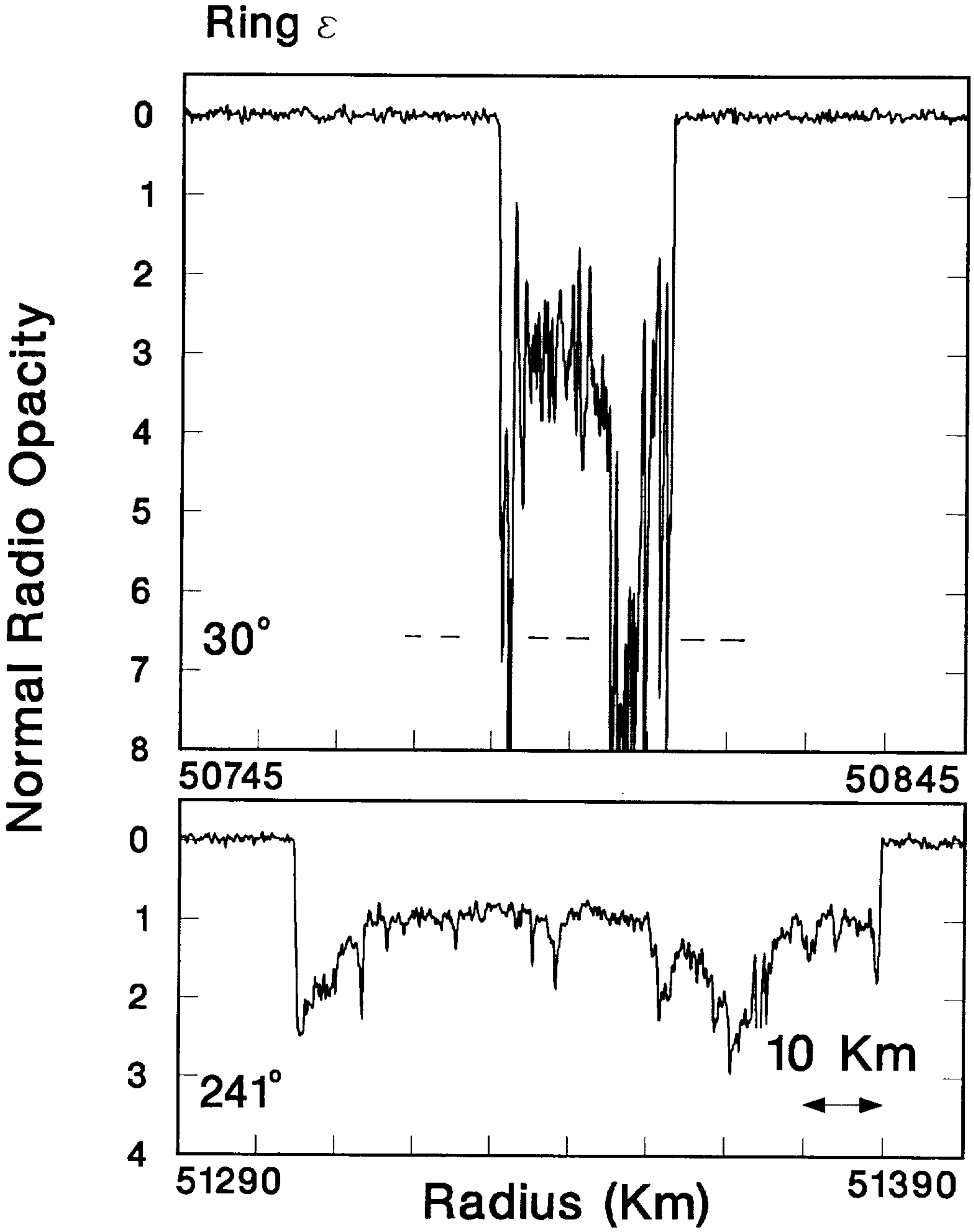

FIG. 19: Opacity profile of Ring ε, at resolution 200 m. Rich structural detail is still clearly evident at this resolution. Although the opacity threshold level increases to 6.6, compared to 5.2 at 50 m resolution, the edge and core opacities at ingress (top) remain noise limited. Note the near absence of edge overshoots at this resolution. To first order, the background opacity level decreases by about a factor of three as the ring width increases by about the same factor.

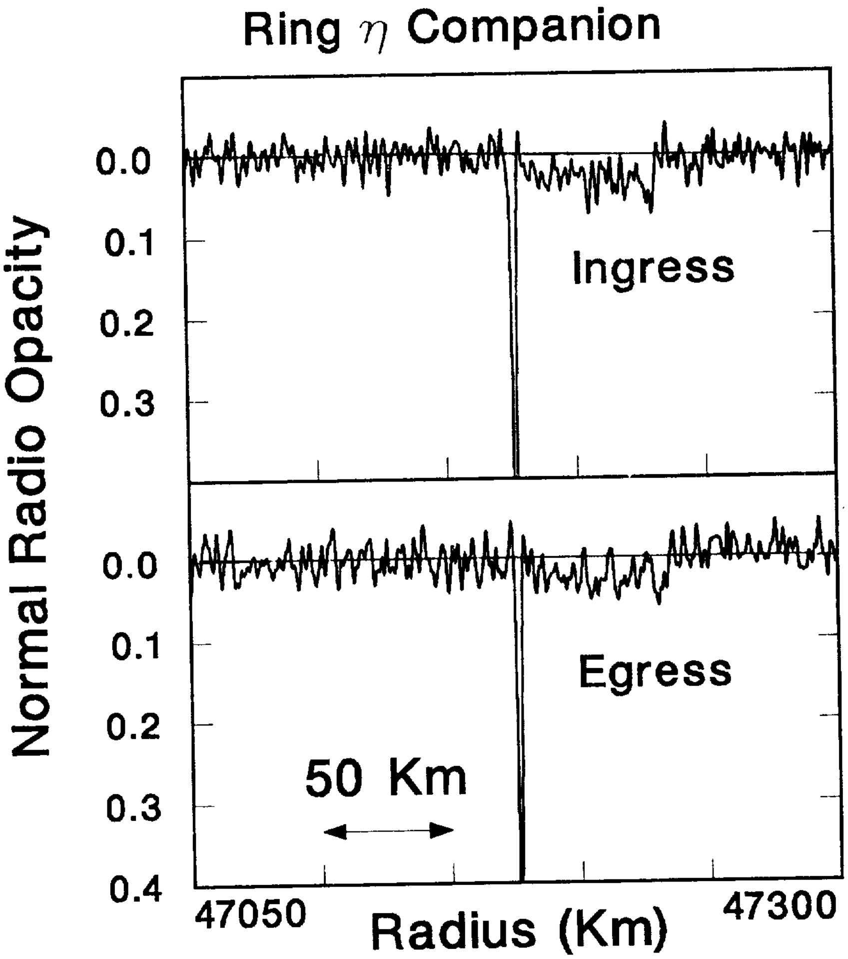

FIG. 20: Ring η and its tenuous outer companion observed at ingress and egress at 3.6 cm wavelength. Resolution is 1 km. Its width (~ 55 km) and opacity (~ 0.03) are similar for both observation longitudes, indicating a nearly circular feature. This profile was obtained by combining the data collected from the Parkes and Canberra antennas as described in Gresh *et al.* (1989).

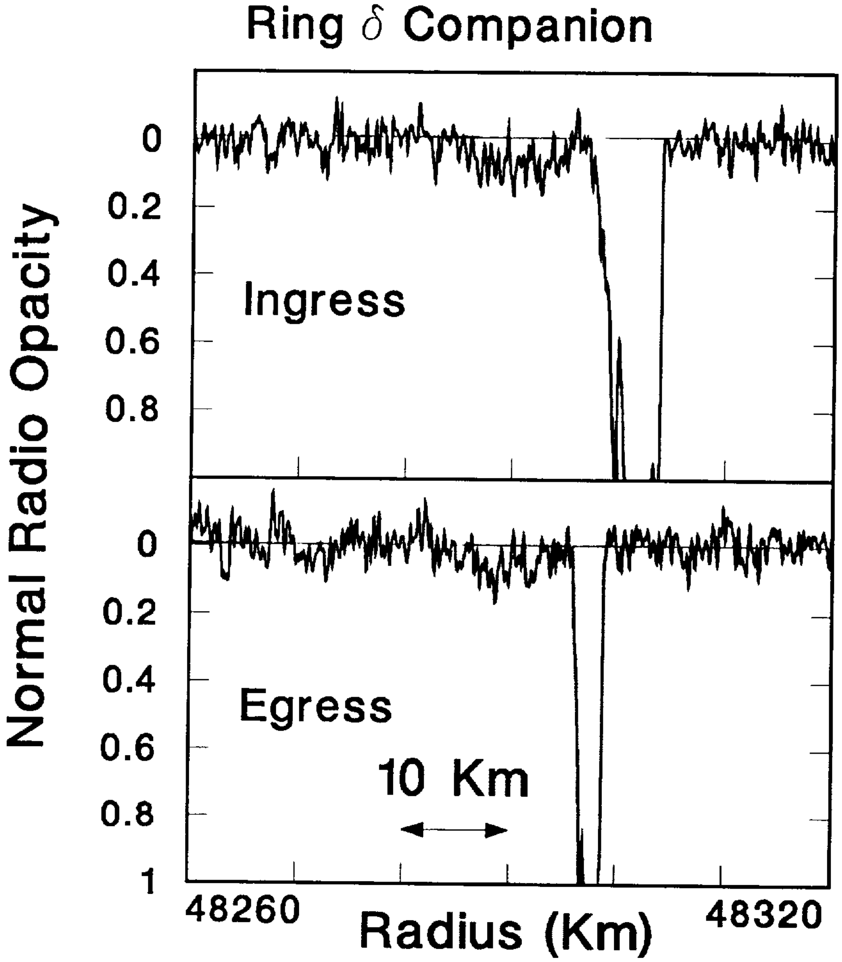

FIG. 21: Ring δ and its tenuous inner companion observed at ingress and egress at 3.6 cm wavelength. Resolution is 200 m. Its width (~ 10 km) and opacity (~ 0.06) are nearly identical at the two observation longitudes.

Ring	Side	Radial Location Inner (km)	 Outer (km)	Width W (km)	$\int \tau$(3.6 cm) 1 km res^a (km)	Mean Opacity $< \tau(3.6\text{ cm}) >^b$
η	ing	47180	47232	52	1.35 ± 0.17	0.026 ± 0.003
η	egr	47180	47235	55	2.03 ± 0.18	0.037 ± 0.003
δ	ing	48284	48295	11	0.64 ± 0.08	0.058 ± 0.007
δ	egr	48283	48293	10	0.56 ± 0.08	0.056 ± 0.008

TABLE 3: Measured widths and opacities of the tenuous companions of Rings η and δ.

^{a}: "res" stands for resolution.
^{b}: Defined as $\frac{1}{W} \int_W \tau(3.6\text{ cm})$

3.4 Edge Characteristics

Table 4 lists the widths of the rings as observed in the radio data. The estimates of edge locations correspond to the opacity level $\tau = 0.1$. Ring width should be accurate to $\sim \pm 50$ m for rings with sharp inner and outer edges and $\sim \pm 200$ m for rings with one or more diffuse edges.

Table 4 also gives values for peak opacity τ_e reached in the immediate neighborhood of each edge. For abrupt, deep edges the value of τ_e is well-defined, but for relatively diffuse edges the choice is more subjective. In all cases, 200 m resolution profiles are used to reduce noise contamination. Note in particular the unusually large value $\tau_e > 5$, reached at the inner and outer edges of Ring γ egress despite a width of only 1.6 km. Comparable τ_e's are only reached by both edges of Ring ϵ ingress, when the ring is nearly at its minimum width.

The last entry of Table 4 gives a measure of relative edge sharpness, taken to be $(\tau_e - 0.1)$ divided by the radial distance over which the edge opacity changes from 0.1 to τ_e. The measure is therefore a typical gradient of the edge profile, which is not necessarily the true gradient near the onset of the edge. A gradient less than $\sim 1\ \tau$/km indicates a relatively diffuse edge, while a gradient greater than $\sim 10\ \tau$/km indicates an extremely sharp edge. Except in a few cases, particularly Ring β, values in Table 4 indicate that the Uranian rings are characterized by a gradient $\gtrsim 1\ \tau$/km. Furthermore, a general pattern of outer edges sharper than the inner ones is apparent, with the prominent exception of the edges of Ring η egress, where this behavior is reversed. In the cases of Rings γ, δ, and ϵ, edges become less sharp as ring width increases, for some almost in direct proportion. The sharpest edges appear on Ring γ egress, Ring δ egress and Ring ϵ ingress. These rings are also the ones with

Ring	Side	True Anom. (deg)	Width[a] W (km)	Edge Opacity[b] Inner	Edge Opacity[b] Outer	Edge Sharpness[c] (τ/km) Inner	Edge Sharpness[c] (τ/km) Outer
6	ing	144.3	1.52	1.16	1.16	1.02	2.17
	egr	2.6	1.72	0.64	0.45	0.98	1.33
5	ing	150.0	2.75	0.49	0.84	1.14	1.92
	egr	7.9	2.62	1.75	2.40	1.33	3.85
4	ing	71.2	1.95	0.83	1.70	1.08	4.35
	egr	288.9	2.67	0.64	1.35	0.33	5.56
α	ing	124.4	10.59	0.28	0.86	0.40	0.70
	egr	340.2	4.22	0.64	1.43	4.55	3.33
β	ing	13.9	7.03	0.27	0.86	0.25	0.81
	egr	228.9	11.19	0.20	0.31	0.06	0.85
η	ing	4.5	1.54	1.07	0.70	1.41	3.45
	egr	218.3	1.53	1.08	0.33	4.76	1.04
γ	ing	293.8	3.83	1.53	3.20	5.56	6.67
	egr	147.3	1.63	5.89	7.45	12.50	14.29
δ	ing	122.5	6.70	1.01	1.18	0.38	5.00
	egr	335.5	2.70	2.14	4.60	1.49	12.50
ϵ	ing	30.0	22.43	5.29	5.19	14.29	16.67
	egr	241.2	74.93	2.50	1.79	2.63	3.33

TABLE 4: Widths and edge characteristics of observed profiles

[a]: Uncertainty is ~ ±50 m for rings with very sharp edges and ~ ±200 m for rings with at least one diffuse edge.
[b]: Defined as the peak opacity reached in the immediate neighborhood of the edge, τ_e. It is a well defined parameter for abrupt opaque edges, otherwise τ_e is somewhat subjective.
[c]: Defined as $(\tau_e - 0.1)$ divided by the radial distance in kilometers over which the edge opacity increases from 0.1 to τ_e. It represents a characteristic gradient of the opacity profile in the neighborhood of an edge, but not necessarily the gradient at the onset of the edge. Value $\lesssim 1$ indicates a relatively diffuse edge, while a value $\gtrsim 10$ indicates an extremely sharp edge. Abrupt edges are characterized by values $\gtrsim 1$.

the largest opacity τ_e. It is interesting to note that the edge sharpness of several ringlets in Saturn's rings also appears to increase with increasing edge opacity (*v.*, *e.g.*, Cuzzi *et al.*, 1984).

3.5 Eccentricity Gradients of Rings α, β, and ϵ

The first dynamical problem we address with the help of the high-resolution profiles is that of maintenance of eccentricity. In the absence of additional forces, streamlines of ring particles in eccentric orbits would precess at a rate which depends on their semimajor axis. If ω is the location of the line of apsides[2] of an eccentric orbit with semimajor axis a, then the rate of change of this location would be given approximately by

$$\frac{d\omega}{dt} = \frac{3}{2} J_2 R^2 (GM)^{1/2} a^{-7/2}$$

where M, R, and J_2 are the mass, radius, and dynamical oblateness[3] of the planet, and G is the gravitational constant. Therefore adjacent streamlines with slightly different semimajor axes will precess at different rates, and collisions will result, leading to circularization of an eccentric ring. The time scale for disturbances due to differential precession is quite short; for Ring ϵ, the inner edge of the ring would precess an entire revolution relative to the outer edge in less than 200 years. Thus, the fact that eccentric rings with locked precession are observed (*v.*, *e.g.*, Elliot and Nicholson, 1984) must be explained by an additional force to counteract differential precession.

Goldreich and Tremaine (1979b) hypothesized that the necessary force was supplied by self-gravity between ring particles. They developed a method by which, given an observation of one optical depth profile, and assuming that mass density is proportional to optical depth, one could determine $e(a)$ such that self-gravity forces balance forces causing the differential precession. This is accomplished by integrating the gravitational effect of each streamline on each of the other streamlines over an entire orbit. For a system of N streamlines, this leads to a set of N equations in N unknowns which may be solved directly, giving not only the unknown eccentricity of $(N-2)$ streamlines (the eccentricity of the inner and outer streamlines are known from observation of the

---

[2] The line of apsides is the line connecting the center of the planet to periapsis on the orbit.

[3] The dynamical oblateness J_2 is the coefficient of the second harmonic of the planet's gravitational potential U. The coefficients J_n are defined by

$$U = \frac{GM}{r}\left[1 - \sum_{n=2}^{\infty} J_n \left(\frac{R}{r}\right)^n P_n(\sin\theta)\right]$$

where $P_n(\sin\theta)$ is the Legendre polynomial, θ is defined in a spherical coordinate system, R is the equatorial radius of the planet, and r is distance from the center of the planet.

ring edges), but also the total mass of the ring and the precession rate of the ring as a whole. We use this procedure to calculate theoretical eccentricity gradient profiles using only one of the two observed radio occultation profiles. The result is then tested for self-consistency against the second observed profile.

Alternatively, we use two observed radio occultation profiles of each ring to derive an eccentricity gradient profile as follows (Marouf *et al.*, 1987). First, we estimate the orbital parameters a and e of the inner edge of a ring by using the two measured inner edge radii, along with the assumption that the angle of periapse is as given in Table 4. The orbit of the outer edge of the ring is estimated similarly. (We found it necessary to use this procedure to derive a and e rather than use the values given in French *et al.* (1986) because of small but significant differences between predicted and actual locations of the ring edges.) Then, we use a variation on this basic technique to construct an eccentricity profile across the entire ring. Given the observation that integrated optical depth is approximately the same for the two observed profiles (as we shall see in Chapter 4), we define streamlines as the contours which confine equal amounts of integrated optical depth in the two profiles. Assuming that the observed angle of periapse is constant across the ring, the two radii that confine the same integrated optical depth are sufficient to determine a and e for each streamline, and hence an eccentricity profile across the ring. (A more detailed account of the procedure we use may be found in Appendix C.) Subsequently, we compute numerically the eccentricity gradient profile $q(a)$, where

$$q \equiv a\frac{de}{da}.$$

We designate the profile obtained using this technique "self-consistent" if the eccentricity gradient q remains between 0 and 1, a necessary condition for non-crossing streamlines. This eccentricity gradient may then be compared to that computed from the self-gravity theory.

Only Rings α, β, and ϵ have been analyzed in this way. The reason for this is that they show the most well-behaved width *vs* true anomaly behavior, as has been discussed by French *et al.* (1988). This indicates that a simple eccentric streamline model is in good agreement with the observed global behavior of these rings. The inner rings, for example, show no simple relationship between width and true anomaly, indicating that more complicated perturbations to the streamlines may be at work. The only other ring which shows potential for a similar analysis is Ring δ, which has been shown (French *et al.*, 1988) to exhibit a relationship between its width and its phase relative to the normal mode excited in it. A preliminary analysis along the lines suggested here indicates that the streamlines may be perturbed in the region of the putative wave at the inner edge of Ring δ (Marouf *et al.*, 1988).

Figure 22 shows q *vs* a for Rings α, β, and ϵ. In each panel, the $q(a)$ profile derived from the empirical method described above and that derived from the self-gravity theory are shown. The solid curve is the "self-consistent" q profile calculated using 19, 29, and 92 streamlines for Rings α, β, and ϵ, respectively; the dashed curve is that obtained by using Goldreich and Tremaine's self-gravity theory, calculated using 20, 20, and 45 streamlines, respectively. For comparison we also show a dotted line with a constant value of q, representing the simple model of a linear taper in eccentricity between observed inner and outer edge values. These "average" values are 0.68, 0.48, and 0.27 for Rings ϵ, α, and β, respectively.

The agreement between the two methods is fairly good for Ring α, except perhaps near the edges. However, as we will discuss below, there are other reasons for doubting the applicability of the self-gravity theory for this particular ring. For Rings β and ϵ, there is little agreement between the two $q(a)$ profiles, casting doubt on the validity of the self-gravity model, at least in its most basic form used here. Comparison with a more elaborate model which includes collisions between ring particles (Borderies *et al.*, 1983) has not been attempted; however this model appears to imply that such collisional forces will result in apse misalignment of the inner and outer edges. There is clear evidence that the apses of the edges of Ring ϵ are *not* misaligned (French *et al.*, 1986; French, *et al.*, 1989), and there is similar, though weaker, evidence that Rings α and β are also not misaligned (French, *et al.*, 1989).

In order to assess the impact of the differences between the $q(a)$ profiles in Figure 22, we have used the calculated eccentricity gradients to "propagate" a profile observed at one true anomaly to the true anomaly of the second observed profile. This is accomplished by using the eccentricity gradient to determine the relative amount of stretch or compression of the streamlines from one true anomaly to the other (see Appendix C). The stretch or compression results in a decrease or increase, respectively, of the optical depth at the location of the streamline. The propagated profile is then compared to the actual observed second profile. For the case of the "self-consistent" eccentricity gradient, the procedure is guaranteed to give agreement, since the eccentricity was determined from the two profiles; for the self-gravity case it serves as a test of the validity of the theory.

The result of this procedure for Ring ϵ is shown in Figure 23. The top panel shows the mapping using the "self-consistent" eccentricity gradient, and as expected, the two profiles follow one another closely. However, slight differences persist because of a small difference in integrated optical depth

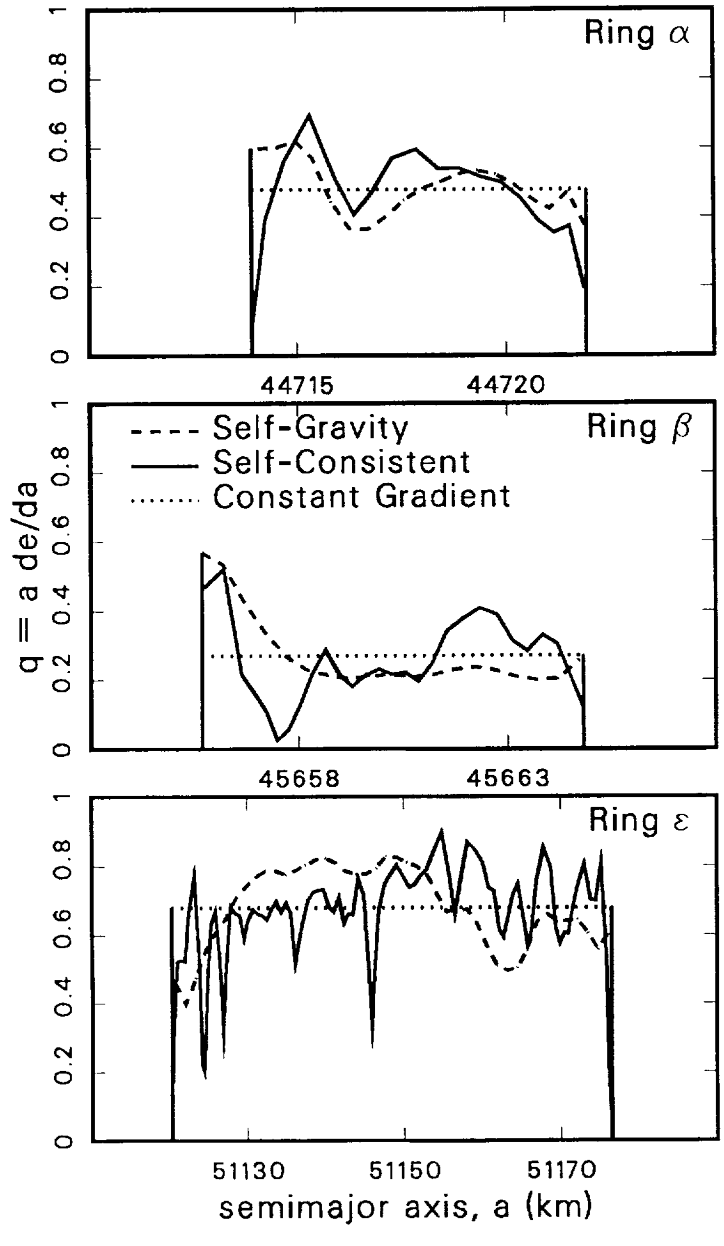

FIG. 22: Eccentricity gradient profiles for Rings α, β, and ϵ, derived from empirical "self-consistent" theory (solid curve), and from self-gravity theory (dashed curve). The dotted curve shows the average q for the ring for comparison. Agreement between the two methods is fairly good for Ring α, but significant differences exist for Rings β and ϵ, indicating weaknesses in the self-gravity determination of eccentricity.

(see Chapter 4). The bottom panel shows the result when the egress profile is mapped to the ingress true anomaly using the self-gravity eccentricity gradient. Significant differences from the actual observed profile throughout the ring are clearly evident, indicating that the self-gravity theory does not correctly predict profile evolution with longitude.

As noted above, under the assumptions of the self-gravity theory, the shape of the optical depth profile of the ring, combined with the gravitational parameters of the central body, yield not only the eccentricity gradient profile, but also the mass of the ring. This is because the force which opposes the tendency for differential precession is proportional to the mass of the streamlines. This mass estimate is derived independently from the average optical depth. For the case of Ring α, the predicted surface mass density is about 2 g-cm^{-2} (Goldreich and Porco, 1987). For a ring with an average optical depth of about unity, this is quite small. For example, in Saturn's Ring A, with average normal optical depth of about 0.7, the surface mass density has been estimated at between about 30 and 40 g-cm^{-2} (*v.*, *e.g.*, Cuzzi *et al.*, 1984). The small surface mass density per unit optical depth estimate points to small particles, as optical depth increases with the area of the particle, while mass increases as the volume. However, clear differences between τ(3.6 cm) and τ(13 cm) were seen in Saturn's Ring A (indicating a relative abundance of centimeter-sized particles), while, as we shall see in Chapter 4, *no* clear difference is seen in Ring α (indicating a relative depletion of centimeter-sized particles). Therefore, the low surface mass density estimate from the self-gravity theory appears to be inconsistent with the observations. In addition to the lack of clear differential optical depth between the two radio wavelengths, it has been pointed out (Goldreich and Porco, 1987) that there is other evidence that the particles in Ring α cannot be as small as this surface mass density estimate indicates. Uranus has an extremely extended hydrogen atmosphere, which exists well into the region of the rings (Broadfoot *et al.*, 1986). Estimates of the drag force of this atmosphere on ring particles indicates that particles smaller than perhaps a centimeter in size would have a very short lifetime (Goldreich and Porco, 1987). Similar difficulties are present with the surface mass density estimate for Ring β of 1.5 g-cm^{-2}. For Ring ϵ, the drag problem is less severe both because the hydrogen atmosphere is significantly less dense at the orbit of Ring ϵ, and because self-gravity predictions for its mass indicate a value of approximately 30 g-cm^{-2}, implying larger particles. In Chapter 4 we will investigate the mass of Ring ϵ in more detail.

We have shown above that two lines of evidence indicate that problems exist with the self-gravity theory: the disagreement between observed and predicted eccentricity gradients, and, at least for Rings α and β, the fact that the predicted surface mass density is too small, based on both observed

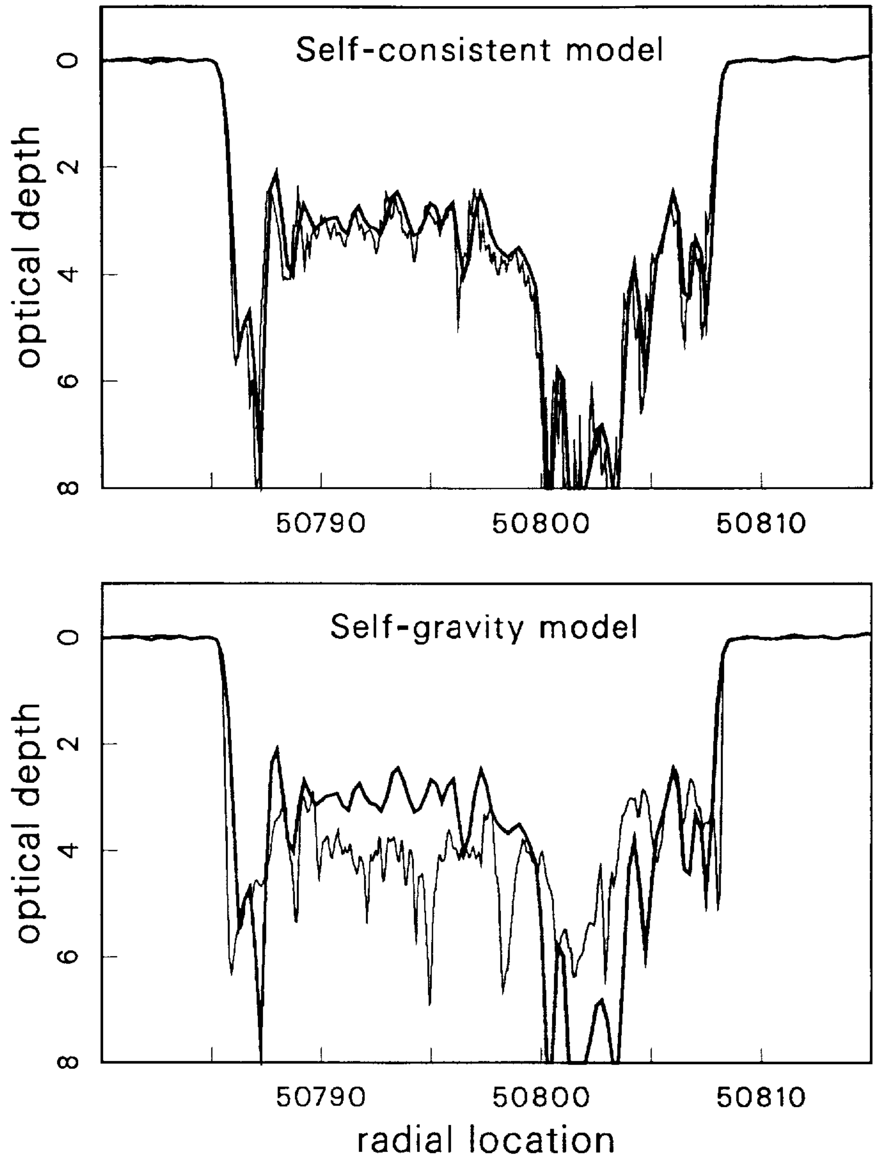

FIG. 23: Propagation of Ring ϵ egress profile to ingress true anomaly using both the "self-consistent" (top panel) and the self-gravity (bottom panel) eccentricity gradients. Heavy curve is measured profile; lighter curve is propagated profile. The agreement between the two profiles in the top panel is excellent, as is expected given the method of determining this gradient; the bottom panel shows that the differences in q noted in Figure 22 are significant, as the two profiles show very poor agreement. The fact that the self-gravity theory, at least in its basic form used here, does not predict the actual profile evolution with longitude indicates that more work to explain observed locked precession remains to be done.

microwave opacities and on calculated drag torques. These results indicate that the self-gravity theory used here is, at best, incomplete at this time. The empirically derived eccentricity gradients should serve as an additional constraint on any modifications to the self-gravity theory or alternative theories proposed to explain the observed locked precession of elliptical rings.

3.6 Search for Shepherd Satellites to Confine the Rings

The second dynamical problem we shall address is the confinement of many of the rings. Of the nine pre-Voyager Uranian rings, only three have been associated with resonances of known satellites (Porco and Goldreich, 1987). The encounter of Voyager 2 with Uranus resulted in the discovery of ten small satellites (Smith *et al.*, 1986), two of which, Cordelia and Ophelia, were found bracketing Ring ϵ, just as the shepherding theory of ring confinement (Goldreich and Tremaine, 1979a) predicted. The inner edge of Ring ϵ is believed to be shepherded by an outer eccentric resonance (OER) of Cordelia, while the outer edge of Ring ϵ is thought to be shepherded by an inner eccentric resonance (IER) of Ophelia (Goldreich and Porco, 1987). In addition, the outer edge of Ring δ has been associated with an IER of Cordelia, and the outer edge of Ring γ has been associated with an IER of Ophelia. Perhaps not coincidentally, these edges are among the sharpest in the Uranian system (Table 4). The other six rings have as yet not been associated with any resonances of any of the known satellites; yet, as Table 4 shows, many of the edges are quite sharp, indicating that a confinement mechanism is at work. We hypothesize that perhaps one or more ***unknown*** satellites shepherd these rings, and attempt to find candidate locations for satellites which might shepherd several edges simultaneously. These satellites would necessarily be quite small in order to explain why they were not seen in the Voyager images; it has been estimated that the detection threshold for the Voyager cameras is a satellite approximately 10 km in radius (Smith *et al.*, 1986).

The general resonance condition for rings and satellites in coplanar orbits is (Porco and Goldreich, 1987):

$$mn - q\kappa - mn_s - k\kappa_s = 0 \tag{8}$$

where m, q, and k are integers (m is a positive integer), n is the mean motion[4] of the ring particle and κ is the epicyclic frequency of the ring particle[5]. n_s and κ_s are the corresponding values for the satellite.

---

[4] Mean motion is the average angular velocity of the orbiting particle.

[5] The epicyclic frequency is the rate at which the radius of a particle on an eccentric orbit varies from the average circular orbit. For a spherically symmetric central body, $\kappa = n$; κ not equal to n results in apsidal progression.

The order of the resonance is defined as $|k| + |q|$, so first-order resonances have either $(k = 0, q = \pm 1)$ or $(q = 0, k = \pm 1)$. First-order resonances are the strongest resonances, since the strength of the perturbation potential is proportional to $e^{|q|} {e_s}^{|k|}$, where e is the eccentricity of the ring and e_s is the eccentricity of the satellite. The $q = 0$ resonances are corotation resonances and are not considered further here.

Let us consider the $k = 0$ resonances. The resonance condition then becomes

$$\kappa = \pm m(n_s - n).$$

Given the semimajor axis a of a ring edge, we compute n and κ of the ring using the mass of Uranus given by Tyler *et al.* (1986) and the gravitational harmonics of Uranus given by French *et al.* (1988). We then find the possible satellite positions corresponding to solutions of the above resonance condition. We hope to find one satellite at semimajor axis a_s which has first-order resonances at several observed ring edge locations.

We have found that generally there are several possible satellite orbits which may shepherd *two* rings simultaneously, particularly if the rings are near one another. Therefore, even though the existence of satellites which shepherd only two ring edges is certainly possible (Cordelia and Ophelia appear to belong to this category), given the data available it is an ill-defined problem, since there are usually multiple solutions. For this reason we restrict our attention to possible orbit locations which have first-order resonances at the edges of *three* or more rings. The problem we pose is: *If* a given set of three ring edges is confined by resonances with *one* satellite, where could that satellite be, if anywhere?

We first consider the innermost three rings. Rings 6, 5, and 4 share a common morphology of sharp outer edges and diffuse inner edges (Section 3.2). We hypothesize that the outer edges of these rings are all shepherded by a single satellite exterior to Ring 4. We compute all possible n_s which satisfy the resonance condition for all three rings, while also constraining m so that the resonances are spaced by more than approximately 3 km, the width of the rings. For the semimajor axis of the ring edge, we use the semimajor axis of the middle of the ring (French *et al.*, 1988) and add to it half the average width of the ring as determined by the radio occultation experiment (Table 4). As these rings do not show a clear relationship between true anomaly and ring width (French *et al.*, 1986), this is a reasonable procedure.

We have found that an object orbiting with semimajor axis 42900.8 km would have the first-order resonances listed in Table 5. However, given the resonance spacing at the locations of these three rings (Table 5), the statistical significance of such an event may not be particularly strong, and it is not possible to make a definitive statement regarding the existence of such a satellite.

We have also found that a satellite orbiting with a semimajor axis of 47166 km (which is ~ 10 km inside the orbit of the almost-circular Ring η) would have the first-order resonances as listed in Table 6. The low order of these resonances, and the associated large resonance spacings (Table 6), makes this location much more statistically significant. In this case, we find that a single object could have a first-order resonance 1.6 km outside the outer edge of Ring 4 (7:6), precisely at the outer edge of Ring α (13:12), approximately at the mean semimajor axis of Ring β (21:20), and approximately 0.6 km outside the inner edge of Ring γ (68:69). In addition, there is a weaker, second-order resonance (55:57) excited by such an object which lies within Ring δ (at ~ 48300 km), and may be associated with the wavelike feature observed there (Marouf *et al.*, 1988). If in fact such a satellite is confining these rings, one would expect the resonance locations to be precisely at the outer edges of Rings 4, α, and β, and precisely at the inner edge of Ring γ. However, uncertainties in the actual ring locations are on the order of 1 km (French *et al.*, 1988), and the details of ring width variations are not well understood for many of the rings. As an example of typical residuals for *known* resonances in the Uranian rings, the predicted locations of the viscous instablity resonances for Rings γ and δ differ by ~0.5–1 km from the actual ring positions, and the differences between the shepherding resonance locations for Ring ϵ and the actual position of its edges are ~ 0.5 km (French *et al.*, 1988). Thus the residual errors reported here are somewhat, but not grossly, larger than those already observed in the system.

We now investigate whether a satellite small enough to have been missed in the ring satellite search by Voyager would be large enough to confine these rings. For shepherding to take place, the gravitational torque applied by the satellite must exceed the viscous torque of the ring[6]. Goldreich and Porco (1987) discuss the shepherding mechanism for the Uranian rings, and point out that any torque large enough to shepherd a ring edge must necessarily result in non-linear perturbations to the ring particle streamlines. The "critical" torque T_{crit}, at which the perturbations become non-linear, is given approximately by (Goldreich and Porco, 1987)

$$T_{\text{crit}} \simeq \frac{\pi^2 \sigma^3 n^2 a^8}{6 M_U^2}, \tag{9}$$

where σ is the surface mass density of the ring, n and a are the mean motion and semimajor axis of the ring orbit, and M_U is the mass of Uranus.

---

[6] Viscous torque is the collisional dissipation of energy which results in ring spreading.

$(m+k):(m-q)$ $k=0, q=+1$	Resonance Spacing (km)	R_e^a (km)	Ring Mean Outer Edge (km)
27:26	40	41838.4	41838.0 (6)
43:42	16	42235.2	42236.1 (5)
87:86	4	42572.5	42572.1 (4)

TABLE 5: First-order resonances of a satellite at semimajor axis 42900.8 km. The estimated error in ring position is approximately 1 km based on residual trajectory uncertainty. However an error in trajectory would be expected to offset all rings in the same direction by approximately the same amount. There is additional uncertainty in the location of the edge of the ring due to the lack of understanding of how the width of the ring changes with azimuth. The widths of these rings change by up to about 25% (less than 1 km) from the ingress to egress measurements of the radio occultation experiment (Table 4).

[a] R_e is the eccentric resonance location.

$(m+k):(m-q)$ $k=0, q=\pm1$	Resonance Spacing (km)	R_e (km)	Ring Edge (km)
7:6	> 600	42573.7	42572.1 (4, outer)
13:12	200	44722.0	44722.1 (α, outer)
21:20	70	45660.6	45665.0 (β, outer)
68:69	7	47626.1	47625.5 (γ, inner)

TABLE 6: First-order resonances of a satellite at semimajor axis 47166.0 km. Edge locations for Rings 4 and γ are determined using the same procedure as described in the text for Rings 6, 5 and 4; edges for Rings α and β are determined by fitting ellipses to the measured inner and outer edges of these rings in the radio data. Note the very large resonance spacings, indicating high statistical significance for this possible satellite location.

The applied nonlinear torque T_{nl} is given by

$$T_{nl} \simeq \frac{3.7 m M_s \sigma^2 n^2 a^6}{M_U^2}, \tag{10}$$

where M_s is the mass of the shepherding satellite and m is azimuthal number of the resonance, from Eq. 8. Since T_{nl} must exceed $T_{\rm crit}$, we may combine Eqs. 9 and 10 to obtain

$$\sigma \lesssim \frac{2.25 m M_s}{a^2}.$$

The maximum mass of the satellite may be approximately computed by assuming that any satellite larger than approximately 10 km in radius would have been detected in the Voyager images (Smith *et al.*, 1986), and assuming a density for the satellite equal to that of the other Uranian satellites, 1.4 g-cm^{-3} (Tyler *et al.*, 1986). We thus obtain $M_s \lesssim 6 \times 10^{18}$ g. Using the semimajor axes of the rings given in Table 2, and the values for m given in Table 6, we find that

$$\begin{aligned} \sigma(\text{Ring } 4) &\lesssim 5.2 \text{ g-cm}^{-2} \\ \sigma(\text{Ring } \alpha) &\lesssim 8.8 \text{ g-cm}^{-2} \\ \sigma(\text{Ring } \beta) &\lesssim 13.6 \text{ g-cm}^{-2} \\ \sigma(\text{Ring } \gamma) &\lesssim 40.5 \text{ g-cm}^{-2} \end{aligned}$$

These maximum values for the surface mass density for Rings 4, α, and β are somewhat small, given the relatively large microwave opacities observed at both the 3.6 and 13 cm wavelengths. However, these bounds are highly sensitive both to the value chosen for the maximum radius of the satellite, and to the details of the viscosity model used. An upper limit on the size of the satellite of 15 km rather than 10 km would increase the maximum values of σ by more than a factor of three. We note that the smallest objects actually seen by the Voyager cameras at Uranus were $\sim$ 20 km in radius (Smith *et al.*, 1986). Of course, given the estimated location for this possible shepherding satellite of only $\sim$ 10 km inside the edge of Ring η, we are hypothesizing a situation where the shepherding satellite is essentially bumped up against, or actually within the ring. Under such circumstances we would expect to see severe perturbations of Ring η along the lines of the "braided" Ring F of Saturn. However, no such perturbations are seen. We note that, as theoretical modeling of viscosity in planetary rings is still an active area of research, bounds on surface mass density based on the models considered here may be subject to change as a better understanding of this mechanism is reached.

We may also investigate what perturbations such an object might excite on the edges of the rings it confines. A shepherding satellite will produce a wavy edge, with the number of wavelengths along the circumference equal to the m-number of the resonance. The amplitude of the disturbance depends on the mass of the satellite and the distance of the satellite from the ring as (Freedman *et al.*, 1983):

$$|\Delta r| \simeq 3 \text{ km} \left(\frac{M_s}{10^{19} \text{ g}}\right) \left(\frac{a_s}{50,000 \text{ km}}\right)^3 \left(\frac{100 \text{ km}}{a_s - a}\right)^2$$

where a_s is the semimajor axis of the satellite. This equation implies that for Rings 4, α, and β, the perturbations would be only a few meters, far below the possibility for detection. For Ring γ, the perturbation would be on the order of 70 m, which given the current level of understanding of the orbit of this ring (French *et al.*, 1988), would also not be detectable.

3.7 Summary and Discussion

In this chapter, we described the diffraction-reconstruction procedures used to improve the resolution of initially diffraction-limited raw data by more than an order of magnitude. Extension of the algorithm to handle the significantly eccentric Uranian rings was also described.

We discussed qualitatively the appearance of the rings and how they vary from one observation azimuth to the other. Many edges were observed to be quite sharp; however there is tendency for outer edges to be sharper than inner edges, indicating a possible difference in the confinement mechanism for the two edges.

We then described the way in which the fine-resolution profiles may be used to investigate two dynamical problems. In the first, we used two observed profiles for each of Rings α, β, and ϵ to construct empirically an eccentricity gradient profile $q(a)$ for these rings. The results were then compared to the predictions of the self-gravity theory for uniform ring precession. We found that for Rings ϵ and β the empirical $q(a)$ profiles did not agree well with those predicted. This result is one indication that problems exist with the self-gravity theory, at least in its basic form used here. The small surface mass densities predicted by the theory for Rings α and β are likewise inconsistent with both the microwave opacities observed and with the large drag torque exerted on the rings by the hydrogen atmosphere.

The second ring dynamics problem addressed was that of ring confinement. High resolution profiles of the rings show that many ring edges are quite sharp, indicating a confining force. Although satellites were found to shepherd both edges of Ring ϵ, and the outer edges of Rings γ and δ, the confinement mechanism of all of the other edges remain unknown at this time. We hypothesized that satellites too small to be seen by the Voyager cameras are in fact shepherding these edges, and found two locations where a satellite might confine at least three rings. The more significant of the two, near Ring η, could simultaneously shepherd four edges with low order resonances. The torque which would be available from such a small, unseen, satellite appears to be roughly sufficient to shepherd these four rings. However, one would expect significant disturbance to Ring η due to its proximity to such a satellite, and such disturbance is not observed. Unfortunately, the calculated perturbations to the edges of Rings 4, α, β, and γ are too small to be detectable in the current set of observations, so confirmation of such a location would be difficult.

Chapter 4

Differential Measurements and Implications for Physical Properties

In the previous chapter, we discussed the application of the radio occultation measurements to problems of ring structure and dynamics, including maintenance of eccentricity and ring confinement. Because the 13 cm wavelength signal has approximately 14 dB lower signal-to-noise than the 3.6 cm signal, high resolution reconstruction of detailed ring structure (Chapter 3) is possible only for the shorter wavelength. However, reconstructed coarse-resolution profiles at the longer-wavelength contribute significantly to study of the particle sizes in the rings, as we demonstrate below.

In this chapter, we discuss the dual-wavelength data and present measurements of integrated optical depth and phase delay. To reduce noise in the 13 cm data, we consider profiles at 500 m resolution. The measurements are then used to constrain physical properties of the rings, such as ring thickness and particle sizes. We present a short summary of three models for the interaction of radio waves with rings, in all three cases starting from Mie theory for scattering by a sphere. Then, these models are used to investigate the problem of ring thickness, where we show that the measurements are consistent with a many-particle-thick model whose vertical thickness is either constant or varies inversely with ring width. Finally, we discuss ways in which the dual-wavelength measurements may be used to constrain the particle size distributions, and in addition, point out some difficulties in the interpretation of the measurements, due presumably to a breakdown of the assumptions of standard radiowave-ring interaction models.

4.1 Differential Measurements

As described in Chapter 2, the radio occultation experiment provides observations of both τ and ϕ_c at $\lambda = 3.6$ and 13 cm. The two wavelengths are coherently derived from Voyager's onboard Ultra-Stable Oscillator and are harmonically related by the exact ratio 3/11. In principle, the experiment yields four independent profiles: $\tau(3.6\text{ cm})$, $\tau(13\text{ cm})$, $\phi_c(3.6\text{ cm})$, and $\phi_c(13\text{ cm})$. Phase fluctuations due to oscillator instabilities can be essentially removed if differential phase

$$\Delta\phi_c \equiv \phi_c(13\text{ cm}) - \frac{3}{11}\phi_c(3.6\text{ cm})$$

is considered instead of individual absolute phases.

Because of lower transmitted power, and lower antenna gain both on Voyager and on the ground, the observed free-space value of SNR_0 at 13 cm wavelength was smaller than that at 3.6 cm by approximately 14 dB ($\sim$ 32 vs $\sim$ 46 dB). This large difference causes $\tau(13\text{ cm})$ and $\phi_c(13\text{ cm})$ to be significantly noiser at the same resolution. At 50 m resolution, for example, the free-space standard deviation in measured optical depth $\sigma_\tau(13\text{ cm}) \simeq 0.45$, compared to $\sigma_\tau(3.6\text{ cm}) \simeq 0.09$. (Further discussion of noise characteristics may be found in Appendix A.) Profiles at 13 cm therefore require significant resolution degradation to reduce $\sigma_\tau(13\text{ cm})$ to useful levels. For this reason, we compare dual-wavelength measurements at 500 m resolution, for which σ_τ in free-space is approximately 3×10^{-2} and 14×10^{-2} at 3.6 and 13 cm, respectively. The corresponding uncertainty in the phase measurement, σ_{ϕ_c}, is equal to 1.8×10^{-2} cycles for the 13 cm data, and 3.6×10^{-3} cycles for the 3.6 cm data.

Here we discuss specifically two representative example profiles at 3.6 and 13 cm. (For completeness, ingress and egress profiles of all nine rings are presented in Appendix B.) The five inner rings (6, 5, 4, α, and β) are exemplified by the Ring α ingress profile, shown in Figure 24. In this figure, the top panel shows normal optical depth τ at both 3.6 and 13 cm, and the bottom panel shows the coherent phase delay for both wavelengths. The most obvious characteristic of the five inner rings is the large phase delay at 13 cm compared to the nearly absent phase delay at 3.6 cm. Note in particular how the shape of the 13 cm phase delay for Ring α closely mimics the shape of the observed optical depth profile at 3.6 cm. The large phase delay at 13 cm wavelength has been one of the most intriguing results of the Uranus ring occultation data, as it is very difficult to produce such a large differential phase effect given the lack of evidence for a corresponding differential opacity as indicated in the top panel of Figure 24. This subject will be pursued further below. The four outer rings (Rings η, γ, δ, and ϵ), are exemplified by the Ring ϵ egress profile shown in Figure 25. Little or no phase delay at either wavelength is evident in this case. Within the noise limitations, little or no difference in normal optical depth is detectable for any of the nine rings, with the possible exception of Ring β (see Figure 87, Appendix B).

We summarize in Table 7 results for integrated (or averaged) optical depth and phase shift. Values for Rings η and δ are for the main cores of these rings, as the SNR of the 13 cm data is too low to allow meaningful comparison with the 3.6 cm data for their tenuous companion rings. Individual uncertainties ($\sim$ 1-σ) were computed using previously published procedures (Marouf *et al.*, 1986) summarized in Appendix A, assuming $\mathrm{SNR}_0 \simeq 46$ and 32 dB at 3.6 and 13 cm, respectively. Comparison of the magnitude of the uncertainties in columns 2 and 3 of Table 7 clearly shows the effect of the 14 dB difference. Also given in columns 4 and 5 of Table 7 are the integrated differential opacity, $\int \Delta\tau$, normalized by the ring width W and by $\int \tau(3.6\text{ cm})$ respectively, where

$$\Delta\tau \equiv \tau(3.6\text{ cm}) - \tau(13\text{ cm}).$$

The average differential opacity $< \Delta\tau > \equiv \int \Delta\tau / W$ is also plotted in Figure 26a, where, for all rings, the uncertainty intervals either include or are close to the $< \Delta\tau >= 0$ level. For rings with dense features (τ comparable to $\tau_{TH}(13\text{ cm})^1 \simeq 4.3$ at 500 m resolution), a reliable estimate of $< \Delta\tau >$ is precluded, resulting in large uncertainty intervals. Figure 26a strongly suggests $< \Delta\tau > \simeq 0$ for *all* cases that are not masked by noise. Nonetheless, within the noise limitations, Table 7 indicates that for the narrow rings (6, 5, 4, η, and δ ingress), ~20–40% differential opacity could go undetected. For the relatively wider α, β, and δ egress cases, this limit is $\sim$ 15%. For Ring ϵ egress, the integrated differential opacity is less than $\sim$ 3%. Because of regions of optical depth exceeding τ_{TH}, no reliable integrated differential opacity measurement is possible for Ring ϵ ingress or for Ring γ.

The last column in Table 7 gives the average integrated differential phase shift $< \Delta\phi_c > \equiv (1/W) \int [\phi_c(13\text{ cm}) - \frac{3}{11}\phi_c(3.6\text{ cm})]$, normalized by $< \tau(3.6\text{ cm}) >$. Because it is an effect per unit optical depth, its value may be directly compared among the rings (Marouf *et al.*, 1982). This is accomplished in Figure 26b. The measurements of this quantity divide the rings into two distinct groups. The first includes the five inner rings (6, 5, 4, α, and β) which have $< \Delta\phi_c > / < \tau(3.6\text{ cm}) >$

---

[1] The threshold opacity τ_{TH} is the smallest ring opacity for which the confidence interval includes $\tau = \infty$. See Appendix A for further discussion of noise in the radio occultation data.

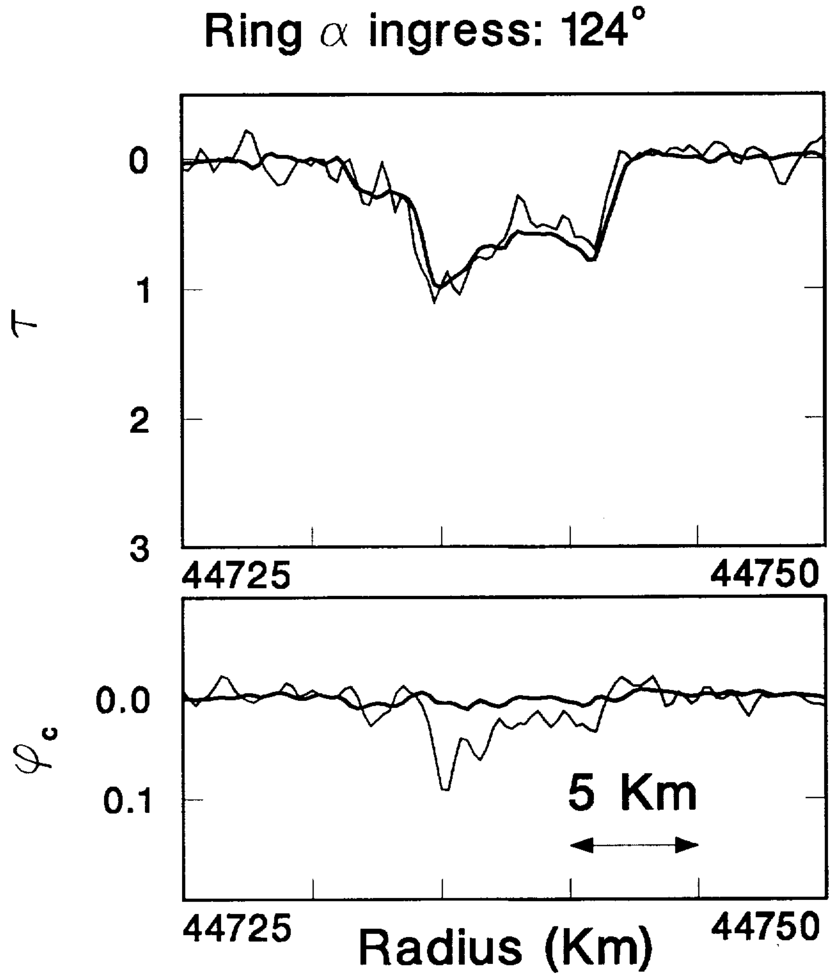

FIG. 24: Opacity and phase profiles of Ring α observed at ingress. ϕ_c is measured in cycles. Angle indicated at the top is true anomaly. Heavy curve is the 3.6 cm wavelength, lighter curve is the 13 cm wavelength. The 13 cm curve is significantly noiser due to lower transmitter power as well as smaller antenna gain for the longer wavelength. Within the measurement error, there is no detectable difference between the optical depths at 3.6 and 13 cm. The phase delay at 13 cm is particularly clear for this ring, and significantly exceeds its value at 3.6 cm. Note how the phase behavior closely mimics the shape of the optical depth curve, clearly indicating that the phase delay is related to the amount of material present in the ring. Discussion of noise limitations may be found in Appendix A; for 500 m resolution, in free space, $\sigma_\tau(13\text{ cm}) \simeq 1.4 \times 10^{-1}$, $\sigma_\tau(3.6\text{ cm}) \simeq 3 \times 10^{-2}$, $\sigma_{\phi_c}(13\text{ cm}) \simeq 1.8 \times 10^{-2}$ cycles, and $\sigma_{\phi_c}(3.6\text{ cm}) \simeq 3.6 \times 10^{-3}$ cycles.

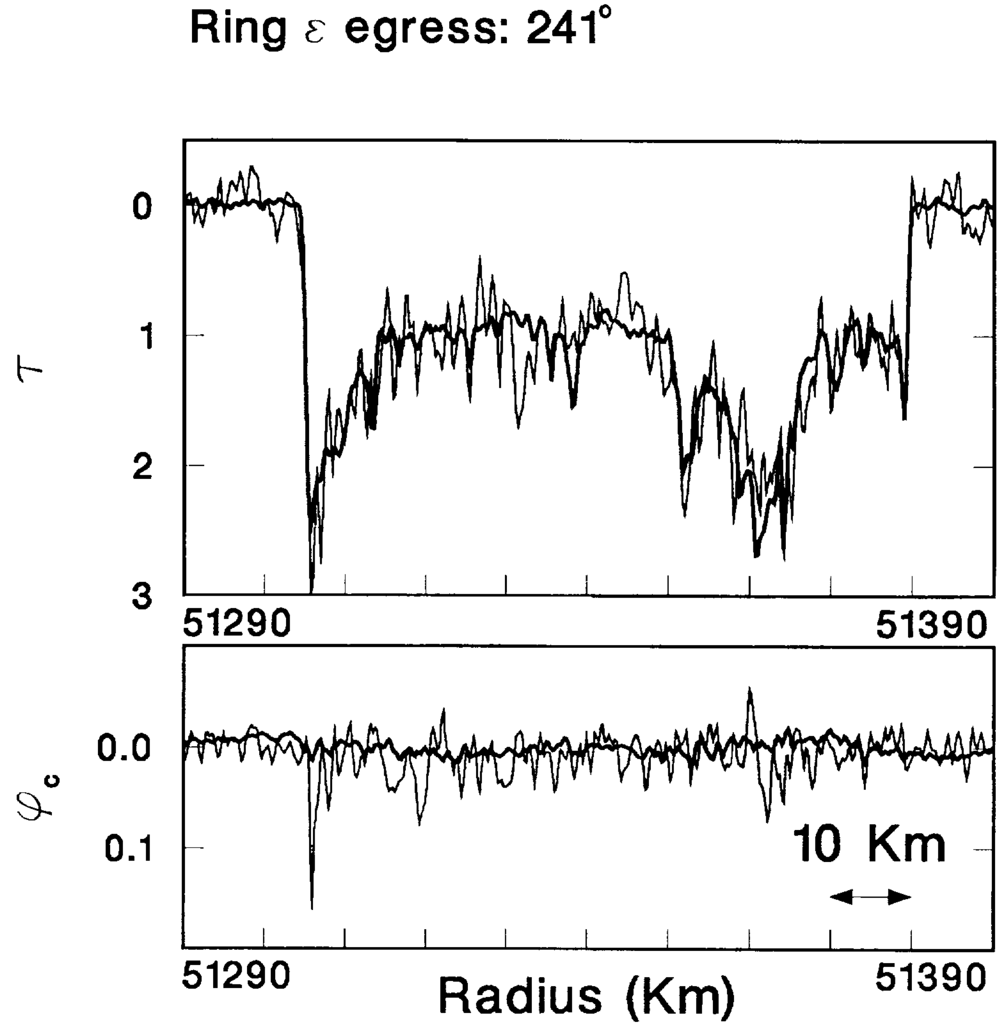

FIG. 25: Opacity and phase profiles of Ring ε observed at egress. See caption of Figure 24 for details. Due to the large width and relatively small optical depth of this ring, measurements here concerning differential optical depth and phase delay have the smallest inherent noise limitations. The top panel clearly shows how the optical depth profiles at the two wavelengths closely follow each other throughout the ring. This is an indication of relative depletion of decimeter and smaller size particles. The bottom panel shows little phase delay at either wavelength, though there is some bias for the 13 cm signal towards phase retardation in the inner region of the ring. This bias shows up in the positive, albeit small, phase retardation measurement in Table 7.

Ring	Side	$\int \tau(3.6\text{ cm})$ (km)	$\int \tau(13\text{ cm})$ (km)	$< \Delta\tau >^a$	$\frac{<\Delta\tau>}{<\tau(3.6\text{ cm})>}$ %	$\frac{<\Delta\phi_c>^b}{<\tau(3.6\text{ cm})>}$ (milli-cycles)
6	ing	0.96 ± 0.07	0.78 ± 0.34	0.12 ± 0.23	19 ± 36	65 ± 25
	egr	0.90 ± 0.07	0.91 ± 0.35	-0.01 ± 0.21	-2 ± 40	47 ± 27
5	ing	1.93 ± 0.08	1.99 ± 0.46	-0.02 ± 0.17	-3 ± 24	43 ± 18
	egr	2.07 ± 0.09	1.60 ± 0.45	0.18 ± 0.18	23 ± 22	50 ± 16
4	ing	1.57 ± 0.08	1.42 ± 0.41	0.08 ± 0.21	10 ± 27	51 ± 19
	egr	1.36 ± 0.08	1.64 ± 0.43	-0.10 ± 0.16	-20 ± 32	55 ± 24
α	ing	6.17 ± 0.15	5.56 ± 0.76	0.06 ± 0.07	10 ± 13	45 ± 9
	egr	6.60 ± 0.6	$6.92^{+0.98}_{-0.72}$	-0.08 ± 0.24	-5 ± 15	60 ± 10
β	ing	4.24 ± 0.12	4.18 ± 0.64	0.01 ± 0.09	0 ± 15	70 ± 11
	egr	4.08 ± 0.13	2.95 ± 0.64	0.10 ± 0.06	27 ± 16	75 ± 12
η	ing	1.00 ± 0.07	0.62 ± 0.33	0.25 ± 0.22	39 ± 34	-17 ± 23
	egr	0.90 ± 0.07	0.69 ± 0.33	0.14 ± 0.22	24 ± 37	-3 ± 28
γ	ing	9.62 ± 0.28	$11.71^{+\infty}_{-1.31}$	$-0.55^{+0.35}_{-\infty}$	$-22^{+14}_{-\infty}$	31 ± 29
	egr	$6.68^{+1.19}_{-0.55}$	$5.42^{+\infty}_{-1.00}$	$0.77^{+0.95}_{-\infty}$	$19^{+23}_{-\infty}$	9 ± 39
δ	ing	5.34 ± 0.13	5.76 ± 0.75	-0.06 ± 0.11	-8 ± 14	12 ± 10
	egr	4.21 ± 0.13	$5.37^{+1.20}_{-0.71}$	$-0.43^{+0.27}_{-0.45}$	-28^{+17}_{-29}	27 ± 17
ϵ	ing	$93.38^{+\infty}_{-2.14}$	$81.03^{+\infty}_{-4.19}$	$0.55 \pm \infty$	$13 \pm \infty$	-2 ± 10
	egr	97.04 ± 0.57	$96.57^{+3.24}_{-2.48}$	0.01 ± 0.04	1 ± 3	8 ± 2

TABLE 7: Total and differential integrated opacity and phase delay measured at 3.6 and 13 cm wavelengths. In all cases, resolution is 500 m.

[a]: The brackets $< >$ denote average value computed by integrating over the width of the ring W and dividing by W. $\Delta\tau \equiv \tau(3.6\text{ cm}) - \tau(13\text{ cm})$.

[b]: $\Delta\phi_c \equiv \phi_c(13\text{ cm}) - \frac{3}{11}\phi_c(3.6\text{ cm})$.

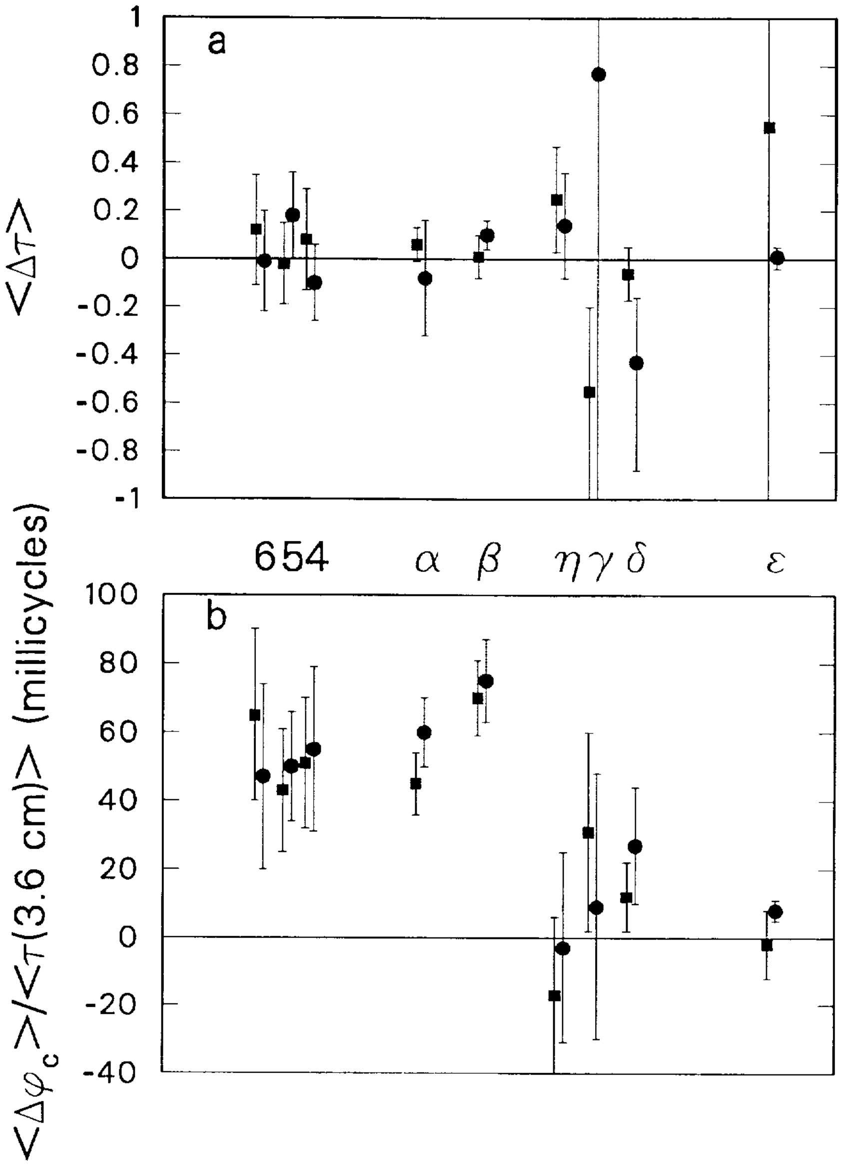

FIG. 26: (a) Average differential opacity observed for each of the nine Uranian rings, shown approximately to scale in distance from the planet. The average is computed by integrating $\Delta\tau \equiv \tau(3.6 \text{ cm}) - \tau(13 \text{ cm})$ over the width of the ring W, and dividing the result by W. The left (squares) and right (circles) symbols for each pair correspond to ingress and egress values, respectively. In all cases, the 1-σ uncertainty interval either includes or is close to zero. The large uncertainty in some cases is caused by features of opacity exceeding the threshold. (b) Average differential phase delay $\Delta\phi_c \equiv \phi_c(13 \text{ cm}) - \frac{3}{11}\phi_c(3.6 \text{ cm})$, per unit average 3.6 cm opacity. The measurements clearly divide the rings into two distinct groups according to distance from Uranus. Numerical values corresponding to points shown in both (a) and (b) are given in Table 7.

$\gtrsim$ 40–75 $\times 10^{-3}$ cycles/unit optical depth. Dispersion is much less noticable among the second group (η, γ, δ, and ϵ), where its value is near zero, in the range -17 to 31×10^{-3} cycles/unit optical depth.

Combined, the above differential opacity and differential phase measurements have important implications for ring particle sizes and the manner in which ring particles are distributed in space. These implications are examined at length in subsequent sections. To relate the observations to physical ring properties, however, we first need to introduce a physical model for the interaction between radio waves and ring particles. A brief summary of three such models is given in the next section and the results are subsequently used to interpret the differential observations above.

4.2 Interaction of Radio Waves with Rings

We start with a description of the extinction behavior of a single particle, and then extend the description to extinction by an ensemble of such particles. In the literature there are three models for the distribution of particles in space that are relevant to planetary rings. The first is a monolayer, in which all the particles lie in a single layer, and are equally illuminated by the incident radiation (although Dones *et al.* (1988) proposed a model in which shadowing at grazing incidence is included). The second is the many-particle-thick model, in which the particles lie in a cloud-like layer which is many particle diameters in thickness. In this model, particles deep within the layer are illuminated by a wave which has been attenuated due to passage through the layer. Bridging these two extremes is a third model, the "thin layer model" proposed by Zebker *et al.* (1985) for features in Saturn's rings, where a layer is a few particles thick. It is important to point out that all of these models assume noncoherent-interactions among the particles. However, it is intuitively clear that this assumption must break down if the packing fraction is not small and hence the particles are close to one another. Extension of the formulation to account for such coherent interactions is attempted in Chapter 5.

All of our numerical computations below are based on the assumption of scattering by nearly-spherical particles. Although approximations to the exact scattering behavior of an arbitrarily-shaped particle exist in the limit of particles very small compared to the incident wavelength (Rayleigh scattering) and in the limit of particles very large compared to the wavelength (geometric optics), these approximations are in general not very useful in the context of scattering of microwave radiation by ring particles. Particles in the rings are often of a size comparable to the radio wavelength. Under these circumstances, an alternative method is required. A very useful theoretical development in electromagnetic scattering theory is the exact solution of the problem of scattering by a sphere of arbitrary size and refractive index. Gustav Mie (Mie, 1908) is usually credited with the solution of this problem, and the mathematical formulation is usually referred to as Mie theory (see, however, Kerker, 1969, p. 4).

4.2.1 Extinction by a single particle

Consider first what measurable effect a single particle has on a plane wave incident along the z-axis (see Figure 27 for geometry). We adopt notation similar to that of Bohren and Huffman (1983), and assume a time variation of the complex field of the form $e^{-i\omega t}$.[2] The amplitude scattering matrix S is defined as follows:

$$\begin{pmatrix} E_{\|s} \\ E_{\perp s} \end{pmatrix} = \frac{e^{ik(r-z)}}{-ikr} \begin{pmatrix} S_{\|} & S_3 \\ S_4 & S_{\perp} \end{pmatrix} \begin{pmatrix} E_{\|i} \\ E_{\perp i} \end{pmatrix}, \tag{11}$$

where $k = 2\pi/\lambda$ and $E_{\|i}$ and $E_{\perp i}$ are the electric field components of the incident wave parallel to, and perpendicular to, respectively, the scattering plane (the plane containing both the incident wave propagation direction and the direction from the particle to the point at which the scattered field is observed). $E_{\|s}$ and $E_{\perp s}$ are the corresponding electric field components of the scattered field. The distance from the scatterer to the observation point is r and the projection of this vector onto the direction of the original ray is z; thus the phase difference between the incident wave and the scattered wave is $k(r-z)$. The matrix S describes the scattered field components in terms of the observation angles and scatterer properties only. For the special case of near-spherical scatterers observed in the near-forward direction, depolarization effects may be neglected; that is, $S_3 \simeq S_4 \simeq 0$ and $S_{\perp}(\theta) \simeq S_{\|}(\theta) \simeq S(\theta)$, where the scattering angle θ (Figure 27) is small ($\sin\theta \simeq \theta$). In this case, the direction of the electric field vector is essentially unaffected by the scattering, and the amplitude of the near-forward field scattered by the object toward the point (x, y) in the observing plane is

$$E_s = E_i \frac{e^{ik(r-z)}}{-ikr} S(\theta).$$

Following an approach similar to that of van de Hulst (1981, p. 30), we assume that x and y are much smaller than z, approximate $r - z$ in the exponent as $(x^2 + y^2)/2z$, and replace r by z in the denominator. Then the total field amplitude may be written as

$$E = E_i + E_s = E_i \left(1 + \frac{S(\theta)}{-ikz} e^{ik(x^2+y^2)/2z}\right),$$

where E_i is the incident field and E_s is the scattered field. The fact that z is large implies that the second term in the parentheses is small. Therefore, the intensity may be written as

---

[2] ω is angular frequency and t is time.

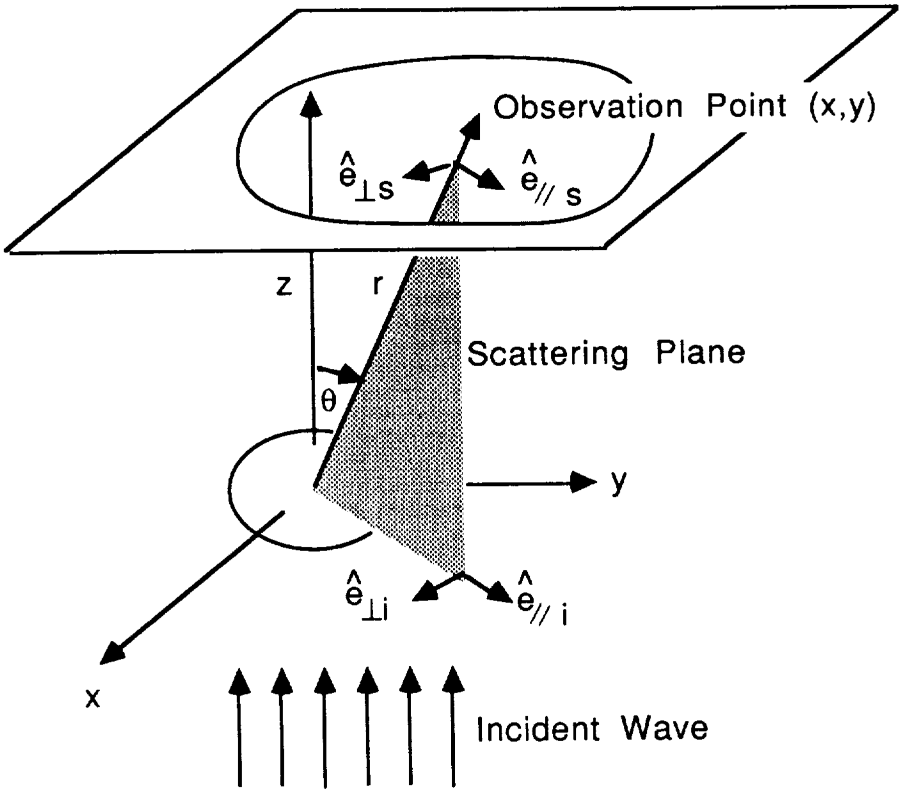

FIG. 27: Geometry for scattering by a single scatterer. The incident plane wave is along the z axis, and the total field is observed in the near-forward direction. The observation plane (x, y) is a distance z from the origin, assumed to be located within the scatterer. The distance from the origin to the observation point is r. The scattering plane is defined as the plane containing both the incident wave direction and the scattered wave direction.

$$I \equiv EE^* = I_i \left(1 + \frac{2}{kz}\mathrm{Re}\left\{iS(\theta)e^{ik(x^2+y^2)/2z}\right\}\right),$$

where Re{·} signifies the real part of the quantity inside the braces, "*" indicates complex conjugate, and $I_i = E_i E_i^*$. The difference $I - I_i$ may be integrated over the entire area of the observing plane to find the change in power due to the presence of the scatterer. The x and y integrals are evaluated by the stationary phase method. The result is

$$\int\int (I - I_i)dx\,dy = -\frac{4\pi}{k^2}\mathrm{Re}\{S(0)\}I_i,$$

where $S(0) \equiv S(\theta = 0)$ is the exact forward scattering amplitude. The object has removed a total power of $C_{\text{ext}} I_i$ from the incident plane wave (hence the negative sign), where C_{ext} is the extinction cross-section defined as

$$C_{\text{ext}} = \frac{4\pi}{k^2} \text{Re}\{S(0)\}.$$

In the preceeding derivation, the integration over x and y was extended to infinity, despite the earlier assumption that θ is small and hence x and y are much smaller than z. The validity of the derivation follows from the fact that strong interference between the incident and scattered wave is primarily confined to a region close to the exact forward direction. As x and y increase, the phase of the scattered wave oscillates rapidly, and the net interference effect contributed from the region beyond the first few Fresnel zones quickly becomes negligible. Therefore, the small θ requirement implies that $\sqrt{\lambda z}/z$ must be small—that is, $z \gg \lambda$, a condition which is easily met in ring occultation experiments.

Extinction by a spherical particle

For the particular case of a sphere of radius a, we may normalize the extinction cross-section defined above by the geometric cross section πa^2 to obtain the extinction efficiency Q_{Mie}:

$$Q_{\text{Mie}} = \frac{4}{(ka)^2} \text{Re}\{S(0)\}. \tag{12}$$

We also define the phase-shift efficiency P_{Mie} analogously as

$$P_{\text{Mie}} = \frac{-2}{(ka)^2} \text{Im}\{S(0)\}, \tag{13}$$

where $\text{Im}\{\cdot\}$ indicates the imaginary part of the term inside the braces. It will be shown subsequently that P_{Mie} controls the phase shift introduced by an assembly of such particles; the sign is chosen so that a positive P_{Mie} represents phase retardation. The factor of two difference between Eqs. 12 and 13 results in symmetric equations for optical depth and phase delay for the many-particle-thick model of a ring, as we shall see below. These terms are generally referred to as Q_{ext} and P_{ext} in the literature, but we use Q_{Mie} and P_{Mie} to distinguish them from other extinction efficiencies, defined in later chapters.

Bohren and Huffman (1983) show that Q_{Mie} may be expressed as

$$Q_{\text{Mie}} = \frac{2}{(ka)^2} \sum_{n=1}^{\infty} (2n+1) \text{Re}\{a_n + b_n\}, \tag{14}$$

where $\{a_n\}$ and $\{b_n\}$ are the classical Mie coefficients, which may be computed numerically given the electric size ka, and the refractive index of the particle, m, relative to that of the medium in which the particle is embedded (*v.*, *e.g.*, Dave, 1968). Similarly,

$$P_{\text{Mie}} = -\frac{1}{(ka)^2}\sum_{n=1}^{\infty}(2n+1)\text{Im}\{a_n + b_n\}. \tag{15}$$

The behavior of Q_{Mie} and P_{Mie} as a function of a, λ, and m may now be illustrated. Figure 28 shows both Q_{Mie} and P_{Mie} for the wavelengths used in this experiment, plotted *vs* the radius of the particle in centimeters. The top panel assumes a lossless refractive index $m = (1.78 + 0.00i)$; the bottom panel assumes a very lossy material with refractive index $m = (1.70 + 0.70i)$. The reasons for choosing these particular values are discussed later, in Section 4.4.1.

In the Rayleigh region ($a \lesssim 1$ cm for the 3.6 cm extinction curves), Q_{Mie} increases very rapidly with increasing particle radius ($Q_{\text{Mie}} \propto (ka)^4$) for the case where there is no absorption (top panel of Figure 28), while P_{Mie} increases much less rapidly ($P_{\text{Mie}} \propto ka$). This behavior is also evident from the small argument limit of the Mie coefficients, where

$$\begin{aligned}
a_1 &\simeq \frac{-i2(ka)^3}{3}\frac{m^2-1}{m^2+2} - \frac{i2(ka)^5}{5}\frac{(m^2-2)(m^2+1)}{(m^2+2)^2} + \frac{4(ka)^6}{9}\left(\frac{m^2-1}{m^2+2}\right)^2 + O[(ka)^7] \\
b_1 &\simeq -\frac{i(ka)^5}{45}(m^2-1) + O[(ka)^7] \\
a_2 &\simeq -\frac{i(ka)^5}{15}\frac{m^2-1}{2m^2+3} + O[(ka)^7] \\
b_2 &\simeq O[(ka)^7].
\end{aligned}$$

To order $(ka)^6$, and assuming m is purely real,

$$Q_{\text{Mie}}\text{ (no absorption)} \simeq \frac{8(ka)^4}{3}\left(\frac{m^2-1}{m^2+2}\right)^2,$$

thus the $a^4\lambda^{-4}$ dependence of Q_{Mie} in this case. However, if there is sufficient loss in the particle (*i.e.*, $\text{Im}\{m\} \neq 0$) such that absorption dominates extinction, then the leading term in Q_{Mie} is

$$Q_{\text{Mie}}\text{ (with absorption)} \simeq 4(ka)\text{Im}\left\{\frac{m^2-1}{m^2+2}\right\},$$

and Q_{Mie} will vary as $a\lambda^{-1}$. This drastic difference in the behavior of Q_{Mie} is clearly visible in Figure 28.

Similarly, it is clear that, regardless of loss in the particle, the leading term in P_{Mie} is the first term of a_1, so that

$$P_{\text{Mie}} \simeq 2(ka)\text{Re}\left\{\frac{m^2-1}{m^2+2}\right\}$$

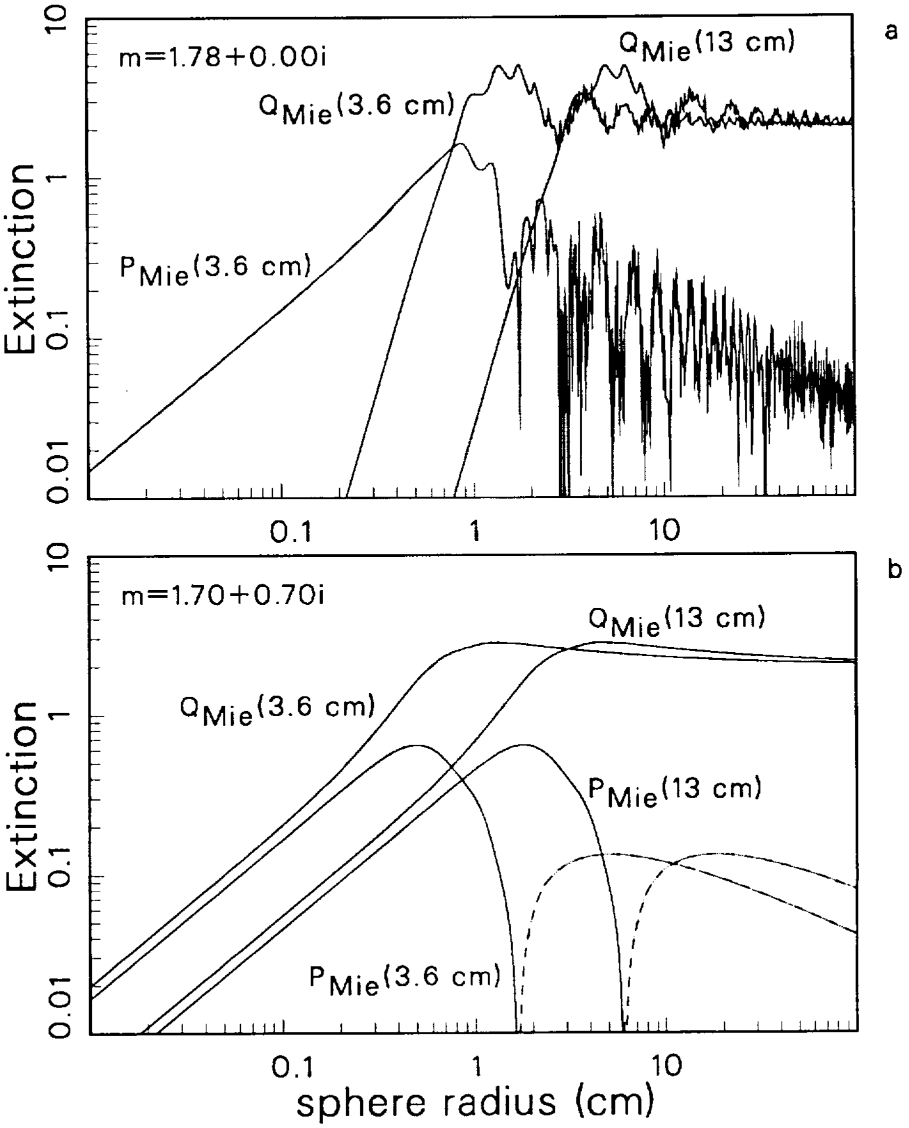

FIG. 28: Extinction curves for a sphere as obtained from Mie theory. The top panel assumes a lossless refractive index, while the bottom panel assumes a very lossy material. For clarity, the $P_{\text{Mie}}(13\text{ cm})$ curve has been omitted from the top panel, but the behavior would mimic $P_{\text{Mie}}(3.6\text{ cm})$, shifted to larger size particles as is demonstrated by the P_{Mie} curves in the lower panel. In the bottom panel, phase retardation is indicated by a solid line, phase advance by a dashed line.

and hence $P_{\mathrm{Mie}} \sim a\lambda^{-1}$ in both Figures 28a and b. A positive P_{Mie} is to be interpreted as phase retardation.

Consider now the behavior of P_{Mie} and Q_{Mie} as the particle becomes very large. In the limit of $a \gg \lambda$, $Q_{\mathrm{Mie}} \rightarrow 2$ and P_{Mie} falls off approximately as a^{-1} and is negative, implying a phase advance. For the lossless refractive index, P_{Mie} oscillates between positive and negative values, but on the average is mostly negative. The asymptotic approach of Q_{Mie} to the value of 2 can be explained as a combination of two components. The portion directly intercepted by the particle is either scattered or absorbed, contributing a value of ~ 1 to Q_{Mie}. The remaining portion of Q_{Mie} comes from diffraction around the edge of the particle, and propagates at a slight angle to the exact forward direction. Depending on the conditions of an occultation experiment, this portion of the diffracted energy may or may not be collected as part of the forward scattered energy. For the case of the radio occultation experiment, almost all of the near-forward diffracted energy is separated from the forward propagating wave by a Doppler shift (Marouf *et al.*, 1982), and the observed extinction efficiency does approach a limiting value of 2 as ka becomes large. Further discussion of conditions under which asymptotic values of extinction efficiency other than 2 might be observed may be found in Cuzzi (1985) and Holberg *et al.* (1987).

Between the asymptotic behavior of the extinction curves at large and small particle size limits, the behavior of Q_{Mie} and P_{Mie} is more complex, particularly in the case with no absorption. Considering the Q_{Mie} curves of Figure 28a in the size range $a \gtrsim \lambda$, we see that there are oscillations about the value of 2, with a superimposed ripple structure of higher frequency. The lower frequency oscillations may be interpreted as an interference effect between the wave which passes directly through the particle and the incident wave. The period of these oscillations is approximately $\Delta a = \lambda/(\mathrm{Re}\{m\} - 1)$. The higher frequency oscillations are due to resonant poles in the Mie coefficients a_n and b_n. The ripple structure is not particularly relevant for our purposes, since absorption, non-sphericity, or a distribution of particle sizes will smooth the high frequency oscillations. The lower frequency interference fringes also become less significant if loss is added to the refractive index (as in Figure 28b), or if a sufficiently broad distribution of particle sizes is assumed.

The important characteristics of scattering by spheres which are relevant to future discussions of the results of the radio occultation experiment are the following:

1. For lossless, small particles, P_{Mie} is much larger than Q_{Mie}, and has a positive sign, (*i.e.*, phase is retarded relative to the original wave, as shown below).

2. For such small particles,

$$Q_{\mathrm{Mie}}(3.6 \text{ cm}) \simeq (11/3)^4 Q_{\mathrm{Mie}}(13 \text{ cm})$$

as the ratio of the radio occultation wavelengths is exactly 11/3. For small lossy particles, on the other hand,

$$Q_{\mathrm{Mie}}(3.6 \text{ cm}) \simeq (11/3) Q_{\mathrm{Mie}}(13 \text{ cm}).$$

For both lossy and lossless small particles

$$P_{\mathrm{Mie}}(3.6 \text{ cm}) \simeq (11/3) P_{\mathrm{Mie}}(13 \text{ cm}).$$

3. As the size of the particle becomes much larger than λ, Q_{Mie} approaches a limiting value of 2. The approach is slow, however, and differences between $Q_{\mathrm{Mie}}(3.6$ cm) and $Q_{\mathrm{Mie}}(13$ cm) persist for a as large as ~ 1 m, as may be seen in Figure 28b.

4. There are only two ways in which $Q_{\mathrm{Mie}}(3.6$ cm) can approximately equal $Q_{\mathrm{Mie}}(13$ cm). The first is if $a \gtrsim 1$ m; the second is if a happens to fall close to a crossing point of the Q_{Mie} curves. For a particle with loss (Figure 28b) or for a broad size distribution of particles (as will be shown below), there is only one such crossing point, at $a \simeq$ few centimeters (the exact value is dependent on the refractive index m). For a monodispersion of lossless particles, there are a number of such crossing points (Figure 28a).

Below, we extend the above results to describe the scattering behavior of a collection of spheres, an assumed model of planetary rings. The three vertical distributions we shall consider are the monolayer, thin-layer, and many-particle-thick models. In all three, it is assumed that each particle scatters independently of its neighbors. This assumption is critically examined later, in Chapter 5. A common rule of thumb is that the area or volume fraction occupied by the particles must be smaller than about 1% for coherent interactions between the particles to be negligible.

4.2.2 The monolayer model

The first model we consider is the monolayer model, in which the centers of all the particles are assumed to lie in a plane, as schematically depicted in Figure 29. The field observed at point $P(0,0,z)$ is a superposition of the incident field E_i and the fields scattered from each particle in the layer. Coherent addition of these fields will be limited to particles within the first few Fresnel zones. As before, over such an "active region," $\theta \sim \sqrt{x^2+y^2}/z \sim \sqrt{\lambda z}/z$ is very small if $z/\lambda \gg 1$ and one

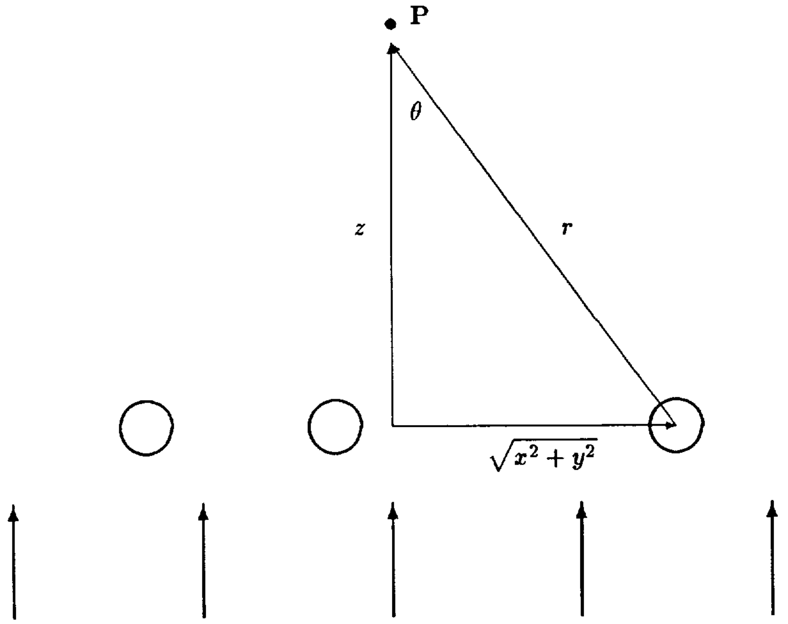

FIG. 29: Geometry of scattering by a monolayer for normal incidence. The observation point is at **P**, located a distance z from the monolayer. Particles in the layer are at a point (x, y) from the origin (in the layer) and at a distance r from the observation point. For $z \gg \lambda$, θ is small and $r \simeq z + (x^2 + y^2)/2z$. The observed field is the superposition of scattered fields from each particle in the layer.

may neglect polarization effects. For small θ, $r \simeq z + \frac{x^2+y^2}{2z}$, and the field at P due to a particle at (x, y) is therefore approximately given by

$$E_s = \frac{e^{ik(x^2+y^2)/2z}}{-ikz} S(\theta) E_i.$$

The total field at P is the incident field plus the sum of all contributions from the scattering region:

$$E = E_i \left(1 + \sum S(\theta) \frac{1}{-ikz} e^{ik(x^2+y^2)/2z} \right).$$

Assuming that there are a sufficient number of particles in the active region to justify replacing the summation with an integral, we obtain

$$E = E_i \left(1 + \int\int S(\theta) n \frac{1}{-ikz} e^{ik(x^2+y^2)/2r} \, dx \, dy \right),$$

where n is the number of particles per unit ring area, or area density for short. Evaluating the integrals using the stationary phase method, the result for the total field is

$$E = E_i \left(1 - \frac{2\pi}{k^2} n S(0) \right), \tag{16}$$

where $S(0) = S(\theta = 0)$. Introducing a particle size distribution $n(a)$ and making the substitution $4S(0) = (ka)^2[Q_{\text{Mie}} - 2iP_{\text{Mie}}]$, the intensity ratio $I/I_i \equiv |E|^2/|E_i|^2$ reduces to

$$\frac{I}{I_i} = \left|1 - \frac{1}{2}\int_0^\infty \pi a^2 \left(Q_{\text{Mie}} - 2iP_{\text{Mie}}\right) n(a)da\right|^2. \tag{17}$$

Note that, under the condition that the area packing fraction $n(a)\pi a^2$ is small, this implies

$$\frac{I}{I_i} \simeq 1 - \int_0^\infty \pi a^2 Q_{\text{Mie}} n(a)\, da,$$

so that the fraction of intensity removed is simply equal to the average of the extinction cross section per unit ring area. When the particles are large, $Q_{\text{Mie}} \to 2$, and the integral represents twice the fraction of a unit ring area physically blocked by ring particles.

If the incident radiation is now assumed to strike the layer at some angle B (with respect to the layer's interface), we can use an exactly similar approach to obtain

$$\frac{I}{I_i} = \left|1 - \frac{1}{2\mu_0}\int_0^\infty \pi a^2 \left(Q_{\text{Mie}} - 2iP_{\text{Mie}}\right) n(a)da\right|^2, \tag{18}$$

where $\mu_0 = \sin B$. This assumes that B is not so small that the particles begin to shadow one another.

From the definition of the normal optical depth τ,

$$\tau \equiv -\mu_0 \ln\left(\frac{I}{I_i}\right), \tag{19}$$

we may express τ in terms of the physical model parameters as

$$\tau = -2\mu_0 \ln\left|1 - \frac{1}{2\mu_0}\int_0^\infty \pi a^2 \left(Q_{\text{Mie}} - 2iP_{\text{Mie}}\right) n(a)\, da\right|. \tag{20}$$

Similarly, from Eq. 16, averaged over a distribution of particle sizes and generalized to oblique incidence, the phase shift ϕ_c relative to the incident wave is given by

$$\phi_c = \tan^{-1}\left(\frac{\text{Im}\{E/E_i\}}{\text{Re}\{E/E_i\}}\right) = \tan^{-1}\frac{\frac{1}{\mu_0}\int \pi a^2 P_{\text{Mie}} n(a)\, da}{1 - \frac{1}{2\mu_0}\int \pi a^2 Q_{\text{Mie}} n(a)\, da}. \tag{21}$$

4.2.3 The thin-layer model

Eq. 16 for a monolayer is also valid if the particles are spread in a layer of small thickness dl and volume density n_v, provided that the columnar density (area packing fraction) is small. A layer of particles of arbitrary thickness l and volume density n_v can be thought of as a cascade of N layers, each of columnar density $n_v dl = n_v l/N$. In the near absence of coherent multiple reflections between the layers (small volume fraction), Eq. 16 for the normal incidence case becomes

$$E/E_i = \left[1 - \frac{2\pi}{k^2}\frac{n}{N}S(0)\right]^N , \tag{22}$$

so that

$$\frac{I}{I_i} = \left|1 - \pi a^2 \frac{n}{2N}\left(Q_{\mathrm{Mie}} - i2P_{\mathrm{Mie}}\right)\right|^{2N} ,$$

where $n = n_v l$ is the columnar density of the full layer. Introducing a size distribution, generalizing to non-normal incidence, and again neglecting shadowing, we obtain

$$\frac{I}{I_i} = \left|1 - \frac{1}{2N\mu_0}\int_0^\infty \pi a^2\left(Q_{\mathrm{Mie}} - 2iP_{\mathrm{Mie}}\right) n(a)\, da\right|^{2N} . \tag{23}$$

This model is especially useful when the layer is only a few particles thick and was effectively used by Zebker *et al.* (1985) to constrain the particle size distribution of several features in Saturn's rings.

Note that, under the condition that the packing fraction of each layer is small, we obtain

$$\frac{I}{I_i} \simeq \left(1 - \frac{1}{N\mu_0}\int_0^\infty \pi a^2 Q_{\mathrm{Mie}} n(a)\, da\right)^N .$$

4.2.4 Many-particle-thick model

The many-particle-thick model is a cloud-like spatial distribution of particles within a layer of thickness very large compared to individual particle sizes. We may derive the extinction behavior of such a layer from results of the thin layer model described above by letting $N \to \infty$. Eq. 22 therefore reduces to

$$E/E_i = e^{-\frac{2\pi}{k^2}nS(0)} = e^{-\tau/2}e^{i\phi_c},$$

where

$$\tau = \frac{4\pi}{k^2}n\mathrm{Re}\{S(0)\} = \pi a^2 n Q_{\mathrm{Mie}}$$

and

$$\phi_c = \frac{-2\pi}{k^2}n\mathrm{Im}\{S(0)\} = \pi a^2 n P_{\mathrm{Mie}}.$$

In the presence of a particle size distribution and for oblique incidence, τ and ϕ_c become

$$\tau = \int_0^\infty \pi a^2 Q_{\mathrm{Mie}} n(a)\, da \tag{24}$$

and

$$\phi_c = \frac{1}{\mu_0} \int_0^\infty \pi a^2 P_{\mathrm{Mie}} n(a)\, da. \tag{25}$$

Note that τ is the normal optical depth, while ϕ_c characterizes phase shift along the oblique path. If $n(a)$ is very small, then Eqs. 24 and 25 are the same as Eqs. 20 and 21 for the monolayer. This is because, for a tenuous ring, each particle is equally illuminated by the incident radiation, regardless of vertical placement.

4.3 Vertical Profile

We now attempt to discriminate between the models introduced above based on the actual observations. Of primary importance in this regard is the observation that the integrated optical depth is nearly conserved as ring width changes (Table 7).

We begin by assuming that the columnar number density $n(a)$ varies as $1/W$, where W is the ring width. This assumption would be violated, for example, if the ring is significantly clumpy. Even for a "well-behaved" elliptical ring, the assumption is not strictly true since the velocity of a ring particle varies with azimuth as

$$v^2 = \frac{GM}{a_r(1-e^2)}(1 + 2e\cos\theta_p + e^2),$$

where GM is the gravitational constant times the mass of Uranus, a_r is the semimajor axis of the particle's orbit, e is the eccentricity, and θ_p is the angle from orbit periapsis. In the small eccentricity limit,

$$v \simeq \sqrt{\frac{GM}{a_r}}(1 + e\cos\theta_p).$$

We would expect the density of particles to vary inversely with particle velocity; the fractional difference in density between periapsis and apoapsis should be approximately $2e$. The most eccentric Uranian ring, Ring ϵ, has eccentricity $e \simeq 8\times10^{-3}$ (French *et al.*, 1988), thus the difference in density as a function of longitude should never exceed about 1.5%.

With these caveats in mind, the assumption that $n(a)$ is inversely proportional to ring width W requires that the quantity

$$\int_W dr \int_0^\infty \pi a^2 Q_{\mathrm{Mie}}(\lambda, a, m) n(a) da$$

Ring	$\int_w (1 - X_r)$		$\int_w \tau$	
	ingress	egress	ingress	egress
6	0.42 ± 0.03	0.40 ± 0.03	0.96 ± 0.07	0.90 ± 0.07
5	0.80 ± 0.05	0.80 ± 0.04	1.93 ± 0.08	2.07 ± 0.09
4	0.65 ± 0.04	0.60 ± 0.05	1.57 ± 0.08	1.36 ± 0.08
$*\alpha$	2.63 ± 0.16	2.37 ± 0.07	6.17 ± 0.15	6.60 ± 0.60
β	1.80 ± 0.10	1.90 ± 0.14	4.24 ± 0.12	4.08 ± 0.13
η	0.44 ± 0.03	0.41 ± 0.03	1.00 ± 0.07	0.90 ± 0.07
$*\gamma$	2.68 ± 0.07	1.38 ± 0.04	9.62 ± 0.28	$6.68^{+1.19}_{-0.55}$
$*\delta$	2.18 ± 0.10	1.46 ± 0.05	5.34 ± 0.13	4.21 ± 0.13
$*\epsilon$	18.99 ± 0.33	36.60 ± 1.07	$93.38^{+\infty}_{-2.14}$	97.04 ± 0.57

TABLE 8: Comparison of monolayer and many-particle-thick models for applicability to the Uranian rings. For a monolayer ring the quantity $\int_w (1 - X_r)$ is expected to be maintained at a constant value as ring width changes. For a many-particle-thick ring the quantity $\int_w \tau$ is expected to remain constant. The symbol "*" indicates those rings for which the many-particle-thick model is superior to the monolayer model. Meaningful distinction is not possible for the other rings, mainly because their widths do not change significantly between the observations.

be conserved at all observation longitudes. For a many-particle-thick ring model, this implies (see Eq. 24)

$$\int_W \tau = \text{constant},$$

while for a monolayer model it implies (see Section 4.2.2)

$$\int_W (1 - X_R) = \text{constant},$$

where $X_R \equiv \mathrm{Re}\{E/E_i\}$.

Table 8 gives the integrated quantities $\int_W (1 - X_R)$ and $\int_W \tau$ for each of the nine Uranian rings at both observation longitudes. For many of the rings, the width does not change enough between the two observation points to allow a meaningful distinction between the two models. However, for Rings α, γ, δ, and ϵ, the many-particle-thick model provides a better match to the observations. The most clear distinction is for Ring ϵ, where the integrated quantities $(1 - X_R)$ differ by almost a factor of two between the two observations, clearly *not* a constant value.

In order to investigate how thick "many-particles-thick" is, we note that variation of the columnar density $n = l n_v$ with longitude can either be due to variation in the volume density n_v in a ring of constant thickness, variation in ring thickness l while maintaining a constant n_v, or variation in both. Here, we consider the implications of the first two alternatives.

For the case $l =$ constant and $n_v \propto 1/W$, the ring thickness l is determined by the large mean opacity observed near periapsis. As discussed in Section 4.2.3, for small packing fraction, the number of layers N and the optical depth τ are related by the equation

$$e^{-\tau/\mu_0} \simeq \left(1 - \frac{1}{2\mu_0 N} \int_0^\infty \pi a^2 Q_{\mathrm{Mie}} n(a) da\right)^{2N},$$

or, grouping the N dependent terms on one side,

$$\int_0^\infty \pi a^2 Q_{\mathrm{Mie}} n(a) da = 2\mu_0 N \left(1 - e^{-\tau/\mu_0 N}\right).$$

In the limit $N \to \infty$, the right hand side $\to \tau$, as is expected for a many-particle-thick model. A lower bound on N may be obtained by expanding the exponential on the right-hand-side and determining the condition under which the contribution of the second-order term in $(\tau/\mu_0 N)$ is negligible. The result is

$$\frac{\tau}{4\mu_0 N} \ll 1.$$

For the Uranian ring occultation geometry, $\mu_0 \simeq 1$, so the condition is $\tau/4N \ll 1$, or, at the 10% level, $N \gtrsim 2.5\tau$. For Ring ϵ, the average τ at the narrower ingress observation is approximately 4; therefore we require $N \gtrsim 10$ layers in order to satisfy the above inequality. For Ring α, where $\tau \simeq 1.5$, this implies $N \gtrsim 4$. For Ring γ, the large optical depth observed implies $N \gtrsim 10$; the result for Ring δ is $N \gtrsim 4$.

Conversion of limits on N to actual ring thicknesses can be accomplished only if one knows the typical thickness of an individual layer and the typical distance between such layers. This requires an estimate of the particle sizes and separation distances. In order for this model to be at all self-consistent, we require separations between particles to be large enough to exclude coherent interaction effects; in Chapter 5 we show that this requires a typical separation between particles exceeding ~ 5 radii. For Ring ϵ, we find below that typical sizes inferred depend on the steepness of the size distribution. For a moderately steep power law size distribution, with power index $\gtrsim 3$, the observations imply an "effective" particle radius $\gtrsim$ 70 cm; for a less steep size distribution ($q \simeq 2.75$), the effective radius may be in the ten-centimeter size range. Given these results, the minimum thickness of Ring ϵ would exceed about 30 meters in the first case and would exceed several meters in the second.

Alternatively, if $l \propto 1/W$ and $n_v =$ constant, the ring would be thinnest at apoapse, and gradually thicken to a maximum value at periapse. For Ring ϵ, the requirement $\tau/4N \ll 1$ implies

$$N(241°) \gtrsim 3 \quad \text{and} \quad N(30°) \gtrsim 10,$$

where a mean τ of $\sim$ 1.3 and 4 are assumed at the true anomalies indicated, respectively. The physical thickness would vary in a corresponding fashion. This alternative model of Ring ϵ appears to be new. Its dynamical feasibility remains an open question, however, given that particle inclinations have to significantly dampen over as short a time interval as half an orbital period.

Most models of dynamics favor thin rings over thick ones (*v.*, *e.g.*, Goldreich and Porco, 1987). Particles in thick rings have larger random (*i.e.*, non-Keplerian) velocities than do particles in thin ones. Consequently, particles in thick rings suffer more dissipative collisions with one another, thus thick rings have shorter spreading times. Given the maximum torques available from the shepherd satellites Cordelia and Ophelia, Goldreich and Porco (1987) discuss the thickness of Ring ϵ, and place a limit of a few meters on its thickness, consistent only with the estimate obtained above assuming a size distribution with $q \simeq 2.75$. However, this does not necessarily rule out the steeper size distribution model, as dynamical theories, particularly those regarding ring viscosity, remain an active area of research at this time.

4.4 Implications for Particle Sizes

The theoretical models discussed above can be used to constrain particle sizes in the Uranian rings. As stated before, we assume spherical ring particles, and use Mie theory to compute the scattering behavior of the individual particles.

We have shown in Section 4.2.1 that, for particles of size smaller than or comparable to the wavelength, extinction of the incident wave is a strong function of the size of the particle. For a particle in this size range, the extinction decreases as the incident wavelength increases. For this reason, a difference in extinction between signals of two wavelengths is a strong indicator of particles roughly of a size between those two wavelengths. This technique has been used, in part, to infer particle sizes in Saturn's rings (Marouf *et al.*, 1983; Zebker *et al.*, 1985). Here we apply a similar analysis to the Uranian ring measurements.

For brevity, we concentrate below on the many-particle-thick model. For most rings, a nearly conserved integrated opacity at the two observation longitudes supports the many-particle-thick ring model, as discussed in the previous section. Nonetheless, we have also carried out similar calculations assuming the thin-layer and monolayer ring models, and the results remained qualitatively similar to the results reported below, as discussed further at the end of this section. It is worth emphasizing again that all three models assume that the particles in the ring are well-separated from one another, so that their individual scattering behaviors are not affected by one another.

For computational purposes, we use as a model for the size distribution $n(a)$ a Saturn-ring-like power law of the form

$$\begin{aligned} n(a) &= n_0 \left(\frac{a}{a_0}\right)^{-q} && a_{\text{min}} < a < a_{\text{max}} \\ n(a) &= 0 && \text{otherwise.} \end{aligned} \tag{26}$$

Here, $n(a)da$ is the columnar number density of particles in the size range a to $a + da$, a_0 is an arbitrary reference size, and q is the power law index. Larger values of q ($q > 4$) model a near-monodispersion of particles of size $\simeq a_{\text{min}}$. The coefficient $n_0 \equiv n(a_0)$ sets the absolute number density of particles. Power law indices inferred in Saturn's rings are in the range of approximately 2.8–3.4 (Marouf *et al.*, 1983; Zebker *et al.*, 1985); theoretical models and simulations of ring erosion processes predict values of approximately 3 (*v.*, *e.g.*, Hartmann, 1969). The upper and lower size cutoffs of the size distribution are denoted by a_{max} and a_{min}, respectively. Physically, a_{min} is typically set by Poynting-Robertson or exospheric drag, while a_{max} could be set, for example, by tidal disruption of loosely-accreted particles (Weidenshilling *et al.*, 1984; Longaretti, 1989). In the following sections we attempt to set bounds on these parameters of the size distribution using the many-particle-thick ring model. We begin with Ring ϵ, which at egress has the best-determined measurements of optical depth and phase delay due to its large width and relatively low optical depth.

4.4.1 Ring ϵ

As Table 7 indicates, at egress (true anomaly 241°) and at 500 m resolution, the integrated optical depth of Ring ϵ at 3.6 cm wavelength is 97.04 ± 0.57, while at 13 cm it is $96.57^{+3.24}_{-2.48}$. The effect of the lower signal-to-noise ratio for the longer wavelength is clearly evident in the larger uncertainty interval of the 13 cm measurement. The corresponding normalized differential phase delay per unit optical depth measured is 8 ± 2 millicycles. Below, we use these measurements to set bounds on a_{min}, a_{max}, and q, assuming a variety of refractive indices.

Figure 28 showed the extinction curves Q_{Mie} and P_{Mie} for a single particle as a function of particle size. We now include the effect of a size distribution, and display the computations in an alternative form, shown in Figure 30, where differential optical depth $\Delta\tau$ is plotted *vs* differential phase delay $\Delta\phi_c$, parameterized by the minimum size cutoff a_{min}. The differential parameters are computed in terms of P_{Mie} and Q_{Mie} using the definitions

$$\begin{aligned}\Delta\tau &\equiv \tau(3.6\text{ cm}) - \tau(13\text{ cm}) \\ &= \int_{a_{\min}}^{a_{\max}} \pi a^2 n(a)[Q_{\text{Mie}}(3.6\text{ cm}) - Q_{\text{Mie}}(13\text{ cm})]da\end{aligned}$$

and

$$\begin{aligned}\Delta\phi_c &\equiv \phi_c(13\text{ cm}) - \frac{3}{11}\phi_c(3.6\text{ cm}) \\ &= \int_{a_{\min}}^{a_{\max}} \pi a^2 n(a)\left[P_{\text{Mie}}(13\text{ cm}) - \frac{3}{11}P_{\text{Mie}}(3.6\text{ cm})\right]da.\end{aligned}$$

The 3/11 factor is the exact ratio of the two radio wavelengths. This particular form for $\Delta\phi_c$ ensures removal of random phase fluctuations caused by short term instability of the reference oscillator. In computing all curves in Figure 30, a_{max} has been fixed at 5 m.

For a relatively narrow size distribution (q large), the minimum size a_{min} is the controlling factor for the predicted τ and ϕ_c, whose behavior follows the Q_{Mie} and P_{Mie} curves of Figure 28. As Figure 28 demonstrates, the differential optical depth starts at a large value for very small particles, becomes negative in the resonance region (around the experiment wavelengths), and asymptotically approaches zero as the particles become quite large. Differential phase delay begins at a small positive value, reaches a maximum in the resonance region, and asymptotically approaches zero from the negative side. This behavior closely resembles the behavior of the curve $q = 4$ in Figure 30.

For broader size distributions, ($q < 3.5$), the curves in Figure 30 show less dependence upon the value of a_{min}. This is due to the relatively larger number of big particles, which tends to dilute the effect of the minimum size. In these cases, the chosen value of a_{max} will have a stronger effect on the shape of any given curve. In general, this dilution effect implies that, the broader the size distribution, the smaller will be the maxima of differential optical depth and differential phase. The contribution of the refractive index to the behavior of the curves may be seen in the lower panels of Figure 30. Introducing loss into the refractive index tends to decrease the differential optical depth and phase delay excursions, while a decrease in the real part of the refractive index slows the progression along the spiral as a function of a_{min}. This is because $(\text{Re}\{m\} - 1)ka$ is approximately the quantity which controls the extinction behavior.

Also shown in Figure 30 is the measurement point for Ring ϵ at egress, along with the 1- and 2-σ confidence regions (boxes). (Measurements for other rings are also shown, but are discussed in a subsequent section.) As evident, the region of the parameter space with $q \simeq 2.75$ has a

See following page.

FIG. 30: Differential extinction parameters for assumed power-law size distributions, parameterized in q. The large panel assumes a lossless refractive index of $m = 1.78 + 0.00i$; the bottom panels are for other, somewhat lossy refractive indices. Each curve is parameterized by the minimum size of the size distribution a_{min}; a_{max} is fixed as indicated. Five curves in the top panel represent five power law indices ranging from 2.5 to 4; in addition, the curve labeled "narrow" is a narrow dispersion of particle sizes uniformly distributed from $0.7a$ to $1.3a$ (30% dispersion). This curve begins at size $a = 2.3$ cm and ends at size $a = 3.8$ cm. The bottom panels show curves for the same values of q with the exception of $q = 2.75$, which is not shown, and the same narrow distribution. $\Delta\tau \equiv \tau(3.6\text{ cm}) - \tau(13\text{ cm})$; $\Delta\phi \equiv \phi_c(13\text{ cm}) - (11/3)\phi_c(3.6\text{ cm})$. Also shown is the measurement point for Ring ϵ (egress), along with its 1-σ (dashed line) and 2-σ (dotted line) confidence intervals. Similar measurement points and uncertainty regions for an average of the measurements of Rings α and β and for an average of the measurements of Rings 6, 5, and 4 are shown.

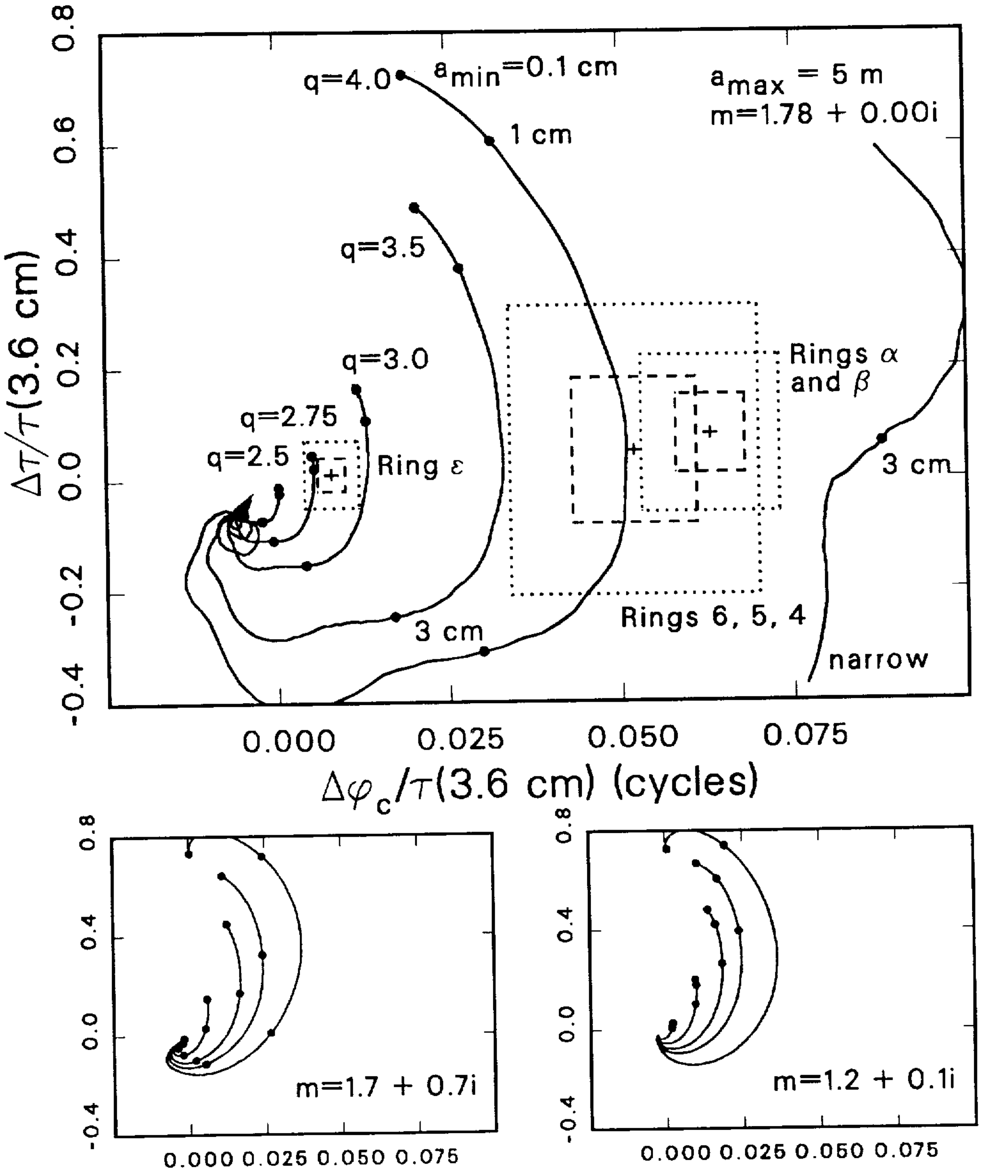
q=4.0
a_{min}=0.1 cm
1 cm
a_{max} = 5 m
m=1.78 + 0.00i
q=3.5
q=3.0
q=2.75
q=2.5
Ring ε
Rings α and β
3 cm
3 cm
Rings 6, 5, 4
narrow
$\Delta\tau/\tau$(3.6 cm)
$\Delta\varphi_c/\tau$(3.6 cm) (cycles)
0.8
0.6
0.4
0.2
0.0
-0.2
-0.4
0.000
0.025
0.050
0.075
m=1.7 + 0.7i
m=1.2 + 0.1i
0.8
0.4
0.0
-0.4
0.000 0.025 0.050 0.075
0.8
0.4
0.0
-0.4
0.000 0.025 0.050 0.075

See following page.

FIG. 31: Regions of $(a_{\rm min}, a_{\rm max})$ parameter space consistent with Ring ϵ measurements, for $q = 2.5$ and $q = 2.75$. The horizontal axis in each panel is $a_{\rm min}$, the vertical axis is $a_{\rm max}$; therefore a diagonal line $a_{\rm min} = a_{\rm max}$ represents a ring composed of a single size of particle. The two columns represent different power law indices q; the three rows represent different refractive indices. Within each panel, the shaded region is that portion of the $(a_{\rm min}, a_{\rm max})$ space which is consistent with the (2-σ) measurement of differential optical depth for Ring ϵ. The smaller region, outlined in a heavy line, is the region consistent with *both* the differential optical depth *and* the (3-σ) differential phase delay measurement. Contours of constant σ/ρ are also given, where σ is the surface mass density of the ring and ρ is the bulk density of a ring particle.

portion contained within the uncertainty region of this measurement. The extent of such a region is dependent on $a_{\rm min}$, $a_{\rm max}$, and the assumed refractive index m. We investigate further dependence of the extinction behavior on these members of the parameter space by adopting the alternate format shown in Figures 31 and 32. Here, each panel corresponds to an assumed q and m, and regions consistent with the differential observations are identified in the $(a_{\rm min}, a_{\rm max})$ domain, represented by the two axes of each panel. Figure 31 considers power law indices q of 2.5 and 2.75; Figure 32 considers $q = 3.0$ and 3.5.

Figures 31 and 32 contain a good deal of information. We will interpret these figures in stages, starting by relating the presentation here to figures we have previously discussed. The advantage of the format of Figures 31 and 32 is that it allows one to identify immediately the implications of the measurements of Ring ϵ as parameters $a_{\rm min}$, $a_{\rm max}$, and q are varied, and also to recognize the effect of a lossless refractive index (top row), a very lossy refractive index (center row), and a somewhat lossy, smaller refractive index (bottom row). Conceptually, we think of these three model refractive indices as lossless ice, very lossy material such as carbon, and somewhat lossy, fluffy ice, respectively.

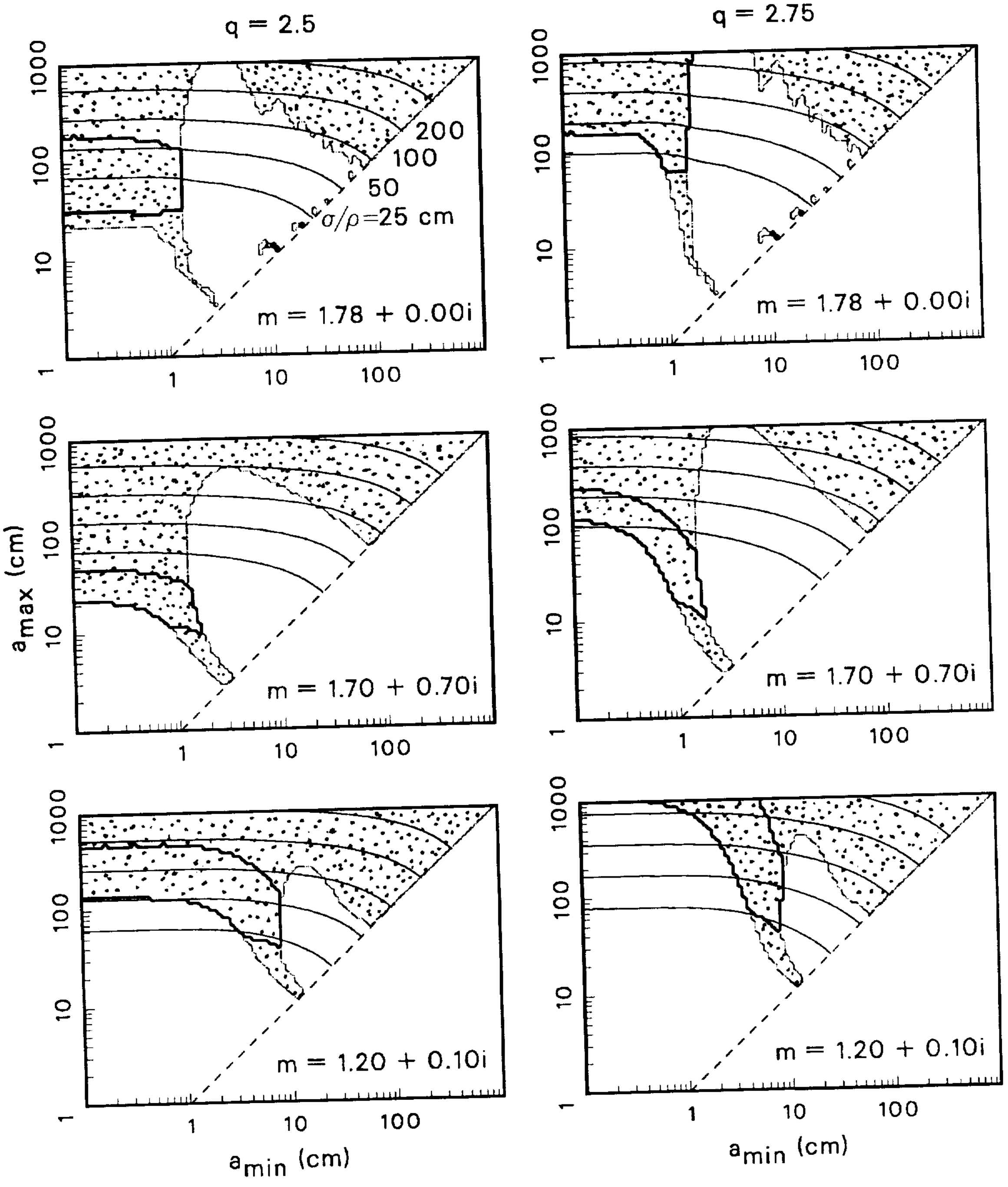
q = 2.5
q = 2.75
200
100
50
σ/ρ=25 cm
m = 1.78 + 0.00i
m = 1.78 + 0.00i
m = 1.70 + 0.70i
m = 1.70 + 0.70i
m = 1.20 + 0.10i
m = 1.20 + 0.10i
a_max (cm)
a_min (cm)
a_min (cm)
1
10
100
1000

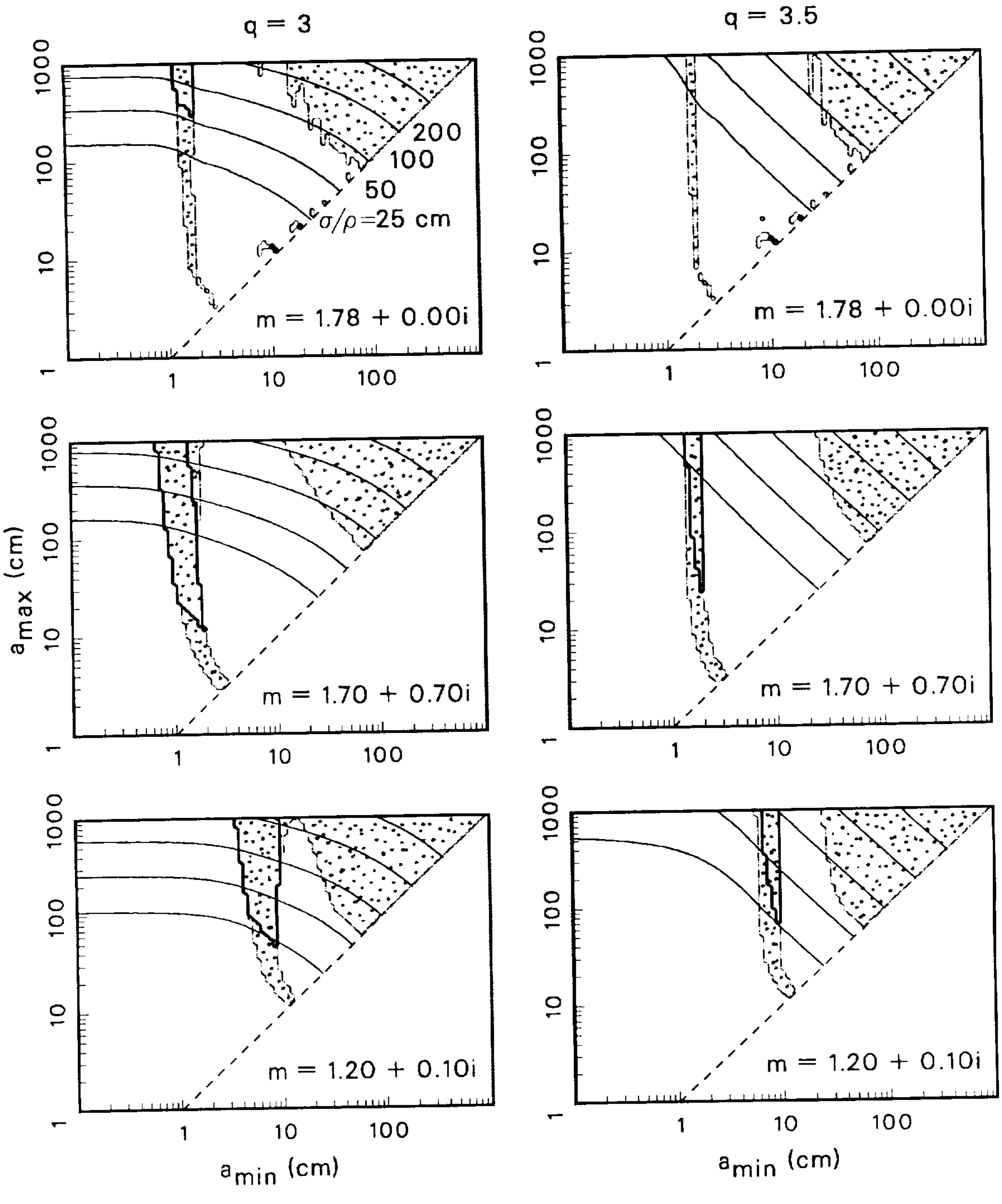

FIG. 32: Regions of $(a_{\rm min}, a_{\rm max})$ parameter space consistent with Ring ϵ measurements, for $q = 3.0$ and $q = 3.5$. See caption of Figure 31 for details.

Few measurements of material properties at outer solar system temperatures are available, and little is known of the bulk material making up the rings. The very low albedo of ring particles and the absence of wavelength dependence in their spectral relativity are consistent with carbon material (Porco *et al.*, 1987), but this might only be a thin coating on the surface of an otherwise unidentified bulk composition.

The irregular curves in Figures 31 and 32 identify the boundaries of the regions in the $(a_{\rm min}, a_{\rm max})$ domain which are consistent with the (2-σ) confidence region of the $\Delta\tau$ measurements for Ring ϵ egress. It may be recalled that these measurements indicate that $\Delta\tau/\tau(3.6\text{ cm}) = 1 \pm 6\%$. The smaller regions, outlined in a heavier pen, represent those regions consistent with *both* the $\Delta\tau$ and $\Delta\phi_c$ measurements; for the present time we will postpone discussion of these smaller regions. The diagonal lines in Figures 31 and 32 correspond to $a_{\rm min} = a_{\rm max}$, that is, a monodispersion of particles of size $a = a_{\rm min}$, regardless of the nominal value of q. Therefore, for each row, the allowable regions have the same shape near the diagonal line. The general behavior of these regions near the diagonal line follows closely the behavior of the extinction curves for a single particle, previously discussed in Section 4.2.1. Recalling Figure 28, for a lossless refractive index $m = 1.78 + 0.00i$, $\tau(3.6\text{ cm}) \simeq \tau(13\text{ cm})$ (*i.e.*, $Q_{\rm Mie}(3.6\text{ cm}) \simeq Q_{\rm Mie}(13\text{ cm})$) for several different ranges of a: near $a \simeq 3$ cm, at a number of other points at larger values of a where the 3.6 and 13 cm curves cross, and finally $a \gtrsim 70$ cm. This behavior may also be seen in the top rows of Figures 31 and 32. The small "islands" running close to the diagonal line represent the multiple crossing points and the region $a_{\rm min} \gtrsim 70$ cm corresponds to the radius range in Figure 28 where the difference between the $Q_{\rm Mie}(3.6\text{ cm})$ and $Q_{\rm Mie}(13\text{ cm})$ curves is consistent with the small $\Delta\tau$ observed. For a lossy refractive index (bottom two rows), these "islands" disappear, leaving only the first crossing point and the large-particle regions.

As we move upwards from the diagonal line ($a_{\rm max} > a_{\rm min}$), we allow for a broader size distribution of particles, and the shapes of the regions consistent with the measurement change. We find that, for the lossless refractive index, the small islands disappear as we move away from the diagonal line, indicating that these extra crossing points no longer exist when a distribution of particle sizes is considered. We also find that the large-particle region moves leftward, since if $a_{\rm max}$ is increased beyond $\sim$ 70 cm, then $a_{\rm min}$ may be decreased to a smaller value while maintaining $\tau(3.6\text{ cm}) \simeq \tau(13\text{ cm})$.

In Figure 32, note the allowable narrow vertical region around $a_{\rm min} = 3$ cm for the top two rows and near $a_{\rm min} = 10$ cm for the bottom row, for the cases $q = 3.0$ and $q = 3.5$. This region corresponds to the first crossing point of the 3.6 and 13 cm extinction curves (see Figure 28). As the relative number of large particles is increased by letting $q = 2.5$ or 2.75, as in Figure 31, we find that these vertical narrow regions broaden, and significantly more of the parameter space becomes consistent with the measurements.

At this point we may introduce discussion of the smaller regions in Figures 31 and 32, outlined with a heavy pen. These regions are where not only $\Delta\tau/\tau(3.6 \text{ cm})$ is consistent with the measurements, but also $\Delta\phi_c/\tau(3.6 \text{ cm})$. These regions are more restrictive that the regions previously discussed; in fact for the power law indices $q = 3.0$ and 3.5 in Figure 32 they are so restrictive that it seems unlikely that these are the true constraints on the size distribution. For instance, for $q = 3.0$ or $q = 3.5$, note that only a portion of the vertical column is allowed, and *none* of the large-particle region is consistent with both the $\Delta\tau$ and the $\Delta\phi_c$ measurements. The reason for this is that we have measured a small, but finitely positive, differential phase delay for Ring ϵ (see Table 7). Large particles are expected to have a very small phase *advance* (see Figure 30).

In general, for the cases $q = 2.5$ and $q = 2.75$ considered in Figure 31, the regions consistent with both the $\Delta\tau$ and $\Delta\phi_c$ measurements are almost as restrictive as those for the cases $q = 3$ and $q = 3.5$. However, for these lower values of q, $a_{\min}$ is relatively loosely constrained and $a_{\max}$ is the parameter which is constrained. For example, for the refractive index $m = 1.70 + 0.70i$ and $q = 2.75$ case considered in Figure 31, $a_{\max}$ must lie between 1.15 m and 2.40 m in order for the predicted $\Delta\tau$ and $\Delta\phi_c$ to match the observations. Similar results hold for all but the lossless refractive index case for $q = 2.75$. For this combination of parameters, both a wide range of $a_{\max} \gtrsim 165$ m and a wide range of $a_{\min} \lesssim 2$ cm are allowed by the observational measurements. Thus we find that with the exception of the $m = 1.78 + 0.00i$, $q = 2.75$ case, all of the regions consistent with *both* the $\Delta\tau$ and $\Delta\phi_c/\tau(3.6 \text{ cm})$ measurements are fairly restrictive, and depend intrinsically on the wavelengths used in this experiment. For example, the narrow vertical columns in Figure 31 and 32 lie at the crossing points of the extinction curves for $\lambda = 3.6$ and 13 cm.

We investigate further the case $q \simeq 2.75$ and lossless refractive index with the aid of Figure 33, which shows the predicted values for $\Delta\tau/\tau(3.6 \text{ cm})$ and $\Delta\phi_c/\tau(3.6 \text{ cm})$ as a function of q. For these curves, $a_{\min}$ has been fixed in the Rayleigh regime ($a_{\min} = 0.1$ cm), and we explore the sensitivity to $a_{\max}$ and q, requiring both the $\Delta\tau/\tau(3.6 \text{ cm})$ and $\Delta\phi_c/\tau(3.6 \text{ cm})$ curves to lie within the confidence interval of each measurement, marked with horizontal lines. Thus, for $a_{\max} = 2$ m, for example, any $q \lesssim 2.8$ is consistent with the $\Delta\tau$ observation, while $2.5 \lesssim q \lesssim 3$ is required to satisfy the $\Delta\phi_c$ observation; agreement with both observations requires $2.5 \lesssim q \lesssim 2.8$. Similar limits on q as a function of $a_{\max}$ are shown in Figure 34. Clearly, for $q \simeq 2.75$, there is a broad range of $a_{\max}$ which will result in a match to the observations. Similar conclusions hold if the particles are slightly lossy (dashed curves in Figure 34), except that q becomes more tightly confined to a smaller value $q \simeq 2.65$.

We now consider the issue of the mass of Ring ϵ. Figures 31 and 32 display contours of constant σ/ρ, where σ is the surface mass density (g-cm^{-2}) and ρ is the particle mass density (g-cm^{-3}). This quantity is determined at each point in the region by using the size distribution at that point combined with the measured optical depth of the ring, which sets the coefficient n_0 of Eq. 26.

If we confine our attention to regions consistent with both the $\Delta\tau$ and the $\Delta\phi_c/\tau(3.6 \text{ cm})$ measurements, and in addition, do not consider regions for which the range of allowed distributions is overly restrictive, we find that only the case $m = 1.78+0.00i$, $q = 2.75$ provides a plausible match to the observations. For this case, σ/ρ may be as small as ~ 50 cm, and assuming an ice-like particle material with $\rho \sim 1$ g-cm^{-3}, this implies $\sigma \gtrsim 50$ g-cm^{-2}.

As discussed further below, we have reasons to believe that the phase delay measured for the inner Uranian rings is anomalous, and may be caused by something other than particle sizes. It may also be the case that the phase behavior of Ring ϵ is not caused by particle sizes. In this case we may consider the regions in Figures 31 and 32 which do not necessarily match the $\Delta\phi$ behavior, but for which the $\Delta\tau$ behavior does match the observations. Allowed regions in this case include particles of effective radius $\gtrsim 70$ cm and surface mass density $\gtrsim 80$ g-cm^{-2}, irrespective of q (the upper-right shaded regions). For $q = 2.5$ and 2.75, they also include broad distributions for which the limits on $a_{\min}$ and $a_{\max}$ are refractive index dependent (see Figure 31). Smaller limits on σ are imposed in this case; for example, for $q = 2.5$ and $m = 1.78 + 0.00i$, $\sigma \gtrsim 10$ g-cm^{-2} provided $a_{\min} \lesssim 2$ cm and $a_{\max} \gtrsim 20$ cm.

While the above results are based on the assumption of the many-particle-thick model, it can be shown that similar conclusions are reached for the monolayer or thin-layer models. This may be seen for the case of the monolayer model, for example, by noting that the theoretical curves in Figure 30 remain unchanged provided that the axes are properly interpreted in terms of observables relevant to that model. To determine these observables, we recall that for a many-particle-thick model, $\Delta\tau/\tau$ and $\Delta\phi_c/\tau$ plotted in Figure 30 are computed in terms of the physical model parameters using the relation

$$\frac{\Delta\tau + i\Delta\phi_c}{\tau(3.6 \text{ cm})} = \frac{\int_0^\infty \pi a^2 n(a) \left[\Delta Q_{\text{Mie}} + i\mu_0^{-1}\Delta P_{\text{Mie}}\right] da}{\int_0^\infty \pi a^2 n(a) Q_{\text{Mie}} da}, \tag{27}$$

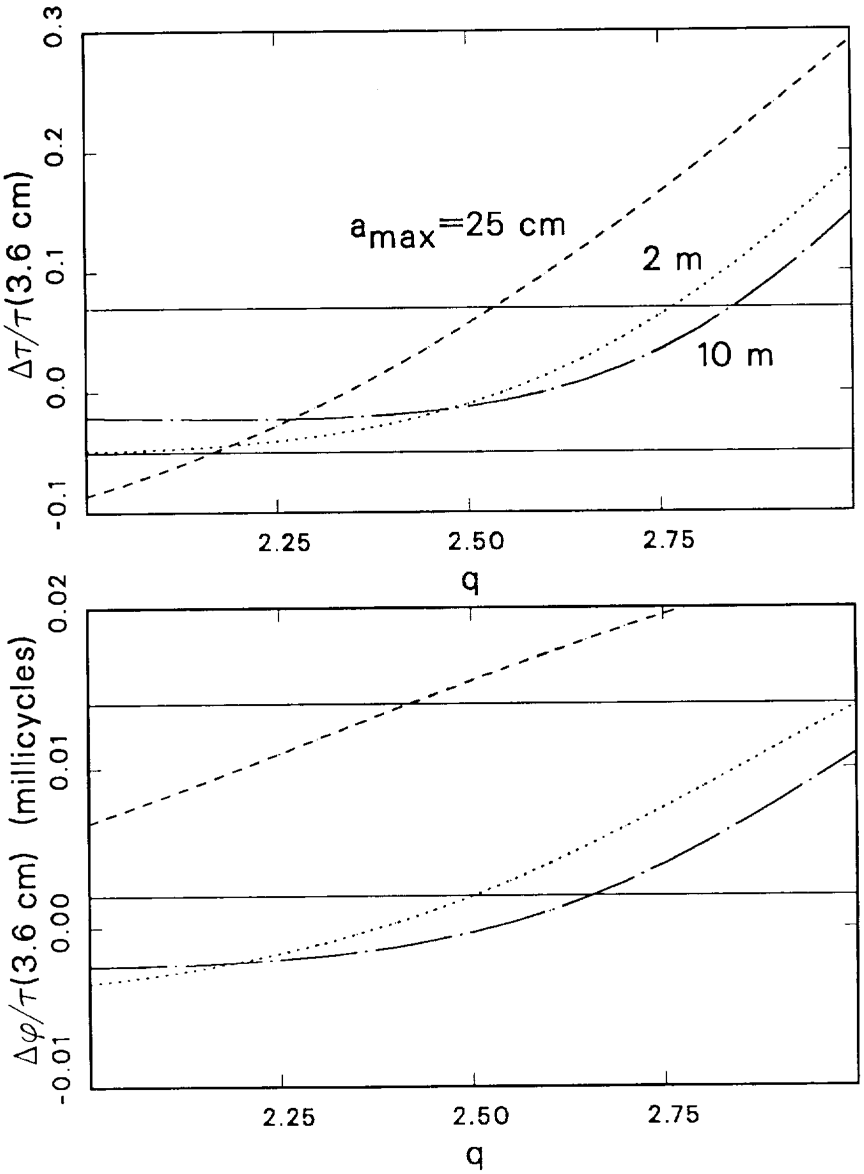

FIG. 33: $\Delta\tau/\tau$(3.6 cm) and $\Delta\phi_c/\tau$(3.6 cm) *vs* power law index q, assuming refractive index $m = 1.78 + 0.00i$. Three values of $a_{\rm max}$ are shown; $a_{\rm min}$ has been fixed in the Rayleigh regime ($a_{\rm min} = 0.1$ cm). Top panel shows $\Delta\tau/\tau$(3.6 cm), along with horizontal lines at -0.05 and 0.07, which mark the 2-σ confidence interval for the Ring ϵ egress measurement. Lower panel shows $\Delta\phi_c/\tau$(3.6 cm), along with the 3-σ confidence interval for the measurements.

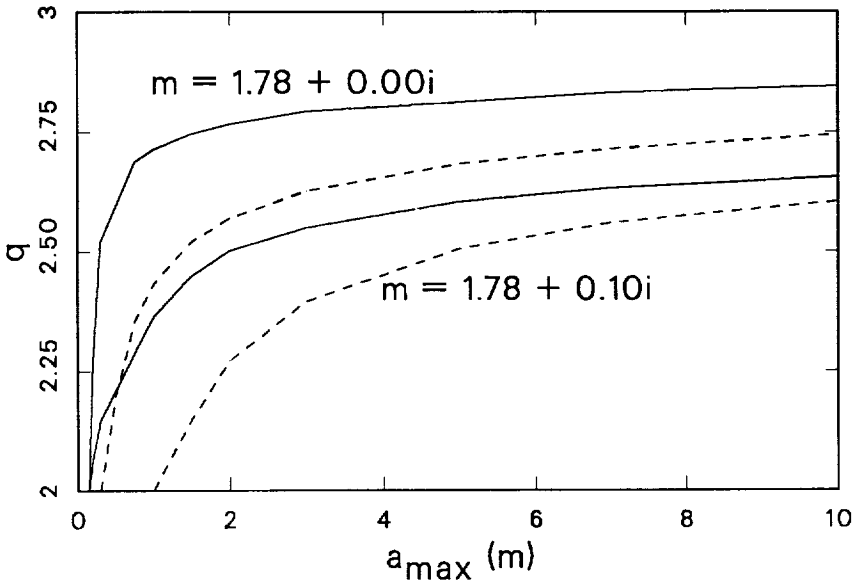

FIG. 34: Range of powerlaw index q consistent with Ring ϵ measurements, for $a_{\rm min}$ in the Rayleigh regime. For a given $a_{\rm max}$, the range of q consistent with the measurements lies between the two curves of a given line type. Curves for $m = 1.78{+}0.00i$ are drawn with solid lines; curves for $m = 1.78{+}0.10i$ are drawn with dashed lines. Generally, the top curve of each pair is determined by the $\Delta\tau/\tau$(3.6 cm) measurement, and the bottom curve of each pair is determined by the $\Delta\phi_c/\tau$(3.6 cm) measurement. This is true for the case $m = 1.78 + 0.10i$, regardless of $a_{\rm max}$. For the $m = 1.78 + 0.00i$ case, it is true for $a_{\rm max} > 50$ cm, but for $a_{\rm max} \leq 50$ cm, this dependency is switched.

where $\Delta Q_{\rm Mie} = Q_{\rm Mie}(3.6\ {\rm cm}) - Q_{\rm Mie}(13\ {\rm cm})$ and $\Delta P_{\rm Mie} = P_{\rm Mie}(13\ {\rm cm}) - \frac{3}{11}P_{\rm Mie}(3.6\ {\rm cm})$. A similar relation for the monolayer model can be obtained starting from our previous result (see Eq. 17):

$$\frac{E}{E_i} \equiv X_R + iX_I = 1 - \frac{1}{2\mu_0}\int_0^\infty \pi a^2 n(a)\left(Q_{\rm Mie} - i2P_{\rm Mie}\right) da$$

to obtain

$$\frac{2\mu_0\Delta X_R + i\Delta X_I}{2\mu_0(1 - X_R(3.6\ {\rm cm}))} = \frac{\int_0^\infty \pi a^2 n(a)\left[\Delta Q_{\rm Mie} + i\mu_0^{-1}\Delta P_{\rm Mie}\right] da}{\int_0^\infty \pi a^2 n(a) Q_{\rm Mie} da}, \tag{28}$$

where $\Delta X_R = X_R(13\ {\rm cm}) - X_R(3.6\ {\rm cm})$ and $\Delta X_I = X_I(13\ {\rm cm}) - \frac{3}{11}X_I(3.6\ {\rm cm})$. Equations 27 and 28 immediately imply that, for the same model parameters, the theoretical curves in Figure 30 also apply for the monolayer model, provided that the horizontal axis now represents $2\mu_0\Delta X_R/[1 - X_R(3.6\ {\rm cm})]$ and the vertical axis represents $\Delta X_I/[1 - X_R(3.6\ {\rm cm})]$. The nominal measured values fall at approximately the same locations relative to the theoretical curves, and the overall conclusions based on the many-particle-thick model remain qualitatively invariant.

There is evidence that Ring ϵ is relatively depleted in sub-centimeter sized particles. Reported values of integrated optical depth at much shorter wavelengths (French *et al.*, 1988; Colwell *et al.*, 1989) are comparable to the radio values presented here. Ring ϵ is the best measured ring in all data sets, and the integrated optical depth measured by the Voyager UVS and PPS experiments is in fact somewhat *smaller* than the value measured at centimeter wavelengths (Holberg *et al.*, 1987)—a true puzzle if this claim is correct. On the other hand, ground-based measurements of stellar occultations, while somewhat uncertain due to diffraction limitations, indicate an integrated optical depth for Ring ϵ at a wavelength of 2.2 μm that is approximately 80–100 km (French *et al.*, 1988). Thus, there is no evidence for significantly greater extinction at the much shorter wavelengths than at microwave wavelengths, indicating a relative depletion of sub-centimeter size particles. However, this does not rule out $a_{\min}$ in the sub-centimeter size range if $q < 3$, as, in such a case, the optical depth is controlled primarily by the large particles.

4.4.2 Other outer rings (η, γ, and δ)

Rings η, γ, and δ appear to be qualitatively similar to Ring ϵ, as may be seen in Figure 26, which shows the average differential optical depth and average differential phase delay for all nine rings. For each of the outer rings, there is little evidence for differential optical depth, and also little phase delay at either wavelength. However, the uncertainties for these narrower and often much more optically thick rings are much larger than for Ring ϵ, so it is not meaningful to set bounds on the size distribution in the way we did for Ring ϵ. There is no reason to believe, however, that the particle size distributions in these other outer rings are significantly different than in Ring ϵ. The lack of differential optical depth at the two radio wavelengths, and the near equality between the radio and reported values for integrated optical depth observed at much shorter wavelengths (French *et al.*, 1988; Colwell *et al.*, 1989), leads us to the conclusion that these rings are also relatively depleted in centimeter and smaller size particles.

4.4.3 Inner rings (6, 5, 4, α, and β)

We now consider the five inner rings, Rings 6, 5, 4, α, and β. Figure 26 shows that, unlike Rings η, γ, and δ, the qualitative behavior of these rings differs substantially from that of Ring ϵ. For each of these inner rings, there is significant phase delay at 13 cm relative to that at 3.6 cm. When

Rings	$\frac{<\Delta\tau>}{<\tau(3.6\text{ cm})>}$ %	$\frac{<\Delta\phi_c>^{b}}{<\tau(3.6\text{ cm})>}$ (millicycles)
6, 5, and 4	5 ± 13	52 ± 9
α and β	8 ± 7	63 ± 5
ϵ	1 ± 3	8 ± 2

TABLE 9: Average differential optical depth and differential phase delay for the five inner rings as compared to Ring ϵ (egress) (See Table 7).

normalized by the optical depth at 3.6 cm, these phase delays range from approximately 40 to 75 millicycles per unit optical depth (Table 7). However, like the four outer rings, none of these inner rings (with the possible exception of Ring β) shows significant differential optical depth, although within the relatively large measurement uncertainties (due to the narrow widths of these rings), differences of between 15 and 40% could go undetected.

The best-measured of the five inner rings are Rings α and β, due to their relatively greater widths. Because the phase and optical depth behavior of these rings appears to be consistent both among themselves and also at the two observation longitudes (see Figure 26), we choose to average the measurements together in order to decrease the measurement uncertainty. For the same reason, we average the measurements for the three innermost rings, Rings 6, 5, and 4. Results are shown in Table 9, and also plotted together with the corresponding uncertainty regions in Figure 30.

In constrast to the measurement point for Ring ϵ, Figure 30 shows that the measured differential phase for Rings 6, 5, and 4 matches only a very small portion of the $q = 4$ curve[3]. This is equivalent to requiring that the particles be of essentially a single size, have a nearly lossless refractive index, and be precisely at the maximum phase point of the 13 cm extinction curve (Figure 28)[4]. The measurement point for Rings α and β shows even larger phase delay than that for Rings 6, 5, and 4; Figure 30 shows that while such delays *are* possible to obtain with a very narrow size distribution, the allowable range of sizes is quite small; slightly smaller or larger particles will show significant differential optical depth, which is not observed. Furthermore, this narrow size range is refractive index dependent. As these seem to be highly artificial conditions, it is plausible that the phase

---

[3] The phase behavior of these inner rings is precisely opposite to what one would expect to observe from a simple slab of dielectric material. In this case, one would expect the 3.6 cm wavelength to be delayed by 11/3 as much as the 13 cm wavelength. Our definition of $\Delta\phi_c$ would result in $\Delta\phi_c \simeq 0$ for such a slab; however, its presence would be detectable in the individual measurements of ϕ_c.

[4] The maximum $\Delta\phi_c/\tau(3.6\text{ cm})$ is for a strict monodispersion of lossless particles of size about 2.8 cm (for refractive index $m = 1.78 + 0.00i$), and is ~ 0.15 cycle. Addition of loss to the refractive index ($m = 1.78 + 0.10i$) reduces this maximum to ~ 0.09 cycles; a slight dispersion of sizes between plus and minus 50% of a central size has a maximum $\Delta\phi_c/\tau(3.6\text{ cm}) \sim 0.08$ cycles, at a central size of 2.4 cm.

behavior of the inner rings (and perhaps Ring ϵ as well, albeit to a smaller extent), is *not* due to particle sizes, but rather due to some other unmodelled physical process. In addition, the particle sizes implied by the part of the curve closest to the inner ring measurements are too small to be consistent with lifetime estimates for particles in the rings due to atmospheric drag, an issue discussed in Chapter 3. Finally, an indication that these rings are significantly depleted in sub-centimeter sized particles is the near equality between the radio and other measurements at shorter wavelengths (French *et al.*, 1988, Colwell *et al.*, 1989).

4.4.4 Tenuous ring companions

The tenuous companions of Rings η and δ were shown in Figures 20 and 21. Approximate locations and estimated integrated opacity at 3.6 cm for these companion rings have been given in Table 3. Because the mean opacity at 3.6 cm is comparable to Earth-based stellar occultation values (Elliot and Nicholson, 1984), a significant fraction of the particles in these tenuous companions must exceed a few centimeters in size.

4.4.5 Rings discovered by Voyager

Voyager discovered several new ring features in backscatter (on approach to the planet) and during ring-plane crossing (Smith *et al.*, 1986), none of which are detectable in the radio data. One feature is quite wide, and very tenuous, spanning the distance between 37,000 and 39,500 km from Uranus (Smith *et al.*, 1986). Its optical depth is estimated to be approximately 1×10^{-3}, which is well below the detection sensitivity of the radio experiment, given the magnitude of typical fluctuations in signal level ($\sigma_\tau \sim 0.02$) in non-ring regions. A second feature, Ring 1986U1R, is located approximately 50,000 km from Uranus (Smith *et al.*, 1986; French *et al.*, 1988), and has an optical depth measured by the Voyager PPS experiment of $\tau \simeq 0.1$ (Lane *et al.*, 1986). The data in the vicinity of this ring have been reconstructed from the raw radio data at a resolution of 200 m assuming that the ring is circular and that it lies in the mean plane of the rings. There is no evidence for 1986U1R in the radio data, but as its optical depth as reported by PPS is near the detection threshold of the radio experiment, no definitive conclusion can be drawn. This ring was also undetectable in ground-based observations of the Uranian rings at a wavelength of 2.2 μm (Kangas and Elliot, 1987). The ring would not be detectable at 3.6 cm wavelength if the majority of the particles are much smaller than the radio wavelength, as Holberg *et al.* (1987) indicate is likely. A missed radio detection could also occur if 1986U1R is azimuthally clumpy, as reported by Ockert *et al.* (1987). A third feature reported by Smith *et al.* (1986) is a companion to Ring β, located at approximately 45,736 km, with a brightness of approximately 0.1 that of Ring β. We do not detect this feature in the radio data.

4.5 Discussion and Limitations

In this chapter we presented the integrated opacity and phase measurements for the Uranian rings at wavelengths of 3.6 and 13 cm. We then described the standard theory for interpreting such measurements in terms of physical properties of the rings and used these models to place some constraints on the vertical profile of the rings. Monolayer and many-particle-thick models result in different predictions for how integrated optical depth should vary as a function of ring width. We find that, for those rings where a clear distinction between the models can be made, the many-particle-thick model is a better fit to the observations. Lower bounds were placed on the thickness in terms of numbers of "layers" in the ring. In addition, we proposed an alternative model for Ring ϵ in which the thickness of the ring does not remain constant in longitude, but rather varies inversely in proportion to the varying width.

In this chapter, we also conducted an analysis of particle sizes in the Uranian rings using the standard theories outlined above. The most striking observation is the large differential phase for the inner Uranian rings (6, 5, 4, α, and β). The large phase delay for the 13 cm wavelength implies an extremely small possible range of particle sizes assuming the standard theories. What is required is a near-monodispersion of particle sizes at the crossing point of the extinction curves for $\lambda = 3.6$ and 13 cm. Only this narrow size distribution can produce such large differential phase per unit optical depth. We note here that this anomalous phase behavior is present in some places in Saturn's rings as well. Embedded particle-accumulation-groups (PAGs in the nomenclature of Rosen, 1989) in Saturn's Ring C are qualitatively similar to the Uranian rings. They are sharp-edged and relatively optically thick accumulations of material, although their widths are generally much greater than those of the Uranian rings. These features show phase delay behavior quite similar to that of the inner Uranian rings, with ϕ_c(13 cm) significantly larger than ϕ_c(3.6 cm) (see Figure 17 of Marouf *et al.* (1986), and Saturn ring maps in Rosen, 1989). The magnitude of the phase delay per unit (normal) optical depth is several times larger than that observed in the Uranian rings; given the much longer path length through Saturn's rings due to the grazing incidence of that occultation, the phase delay per unit amount of material is roughly comparable. However, there is clear evidence for differential optical depth in the Ring C PAGs, while no such evidence is seen in the Uranian rings.

The results for the inner rings upon application of the standard theories may imply that the large observed phase delay is in fact ***not*** due to particle sizes. A monodispersion of particles of a very particular size (a size which is directly related to the wavelengths used in the experiment) does not seem to be a likely size distribution. Therefore we hypothesize that such phase behavior is due to some other, unknown, cause.

We conducted a more extensive analysis of particle sizes in Ring ϵ, for which the highest confidence measurements exist. If we consider both the differential optical depth and differential phase delay measurements, we find that particle size distributions are rather tightly constrained. For $q \gtrsim 3$, a_{min} is required to be at the crossing point of the Mie extinction curves for $\lambda = 3.6$ and 13 cm. For $q < 3$, a_{min} is rather loosely constrained to be $\lesssim 1$ cm but a_{max} is then tightly constrained. The exception is the case $m = 1.78 + 0.00i$, $q = 2.75$, for which a relatively broad range of sizes is allowed, so long as $a_{\mathrm{min}} \lesssim 2$ cm, and $a_{\mathrm{max}} \gtrsim 165$ cm. In this case, $\sigma \gtrsim 50$ g-cm^{-2}, assuming an ice-like bulk particle density. Given the results for the inner rings reported above, we also allow for the possibility that the phase behavior is not due to particle sizes, and consider the implications of the differential optical depth measurements alone. In this case the measurements allow typical particle sizes exceeding ~ 70 cm in radius, independent of q, and the corresponding surface mass densities are large ($\sigma \gtrsim 80$ g-cm^{-2} if the bulk density is ~ 1 g-cm^{-3}). If $q < 3$, the minimum size can be in the Rayleigh region ($a_{\mathrm{min}} \lesssim 1$ cm) provided that a_{max} exceeds a refractive index dependent value. In this case σ can be as small as 10 g-cm^{-2} Other outer rings (Rings η, γ, and δ) have optical depth and phase delay behavior similar to that of Ring ϵ.

The three models proposed to describe extinction by planetary rings have several strengths but also several serious weaknesses. The first strength derives from the relative ease with which the Mie coefficients for scattering by a sphere may be computed. Efficient algorithms (*e.g.*, Dave, 1968) are readily available to solve the problem of scattering by a sphere of arbitrary refractive index and of essentially any size. A distribution of sizes can be incorporated easily. Secondly, the monolayer and many-particle-thick models are simple to describe, and form two endpoints of a continuum of possible vertical distributions. With such models, parameters of the size distribution can be easily varied in an attempt to match a set of observations. For these reasons, this approach to the problem has become quite standard in the field, and in many cases has yielded consistent results in analyzing particle size distributions.

The weaknesses of these models are several. The first derives from the basic assumption of sphericity of the ring particles. The simple geometry of a sphere allows the type of efficient solution that Mie theory provides. It is most certainly only an approximation to the true shape of a ring particle—a class of objects of which not a single specimen has been directly observed. Some characteristics of scattering by spheres (particularly lossless ones) are due to the perfect symmetry of the object, and would disappear for a roughened particle. The use of a size distribution generally mitigates such artifacts in the scattering behavior. However if the particles are *significantly* non-spherical, then Mie theory is no longer a valid approximation to the scattering behavior. An additional implicit assumption in Mie scattering theory is that the particles carry no free charge. An interesting hypothesis for the cause of the anomalous phase behavior is that, because the inner rings are immersed in the extended outer atmosphere of Uranus, there is a charging of the ring particles by the plasma. However, when we investigated this hypothesis using a variant of Mie theory developed by Bohren and Hunt (1977), we found that charging voltages necessary to cause detectable changes to the scattering behavior were in the megavolt range, which seems highly unlikely.

Probably a more serious flaw to the theories than the assumption of sphericity is the assumption that there are no coherent interactions between the particles. As the particles become closer to one another, at some point they will sense each other's presence coherently, and a pair of particles will begin to behave more like an elongated, larger particle. The classical models require that the particles remain far enough from one another to avoid such interactions—real planetary rings may not be so constrained.

Past analyses of radio occultation observations of rings suffer from probable violation of this assumption to some degree. The occultation by Saturn's rings was at an extremely grazing incidence angle of only 6° (Tyler *et al.*, 1983). Because of this, shadowing of ring particles behind one another is probably significant. For the Uranian ring occultation experiment, although the incidence angle was near-normal, the optical depths observed for several of the rings imply a large number of particles in a small area. Unless the ring is extremely thick in the vertical dimension, volume densities must become fairly large, and violation of the large-separation assumption is possible. Although for Ring ϵ the conservation of integrated optical depth seems to imply that shadowing effects on the optical depth are not significant, it remains to be investigated whether the anomalous phase behavior observed might be a coherent interaction or other close-packing effect. In the following chapter we address the problem of coherent interactions in more detail.

Chapter 5

Coherent Scattering by Clusters of Spheres

The models for scattering of radio waves by planetary rings outlined in Chapter 4 rely on the important assumption that the scattering behavior of an individual ring particle is not influenced by other particles situated nearby. It is clear that this assumption is invalid if the particles are arbitrarily close. For example, a cluster of particles in close proximity will look like a single larger particle to the incident wave, and we have already seen that extinction efficiency can be a strong function of particle size. Furthermore, interference effects between two particles of size comparable to the wavelength cannot be neglected when the particles are close to one another. Wang *et al.* (1981) studied the scattering behavior of touching spheres a few ka in size as a function of scattering angle and found that, at a particular angle, constructive interference causes a dramatic enhancement in scattering over that predicted by the theory for non-interacting spheres.

As discussed in Chapter 4, previous analyses of radio occultation results have relied on the non-interacting-particles models outlined in that chapter. The attraction of these models is that, given assumptions for parameters of a particle size distribution and a refractive index, it is straightforward to compute optical depth and phase delay as a function of incident wavelength. Parameters of the size distribution can then be varied until the predictions of the model reasonably match the set of observations at different wavelengths.

The motivation for understanding when and how the scattering models break down should be obvious. Even for cases when the simple models appear to give reasonable results for particle sizes and ring properties, it is important to know how sensitive the results are to the assumption that close proximity of the particles does not affect the scattering behavior of the ensemble. In addition, as discussed in Chapter 4, some observations are inherently inconsistent with the theoretical results based on the assumption of non-interacting, spherical, homogeneous particles. In this case, it is important to investigate the possibility that it is close packing of the particles which is causing the discrepancy. Quantitative characterization of close-packing effects, and identification of the range of particle sizes, separations, and incidence geometry for which they are significant, is important for present and future analyses of ring occultation measurements. Limited progress in this regard has been previously reported (Marouf, 1975).

In this chapter we lay the foundation work necessary to achieve this more ambitious objective. First, an analytical solution of the problem of scattering by two or more arbitrarily placed spheres is used to compute numerically the complex extinction for several arrangements and sizes of particles. The results are compared to the non-interacting-particle results and coupling effects are identified and characterized. Second, we develop a framework for using the two-sphere results to determine the complex extinction caused by a ring composed of many particles. This is accomplished by decomposing the problem of interaction between many spheres into a set of pairwise interactions. Such an approach is validated through comparison with exact solutions for clusters of spheres. The pairwise-approximation is then used to investigate extinction by a monolayer ring and the results are discussed in the context of ring measurements.

5.1 Coherent Scattering by Two Spheres

The problem of scattering by two or more spheres has almost as long a history as the problem of scattering by a single sphere, discussed in Chapter 4. One approach to the problem has been to use the modal expansion method developed for a single sphere, together with the translation-addition theorem of spherical harmonics, to express the spherical waves excited in one sphere in a reference frame centered on the other sphere(s). Trinks (1933) was the first to investigate this approach, but the complexity of the translation-addition theorem he used limited his results to spheres of radius much smaller than the wavelength (the Rayleigh regime). Liang and Lo (1967) took the problem a step forward by utilizing the translation-addition theorem of Stein (1961) and Cruzan (1962). Unfortunately, the time needed to calculate the translation coefficients was still a limitation, and only spheres smaller than $\sim \lambda$ in radius could be considered. Bruning and Lo (1971) derived a recursion relation which permitted much faster computation of the translation coefficients, permitting spheres of radius as large as tens of wavelengths to be considered. Other computational results for scattering by two spheres based on the matrix inversion method of Bruning and Lo (1971) have been reported by Dean (1982). The present work uses an adaptation of a FORTRAN program written by Kirk Fuller (Fuller, 1987) to solve the multiple scattering problem by clusters of up to five spheres using an order-of-scattering approach or a matrix inversion approach. The limit of five is set by the computational complexity of the problem.

Both Fuller's and Dean's computational results have been successful in reproducing close spacing effects observed in microwave laboratory measurements (Wang, 1979, Wang *et al.*, 1981, Kattawar and Dean, 1983, Fuller *et al.*, 1986). Borghese *et al.* (1984a), Borghese *et al.* (1984b), and Sindoni *et al.* (1984) have pursued computational studies of scattering by clusters of spheres using a similar technique, although because they have concentrated on studying the effects of as many as 20 spheres, the sizes they have considered have necessarily been quite small, with ka generally less than 0.1.

The modal expansion method utilized here, while limited to spheres, has the advantage that bodies of a relatively broad range of sizes may be treated efficiently. Other methods, while more general, have their own limitations. For example, while computational procedures such as the T-matrix algorithm (Waterman, 1965; 1971) or the uni-moment method (Mei, 1974) are more adaptable to scatterers of arbitrary shape, computational demands grow rapidly with the size of the scatterer, and the methods are not generally practical for bodies larger than a wavelength or so in size.

The choice of a sphere as the scattering object is directly tied to the modal expansion method used to solve the scattering problem. Many of the characteristics of scattering by non-spheres may be inferred from the scattering behavior of spheres, particularly for randomly-oriented, slightly roughened spheres, and observations in the near-forward direction. Results must be regarded with due care, however. There are some aspects of scattering by spheres which are due entirely to their perfect symmetry, one example being the ripple structure evident in Figure 28 of Chapter 4.

The radio occultation experiment transmits a radio wave through the rings, and the attenuated and phase-shifted signal is received on Earth. For this reason, the quantity of most interest here is the extinction, that is, the removal of energy from the incident beam in the exact forward direction. We have found that relatively little work has been reported on this problem; most researchers have been primarily interested in the scattering behavior as a function of observation angle. Furthermore, discussion of the imaginary part of the extinction is particularly sparse (even for single spheres), presumably because the motivation for many scattering problems is derived from uses of incoherent sources.

In analogy to the extinction parameters Q_{Mie} and P_{Mie} introduced in Section 4.2.1 for single spheres, we define

$$Q^{(N)} = \frac{4\pi}{k^2 G}\mathrm{Re}\{S^{(N)}\} \tag{29}$$

$$P^{(N)} = -\frac{2\pi}{k^2 G}\mathrm{Im}\{S^{(N)}\}, \tag{30}$$

where $S^{(N)}$ is the forward scattering amplitude of N spheres, and the total cross-sectional area G is defined by

$$G \equiv \sum_{i=1}^{N} g_i,$$

where g_i is the cross-sectional area of the ith sphere. In a parallel manner, we also define

$$Q^{(N)}_{\mathrm{n.i.}} = \frac{4\pi}{k^2 G}\mathrm{Re}\{S^{(N)}_{\mathrm{n.i.}}\} = \frac{4\pi}{k^2 G}\mathrm{Re}\sum_{i=1}^{N} S^{(1)}_i \tag{31}$$

$$P^{(N)}_{\mathrm{n.i.}} = -\frac{2\pi}{k^2 G}\mathrm{Im}\{S^{(N)}_{\mathrm{n.i.}}\} = \frac{4\pi}{k^2 G}\mathrm{Im}\sum_{i=1}^{N} S^{(1)}_i, \tag{32}$$

where $S^{(N)}_{\mathrm{n.i.}}$ is the forward scattering amplitude of N noninteracting particles, which is simply the sum of the individual forward scattering amplitudes $S^{(1)}_i$.

5.1.1 Theoretical framework

Figure 35 shows the relevant geometrical parameters for the two-sphere problem. The incident field is $\mathbf{E_i}$ with scattered wave vector $\mathbf{k_i}$, and the field measured in the exact forward direction in the plane containing the scatterers is $\mathbf{E}$, with wave vector $\mathbf{k_s} = \mathbf{k_i}$. The angle between the exact forward direction and a line connecting the centers of the spheres is α. Without loss of generality, we consider only two possible polarization directions for the electric field, $\hat{\mathrm{e}}_{\|}$ and $\hat{\mathrm{e}}_{\perp}$, with $\hat{\mathrm{e}}_{\|}$ a unit vector lying in the plane of the scatterers and $\hat{\mathrm{e}}_{\perp}$ a unit vector lying perpendicular to that plane. In general, the spheres may be of different sizes, but for simplicity, we assume that they are of identical radius a and that their centers are separated by a distance d. These length scales can be made non-dimensional by multiplying them by the incident wavenumber $k = 2\pi/\lambda$.

It is assumed that the field scattered by two spheres may be expanded as

$$\mathbf{E_s}(\mathbf{r}) = \sum_{n=1}^{\infty}\sum_{m=-n}^{n}\sum_{l=1}^{2}\left({}^l a_{mn}\,{}^l\mathbf{N}^{(3)}_{mn}(\mathbf{r}) + {}^l b_{mn}\,{}^l\mathbf{M}^{(3)}_{mn}(\mathbf{r})\right),$$

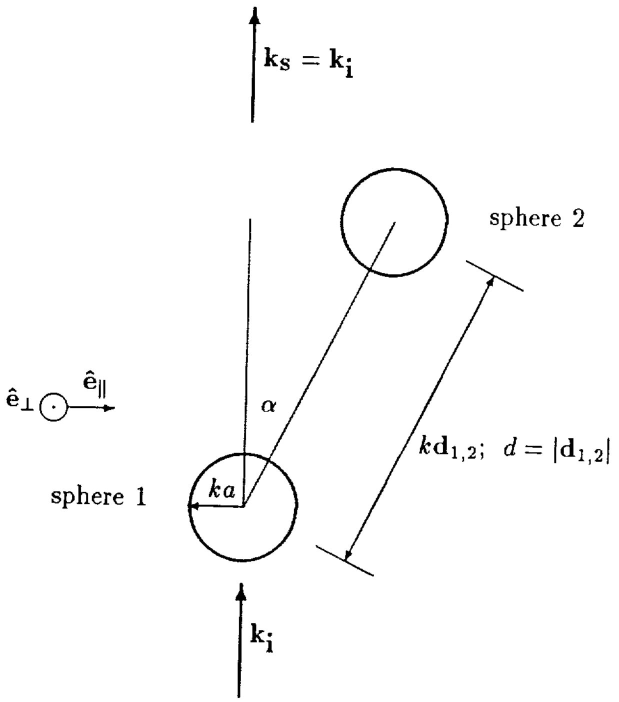

FIG. 35: Relevant geometrical parameters of the two-sphere scattering problem. The incident electric field is $\mathbf{E_i}$, which is polarized along one of the two orthogonal directions $\hat{e}_\parallel$ or $\hat{e}_\perp$. The spheres are of dimensionless size ka and their centers are separated by a distance kd, where k is the wavenumber of the incident wave. The orientation angle α is the angle between the forward direction and a line connecting the centers of the two spheres. The received field $\mathbf{E}$ is measured in the forward direction, in the plane containing the scatterers.

where ${}^la_{mn}$ and ${}^lb_{mn}$ are the expansion coefficients for the lth sphere, and ${}^l\mathbf{N}^{(3)}_{mn}(\mathbf{r})$ and ${}^l\mathbf{M}^{(3)}_{mn}(\mathbf{r})$ are the vector spherical harmonics in a coordinate system centered on the lth scatterer, *e.g.*, ${}^l\mathbf{M}^{(3)}_{mn}(\mathbf{r}) \equiv \mathbf{M}^{(3)}_{mn}[k(\mathbf{r}-\mathbf{r}_l)]$. Explicit forms and discussion of the vector spherical harmonics may be found in basic electromagnetics texts, for example, Stratton (1941), Jackson (1975), or, more recently, Bohren and Huffman (1983).

The incident plane wave is expanded in a spherical coordinate frame centered on one of the spheres, assumed to be located at the origin. For reasons discussed below, it is advantageous to orient the two spheres along the z-axis. The expression for the incident plane wave, expressed in spherical coordinates centered on sphere 1 (at the origin) is

$$\mathbf{E_i}(\mathbf{r}) = E_0 \sum_{n=1}^{\infty} \sum_{m=-n}^{n} \left({}^1p_{mn}\, {}^1\mathbf{N}^{(1)}_{mn} + {}^1q_{mn}\, {}^1\mathbf{M}^{(1)}_{mn} \right),$$

where $\mathbf{M}_{mn} = \mathbf{M}_{emn} + i\mathbf{M}_{omn}$, $\mathbf{N}_{mn} = \mathbf{N}_{emn} + i\mathbf{N}_{omn}$, and the multipole coefficients are defined by

$$\begin{aligned} {}^1p_{mn} &= -i^n \frac{2n+1}{n(n+1)} \frac{(n-m)!}{(n+m)!} \left[-i \frac{\partial}{\partial\theta} P_n^m(\cos\alpha) \sin\gamma_p + \frac{m}{\sin\theta} P_n^m(\cos\alpha) \cos\gamma_p \right] \\ {}^1q_{mn} &= i^n \frac{2n+1}{n(n+1)} \frac{(n-m)!}{(n+m)!} \left[i \frac{m}{\sin\theta} P_n^m(\cos\alpha) \sin\gamma_p - \frac{\partial}{\partial\theta} P_n^m(\cos\alpha) \cos\gamma_p \right] \end{aligned} \tag{33}$$

In Eq. 33, γ_p is an angle in the plane orthogonal to the incidence direction and indicates the polarization direction of the incident wave; $\gamma_p = 0$ and $\gamma_p = \pi/2$ are polarization in the $\hat{\mathbf{e}}_{\|}$ and $\hat{\mathbf{e}}_{\perp}$ directions respectively. The coefficients of the plane wave about the second sphere are found simply by multiplying ${}^1p_{mn}$ and ${}^1q_{mn}$ by the phase factor $\exp(ikd\cos\alpha)$.

A critical requirement for the development of the theory of the two-sphere scattering problem is to expand the fields scattered by the first sphere in the coordinate frame of the second sphere. This is accomplished through the use of a translation-addition theorem (Stein, 1961; Cruzan, 1962). In the special case in which the coordinate translation is along the z-axis (hence the reason for the general form for the plane wave expansion above), the theorem gives

$$\begin{aligned} {}^1\mathbf{M}^{(3)}_{mn} &= \sum_{\nu=\max(1,m)}^{\infty} \left({}^2\mathbf{M}^{(1)}_{m\nu} A^{mn}_{m\nu}(k\mathbf{d}_{1,2}) + {}^2\mathbf{N}^{(1)}_{m\nu} B^{mn}_{m\nu}(k\mathbf{d}_{1,2}) \right) \\ {}^1\mathbf{N}^{(3)}_{mn} &= \sum_{\nu=\max(1,m)}^{\infty} \left({}^2\mathbf{N}^{(1)}_{m\nu} A^{mn}_{m\nu}(k\mathbf{d}_{1,2}) + {}^2\mathbf{M}^{(1)}_{m\nu} B^{mn}_{m\nu}(k\mathbf{d}_{1,2}) \right), \end{aligned}$$

ka	CPU time (sec)
0.2	1.2
0.5	2.0
1.0	3.1
2.0	4.6
5.0	25.7
10.0	106
20.0	740

TABLE 10: CPU time to compute the scattering amplitude of a pair of spheres of equal electric size ka on a DEC microVAX.

where $\mathbf{d}_{1,2} = \mathbf{r}_2 - \mathbf{r}_1$. The translation coefficients $A_{m\nu}^{mn}$ and $B_{m\nu}^{mn}$ are computable quantities which depend on the geometry of the configuration. Further discussion of these terms may be found in Liang and Lo (1967) and Bruning and Lo (1971).

In contrast to Bruning and Lo (1971), who use a matrix inversion method to solve the problem of scattering by two spheres, Fuller (1987) uses an order-of-scattering approach. The incident plane wave impinges on each of the two spheres, and excites from each of them a scattered field. These fields propagate both toward the observer and also toward the other sphere, where further scattering takes place. The process is iterated until the waves scattered between the particles become negligible in amplitude. The translation-addition theorem is used to express the fields excited in one sphere in the coordinate frame of the other sphere in order to compute the next scattering order. Fuller (1987) found that for pairs of spheres, the order-of-scattering approach was computationally more efficient than solving the scattering problem via direct matrix inversion. In practice, computational results for pairs of spheres of size up to $ka \simeq 20$ are feasible, with computation time increasing rapidly as ka exceeds ~ 10. Table 10 shows the CPU time for our computation of the exact forward scattering amplitude as the size of the spheres is increased. However, when a lossless refractive index is used, certain sizes of particles exhibit resonant behavior. At these sizes, the order-of-scattering approach may fail (Fuller, 1989), and the matrix inversion method (also included in Fuller's code) can be used instead.

5.1.2 Polarization effects

Because of spherical symmetry in the case of non-interacting spheres, there is no difference in the scattering behavior of the two possible incident polarizations. For a pair of coherently interacting spheres, however, the symmetry is in general broken, and we must consider the two incidence polarization directions separately. (Endfire incidence, or $\alpha = 0$, is a special case in which symmetry *is* preserved.) For the Voyager ring occultation experiments, the incident wave $\mathbf{E_i}$ is right-hand circularly polarized:

$$\mathbf{E_i} = \left(\hat{\mathbf{e}}_{\parallel} - i\hat{\mathbf{e}}_{\perp}\right) E_0 e^{ikz},$$

where an $\exp(-i\omega t)$ harmonic time dependence has been suppressed. Using this along with Eq. 11, the field scattered by an arbitrary (not necessarily spherical) particle is

$$\mathbf{E_S} = \mathbf{E}_{\parallel \mathrm{S}} + \mathbf{E}_{\perp \mathrm{S}} = E_0 \frac{e^{ik(r-z)}}{-ikr} \left(S_{\parallel}\hat{\mathbf{e}}_{\parallel} - iS_{\perp}\hat{\mathbf{e}}_{\perp}\right).$$

This may easily be decomposed into a right circular component with amplitude $(S_{\parallel}+S_{\perp})/2$ and a left circular component with amplitude $(S_{\parallel} - S_{\perp})/2$. During the Uranus ring occultation experiment, the stations on the ground received only the right circular component, so that the quantity of interest in this work is $(S_{\parallel} + S_{\perp})/2$. Note that, had we received the left-circular component, it could have served as a measure of cooperative effects or non-sphericity of ring particles[1].

5.1.3 Computational results

There is a large parameter space to explore even for the simple geometry shown in Figure 35. To fully characterize the effect of coherent interactions, it is necessary to vary the particle size, particle spacing, the refractive index of the particles, the orientation angle α, and the polarization of the incident wave. In this section we present representative examples of computed complex extinction.

Figure 36 shows the exact extinction behavior of touching spheres relative to the non-interacting solution, assuming a refractive index of $m = 1.78 + 0.10i$. Plotted is $Q^{(2)}/Q^{(2)}_{\mathrm{n.i.}}$ *vs* the size parameter ka, where these quantities are as defined in Eqs. 29 and 31. For the incident circular polarization of the radio occultation experiment, the forward scattering amplitude of interest is $(S_{\perp} + S_{\parallel})/2$, where these components may be computed using Fuller's order-of-scattering approach for a pair of spheres. In Figure 36, as well as Figures 37–39, $Q^{(2)}$ is computed using $(S_{\perp} + S_{\parallel})/2$. Later figures will show individual results for both parallel and perpendicular polarized incident radiation, in order to investigate the effect of polarization. The format of Figure 36 was suggested by similar figures in Borghese *et al.* (1984b), who, however, only computed values for extinction up to a size $ka = 1$.

---

[1] In fact, a channel was open for the left circular polarized signal during the Saturn ring occultation experiment. The fact that there was no signal detected in that channel was interpreted as support for the approximate sphericity of the Saturnian ring particles (Simpson *et al.*, 1984).

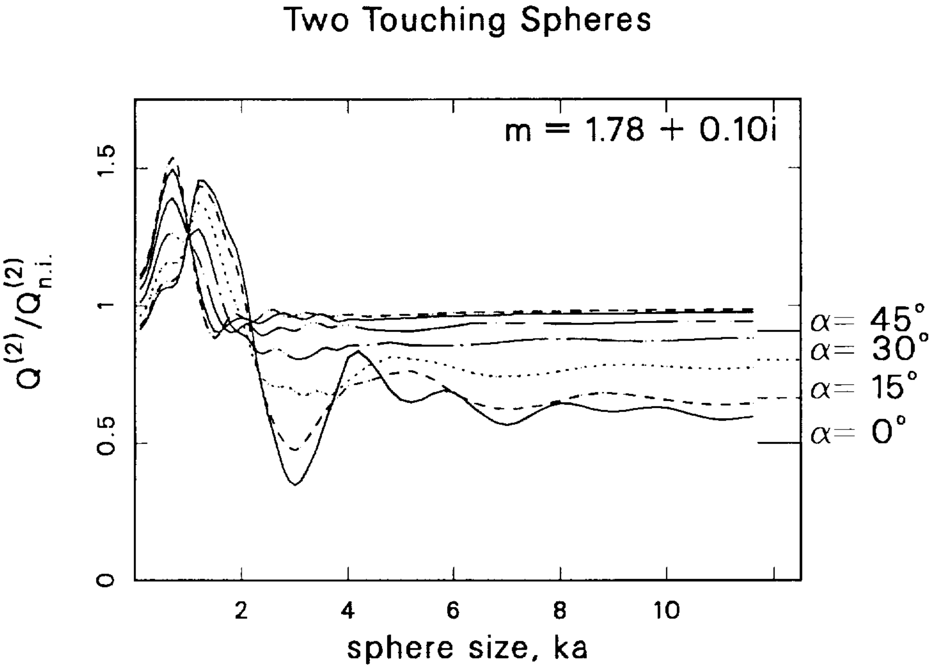

FIG. 36: $Q^{(2)}/Q^{(2)}_{\mathrm{n.i.}}$ extinction curves for touching particles ($kd = 2ka$) with refractive index $m = 1.78 + 0.10i$. Seven orientations are shown, with α ranging from 0 to 90° in 15° increments, and as the size of the touching particles varies from $ka = 0.1$ to $ka = 11.6$. The four short horizontal lines at the right of the figure indicate the predicted value for $Q^{(2)}/Q^{(2)}_{\mathrm{n.i.}}$ from the simple shadowing model described by Eq. 34, for angles $\alpha = 0°$, 15°, 30°, and 45°; the other three values are too close to one another to show on this figure, but would lie at 0.971, 0.996, and 1.0 for $\alpha = 60°$, 75°, and 90°, respectively. The line type of these short lines matches those of the extinction curves.

Therefore, many of the interesting effects for large particles reported below were not explored in that work.

Seven curves are shown, corresponding to orientation angles α in steps of 15°. Over the range of size parameters from 0.1 to 12, the ratio $Q^{(2)}/Q^{(2)}_{\mathrm{n.i.}}$ differs significantly from unity, indicating substantial coherent coupling effects. For particles with $ka \lesssim 2$, such effects are important for all incidence angles α. However, for larger particles, the ratio is close to unity for the broadside incidence case ($\alpha = 90°$), indicating that coherent coupling is small when the wave is incident perpendicular to the line connecting the particles. Physically, these results may be explained by the fact that, as we shall see below, the scattering diagram for small particles is relatively isotropic, so that a particle in any orientation "sees" the scattered field from the other particle. As particles become larger, their scattered fields become more and more peaked in the forward direction, resulting in cooperative effects only when one particle lies roughly behind the other.

For larger particles, as α decreases toward the endfire incidence case, coherent effects increase, and may be interpreted as shadowing of the second particle by the first. In fact, we may construct a simple shadowing model in which the ratio of $Q^{(2)}/Q^{(2)}_{\text{n.i.}}$ is approximated by the projected cross-sectional area of the front particle plus the projected unshadowed cross-sectional area of the back particle, normalized by the total cross-sectional area of the two particles. The ratio $\left[Q^{(2)}_{\text{n.i.}} - Q^{(2)}\right]/Q^{(2)}_{\text{n.i.}}$ defines a "shadow fraction," SF, which is given by

$$SF = \begin{cases} \frac{1}{\pi}\left(\cos^{-1}\left(\frac{kd}{2ka}\sin\alpha\right)\right) + \frac{1}{2\pi}\left(\sin\left(2\cos^{-1}\left(\frac{kd}{2ka}\sin\alpha\right)\right)\right) & \frac{kd}{2ka}\sin\alpha \le 1 \\ 0 & \text{otherwise,} \end{cases} \tag{34}$$

and varies from a maximum of 0.5 when $\alpha = 0$ to a minimum of 0 when the back particle emerges completely from the shadow of the front particle. Computed values of $1 - SF$ are shown in Figure 36 as short line-segments at the right hand vertical axis. Although this "geometric-optics" model is expected to give reasonable values only when the particles are very large, the line-segments in Figure 36 show that the simple shadowing model agrees reasonably well with the asymptotic values of the computed exact curves, even for moderately-sized touching spheres.

Figure 37 shows results for parameters identical, except that $m = 1.70 + 0.70i$, to those in Figure 36. As expected, oscillations are smoothed by the large loss in the particle; however, similar overall agreement with the simple shadowing model persists. Maximum excursions of $Q^{(2)}/Q^{(2)}_{\text{n.i.}}$ from unity are significantly decreased by the large loss in the refractive index.

We now investigate the dependence of $Q^{(2)}/Q^{(2)}_{\text{n.i.}}$ on the separation of the two particles. In Figures 36 and 37 the particles were touching; in Figures 38 and 39 the centers of the particles are separated by three radii. In general, coherent coupling is somewhat reduced as the particle separation increases, as would be expected, but significant coupling clearly remains. However, due to the increased separation, the larger particles move out of each other's shadows for smaller orientation angles α, so that the large shadowing effects are confined to a smaller cone of near-forward angles.

We may also investigate the dependence of coherent coupling on the spacing between the particles for particles of fixed size. Figure 40 shows, for a particle in the Rayleigh regime ($ka = 0.1$), $Q^{(2)}/Q^{(2)}_{\text{n.i.}}$ and $P^{(2)}/Q^{(2)}$ as the separation kd is increased from the point where the spheres are touching to where their centers are separated by 10 radii. $P^{(2)}_{\text{n.i.}}/Q^{(2)}_{\text{n.i.}}$ is also shown for comparison. We choose

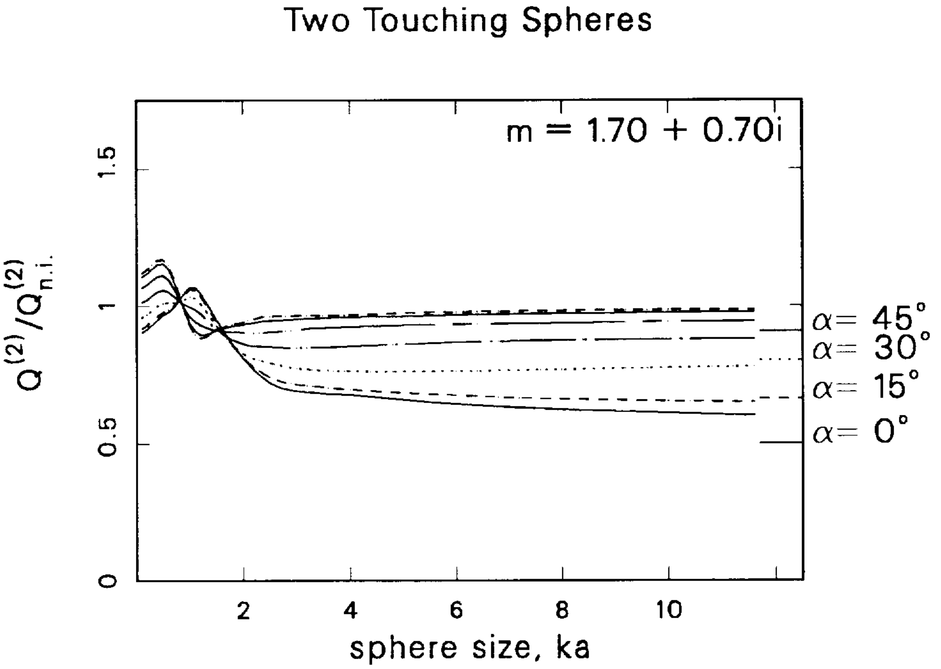

FIG. 37: $Q^{(2)}/Q^{(2)}_{\mathrm{n.i.}}$ extinction curves for touching particles with lossy refractive index $m = 1.70 + 0.70i$. See caption of Figure 36 for details. Curves are significantly smoother compared to those obtained for the less lossy refractive index of Figure 36, and maximum excursions of $Q^{(2)}/Q^{(2)}_{\mathrm{n.i.}}$ are smaller as well.

to normalize $P^{(2)}$ by $Q^{(2)}$ rather than by $P^{(2)}_{\mathrm{n.i.}}$ in order to show the effect of coherent coupling on the *relative* magnitude of $P^{(2)}$, since phase-shift per unit optical depth is the relevant quantity for interpretation of the radio occultation measurements. $P^{(2)}$ and $P^{(2)}_{\mathrm{n.i.}}$ for two spheres are as defined in Eqs. 30 and 32. Results are shown for the three angles $\alpha = 0°, 45°$, and $90°$, and for two incident polarizations. For these small particles, coupling effects are 30% or less, and rapidly decrease as the particles are separated by more than a few radii. For any given orientation angle, coupling effects decrease monotonically with the separation distance. Notably, the coupling effects do not depend on the orientation angle for the perpendicular polarization case.

One may construct a simple model for the interaction process which can shed more light on the behavior of the curves in Figure 40 as well as other figures discussed below. In the limit of large separation, we may use the far-field Mie solution for the field scattered by one sphere as an excitation of the second sphere. This assumes that the second particle subtends a small angle from the viewpoint of the first particle so that the scattered wave may be considered to be a single plane

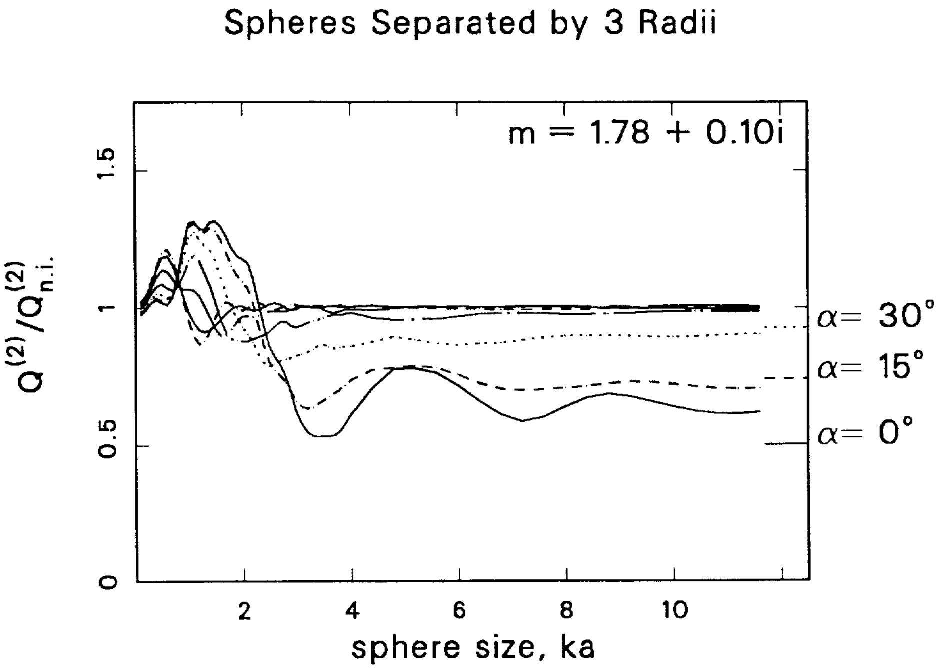

FIG. 38: $Q^{(2)}/Q^{(2)}_{\text{n.i.}}$ extinction curves for separation $kd = 3ka$ and refractive index $m = 1.78 + 0.10i$. See caption of Figure 36 for details.

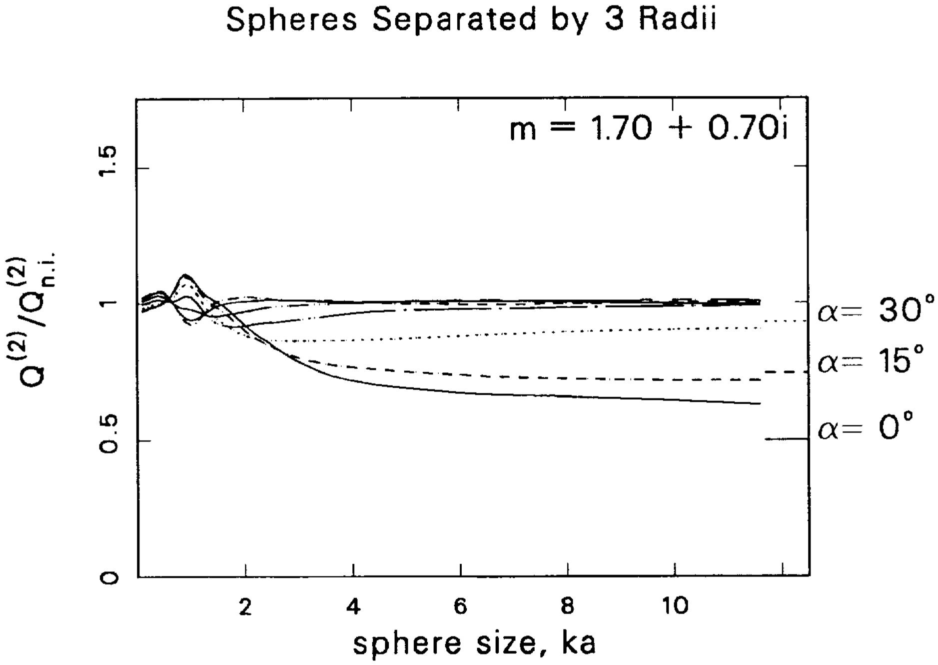

FIG. 39: $Q^{(2)}/Q^{(2)}_{\text{n.i.}}$ extinction curves for separation $kd = 3ka$ and refractive index $m = 1.70 + 0.70i$. See caption of Figure 36 for details.

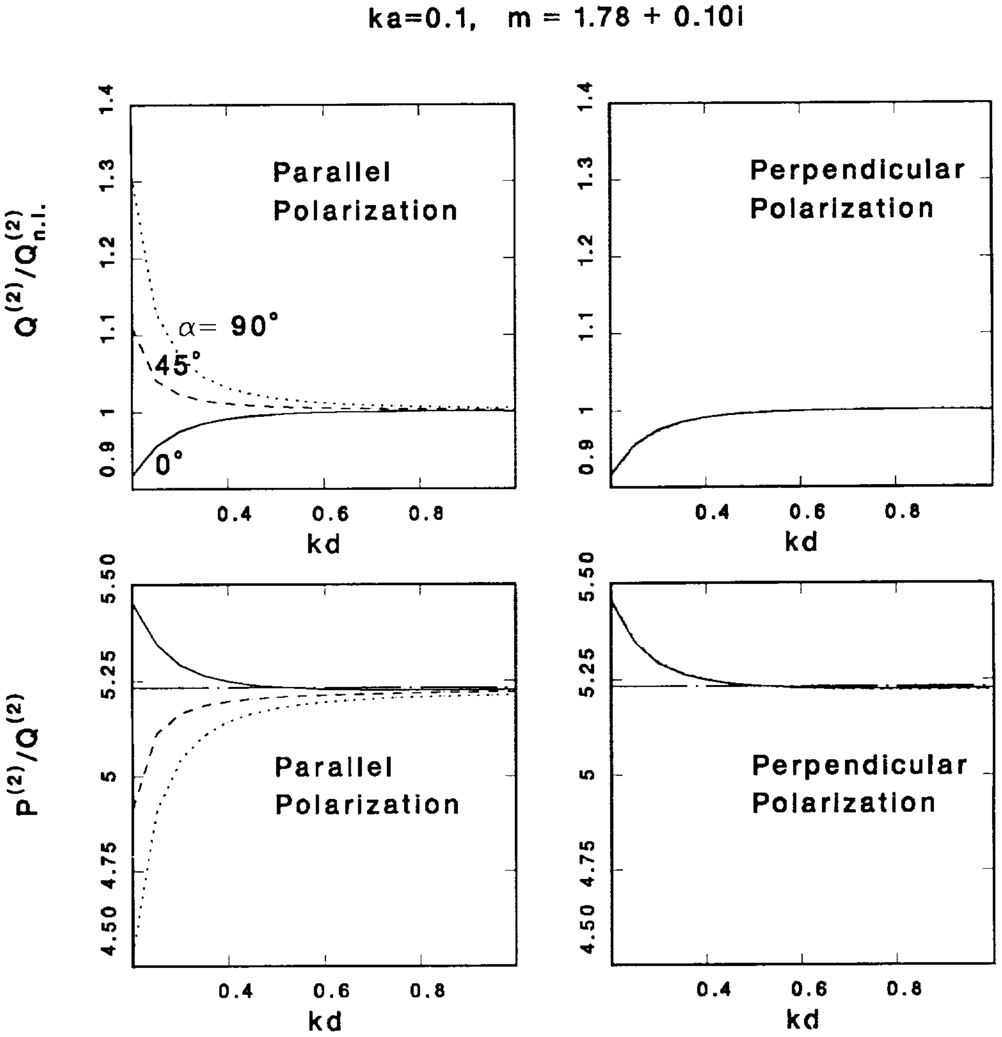

FIG. 40: $Q^{(2)}/Q^{(2)}_{\rm n.i.}$ and $P^{(2)}/Q^{(2)}$ for a particle of size $ka = 0.1$ and refractive index $m = 1.78{+}0.10i$, as the separation is varied from touching ($kd = 0.2$) to $kd = 1.0$. The left-hand panels are for parallel incident polarization, the right-hand panels for perpendicular polarization. In the lower panels, the horizontal line at ~ 5.23 is the non-interacting solution $P^{(2)}_{\rm n.i.}/Q^{(2)}_{\rm n.i.}$.

wave. Including only singly and doubly scattered waves, we obtain

$$S^{(2)}_{\text{asym}} = S^{(2)}_{\text{n.i.}} + \hat{S}^{(2)}_{\text{asym}},$$

where

$$\begin{aligned}\hat{S}^{(2)}_{\text{asym}} &\simeq \frac{[S^{(1)}(\alpha)]^2 e^{ikd(1-\cos\alpha)}}{-ikd} \\ &\quad + \frac{[S^{(1)}(\pi-\alpha)]^2 e^{ikd(1+\cos\alpha)}}{-ikd} \qquad (35)\end{aligned}$$

and $S^{(1)}(\alpha)$ is the scattering amplitude of a single isolated sphere at angle α from the exact forward direction. $\hat{S}^{(2)}_{\text{asym}}$ represents an approximation for the perturbation to $S^{(2)}_{\text{n.i.}}$ which is asymptotically valid in the limit $kd \to \infty$. The first term is a result of the field scattered from sphere 1 of Figure 35 towards sphere 2, and then into the forward direction. Both a phase shift and an amplitude reduction are introduced by this second-order scattering. The second term represents the portion of the incident wave which is scattered first off sphere 2 towards sphere 1 and then into the forward direction. Further scattering orders, as the scattered waves bounce back and forth between the two spheres before being scattered into the forward direction, may easily be included; the result is:

$$\begin{aligned}\hat{S}^{(2)}_{\text{asym}} &= \left(\frac{1}{1-\left[S^{(1)}(\pi)e^{ikd}\,/-ikd\right]^2}\right) \times \\ &\quad \Bigg[\frac{1}{-ikd}\left\{[S^{(1)}(\alpha)]^2 e^{ikd(1-\cos\alpha)}\right\} \\ &\quad + \frac{1}{-ikd}\left\{[S^{(1)}(\pi-\alpha)]^2 e^{ikd(1+\cos\alpha)}\right\} \\ &\quad + \frac{1}{(-ikd)^2}\left\{2S^{(1)}(\alpha)S^{(1)}(\pi-\alpha)S^{(1)}(\pi)e^{2ikd}\right\}\Bigg] \qquad (36)\end{aligned}$$

where we have used

$$\frac{1}{1-x} = \sum_{n=0}^{\infty} x^n$$

to sum the infinite orders of scattering.

Even though the separation of the particles in Figure 40 starts from touching particles ($kd = 2ka = 0.2$), some of the features of the exact solution may be understood by considering the asymptotic model. The scattering amplitudes $|S^{(1)}_{\perp}(\beta)|$ and $|S^{(1)}_{\parallel}(\beta)|$ as a function of scattering angle β for Rayleigh particles are shown in Figure 41. The scattering amplitude for incident parallel polarization has the characteristic "figure 8" pattern of a dipole, with maxima in the forward and backward directions, while that for perpendicular polarization is isotropic. Thus to first order one might expect little dependence of $Q^{(2)}$ on α for the perpendicular case and significant dependence for the parallel case. In addition, one would expect the curves for the two polarizations to look similar for $\alpha = 0$, as the scattering patterns coincide in that direction. In fact it will always be the case that $S_{\parallel}^{(2)}(0) = S_{\perp}^{(2)}(0)$, due to the rotational symmetry of the endfire incidence case. All of these characteristics are evident in Figure 40. Interestingly, however, there is significant interaction for the incident wave polarized parallel to the scattering plane for $\alpha = 90°$, while the simple asymptotic model would predict little interaction due to the null in the scattering pattern at that angle. This is due most probably to the fact that when $kd \ll 1$, near-field components of the dipole field dominate, and there is a maximum of such field in the direction $\alpha = 90°$ (Ramo, *et al.*, 1965), and $\hat{S}^{(2)}_{\text{asym}}$ becomes an inadequate characterization of the interaction.

Because exact scattering computations for two spheres can be significantly time consuming, as Table 10 indicates, it is useful to determine conditions for applicability of the simple asymptotic model. Even though the asymptotic model does not completely characterize coherent coupling effects in all cases, it is conceptually and computationally advantageous to express the exact extinction quantities as a sum of the corresponding asymptotic quantity and a residual term. Here we show the *residual* perturbations to Q_{Mie}, $(Q^{(2)} - \hat{Q}^{(2)}_{\text{asym}})/Q^{(2)}_{\text{n.i.}}$, where $\hat{Q}^{(2)}_{\text{asym}}$ is defined by

$$\hat{Q}^{(2)}_{\text{asym}} = \frac{4}{(ka)^2}\text{Re}\{\hat{S}^{(2)}_{\text{asym}}\}.$$

The deviation of these curves from unity shows the portion of the extinction behavior of two spheres which *cannot* be explained by the simple asymptotic model. Figure 42 shows the result for the small particle of size $ka = 0.1$ which was considered in Figure 40. Clearly, for this very small particle case, the asymptotic model is a poor predictor for the coupling effects, as the curves of Figure 42 do not differ perceptibly from those of Figure 40. The asymptotic model is more successful for larger particles, however, as we discuss below.

Figure 43 shows the behavior of $Q^{(2)}/Q^{(2)}_{\text{n.i.}}$ and $P^{(2)}/Q^{(2)}$ for a particle of size $ka = 1.0$ as the separation is increased from $kd = 2$ (touching) to $kd = 10$. Differences from unity are substantial. For this size particle, there is significant coherent coupling for all three incidence angles. Conspicuously, there are oscillations in both $P^{(2)}$ and $Q^{(2)}$ as a function of separation distance. These may be interpreted as fringes which result from the interference of the wave scattered by only one sphere with the wave scattered from one sphere towards the other and then toward the observer. As may be seen in Eq. 35, the approximation to the scattered signal includes two oscillatory components,

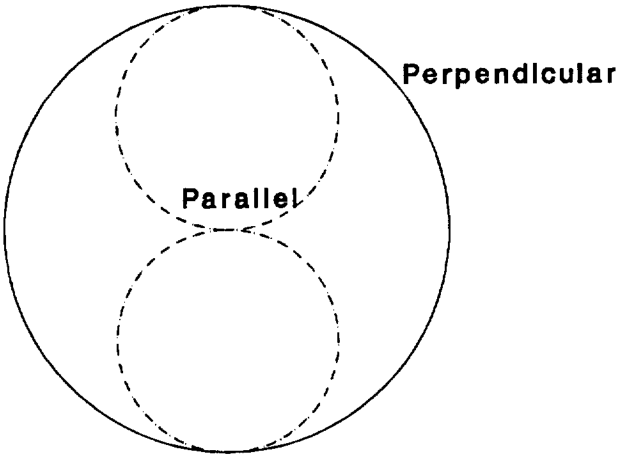

FIG. 41: Scattering diagram $|S(\beta)|$, where β is the scattering angle, of an isolated particle in the Rayleigh regime ($ka = 0.1$) with refractive index $m = 1.78 + 0.10i$, for parallel and perpendicular incident electric fields. The field is incident from below as in Figure 35.

one with a period of $kd = (2\pi)/(1 - \cos\alpha)$ and one with a period $kd = (2\pi)/(1 + \cos\alpha)$. Therefore for $\alpha = 0°$, we would expect to see a single oscillatory component with period $kd = \pi$, while for $\alpha = 90°$ we would expect to see an oscillatory component of period $kd = 2\pi$. This is evident in Figure 43, though the fact that the oscillations do not have zero mean is an indication of more complicated coupling effects than predicted by the simple asymptotic model. (The addition of the higher order scattering terms in Eq. 36 makes no significant difference to the oscillatory behavior of the solution.) These oscillations are not observed for the small particles in Figure 40 because the coupled field strength becomes negligible before the particles are separated by a large enough distance to interfere.

Figure 44 shows the residual perturbation to Q_{Mie} obtained for the parameters of Figure 43. Interestingly, most of the oscillations are removed through this procedure, leaving relatively small residuals, particularly for the case of perpendicular polarization. Note, however, that for the case of parallel polarization and $\alpha = 90°$, the subtraction of the asymptotic expression makes little change to the curves. This is due to the fact that, for this size particle, there is a null in the scattering diagram close to 90° for parallel polarization, and thus the computed asymptotic term is almost

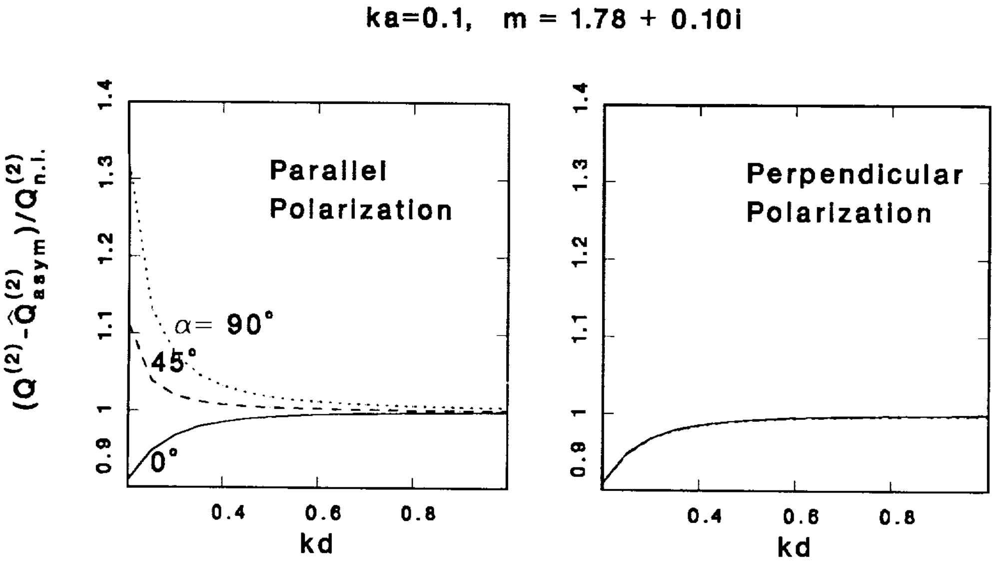
ka=0.1, m = 1.78 + 0.10i

FIG. 42: $(Q^{(2)}-\hat{Q}^{(2)}_{\rm asym})/Q^{(2)}_{\rm n.i.}$ for a pair of spheres of size $ka = 0.1$, refractive index $m = 1.78+0.10i$, as the spacing kd is varied from 0.2 to 1.0. This figure is intended to show residual coherent coupling effects after the simple model for interaction discussed in the text is removed. No difference is seen between these curves and the curves for $Q^{(2)}/Q^{(2)}_{\rm n.i.}$ shown in Figure 40, indicating that the interaction is strongly controlled by close coupling effects. See caption of Figure 40 for further details.

zero. Clearly, interaction effects exist which depend on near rather than far fields. Figure 44 shows that the simple model can be used effectively for this size particle to predict the coupling effect of two particles once they are separated by more than about four radii. When they are closer than this, the behavior needs to be computed using the exact solution. Figure 45 shows the scattering diagram for this size particle.

Figure 46 shows curves for a particle of size $ka = 5$. For spheres this large, the interference oscillations are evident as short period variations in $Q^{(2)}$ and $P^{(2)}$. However, these are superimposed on variations significantly larger which cannot be explained with this simple interference model. In this case, the sensitivity of coupling effects to the incidence angle is clear. For $\alpha = 45°$ and $90°$, coherent coupling effects are already small when the particles are separated by just four radii. However, for the endfire incidence case ($\alpha = 0°$), there are persistent differences from the non-interacting particles solution of 5–10% for kd as large as 50, *i.e.*, 10 radii. This may be interpreted as persistent shadowing of the second particle by the first. We expect that shadowing would become negligible when the first particle fills a space much less than a Fresnel zone when viewed from the second. In that event, the incident plane wave would effectively have filled in the shadow left by the front particle. Since the radius of the first Fresnel zone is given by $\sqrt{\lambda d/2}$, where d is the distance

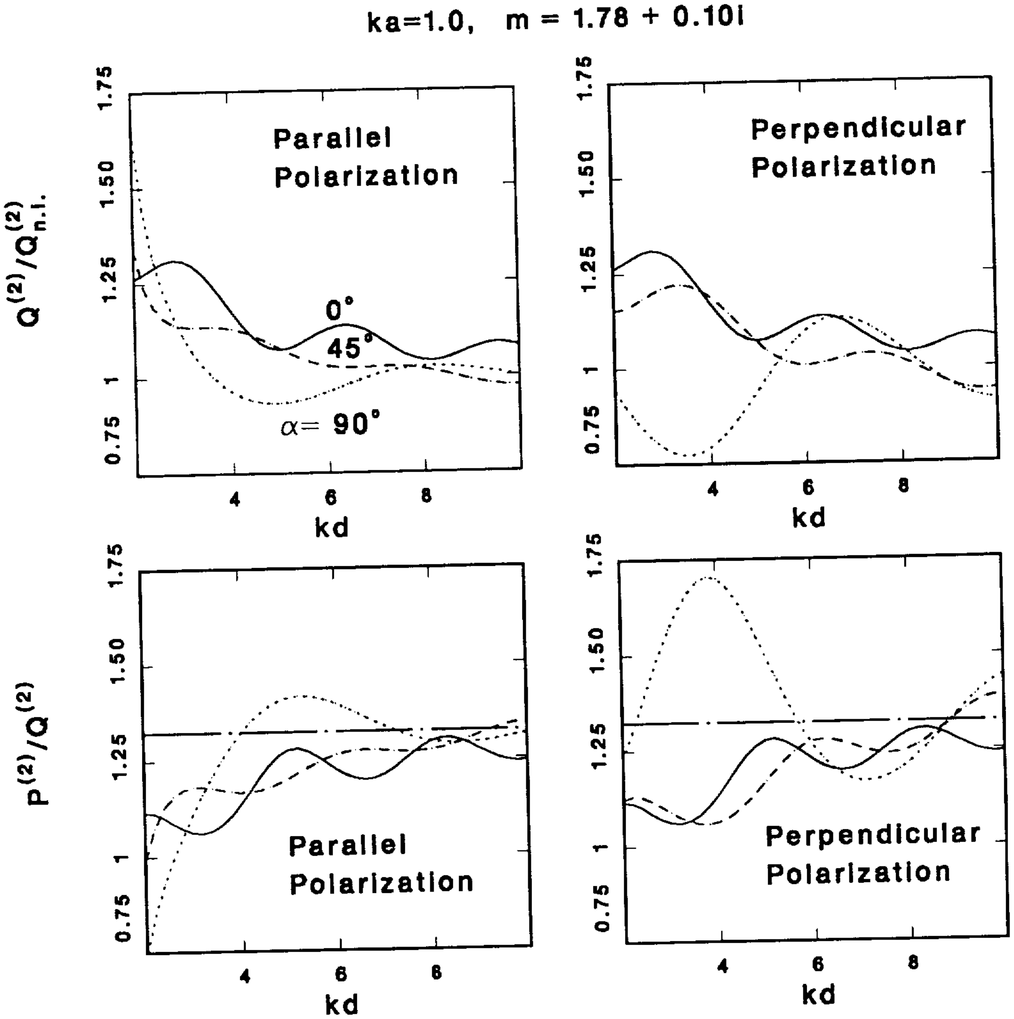

FIG. 43: $Q^{(2)}/Q^{(2)}_{\mathrm{n.i.}}$ and $P^{(2)}/Q^{(2)}$ for a pair of particles of size $ka = 1.0$ and refractive index $m = 1.78 + 0.10i$, as the separation is varied from touching ($kd = 2.0$) to $kd = 10.0$. The left-hand panels are for parallel incident polarization, the right-hand panels for perpendicular polarization. In the lower panels, the horizontal line at ~ 1.32 is the constant ratio $P^{(2)}_{\mathrm{n.i.}}/Q^{(2)}_{\mathrm{n.i.}}$ for non-interacting particles.

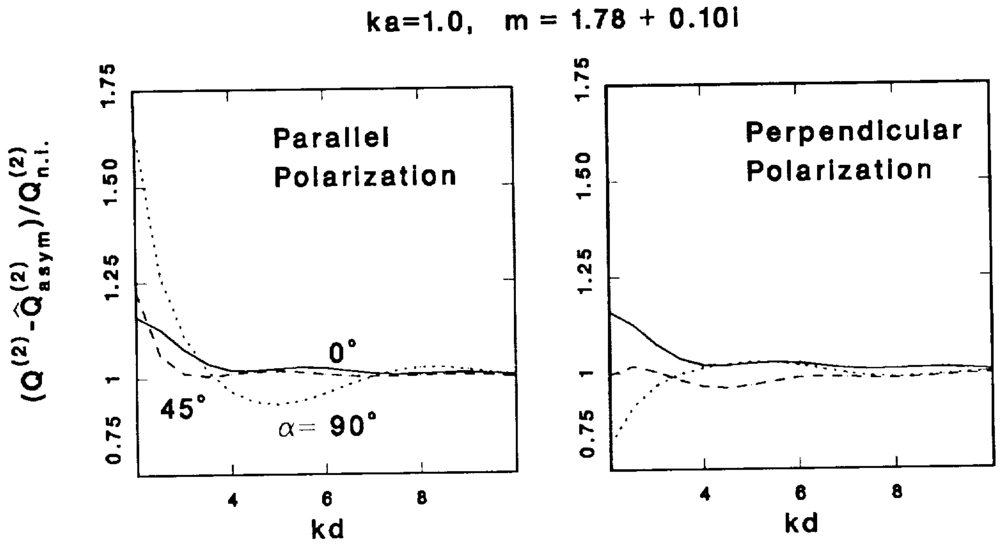

FIG. 44: $(Q^{(2)}-\hat{Q}^{(2)}_{\mathrm{asym}})/Q^{(2)}_{\mathrm{n.i.}}$ for a pair of spheres of size $ka = 1.0$, refractive index $m = 1.78+0.10i$, as the spacing kd is varied from 2.0 to 10.0. This figure is intended to show residual coherent coupling effects after the simple model for interaction discussed in the text is removed. Notice how most of the oscillations seen in Figure 43 have been significantly smoothed by the removal of the simple scattering model predictions.

of the second particle from the first, this requirement implies that, for large particles, shadowing will be insignificant when

$$\sqrt{\lambda d/2} \gg a,$$

or equivalently,

$$kd \gg (ka)^2.$$

Thus, the larger the particle, the more persistent is the shadowing measured in units of the particle radius. For a particle of size $ka = 5$, this relationship requires that the separation be significantly larger than $kd \simeq 25$, which appears to be borne out by the curves in Figure 46. We have investigated further the qualitative behavior of the persistence of shadowing, and find that $kd \gtrsim 2(ka)^2$, or,

$$d \gtrsim 10a^2/\lambda \qquad (37)$$

provides an adequate criterion for determining the minimum separation necessary for shadowing effects to be negligible. Note that, for a particle of this size, there is little dependence of the extinction behavior on the polarization of the incident wave.

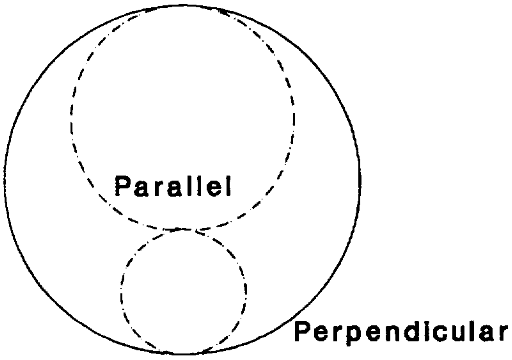

FIG. 45: Scattering diagram $|S(\beta)|$, where β is the scattering angle, of an isolated particle with size in the resonance region ($ka = 1.0$) and refractive index $m = 1.78 + 0.10i$ for parallel and perpendicular incident electric fields. The field is incident from below as in Figure 35.

Figure 47 shows the residual extinction after the asymptotic terms are subtracted. The small scale oscillations due to interference are removed, but most of the coupling remains, particularly for the endfire incidence case. The physical reason for the large effects in the endfire incidence case as compared to the $\alpha = 45°$ and $\alpha = 90°$ cases may be found in the far-field scattering diagram, shown in Figure 48. For a particle this large, the strongest scattering is in the near-forward direction, where the scattering behavior is not strongly dependent on polarization.

To summarize, we find that, for small particles ($ka = 0.1$), coherent interactions become negligible as the particles are separated by more than one radius. The asymptotic model does not seem to be a good model in this case. For a particle in the resonance size range ($ka = 1$), coherent interactions persist for all orientations to a separation of about 10 radii, and the asymptotic model captures much of the coupling behavior, particularly for separations greater than about 4 radii. Quite notably, there is no shadowing (decrease in extinction) for such size particles in the endfire configuration. For large particles ($ka = 5$), the asymptotic model fails to capture significant coherent interactions, particularly for geometries when shadowing is significant.

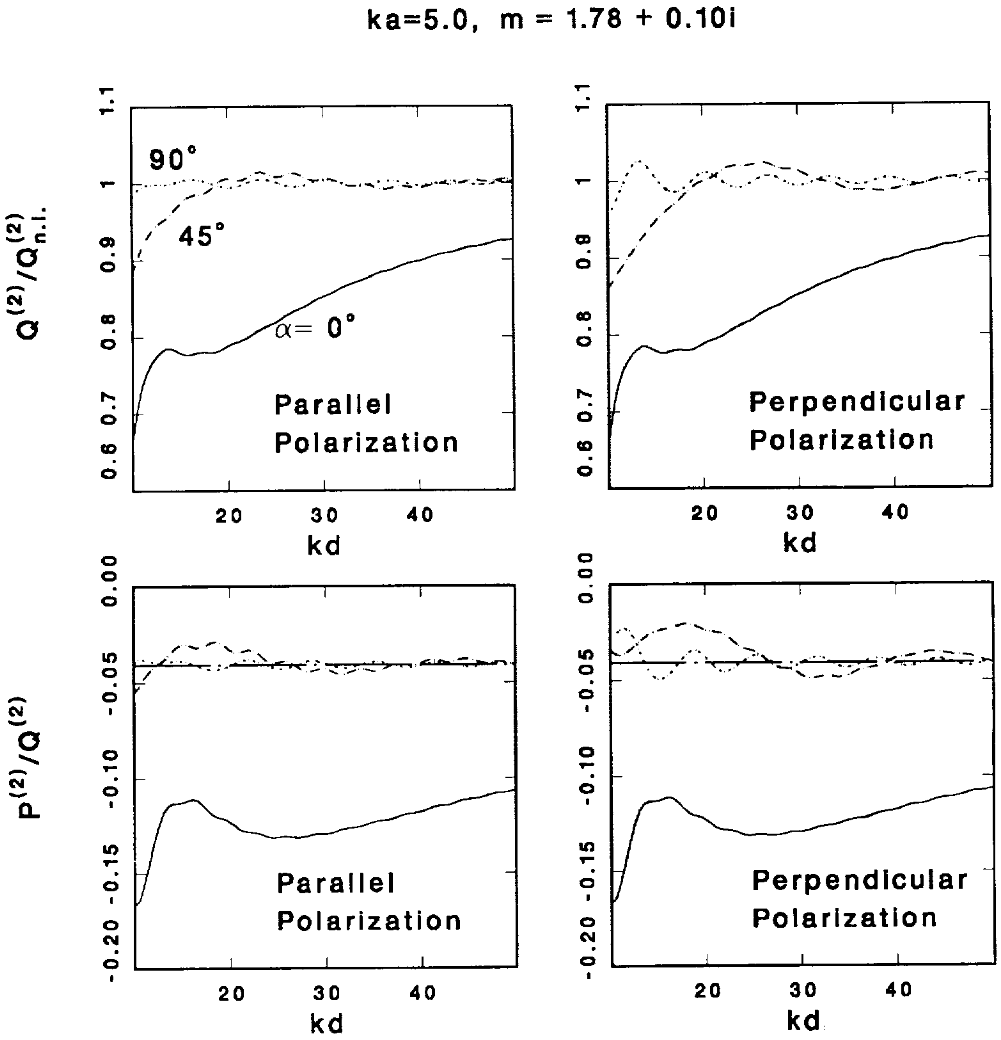

FIG. 46: $Q^{(2)}/Q^{(2)}_{\mathrm{n.i.}}$ and $P^{(2)}/Q^{(2)}$ for a pair of spheres of size $ka = 5.0$ and refractive index $m = 1.78 + 0.10i$, as the spacing kd is varied from touching ($kd = 10.0$) to $kd = 50.0$. The left-hand panels are for parallel incident polarization, the right-hand panels for perpendicular polarization. In the lower panels, the horizontal line at ~ -0.04 is the constant value $P^{(2)}_{\mathrm{n.i.}}/Q^{(2)}_{\mathrm{n.i.}}$ for non-interacting particles. Note the relatively weak dependence of extinction on polarization.

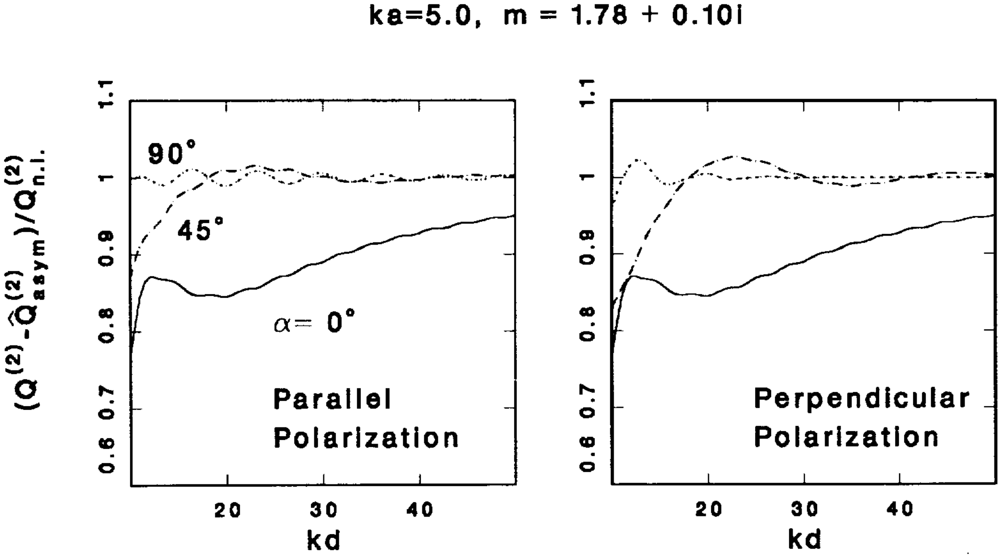

FIG. 47: $(Q^{(2)}-\hat{Q}^{(2)}_{\rm asym})/Q^{(2)}_{\rm n.i.}$ for a pair of spheres of size $ka = 5.0$, refractive index $m = 1.78+0.10i$, as the spacing is varied from touching ($kd = 10.0$) to $kd = 50.0$. This figure is intended to show residual coherent coupling effects after the simple model for interaction discussed in the text is removed. Shorter period oscillations present in Figure 46 are removed by this procedure, but significant differences from unity remain, particularly for the $\alpha = 0$ endfire incidence case, where significant shadowing is observable. Note the relatively weak dependence of extinction on polarization.

Figures 40–46 have been computed assuming lossy particles ($m = 1.78+0.10i$). For comparison, Figures 49–51 show similar results for a very lossy refractive index $m = 1.70 + 0.70i$. The behavior of the curves as a function of size ka and separation distance kd closely follows the behavior of the curves for the less lossy case. Comparing Figures 40 and 49 for $ka = 0.1$ shows that there is no perceptible difference between the $Q^{(2)}/Q^{(2)}_{\rm n.i.}$ curves for such small particles; the $P^{(2)}/Q^{(2)}$ curves have different absolute values, but the qualitative behavior is quite similar. More significant differences become apparent for particle size $ka = 1.0$, shown in Figures 43 and 50. Deviations of both $Q^{(2)}$ and $P^{(2)}/Q^{(2)}$ from the non-interacting case are much smaller for the case of the very lossy refractive index. This is probably because absorption effects significantly reduce the strength of waves participating in the multiple scattering process. The dependence of coherent effects on the orientation angle α is roughly the same for the two refractive indices. For particles of size $ka = 5$ (Figures 46 and 51), we have returned to a situation where the degree of refractive index loss has little effect on the interaction between the particles. Presumably this is because when particles are large enough, *any* small loss in the refractive index causes the absorption cross section to become almost half the extinction cross section. The other half represents energy diffracted in the near-forward direction. This behavior is independent of the exact loss factor. However, noticeable differences in

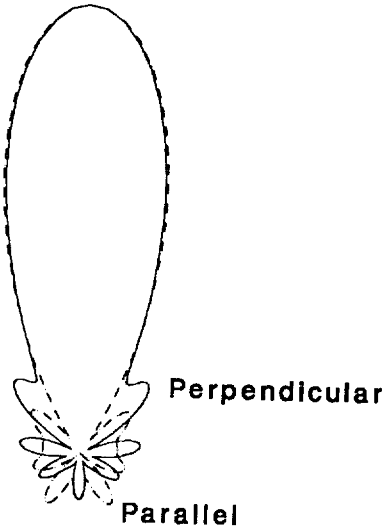

FIG. 48: Scattering diagram $|S(\beta)|$, where β is the scattering angle, of a large, isolated particle ($ka = 5.0$) with refractive index $m = 1.78 + 0.10i$ for parallel and perpendicular incident electric fields. The field is incident from below as in Figure 35.

the phase behavior persist for the $\alpha = 0^\circ$ case, especially for near-touching geometry, as is evident in the lower panels of Figures 46 and 51.

5.1.4 Averaging over scattering angle

It is useful to characterize the average coherent coupling between a pair of particles when their relative orientation is varied over 4π solid angle. In order to accomplish this it is necessary to introduce a fixed reference coordinate system, as is shown in Figure 52. The z-axis in this case is along the incidence direction (wave vector $\mathbf{k}$). The angle between the line connecting the spheres and the incidence direction $\mathbf{k}$ is denoted by α, as in Figure 35. The angle ϕ in Figure 52 determines the orientation of the pair in the plane orthogonal to $\mathbf{k}$. Our previous formulation of the scattering problem above assumed a fixed reference plane containing the incident wave vector $\mathbf{k}$ and the centers of the two particles. For changing orientations, this plane will vary, and thus the polarization of the incident wave needs now to be referenced to the fixed coordinate system. In Figure 52, two arbitrarily orthogonal unit vectors $\hat{p}$ and $\hat{q}$ in the plane orthogonal to $\mathbf{k}$ can be used to represent the

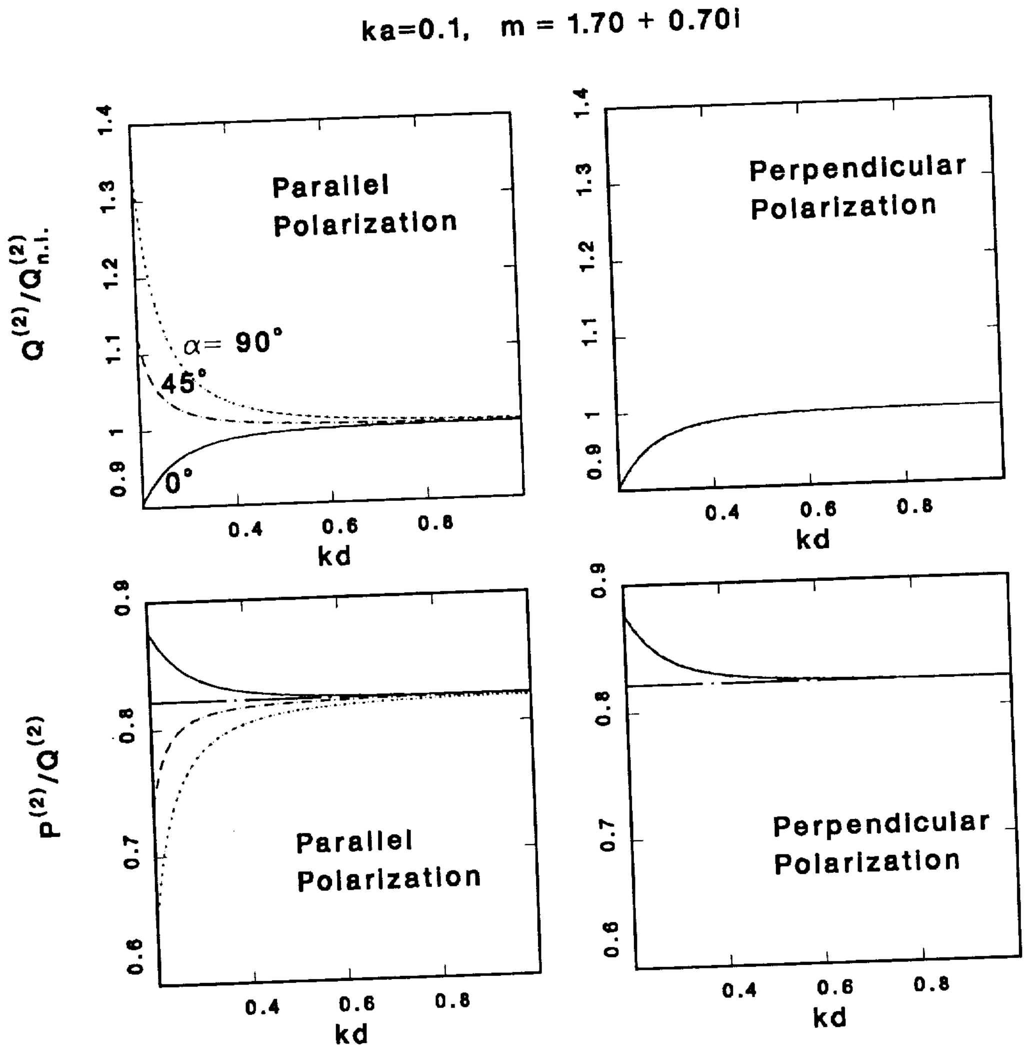

FIG. 49: $Q^{(2)}/Q^{(2)}_{\rm n.i.}$ and $P^{(2)}/Q^{(2)}$ for a pair of spheres of size $ka = 0.1$ and refractive index $m = 1.70 + 0.70i$, as the spacing kd is varied from touching ($kd = 0.2$) to $kd = 1.0$. The left-hand panels are for parallel incident polarization, the right-hand panels for perpendicular polarization. In the bottom panels, the horizontal line at ~ -0.04 is the non-interacting solution $P^{(2)}_{\rm n.i.}/Q^{(2)}_{\rm n.i.}$.

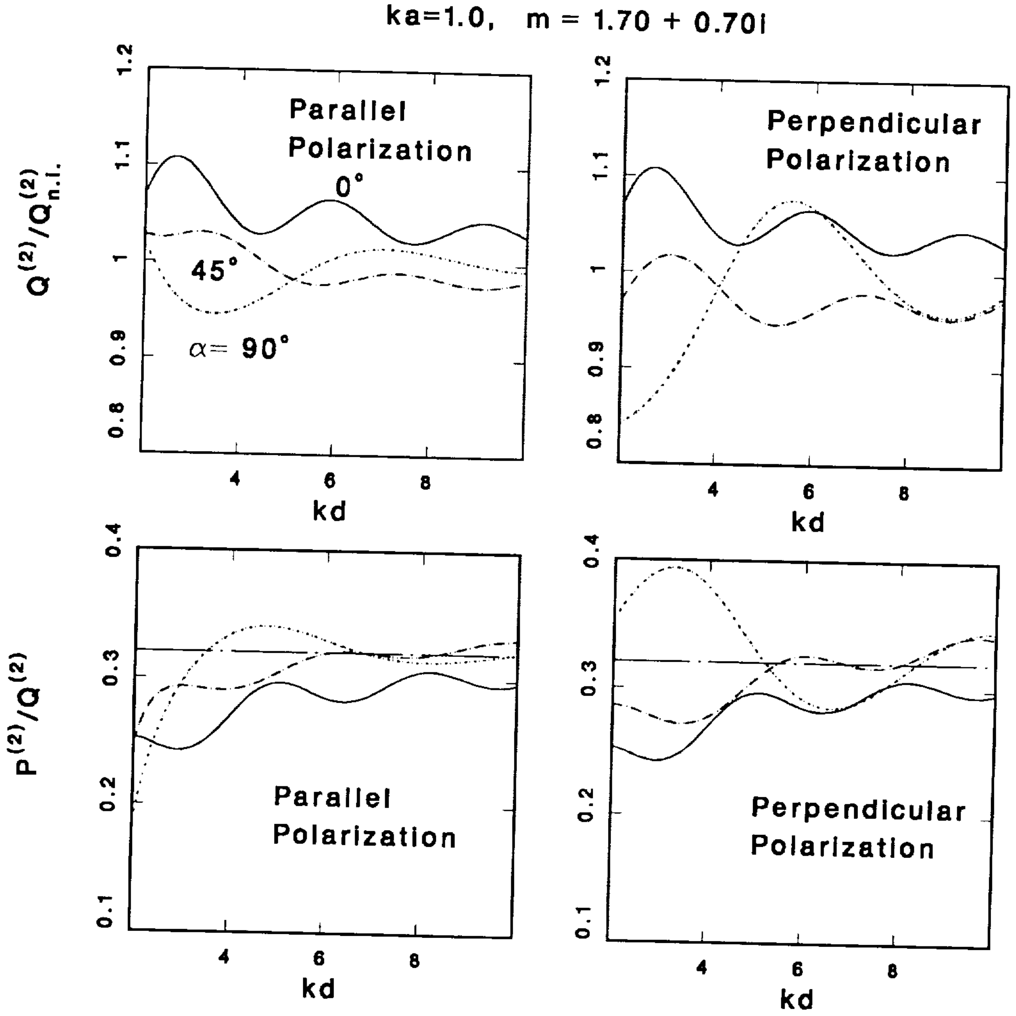

FIG. 50: $Q^{(2)}/Q^{(2)}_{\rm n.i.}$ and $P^{(2)}/Q^{(2)}$ for a pair of spheres of size $ka = 1.0$ and refractive index $m = 1.70 + 0.70i$, as the spacing kd is varied from touching ($kd = 2.0$) to $kd = 10.0$. The left-hand panels are for parallel incident polarization, the right-hand panels for perpendicular polarization. In the bottom panels, the horizontal line at ~ 0.32 is the constant ratio $P^{(2)}_{\rm n.i.}/Q^{(2)}_{\rm n.i.}$ for non-interacting particles.

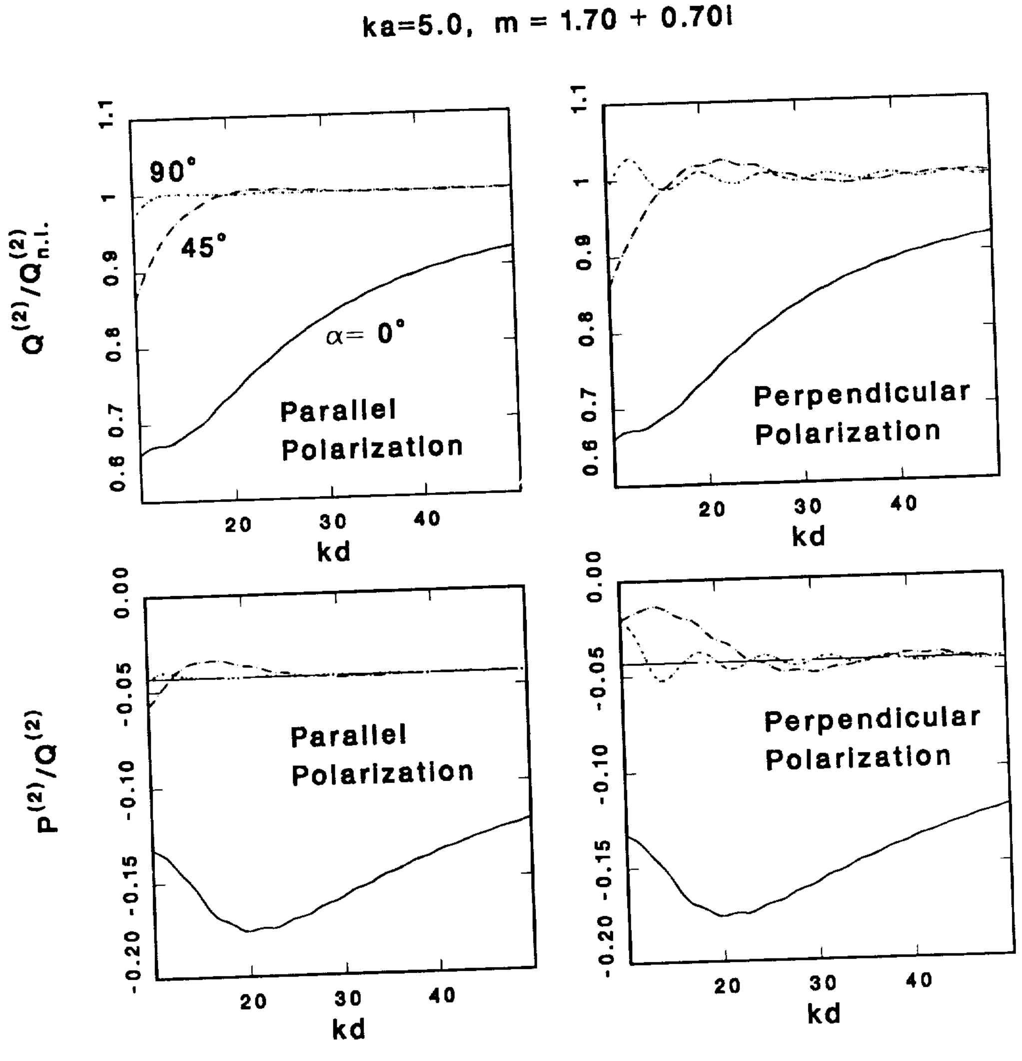

FIG. 51: $Q^{(2)}/Q^{(2)}_{\mathrm{n.i.}}$ and $P^{(2)}/Q^{(2)}$ for a pair of spheres of size $ka = 5.0$ and refractive index $m = 1.70 + 0.70i$, as the spacing kd is varied from touching ($kd = 10.0$) to $kd = 50.0$. The left-hand panels are for parallel incident polarization, the right-hand panels for perpendicular polarization. In the bottom panels, the horizontal line at ~ -0.04 is the constant ratio $P^{(2)}_{\mathrm{n.i.}}/Q^{(2)}_{\mathrm{n.i.}}$ for non-interacting particles.

two orthogonal polarization components of the incident field ($\hat{q} \times \hat{p} = \hat{k}$). The p and q components of the exact forward scattered electric field in the fixed frame can be written therefore as

$$\begin{bmatrix} E_{ps} \\ E_{qs} \end{bmatrix} = \frac{e^{ik(r-z)}}{-ikr} \begin{bmatrix} \cos\phi & -\sin\phi \\ \sin\phi & \cos\phi \end{bmatrix} \begin{bmatrix} S_{\parallel}^{(2)}(0,\alpha) & 0 \\ 0 & S_{\perp}^{(2)}(0,\alpha) \end{bmatrix} \begin{bmatrix} \cos\phi & \sin\phi \\ -\sin\phi & \cos\phi \end{bmatrix} \begin{bmatrix} E_{pi} \\ E_{qi} \end{bmatrix},$$

where the i and s subscripts refer to the incident and scattered fields, as in Chapter 4. Thus

$$\begin{aligned} \begin{bmatrix} E_{ps} \\ E_{qs} \end{bmatrix} &= \frac{e^{ik(r-z)}}{-ikr} \times \\ & \begin{bmatrix} S_{\parallel}^{(2)}(0,\alpha)\cos^2\phi + S_{\perp}^{(2)}(0,\alpha)\sin^2\phi & (S_{\parallel}^{(2)}(0,\alpha) - S_{\perp}^{(2)}(0,\alpha))\sin\phi\cos\phi \\ (S_{\parallel}^{(2)}(0,\alpha) - S_{\perp}^{(2)}(0,\alpha))\sin\phi\cos\phi & S_{\parallel}^{(2)}(0,\alpha)\sin^2\phi + S_{\perp}^{(2)}(0,\alpha)\cos^2\phi \end{bmatrix} \begin{bmatrix} E_{pi} \\ E_{qi} \end{bmatrix}. \end{aligned}$$

In order to obtain the average fields for a given sphere separation, we assume uniform distribution in solid angle, hence integrate over ϕ and α to obtain

$$\begin{aligned} < E_{ps} > &= \frac{e^{ik(r-z)}}{-ikr}\frac{1}{4\pi}\int_0^{\pi} d\alpha \sin\alpha \int_0^{2\pi} d\phi \left(S_{\parallel}^{(2)}(0,\alpha)\cos^2\phi + S_{\perp}^{(2)}(0,\alpha)\sin^2\phi \right) E_{pi} \\ < E_{qs} > &= \frac{e^{ik(r-z)}}{-ikr}\frac{1}{4\pi}\int_0^{\pi} d\alpha \sin\alpha \int_0^{2\pi} d\phi \left(S_{\parallel}^{(2)}(0,\alpha)\sin^2\phi + S_{\perp}^{(2)}(0,\alpha)\cos^2\phi \right) E_{pi}, \end{aligned}$$

where $< \cdot >$ indicates an average over α and ϕ. The cross-polarization terms disappear in the integration over ϕ. Implicitly, $S_{\perp}^{(2)}(0,\alpha)$ and $S_{\parallel}^{(2)}(0,\alpha)$ are also functions of ka, kd, and the refractive index m. Then we may define

$$\begin{bmatrix} < E_{ps} > \\ < E_{qs} > \end{bmatrix} = \frac{e^{ik(r-z)}}{-ikr} \begin{bmatrix} < S_p(0) > & 0 \\ 0 & < S_q(0) > \end{bmatrix} \begin{bmatrix} E_{pi} \\ E_{qi} \end{bmatrix}$$

and obtain

$$< S_q(0) > = < S_p(0) > = \frac{1}{4}\int_0^{\pi} d\alpha \sin\alpha \left[S_{\perp}^{(2)}(0,\alpha) + S_{\parallel}^{(2)}(0,\alpha) \right],$$

where the integration over ϕ has been performed. The corresponding average efficiency factors are given by

$$\begin{aligned} < Q^{(2)} > &= \frac{1}{2(ka)^2}\int_0^{\pi} d\alpha \sin\alpha \left[\mathrm{Re}\{ S_{\perp}^{(2)}(0,\alpha) + S_{\parallel}^{(2)}(0,\alpha) \} \right] && (38) \\ < P^{(2)} > &= \frac{1}{4(ka)^2}\int_0^{\pi} d\alpha \sin\alpha \left[\mathrm{Im}\{ S_{\perp}^{(2)}(0,\alpha) + S_{\parallel}^{(2)}(0,\alpha) \} \right]. && (39) \end{aligned}$$

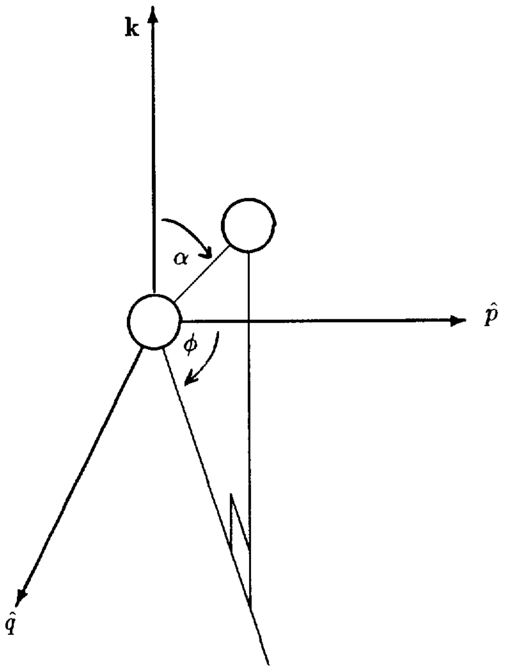

FIG. 52: General coordinate system for arbitrary positioning of pairs of spheres. If more than one pair of spheres is to be considered, the coordinate system in Figure 35 can no longer be used. Here we define a pair of orthogonal unit vectors $(\hat{p}, \hat{q})$ which we use to reference the direction of the electric field of the incident wave. The vector connecting the pair of particles is then defined by its length and by the angles α and ϕ as shown.

Figures 53–55 show the normalized average values $< Q^{(2)}/Q^{(2)}_{\rm n.i.} >$ and $< P^{(2)}/Q^{(2)} >$ for the same particle sizes investigated in Section 5.1.3. Values are computed at increments in α of 5° and then interpolated to increments of 0.05° for the integration, which depends on $\sin\alpha$ as Eqs. 38 and 39 show. These step sizes were found to result in an error of less than 0.05% in practice.

For a particle of size $ka = 0.1$, when averaged over all possible orientation angles, there is a net increase in the extinction efficiency over that of noninteracting particles. The peak value is for the touching case and is $\sim 4\%$. Figure 40 shows that, while small particles may either increase or decrease the extinction (depending on the orientation), angles closer to 90° than to 0° contribute more significantly to the average due to the $\sin\alpha$ term in the integration, leading to a net overall increase in extinction. For a particle of size $ka = 1.0$ (Figure 54), we find a similar net increase in extinction efficiency and a net decrease in the normalized phase efficiency. The peak extinction is again for the touching geometry and is about 25% larger than for noninteracting particles. Finally, for the case of a particle of size $ka = 5.0$, we find that coherent effects exhibit the opposite behavior, *i.e.*, they reduce the extinction efficiency by almost 10% when the particles are touching. In all three cases, the average extinction approaches the value for noninteracting particles to within $\sim 1\%$ when kd exceeds $\sim 5ka$.

In order to qualitatively investigate the asymptotic behavior of extinction as ka becomes very large, we also performed a similar average over orientation for a particle twice as large as the particle in Figure 55. The result is shown in Figure 56. Interestingly, the overall behavior of this $ka = 10$ case is very similar to that of $ka = 5$ when the separation kd is normalized by ka. This suggests that the results have converged, and further results for much larger particles can be obtained through simple geometric scaling.

5.2 Coherent Scattering by an Assembly of Spheres

As indicated earlier, the computational demands of solving the problem of scattering by more than one sphere are severe. Even the problem of only two spheres presents an enormous increase in computation time over that of Mie theory. If one were to try and compute the scattering of a large number of spheres through the exact method outlined above, the problem would become completely unmanageable. Thus practical computational issues force one to find a way of incorporating coherent scattering effects without solving the exact problem.

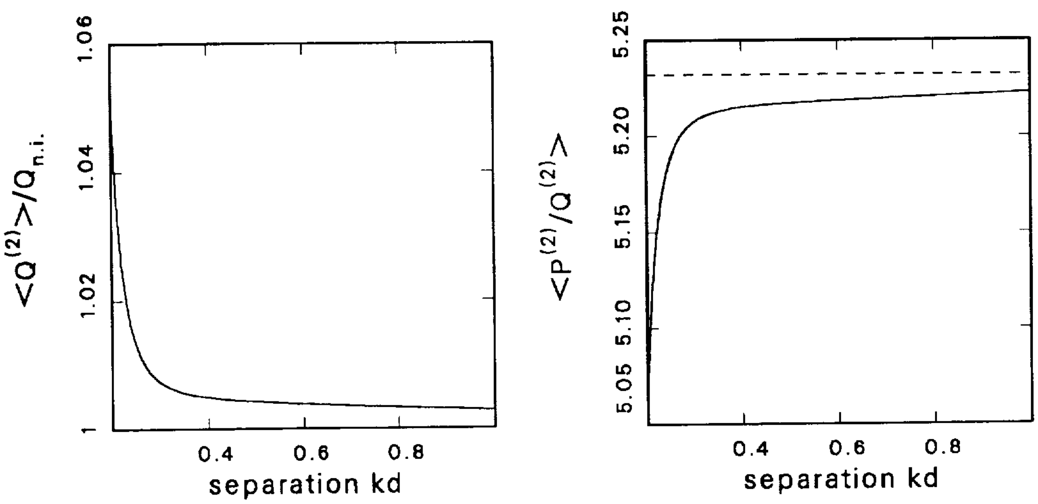

FIG. 53: $< Q^{(2)} > /Q^{(2)}_{\rm n.i.}$ and $< P^{(2)}/Q^{(2)} >$ for a particle of size $ka = 0.1$ as kd is varied from touching ($kd = 0.2$) to a separation $kd = 1.0$. $< >$ indicates an average over 4π. Refractive index $m = 1.78 + 0.10i$. See text for averaging step sizes. The dashed line in the right hand panel represents the constant ratio $P^{(2)}_{\rm n.i.}/Q^{(2)}_{\rm n.i.}$ for the non-interacting solution. Average $Q^{(2)}$ is enhanced relative to $Q^{(2)}_{\rm n.i.}$ for all separations, but is significantly different from $Q^{(2)}_{\rm n.i.}$ only when the particles are closer than about 3 radii. The right-hand panel shows that the average of $P^{(2)}/Q^{(2)}$ is very slightly decreased (*i.e.*, less phase delay) relative to $P^{(2)}_{\rm n.i.}/Q^{(2)}_{\rm n.i.}$ for separations $\lesssim 3$ radii.

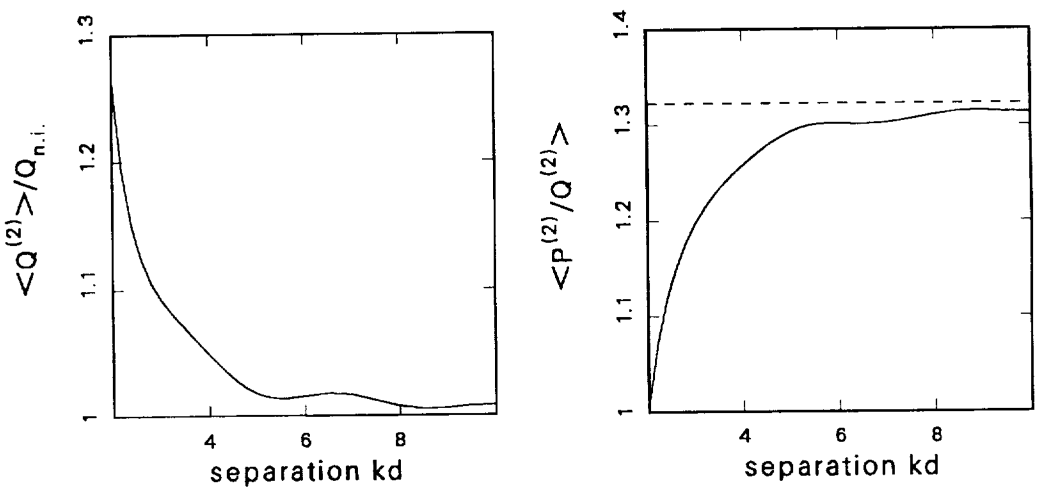

FIG. 54: $< Q^{(2)} > /Q^{(2)}_{\rm n.i.}$ and $< P^{(2)}/Q^{(2)} >$ for a particle of size $ka = 1.0$ as kd is varied from touching ($kd = 2.0$) to a separation $kd = 10.0$. $< >$ indicates an average over 4π. Refractive index $m = 1.78+0.10i$. See text for averaging step sizes. The dashed line in the right-hand panel represents the constant ratio $P^{(2)}_{\rm n.i.}/Q^{(2)}_{\rm n.i.}$ for the non-interacting solution. Average $Q^{(2)}$ is significantly enhanced relative to $Q^{(2)}_{\rm n.i.}$ for separations less than about 4 radii. Average $P^{(2)}/Q^{(2)}$ is decreased relative to $P^{(2)}_{\rm n.i.}/Q^{(2)}_{\rm n.i.}$ (less phase delay) for similar separations; note the much larger effect on $P^{(2)}_{\rm n.i.}/Q^{(2)}_{\rm n.i.}$ relative to the case $ka = 5$ below.

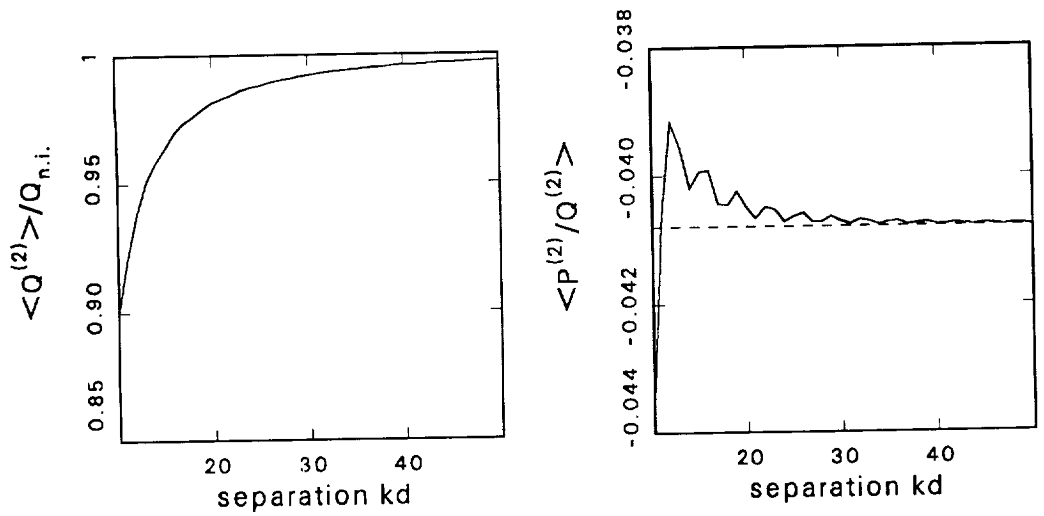

FIG. 55: $< Q^{(2)} > /Q^{(2)}_{\text{n.i.}}$ and $< P^{(2)}/Q^{(2)} >$ for a particle of size $ka = 5.0$ as kd is varied from touching ($kd = 10.0$) to a separation $kd = 50.0$. $< >$ indicates an average over 4π. Refractive index $m = 1.78 + 0.10i$. The dashed line in the right-hand panel represents the constant ratio $P^{(2)}_{\text{n.i.}}/Q^{(2)}_{\text{n.i.}}$ for the non-interacting solution. There is a decrease in $< Q^{(2)} >$ as compared to $Q^{(2)}_{\text{n.i.}}$ of more than 5% for separations less than approximately 3 radii, though differences of more than 1% persist up to at least 8 radii. The effect on $< P^{(2)} >$ is much smaller, as the right hand panel shows.

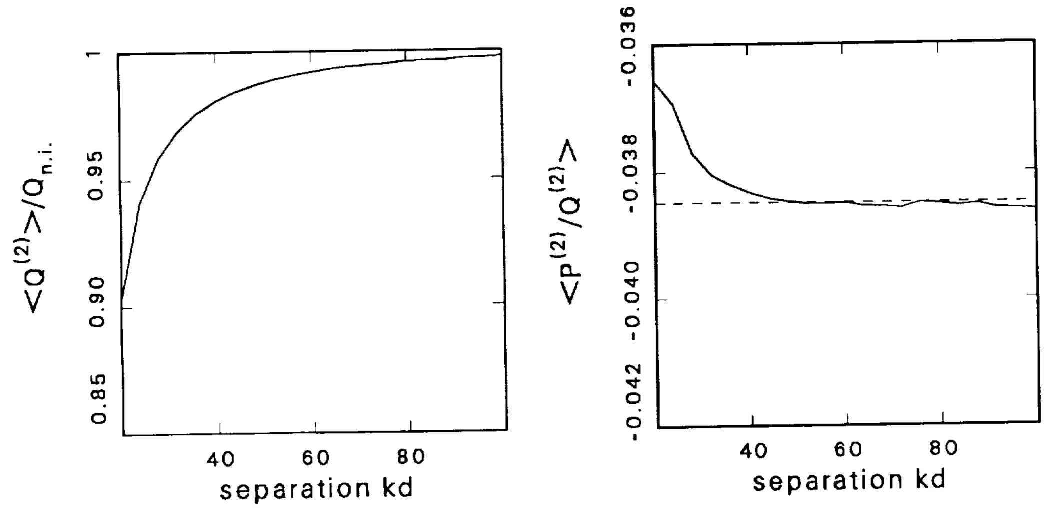

FIG. 56: $< Q^{(2)} > /Q^{(2)}_{\text{n.i.}}$ and $< P^{(2)}/Q^{(2)} >$ for a particle of size $ka = 10.0$ as kd is varied from touching ($kd = 20.0$) to a separation $kd = 100.0$. $< >$ indicates an average over 4π. Refractive index $m = 1.78 + 0.10i$. The dashed line in the right hand panel represents the constant ratio $P^{(2)}_{\text{n.i.}}/Q^{(2)}_{\text{n.i.}}$ for the non-interacting solution. Note the marked similarity to the scattering behavior of a particle half as large, shown in Figure 55.

5.2.1 The pairwise approximation

One approach is to incorporate only the pairwise coherent effects computed using the exact two-sphere solution described above. In this model, each particle interacts coherently with every other particle in its neighborhood, but higher order interactions are neglected. For example, for a set of three particles, the interactions between particles 1 and 2, between particles 2 and 3 and between particles 1 and 3 will be considered, but not the effect of 1 on 3 via 2, etc. Mathematically, for the three particle case we may write

$$\begin{aligned} S_{12}^{(2)} &= S_1^{(1)} + S_2^{(1)} + \delta_{12} \\ S_{23}^{(2)} &= S_2^{(1)} + S_3^{(1)} + \delta_{23} \\ S_{13}^{(2)} &= S_1^{(1)} + S_3^{(1)} + \delta_{13}, \end{aligned} \tag{40}$$

where $S_{ij}^{(2)}$, $(i \neq j)$ is the scattering amplitude $S^{(2)}$ for the pair of particles i and j, computed from the exact two-particle scattering solution, and $S_i^{(1)}$ is the single-particle result computed from the Mie solution. The δ_{ij} terms indicate the portion of the forward scattering amplitude which can be attributed to coherent coupling. These terms may be found by computing $S^{(2)}$ using the exact method and subtracting the Mie solutions from it. While not explicitly indicated, the value of S is polarization-dependent. The approximate total scattering amplitude for the three spheres is written as

$$\tilde{S}^{(3)} \simeq S_1^{(1)} + S_2^{(1)} + S_3^{(1)} + \delta_{12} + \delta_{13} + \delta_{23}.$$

It is not necessary to include any extra phase terms in adding the scattering amplitudes from the three pairs of spheres because we are computing effects in the exact forward direction.

Similarly, for a cluster of N particles, the approximate scattering amplitude is

$$\tilde{S}^{(N)} = \sum_{i=1}^{N} \left[S_i^{(1)} + \sum_{j>i}^{N} \delta_{ij} \right]. \tag{41}$$

We refer to this solution as the pairwise approximation. Implicit in this formulation is the assumption that the most important coherent coupling effects are captured in the interaction between pairs of spheres, and that higher-order scattering effects may be neglected. Below, we investigate the accuracy of this assumption by computing the *exact* scattering amplitude of three spheres and comparing the result to the approximate result using combinations of pairs of spheres. The size of the spheres considered is limited by computational demands of the three-sphere program to be less than $ka \simeq 4$. However, as discussed below, a more specialized algorithm can handle larger spheres if they are constrained to lie along a line.

5.2.2 Regular clusters of spheres

We consider first regular clusters of three spheres and compute the non-interacting scattering amplitude, $S^{(3)}_{\text{n.i.}}$, the exact scattering amplitude using the three-sphere program, $S^{(3)}$, and the approximate scattering amplitude of three spheres using the pairwise approximation, $\tilde{S}^{(3)}$. For the three sphere case, there is no longer a natural definition of $\hat{e}_\perp$ and $\hat{e}_\parallel$, as there was for the two-sphere case. Thus, we may arbitrarily choose an orthogonal set of vectors to represent the two polarization directions. In computing $\tilde{S}^{(3)}$, there are intermediate steps of computing the forward scattering amplitude for each pair of spheres. In these steps, it is important to add up the polarization properly, as described in Section 5.1.4. The final result is the sum of the forward scattering amplitudes for the two chosen polarization directions. The arrangements considered are shown schematically in Figure 57 and are labeled *a*, *b*, *c*, and *d*. Cluster *a* is a broadside linear chain of three spheres, while cluster *b* is a triangular array of spheres in a plane containing the incident wave vector. Cluster *c* is an endfire linear chain of three spheres, and cluster *d* is a triangular array of spheres which lies in a plane perpendicular to the incident wave vector.

Representative computational results are shown in Figures 58–61, which display the normalized extinction efficiencies for different size spheres in each of the four clusters. In all configurations, the spheres are assumed to be touching so as to maximize the effects of coherent coupling. The refractive index used is $m = 1.78 + 0.10i$. The displayed quantities are $Q^{(3)}/Q^{(3)}_{\text{n.i.}}$, $\tilde{Q}^{(3)}/Q^{(3)}_{\text{n.i.}}$, $P^{(3)}/Q^{(3)}$, and $\tilde{P}^{(3)}/\tilde{Q}^{(3)}$, along with $P^{(3)}_{\text{n.i.}}/Q^{(3)}_{\text{n.i.}}$ for comparison. (The " ~ " indicates a quantity computed using the pairwise approximation.) Curves for the exact solution are shown with a dashed curve, and curves for the pairwise approximation are shown with a dotted curve.

In almost all cases, the exact solution for three spheres and the approximate solution agree to within a few percent. For example, in Figure 59, there is little difference between the dashed and dotted curves, even as both of these curves deviate significantly from unity, indicating substantial coherent coupling. This is true both for the Q_{ext} curves and the P_{ext} curves; in the latter case the dashed and dotted curves overlie one another closely. Similar agreement is also seen for clusters *b* and *d* (both triangular clusters) in Figures 59 and 61. However, Figure 60 shows that the endfire configuration causes more trouble for the pairwise approximation. For this case, the exact and

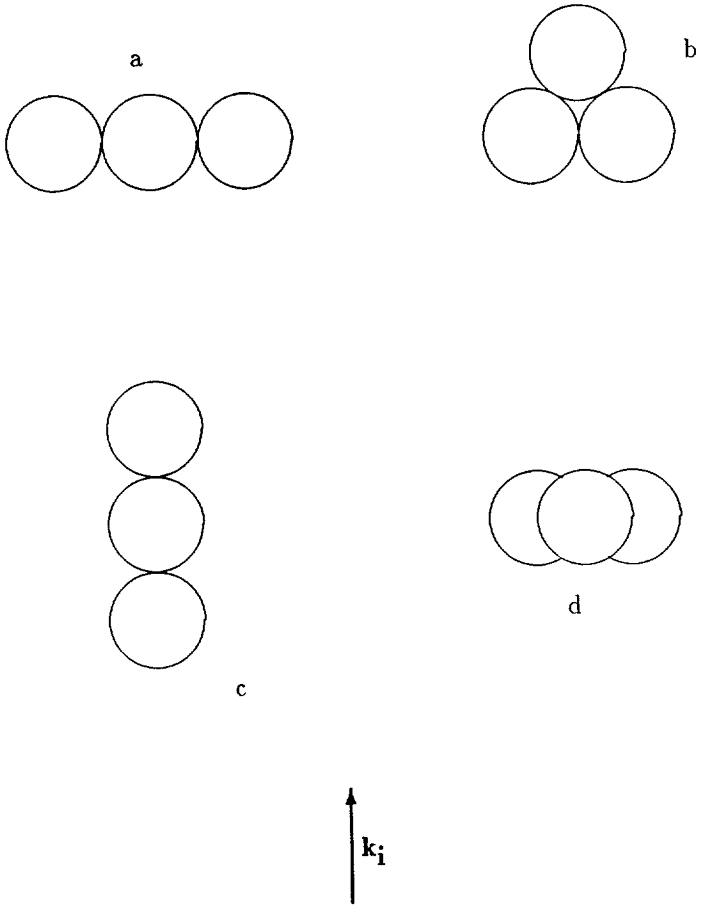

FIG. 57: Four regular clusters of three spheres used for the purposes of testing the pairwise approximation. The direction of the incident wave is shown; the scattered field is observed in the exact forward direction.

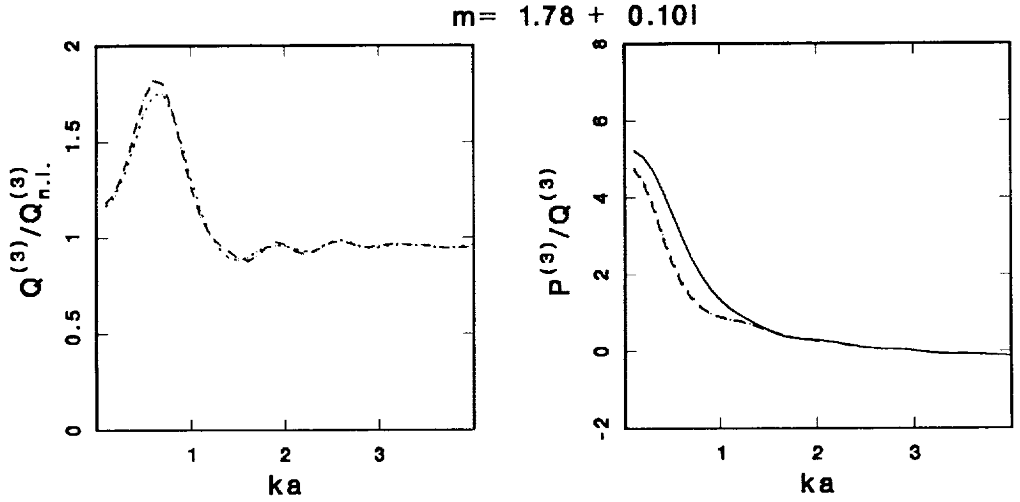

FIG. 58: Testing of the validity of the pairwise approximation for the broadside incidence case (cluster *a* of Figure 57). Refractive index $m = 1.78 + 0.10i$. Shown are curves for $Q^{(3)}/Q^{(3)}_{\text{n.i.}}$ and $P^{(3)}/Q^{(3)}$ (dashed curves) and $\tilde{Q}^{(3)}/Q^{(3)}_{\text{n.i.}}$ and $\tilde{P}^{(3)}/\tilde{Q}^{(3)}$ (dotted curves). In the right-hand panel, $P^{(3)}_{\text{n.i.}}/Q^{(3)}_{\text{n.i.}}$ is shown for comparison (solid line). For this configuration of the spheres, the pairwise approximation agrees with the exact solution to within a few percent.

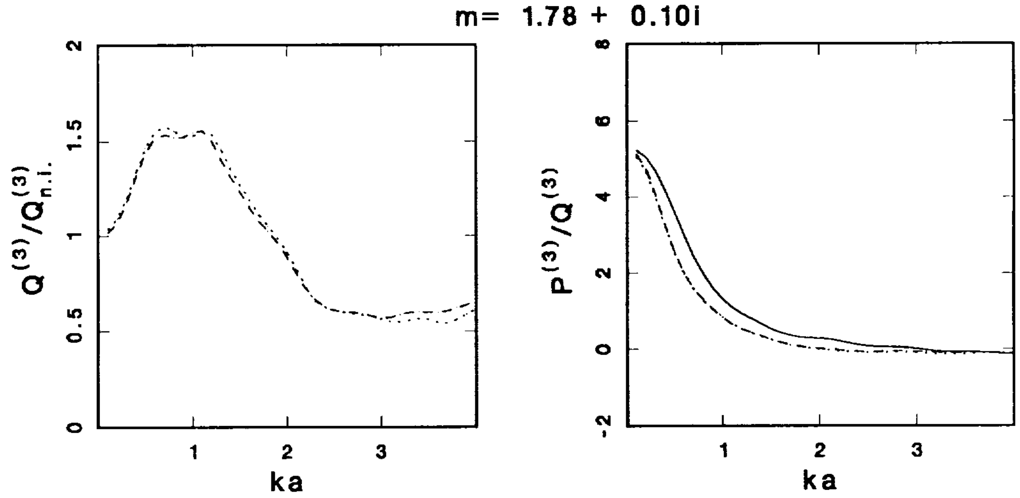

FIG. 59: Testing of the validity of the pairwise approximation for the in-line triangular cluster (case *b* of Figure 57). Refractive index $m = 1.78 + 0.10i$. Shown are curves for $Q^{(3)}/Q^{(3)}_{\text{n.i.}}$ and $P^{(3)}/Q^{(3)}$ (dashed curve) and $\tilde{Q}^{(3)}/Q^{(3)}_{\text{n.i.}}$ and $\tilde{P}^{(3)}/\tilde{Q}^{(3)}$ (dotted curves). In the right-hand panel, $P^{(3)}_{\text{n.i.}}/Q^{(3)}_{\text{n.i.}}$ is shown for comparison (solid line). For this configuration of the spheres, the pairwise approximation agrees with the exact solution to within a few percent.

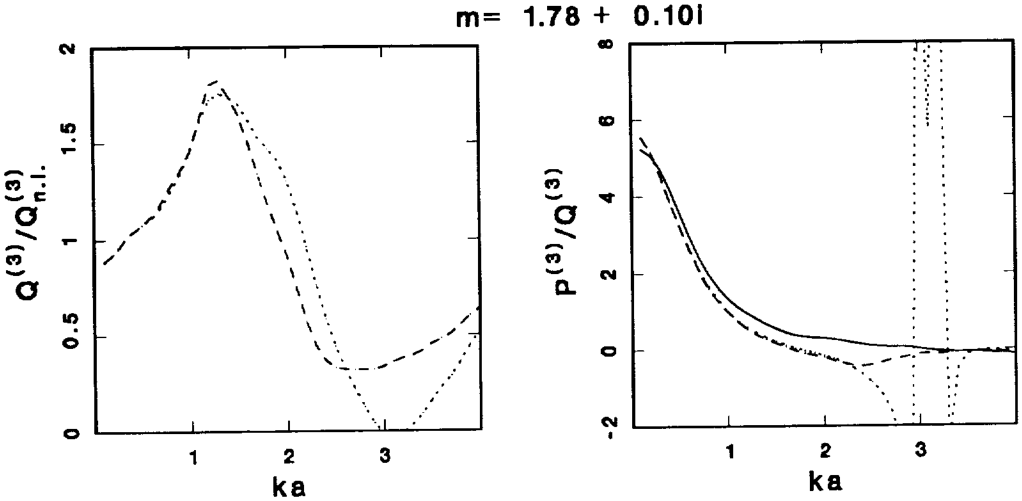

FIG. 60: Testing of the validity of the pairwise approximation for the endfire cluster (case *c* of Figure 57). Refractive index $m = 1.78 + 0.10i$. Shown are curves for $Q^{(3)}/Q^{(3)}_{\mathrm{n.i.}}$ and $P^{(3)}/Q^{(3)}$ (dashed curve) and $\tilde{Q}^{(3)}/Q^{(3)}_{\mathrm{n.i.}}$ and $\tilde{P}^{(3)}/\tilde{Q}^{(3)}$ (dotted curves). In the right-hand panel, $P^{(3)}_{\mathrm{n.i.}}/Q^{(3)}_{\mathrm{n.i.}}$ is shown for comparison (solid line). Differences between the exact solution for three spheres and the pairwise approximation are significant, particularly near $ka = 3$, where $\tilde{Q}^{(3)}$ is non-physically negative (resulting in rapid changes in the ratio $\tilde{P}^{(3)}/\tilde{Q}^{(3)}$). See text for further discussion.

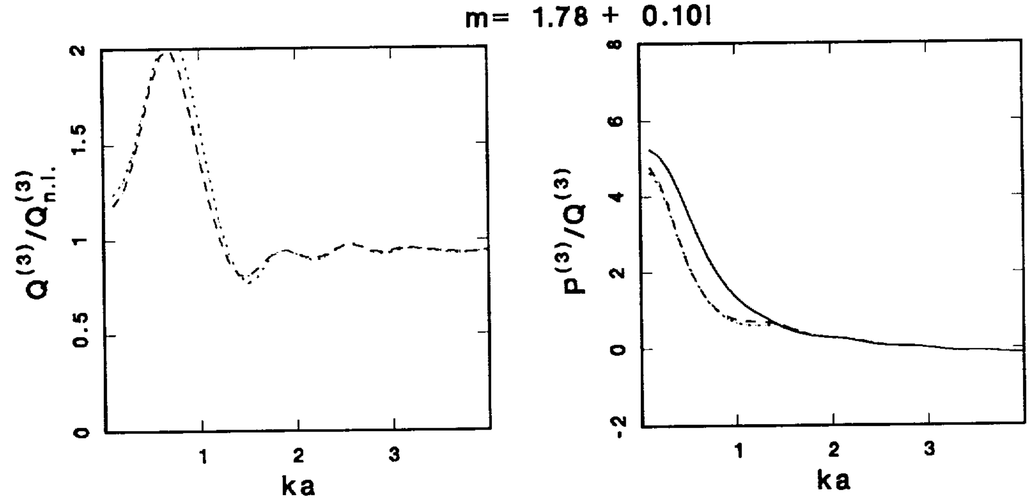

FIG. 61: Testing of the validity of the pairwise approximation for the perpendicular-triangular cluster (case *d* of Figure 57). Refractive index $m = 1.78 + 0.10i$. Shown are curves for $Q^{(3)}/Q^{(3)}_{\mathrm{n.i.}}$ and $P^{(3)}/Q^{(3)}$ (dashed curve) and $\tilde{Q}^{(3)}/Q^{(3)}_{\mathrm{n.i.}}$ and $\tilde{P}^{(3)}/\tilde{Q}^{(3)}$ (dotted curves). In the right-hand panel, $P^{(3)}_{\mathrm{n.i.}}/Q^{(3)}_{\mathrm{n.i.}}$ is shown for comparison (solid line). For this configuration, the pairwise agrees with the exact solution to within a few percent.

approximate curves diverge around $ka = 3$. In fact, $\tilde{Q}^{(3)}$ is seen to be negative in a certain size range, clearly a non-physical result. For the size range over which this occurs, the ratio $\tilde{P}^{(3)}/\tilde{Q}^{(3)}$ fluctuates wildly due to the changing sign of $\tilde{Q}^{(3)}$. The reason for this discrepancy is explored in more detail below.

To investigate the effect of the refractive index assumed, Figures 62–65 show the same quantities for a much more lossy refractive index $m = 1.70 + 0.70i$. The behavior is similar, though as we have seen in Figures 37 and 39, differences from Mie theory are generally reduced in magnitude. The discrepancy between $Q^{(3)}$ and $\tilde{Q}^{(3)}$ for the endfire incidence case (Figure 64) are also much smaller than for the case $m = 1.78 + 0.10i$ (Figure 60).

For completeness, we also report results for the lossless refractive index $m = 1.78 + 0.00i$; Figures 66–69. Conclusions similar to those discussed above for refractive indices $m = 1.78 + 0.10i$ and $m = 1.70 + 0.70i$ hold; however, note the change in the scale used for each figure. In Figures 66, 67, and 69, note how closely the pairwise approximation follows the exact solution. For a lossless refractive index, $P_{\text{ext}}/Q_{\text{ext}}$ grows without limit as particles become very small. There is a significant difference between the values obtained assuming noninteracting particles and the pairwise approximation; the latter remains in very good agreement with the exact solution, however. As for the case $m = 1.78 + 0.10i$, the pairwise approximation has difficulty with the endfire incidence case, particularly in the neighborhood of $ka = 3$.

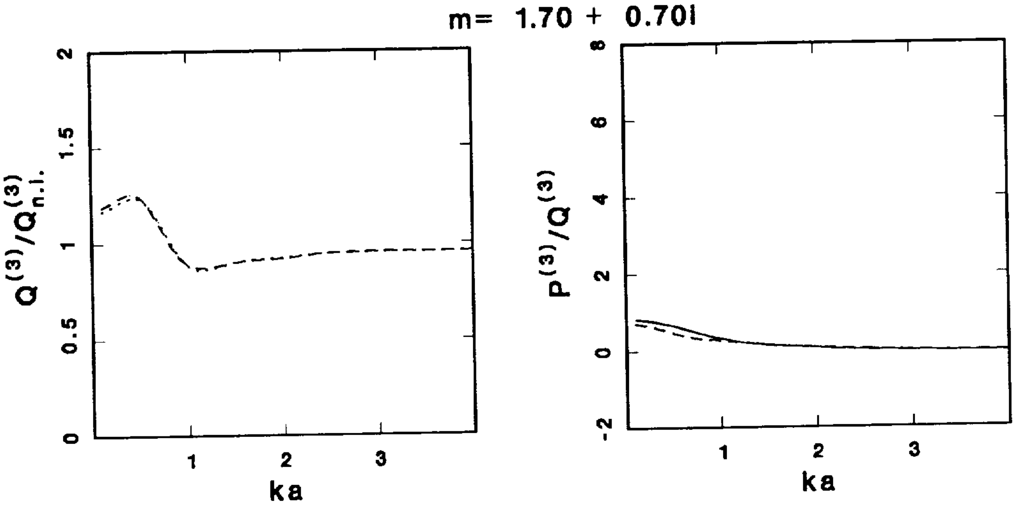

Fig. 62: Test of the validity of the pairwise approximation for the broadside cluster (case *a* of Figure 57). Refractive index $m = 1.70 + 0.70i$. Shown are curves for $Q^{(3)}/Q^{(3)}_{\text{n.i.}}$ and $P^{(3)}/Q^{(3)}$ (dashed curve) and $\tilde{Q}^{(3)}/Q^{(3)}_{\text{n.i.}}$ and $\tilde{P}^{(3)}/\tilde{Q}^{(3)}$ (dotted curves). In the right-hand panel, $P^{(3)}_{\text{n.i.}}/Q^{(3)}_{\text{n.i.}}$ is shown for comparison (solid line). For this configuration of the spheres, the pairwise approximation agrees with the exact solution to within a few percent.

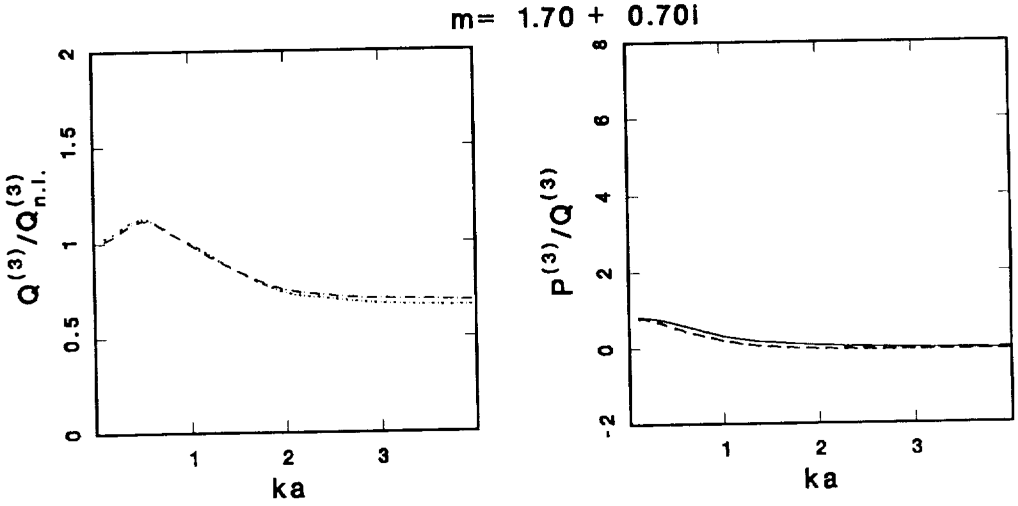

Fig. 63: Test of the validity of the pairwise approximation for the in-line triangular cluster (case *b* of Figure 57). Refractive index $m = 1.70 + 0.70i$. Shown are curves for $Q^{(3)}/Q^{(3)}_{\text{n.i.}}$ and $P^{(3)}/Q^{(3)}$ (dashed curve) and $\tilde{Q}^{(3)}/Q^{(3)}_{\text{n.i.}}$ and $\tilde{P}^{(3)}/\tilde{Q}^{(3)}$ (dotted curves). In the right-hand panel, $P^{(3)}_{\text{n.i.}}/Q^{(3)}_{\text{n.i.}}$ is shown for comparison (solid line). For this configuration of the spheres, the pairwise approximation agrees with the exact solution to within a few percent.

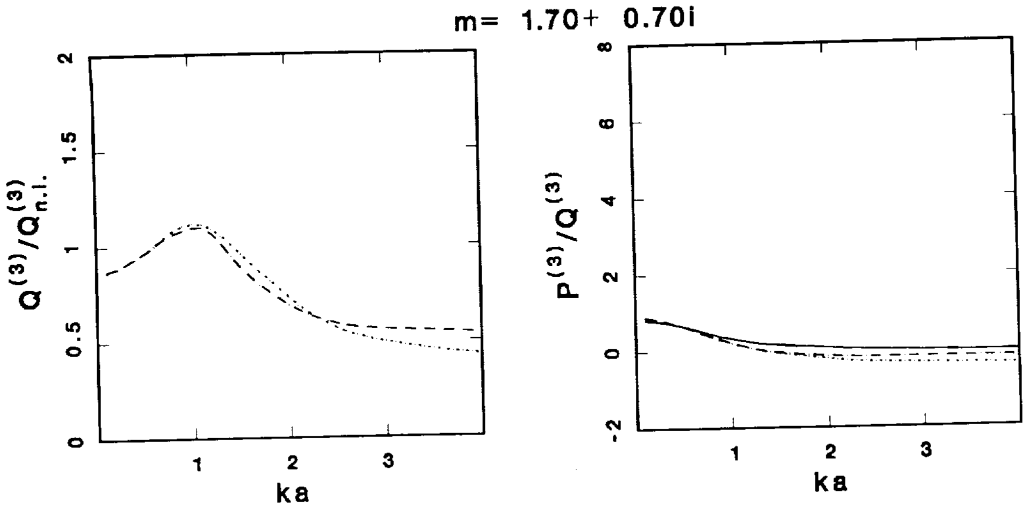

FIG. 64: Test of the validity of the pairwise approximation for the endfire cluster (case c of Figure 57). Refractive index $m = 1.70 + 0.70i$. Shown are curves for $Q^{(3)}/Q^{(3)}_{\text{n.i.}}$ and $P^{(3)}/Q^{(3)}$ (dashed curve) and $\tilde{Q}^{(3)}/Q^{(3)}_{\text{n.i.}}$ and $\tilde{P}^{(3)}/\tilde{Q}^{(3)}$ (dotted curves). In the right-hand panel, $P^{(3)}_{\text{n.i.}}/Q^{(3)}_{\text{n.i.}}$ is shown for comparison (solid line). Larger differences between the exact and the approximate solution are seen here than for other configurations, but the discrepancies are much smaller than for the corresponding configuration with a less lossy refractive index (Figure 60).

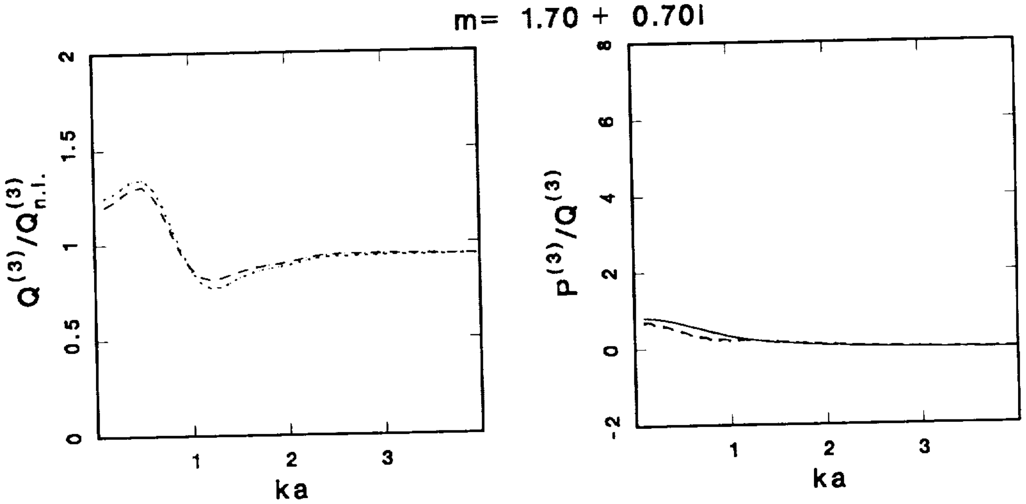

FIG. 65: Test of the validity of the pairwise approximation for the perpendicular-triangular cluster (case d of Figure 57). Refractive index $m = 1.70 + 0.70i$. Shown are curves for $Q^{(3)}/Q^{(3)}_{\text{n.i.}}$ and $P^{(3)}/Q^{(3)}$ (dashed curve) and $\tilde{Q}^{(3)}/Q^{(3)}_{\text{n.i.}}$ and $\tilde{P}^{(3)}/\tilde{Q}^{(3)}$ (dotted curves). In the right-hand panel, $P^{(3)}_{\text{n.i.}}/Q^{(3)}_{\text{n.i.}}$ is shown for comparison (solid line). For this configuration of the spheres, the pairwise approximation agrees with the exact solution to within a few percent.

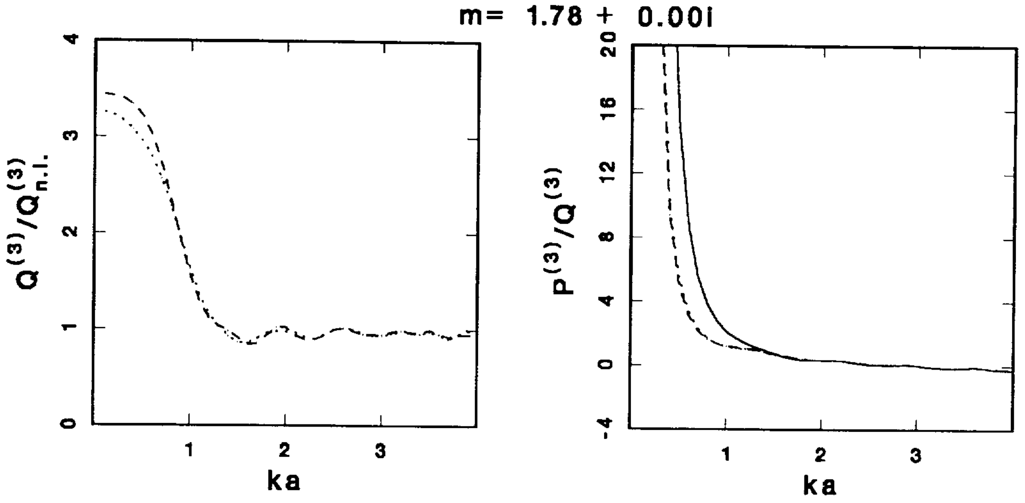

FIG. 66: Test of the validity of the pairwise approximation for the broadside cluster (case a of Figure 57). Lossless refractive index $m = 1.78+0.00i$. Shown are curves for $Q^{(3)}/Q^{(3)}_{\rm n.i.}$ and $P^{(3)}/Q^{(3)}$ (dashed curve) and $\tilde{Q}^{(3)}/Q^{(3)}_{\rm n.i.}$ and $\tilde{P}^{(3)}/\tilde{Q}^{(3)}$ (dotted curves). In the right-hand panel, $P^{(3)}_{\rm n.i.}/Q^{(3)}_{\rm n.i.}$ is shown for comparison (solid line). For this configuration of the spheres, the pairwise approximation agrees with the exact solution to within a few percent.

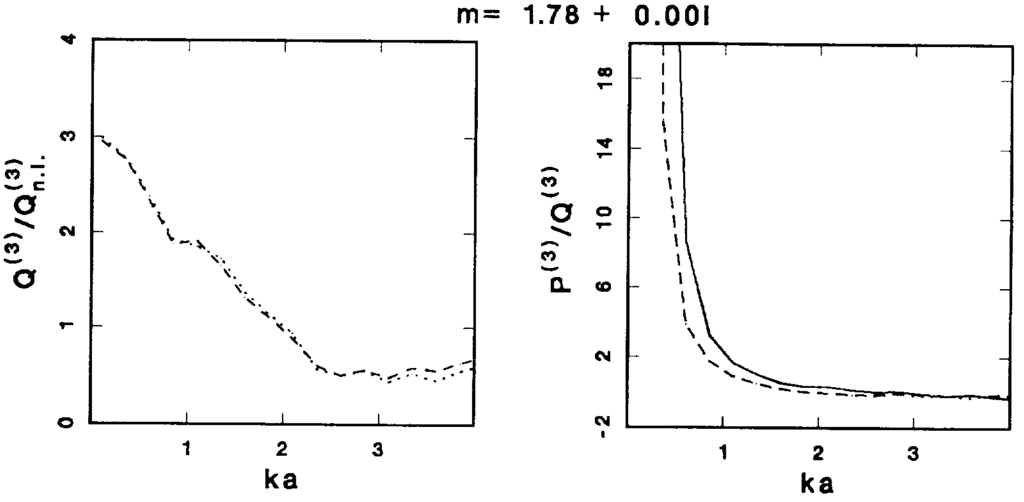

FIG. 67: Test of the validity of the pairwise approximation for the in-line triangular cluster (case b of Figure 57). Lossless refractive index $m = 1.78 + 0.00i$. Shown are curves for $Q^{(3)}/Q^{(3)}_{\rm n.i.}$ and $P^{(3)}/Q^{(3)}$ (dashed curve) and $\tilde{Q}^{(3)}/Q^{(3)}_{\rm n.i.}$ and $\tilde{P}^{(3)}/\tilde{Q}^{(3)}$ (dotted curves). In the right-hand panel, $P^{(3)}_{\rm n.i.}/Q^{(3)}_{\rm n.i.}$ is shown for comparison (solid line). For this configuration of the spheres, the pairwise approximation agrees with the exact solution to within a few percent.

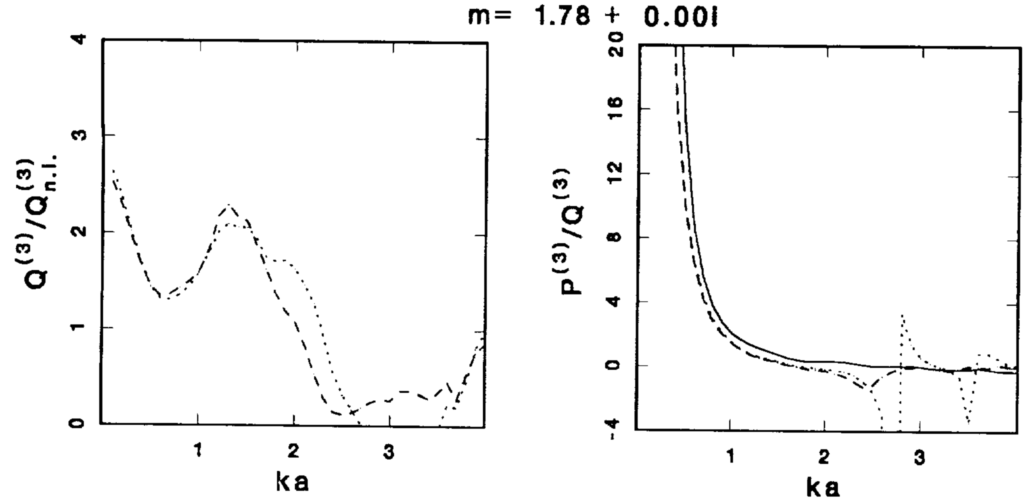

FIG. 68: Test of the validity of the pairwise approximation for the endfire cluster (case c of Figure 57). Lossless refractive index $m = 1.78 + 0.00i$. Shown are curves for $Q^{(3)}/Q^{(3)}_{\text{n.i.}}$ and $P^{(3)}/Q^{(3)}$ (dashed curve) and $\tilde{Q}^{(3)}/Q^{(3)}_{\text{n.i.}}$ and $\tilde{P}^{(3)}/\tilde{Q}^{(3)}$ (dotted curves). In the right-hand panel, $P^{(3)}_{\text{n.i.}}/Q^{(3)}_{\text{n.i.}}$ is shown for comparison (solid line). Once again, the endfire configuration causes the most difficulty for the pairwise approximation, and non-physical results are apparent in the neighborhood of $ka = 3$, where $\tilde{Q}^{(3)}$ is negative.

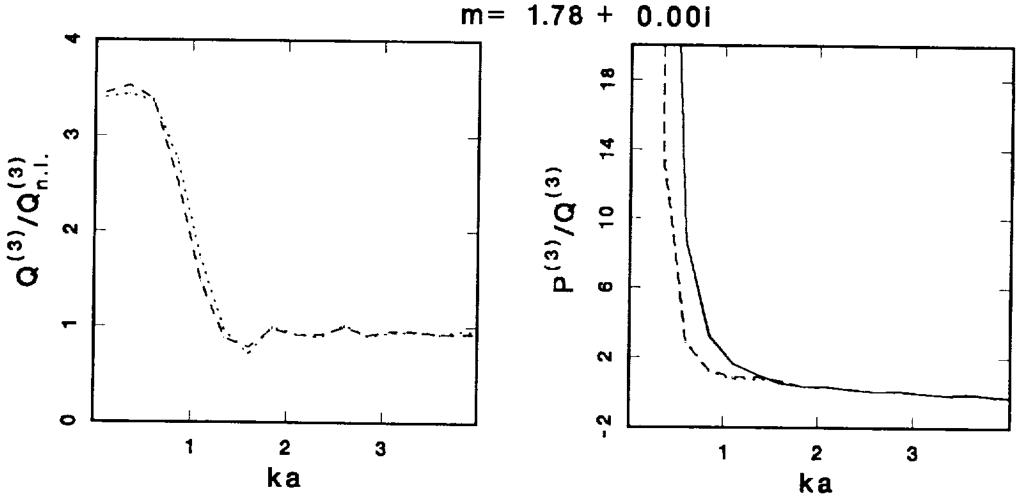

FIG. 69: Test of the validity of the pairwise approximation for the perpendicular-triangular cluster (case d of Figure 57). Lossless refractive index $m = 1.78+0.00i$. Shown are curves for $Q^{(3)}/Q^{(3)}_{\text{n.i.}}$ and $P^{(3)}/Q^{(3)}$ (dashed curve) and $\tilde{Q}^{(3)}/Q^{(3)}_{\text{n.i.}}$ and $\tilde{P}^{(3)}/\tilde{Q}^{(3)}$ (dotted curves). In the right-hand panel, $P^{(3)}_{\text{n.i.}}/Q^{(3)}_{\text{n.i.}}$ is shown for comparison (solid line). For this configuration of the spheres, the pairwise approximation agrees with the exact solution to within a few percent.

5.2.3 Behavior of very small particles

There are some aspects of the curves of Figures 58–69 which can be understood in simple physical terms. As particles become much smaller than a wavelength, their extinction cross section no longer depends on their shape, but only on their volume (Rayleigh scattering; *v.*, *e.g.*, Bohren and Huffman, 1983). This is because the incident wavefront reaches all parts of the scatterer essentially in phase. From the discussion in Section 4.2.1 for small particles,

$$\left.\begin{array}{rcl} \mathrm{Re}\{S^{(1)}\,(\mathrm{lossless})\} & \propto & a^6\lambda^{-6} \\ \mathrm{Re}\{S^{(1)}\,(\mathrm{lossy})\} & \propto & a^3\lambda^{-3} \\ \mathrm{Im}\{S^{(1)}\} & \propto & a^3\lambda^{-3} \end{array}\right\} \quad ka \rightarrow 0,$$

i.e., for lossless particles the real part of the scattering amplitude is proportional to the volume squared, while for lossy particles this quantity is simply proportional to the volume. We would thus expect that, for a closely packed collection of n very small lossless particles, the real part of the forward scattering amplitude would be n^2 times that of an individual particle. Since in Figures 58–69 all curves are normalized by $Q^{(n)}_{\mathrm{n.i.}}$, where $Q^{(n)}_{\mathrm{n.i.}} = nQ^{(1)}$, we might expect that, as the particles become small, $Q^{(3)}/Q^{(3)}_{\mathrm{n.i.}}$ would approach 3 when considering the problem of three lossless particles. In fact, this is approximately the case, as shown in Figures 66–69. For lossy particles, on the other hand, the real part of the scattering amplitude is proportional to volume rather than volume squared, so we would expect the ratio of $Q^{(3)}/Q^{(3)}_{\mathrm{n.i.}}$ to approach unity. Figures 58–65 show this to be the case as well.

Similarly, we may investigate the behavior of the P/Q curves in the Rayleigh limit. For both lossless and lossy particles, the imaginary part of the scattering amplitude is proportional to the volume. Therefore, for very small particles, the close packing of the particles should not affect the total imaginary part of the scattering amplitude. In this case, $P^{(3)}/Q^{(3)}$ asymptotically approaches $P^{(1)}/Q^{(1)}$, which for lossy particles is given by

$$\frac{P^{(3)}}{Q^{(3)}}\,(ka \rightarrow 0) \rightarrow \frac{P^{(1)}}{Q^{(1)}} = \frac{\mathrm{Re}\left[(m^2-1)/(m^2+2)\right]}{2\mathrm{Im}\left[(m^2-1)(m^2+2)\right]}.$$

For $m = 1.70 + 0.70i$ this value is 0.83; for $m = 1.78 + 0.10i$ it is 5.27. These values are in good agreement with the results in Figures 58–65. For lossless particles, P/Q systematically increases as the particles become very small, because Q decreases much more rapidly than P (see Figs. 66–69).

5.2.4 Endfire incidence and the shadowing behavior of large spheres

In the top half of Figure 60, comparison of the curves corresponding to the exact solution and the pairwise approximation shows that the two curves diverge around $ka = 3$. In fact, the pairwise approximation in some cases yields negative $\tilde{Q}^{(3)}$, which is unphysical. Reference to Figure 36 shows that the ratio $Q^{(2)}/Q^{(2)}_{\mathrm{n.i.}}$ has a prominent minimum near $ka = 3$. Therefore the pairwise interaction model appears to overestimate the interaction, resulting in a negative $\tilde{Q}^{(3)}$.

We may investigate this particular orientation in more detail using a specialized algorithm developed by Fuller (1987) for computing scattering by more than two spheres which are constrained to lie on a line. Due to the simplified geometry of this configuration, the translation-addition theorem of spherical harmonics can be adapted so as to reduce program array sizes significantly, and larger spheres than the previous limit of $ka = 4$ may be considered. Since the endfire incidence case is the most troubling from the standpoint of computing the extinction using the pairwise approximation, this simplification is extremely helpful.

Figure 70 compares the exact ratio $Q^{(5)}/Q^{(5)}_{\mathrm{n.i.}}$ to the pairwise approximation $\tilde{Q}^{(5)}/Q^{(5)}_{\mathrm{n.i.}}$ for *five* spheres in the endfire configuration, over a size range from $ka = 0.1$ to 8. Since the endfire incidence case is most sensitive to coherent effects, this is a severe test of the approximation.

First consider the left-hand panels, which show the results including all interactions between particles as described in Eq. 41. As for the case of three spheres, there is a negative value for $\tilde{Q}^{(5)}$ near $ka = 3$. From this point on, as ka increases, $\tilde{Q}^{(5)}$ remains significantly smaller than $Q^{(5)}$, often becoming smaller than zero. Clearly the pairwise approximation is having significant difficulty with this configuration.

Recall that Figures 36–39 showed that, for particles larger than approximately $ka = 5$, a simple geometric model of shadowing was a fairly accurate predictor of the total extinction of two particles. We may use this simple model to gain some insight into the reason for difficulties with the endfire configuration. The geometric shadowing model predicts that, for five particles in this configuration, the ratio $Q^{(5)}/Q^{(5)}_{\mathrm{n.i.}}$ should be approximately 0.2, as only the front particle is unshadowed. The pairwise interaction model, however, considers *all* of the interactions between every pair of particles—ten interactions in all. In considering each of these ten pairwise interactions, approximately one cross-sectional area will be removed through shadowing. Therefore it is not surprising that the pairwise approximation results in non-physical $\tilde{Q}^{(5)}$ for large particles. The question is how to improve the approximation. The problem results from assuming that particle 1 interacts with particle 5, even though particles 2, 3, and 4 lie between them. One possible solution is to consider *only* the interactions between adjacent pairs of particles, that is, between particles 1 and 2, 2 and 3, 3 and 4, and 4 and 5. Our simple model predicts that this will result in removal of approximately four cross-sectional areas due to shadowing, resulting in a final ratio of $\tilde{Q}^{(5)}/Q^{(5)}_{\text{n.i.}}$ of approximately 0.2. The right-hand panels of Figure 70 show the result of applying this modification of the pairwise approximation. Clearly, the agreement between $\tilde{Q}^{(5)}$ and $Q^{(5)}$ is greatly improved relative to the left-hand panels. Note that the ratio $Q^{(5)}/Q^{(5)}_{\text{n.i.}}$ approaches approximately 0.3 rather than the value of 0.2 predicted by the geometric model. Even so, the pairwise approximation with shadowing taken into account approaches essentially the same value as the exact solution. Therefore, it appears that the important issue of shadowing between particles must be carefully considered when using the pairwise approximation. The results of Section 5.2.2 showed that the nominal pairwise approximation worked very well when no more than two particles lay along the incidence direction. This is because *two-particle* shadowing effects are automatically included in the approximation. It is when more than two particles lie along this line that the approximation breaks down.

We may, for completeness, consider the case of a broadside arrangement of five spheres. Our previous work indicates that this arrangement should not cause the pairwise approximation any difficulty, and Figure 71 shows that this is indeed the case. Both the nominal pairwise approximation of Eq. 41 (left panels) and the adjacent-pairs-only formulation (right panels) show that the exact and the approximate solutions agree to within a few percent except in the resonance region, where differences reach ~ 10%.

5.3 Extinction by a Closely-Packed Monolayer

The ultimate goal of characterizing coherent coupling effects is to model the response of a crowded medium to an incident plane wave. Our aim is to answer the question: "In what ways does a ring filled with closely-packed particles extinguish and scatter radio waves differently from a ring in which the same particles are well-separated?" Full analysis of this problem remains an ambitious goal for future work; below we will limit our attention to the idealized case of a monolayer distribution of identical particles.

In order to simplify the computational complexity of the problem, we make the assumption that pairwise coherent coupling effects are the most important; thus we neglect interactions of order higher than 2 among the particles in the medium. Section 5.2 explored the validity of this assumption when applied to clusters of three spheres in various configurations and over a range of sizes up to $ka = 4$. It was found that the pairwise interaction model was remarkably good at predicting the extinction

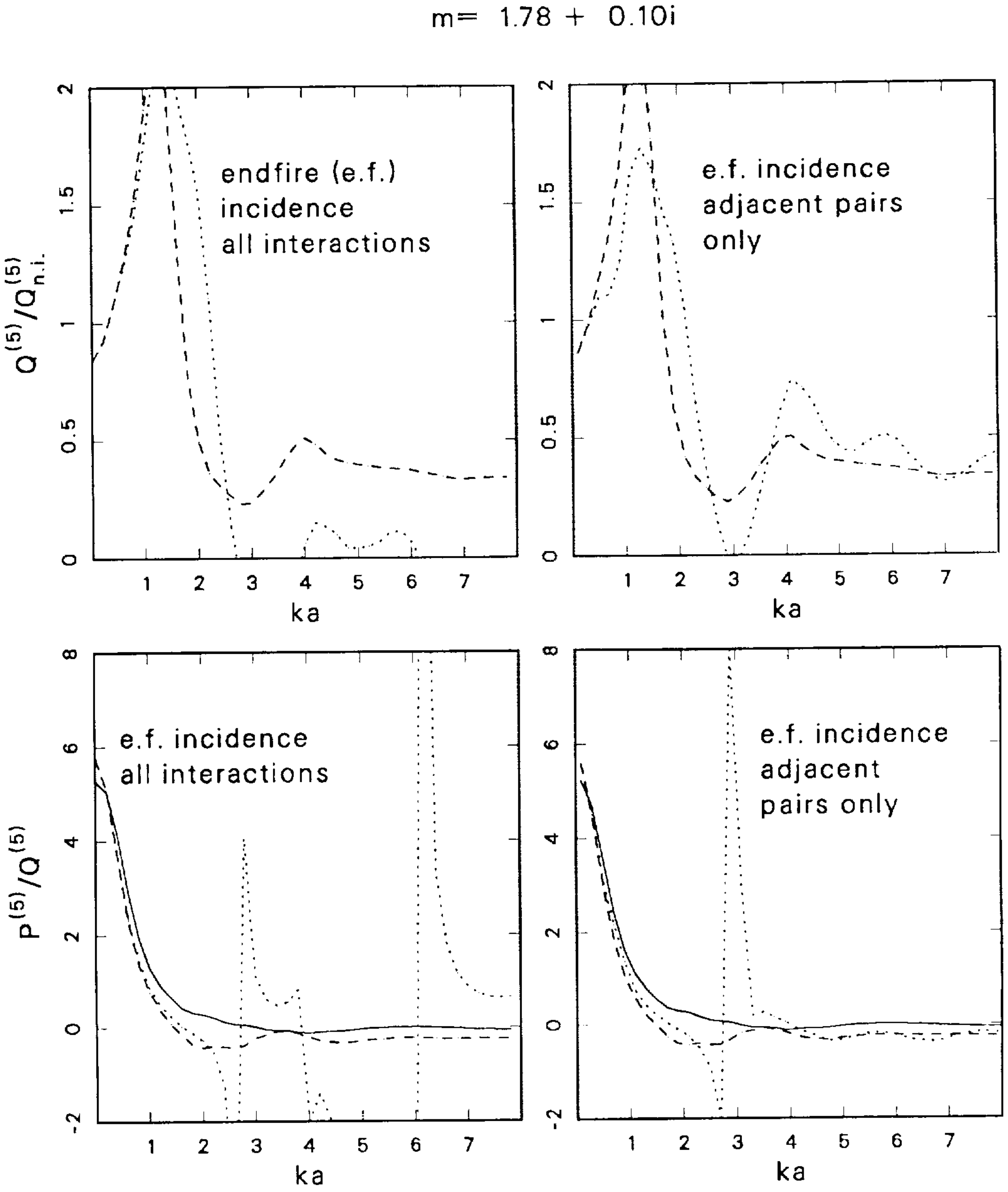

FIG. 70: Comparison between exact and pairwise approximations for extinction by five spheres in an endfire configuration. The dashed curve is the exact solution; the dotted curve is the approximate solution. The solid curve in the bottom panels shows the non-interacting-particles solution $P^{(5)}_{\text{n.i.}}/Q^{(5)}_{\text{n.i.}}$. The left-hand panels are computed using the nominal pairwise approximation of Eq. 41; the right-hand panels are computed using a modification of the approximation which considers only the interactions between adjacent pairs as described in the text. Significant improvement is clearly evident in the latter case.

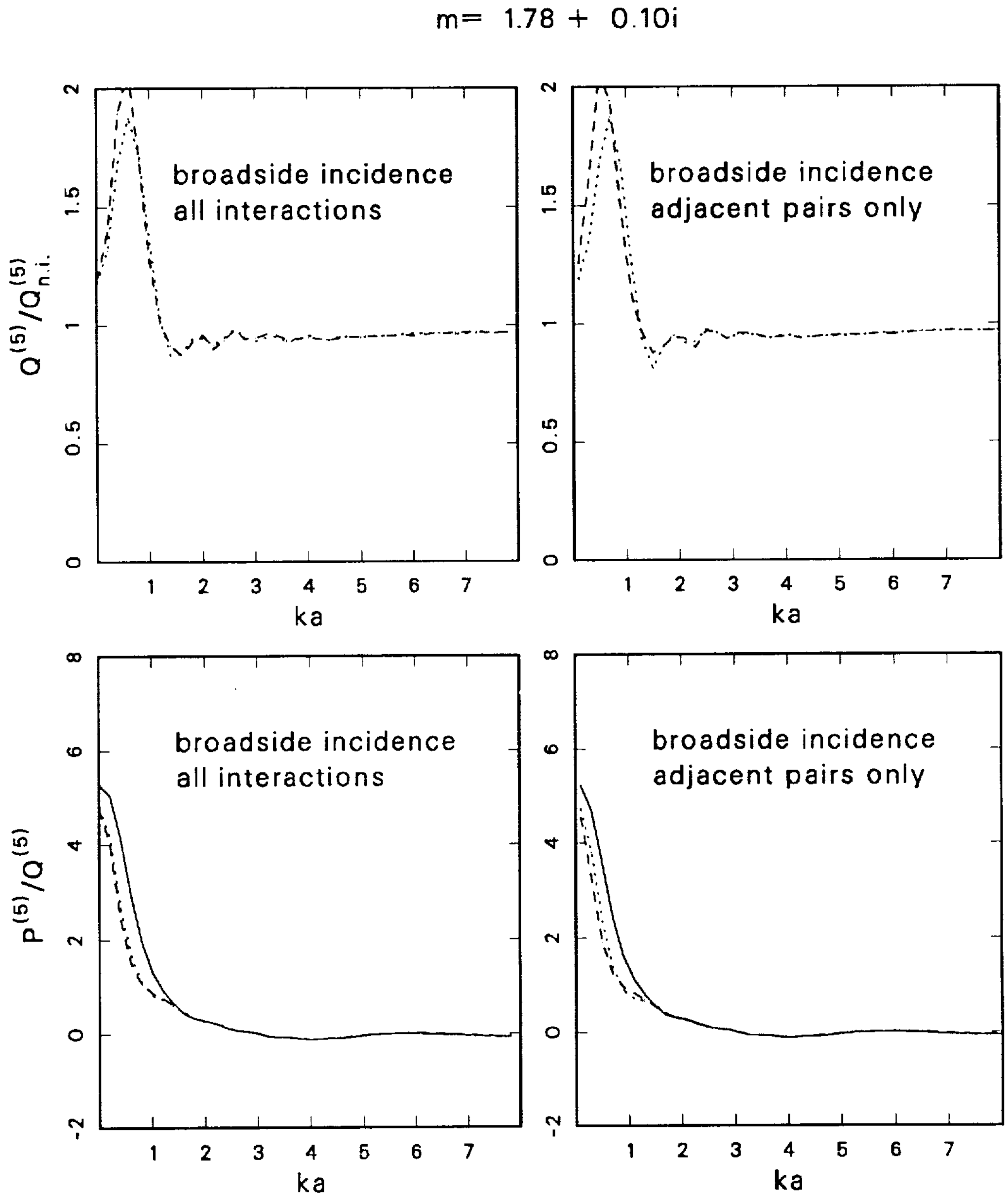

FIG. 71: Exact and pairwise approximations for the extinction of five spheres in the broadside configuration. The dashed curve is the exact solution; the dotted curve is the approximate solution. The solid curve in the bottom panels shows the non-interacting solution $P^{(5)}_{\text{n.i.}}/Q^{(5)}_{\text{n.i.}}$. The left-hand panels use the nominal pairwise approximation of Eq. 41; the right-hand panels use a modification of the approximation which considers only the interactions between adjacent pairs as described in the text. For broadside incidence, unlike the endfire incidence case considered in Figure 70, there is little difference between the two formulations of the approximation.

behavior of three spheres, *except* when the particles are aligned in the endfire configuration. Further study of this particular configuration for up to five spheres and up to a size $ka = 10$ revealed that a simple geometric shadowing model explained much of the discrepancy between the exact and the approximate solution. We thus feel reasonably confident that the pairwise approximation will yield useful results for the extinction behavior of a random ensemble of spheres.

Here we wish to characterize the extinction by a monolayer of closely-packed particles, as a function of particle size, packing fraction, and incidence angle B. We proceed in a sequence of steps. First, we describe the distribution of particle positions in the layer. When a medium is crowded, correlations between particle positions occur and must be considered in the solution of the problem. Second, we determine an expression for the forward scattering amplitude of a single particle in such a layer. This includes a term that represents the response of the particle to the incident plane wave in the absence of all other particles, plus a perturbation term that represents coupling effects due to the presence of other particles in its neighborhood. The scattered field from the entire layer is then found by coherently summing all scattered fields in a manner analogous to that used for the noninteracting particles case of Section 4.2.2, in which the monolayer model was introduced.

5.3.1 Pair correlation function

When considering a medium in which the scattering objects are positioned far apart from one another, it may be assumed that the location of any one particle is independent of the location of other particles in its neighborhood. However, as the medium becomes crowded, the particles begin to cluster in locally semi-periodic structures. Under such conditions, the position of a given particle is correlated to those of its neighbors. In order to compute the scattering behavior of the ensemble, it is important to include this effect in the formulation of the problem.

For spheres and disks in a crowded layer, this is a well-studied problem. Over the last twenty years, various models of the spatial distribution functions have been developed and compared to computer simulations of positions of hard (*i.e.* non-interpenetrating) spheres and disks. A brief definition of terms follows below; a complete discussion of distribution functions may be found in many books on statistical mechanics and the theory of simple liquids (see, for example, Hansen and McDonald, 1976).

Suppose we have a monolayer composed of N identical hard disks (or spheres) randomly distributed over an area A. Let $\mathbf{r_i}$ be the random vector defining the position of particle i relative to some origin, and let $d\mathbf{r_i}$ be an incremental area around $\mathbf{r_i}$. Then let $p^{(n)}(\mathbf{r_1}, ..., \mathbf{r_n})$ be the joint probability density of the n disks located in $\mathbf{dr_1}, \ldots, \mathbf{dr_n}$, irrespective of the positions of disks $n+1, ..., N$ (McQuarrie, 1976). Then we define the correlation function $g^{(n)}$ by

$$p^{(n)}(\mathbf{r_1}, ..., \mathbf{r_n}) = \rho^n g^{(n)}(\mathbf{r_1}, ..., \mathbf{r_n}),$$

where ρ is N/A, or the "average" number of particles per unit area. Note that $p^{(1)}$, which is the probability of any particle being at a particular position, irrespective of the location of *all other* particles in the medium, must be equal to ρ if the medium is homogeneous and isotropic. In the special case of a sparse distribution, the positions of the particles are independent. Then $p^{(n)} = \rho^n$, and $g^{(n)}$ would therefore be equal to unity.

In this work, we consider only pairwise coherent scattering effects, so we may limit our attention to the function $g^{(2)}$, known as the pair-correlation function. In addition, we assume that all of the particles in the layer are the same size. In a homogeneous and isotropic monolayer composed of disks (or spheres), $g^{(2)}$ depends only on the separation distance of the two particles, therefore

$$g^{(2)}(\mathbf{r_1}, \mathbf{r_2}) = g^{(2)}(|\mathbf{r_1} - \mathbf{r_2}|) = g^{(2)}(r_{12}).$$

We simplify the notation by writing $g^{(2)}(r_{12})$ as $g(r)$, where $r = r_{12}$.

Asymptotically, as $r \to 0$, $g \to 0$, since the particles cannot penetrate each other, and as $r \to \infty$, $g \to 1$, since the particle positions become uncorrelated. Relative to the position of any given particle, the number of particles between r and $r + dr$ is given by $\rho g(r) 2\pi r \, dr$.

The model for $g(r)$ that we use is a virial expansion in number density ρ given by Chae *et al.* (1969) under the so-called BGYM (modified Born-Green-Yvon) approximation, namely

$$g(r) = \exp[-\phi(r)/(kT)] \left[1 + g_1(r)\rho + g_2(r)\rho^2 + g_3(r)\rho^3 + \ldots\right],$$

where r is the distance between the centers of the particles, normalized by the diameter of a particle, k is Boltzmann's constant, T is the temperature, and $\phi(r)$ is the potential function. The latter two quantities are important for describing the physics of interaction between fluid molecules. For the hard disk model considered here, $\phi(r)$ is given by

$$\begin{aligned} \phi(r) &= \infty \qquad r \leq 1 \\ \phi(r) &= 0 \qquad r > 1 \end{aligned}$$

and the term $\exp[-\phi(r)/(kT)]$ is simply a step function at $r = 1$.

The number of particles per unit area, ρ, is related to the packing fraction f by $\rho = 4f/\pi$, assuming a normalized particle diameter of unity. The function $g_1(r)$ is given by Chae *et al.* (1969) to be

$$\begin{aligned} g_1(r) &= 2\cos^{-1}(\frac{1}{2}r) - (\frac{1}{2}r)(4 - r^2)^{1/2} \qquad 0 \leq r \leq 2 \\ g_1(r) &= 0 \qquad \mathrm{r} \geq 2 \end{aligned}$$

and numerical values of g_2 and g_3 as a function of r are provided. We use these values to compute $g_2(r)$ and $g_3(r)$ numerically using spline interpolation. The results for several packing fractions are shown in Figure 72. For small packing fractions ($f \lesssim 0.1$), there is little correlation between particle positions, and $g(r) \simeq 1$, $r > 1$. As the packing fraction increases, $g(r)$ peaks near the minimum separation distance $r = 1$ because, under close-packing conditions, the most likely location for the nearest neighbor is the touching geometry. This leads also to a depletion in the now relatively excluded area $r \simeq$1.5–2. As the maximum packing density ($f = \pi/2\sqrt{3} \simeq 0.91$) is approached, $g(r)$ approaches a series of delta functions at the spacing corresponding to a hexagonal arrangement of disks, with peaks at $r = 1, \sqrt{3}, 2$, etc. For packing fractions less than 30%, correlations are insignificant beyond approximately three particle diameters, as Figure 72 demonstrates.

5.3.2 Extinction by an individual particle

We now compute an approximation to the forward-scattering amplitude for a particle embedded in a monolayer containing many particles. If the medium is homogeneous, then on the average the neighborhood of one particle must look the same as the neighborhood of every other particle. For simplicity, we assume that all particles are of identical size and refractive index and calculate S_{pert}, the average perturbed forward scattering amplitude of a single particle. S_{pert} includes both the unperturbed term $S^{(1)}$ as well as coherent coupling terms that model the effect of other particles in the neighborhood. In Section 5.2.1, we have characterized such coupling in terms of δ_{ij}, where $S^{(2)}_{ij} = S^{(1)}_i + S^{(1)}_j + \delta_{ij}$ is the exact solution of the (i, j) pair of particles. Under the pairwise approximation, we may use this result to express S_{pert} as

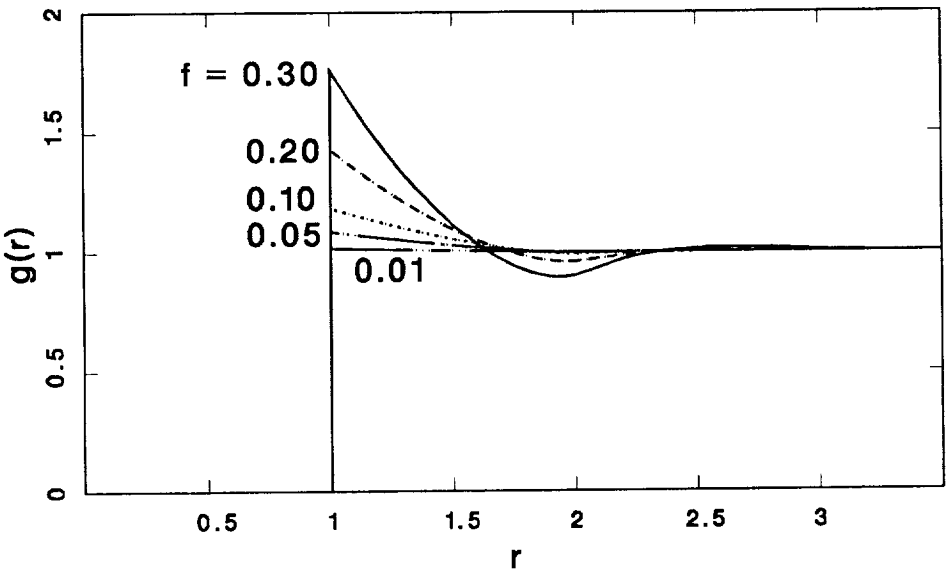

FIG. 72: Radial distribution function $g(r)$ using expansion of Chae *et al.* (1969) for the modified Born-Green-Yvon formulation. Radius r of the horizontal axis is normalized by the diameter of the particles; therefore $r = 1$ corresponds to the minimum separation distance. Curves are shown for area packing fraction f between 0.01 and 0.30. Little correlation between particle postions is seen until the packing fraction exceeds $\sim$ 10%.

$$S_{\text{pert}} = S^{(1)} + \int_0^\infty dr\, r\, \rho\, g(r) \int_0^{2\pi} d\gamma\, \frac{\delta(r,\gamma;B)}{2},$$

where we have dropped the index i since the result applies to any particle. Note that the integral represents an average over all the perturbation terms δ (adjusted by a factor of two to divide the perturbation equally between the two particles involved), weighted by the number of particles at each location. This weighting is computed using the correlation function $g(r)$ discussed above. The variables r and γ represent the coordinates of the perturbing particle relative to the particle of interest in a cylindrical coordinate system where $z = 0$, while B is the angle between the incident wave and the plane $z = 0$ containing the particles.

In order to compute δ, we first convert the position (r, γ) in the plane of the layer into positions in the reference frame of the scattering problem, a transformation which depends on B. If the original coordinates of the point in the plane of the layer are $(r, \gamma, 0)$, then the coordinates in the frame shown in Figure 52 are (r, α, ϕ), where

$$\begin{aligned} \alpha &= \cos^{-1}(\cos B \cos\gamma) \\ \phi &= \tan^{-1}\left(\frac{\tan\gamma}{\sin B}\right) \end{aligned} \tag{42}$$

and γ is measured from a unit vector $\mathbf{u}_0$, which is the projection of $\mathbf{k}$ onto the layer. ϕ is measured from the projection of $\mathbf{u}_0$ onto the plane perpendicular to $\mathbf{k}$. Replacing the number density ρ by $f/\pi a^2$, and using non-dimensional length scales, we obtain

$$S_{\text{pert}} = S^{(1)} + \frac{f}{\pi(ka)^2} \int_0^R d(kr)(kr)\, g(r/2a) \int_0^{2\pi} d\gamma \, \frac{\delta(kr, \gamma; B)}{2}, \tag{43}$$

where R is chosen to be large enough for the coupling term δ to be negligible.

To reduce the computational complexity, we construct a table of $S^{(2)}$ for the two polarizations on a grid in α and kd. Once the table is constructed, other values corresponding to intermediate α and kd are found through interpolation. In this way, one table may be used for any packing fraction and any ring opening angle B. In addition, the values stored are $S^{(2)} - \hat{S}^{(2)}_{\text{asym}}$, which removes much of the fine-scale oscillation as a function of kd and α. After interpolation, $\hat{S}^{(2)}_{\text{asym}}$ is added to the retrieved result. The grid is spaced in 2° in α and 0.2 in kd. For the smallest particle size ($ka = 0.1$), an increment of 0.05 is used for kd. These step sizes are found to result in maximum errors between computed and actual $S^{(2)}$ of less than 0.1%.

5.3.3 Optical depth and phase shift

To obtain the total forward scattered field, we follow procedures similar to those in Section 4.2.2, but in place of the forward scattering amplitude of a single particle $S(0)$, we use the perturbed value $S_{\text{pert}}(0)$ computed from Eq. 43. In a manner exactly analogous to that of Section 4.2.2, we find that

$$E = E_i\left(1 - S_{\text{pert}}(0)\, n\, \frac{2\pi}{k^2}\right) \tag{44}$$

$$\tau = -2\mu_0 \ln\left|1 - \frac{2f}{(ka)^2\mu_0} S_{\text{pert}}(0)\right| \tag{45}$$

$$\phi_c = \tan^{-1}\left(\frac{-\text{Im}\{S_{\text{pert}}(0)\}}{\mu_0(ka)^2/2f - \text{Re}\{S_{\text{pert}}(0)\}}\right). \tag{46}$$

We use Eqs. 45 and 46 to investigate the dependence of τ and ϕ_c on packing fraction f and incidence angle B. Only two representative sizes are considered: $ka = 0.1$ (small particles) and $ka = 5$ (large particles). The integral in Eq. 43 is performed over $2(ka) \leq kr \leq 10ka$ and the increments used are indicated in the captions of Figures 73 and 76. Figure 73 shows the optical depth of a monolayer, normalized by the optical depth assuming non-interacting particles. Deviations of this value from unity indicate significant coherent interaction. We present results for incidence angles B ranging from 90° to 30°. At incidence angles smaller than 30°, shadowing effects begin to invalidate the pairwise approximation. To illustrate why, we may construct a model which explicitly relates the packing fraction f to the closest particle distance by arranging the particles on a hexagonal grid, the most efficient packing arrangement. In this case, the relative interparticle distance is given by

$$d/a = \sqrt{\frac{2\pi}{\sqrt{3}f}}.$$

Using this relation, the shadow of one particle will be cast on a second particle when the incidence angle B satisfies

$$\sin B \lesssim 1.050\sqrt{f}. \tag{47}$$

The angle B at which the shadow is lengthened so that *two* particles lie in the shadow is given by

$$\sin B \lesssim 0.525\sqrt{f}. \tag{48}$$

Therefore "double-shadowing" as defined by Eq. 48 occurs only for incidence angles $B < 30°$. For $B = 20°$, two particles will be shadowed for filling fractions greater than ~ 42%, and for $B = 10°$, such a situation occurs for $f \gtrsim 11\%$. For an incidence angle of 6° (the ring opening for the radio occultation by Saturn's rings), such double-shadowing occurs for all filling fractions greater than ~ 4%. Note that "single-shadowing" as defined by Eq. 47 does *not* invalidate the pairwise approximation, as such an effect *is* included in our formulation. For the reader's convenience, Figure 74 gives the lower limit on B for any given f as expressed by Eqs. 47 and 48; $f \simeq 0.91$ is the maximum possible packing fraction for the hexagonal configuration.

Figure 73 shows that, for small particles, the optical depth of the layer τ slightly decreases as B is increased, but, however, is always larger than $\tau_{\mathrm{n.i.}}$. Figure 40 suggests that this is because, for particles of size $ka = 0.1$, coherent interaction is strongest in the broadside incidence orientation ($\alpha = 90°$), at least for the parallel polarization case.

5.3.4 Shadowing model

For large particles, deviations of $\tau/\tau_{\mathrm{n.i.}}$ are very small for incidence angles $B = 90°$ and $B = 60°$. As B decreases further, $\tau/\tau_{\mathrm{n.i.}}$ decreases for large packing fractions. This suggests that shadowing is the

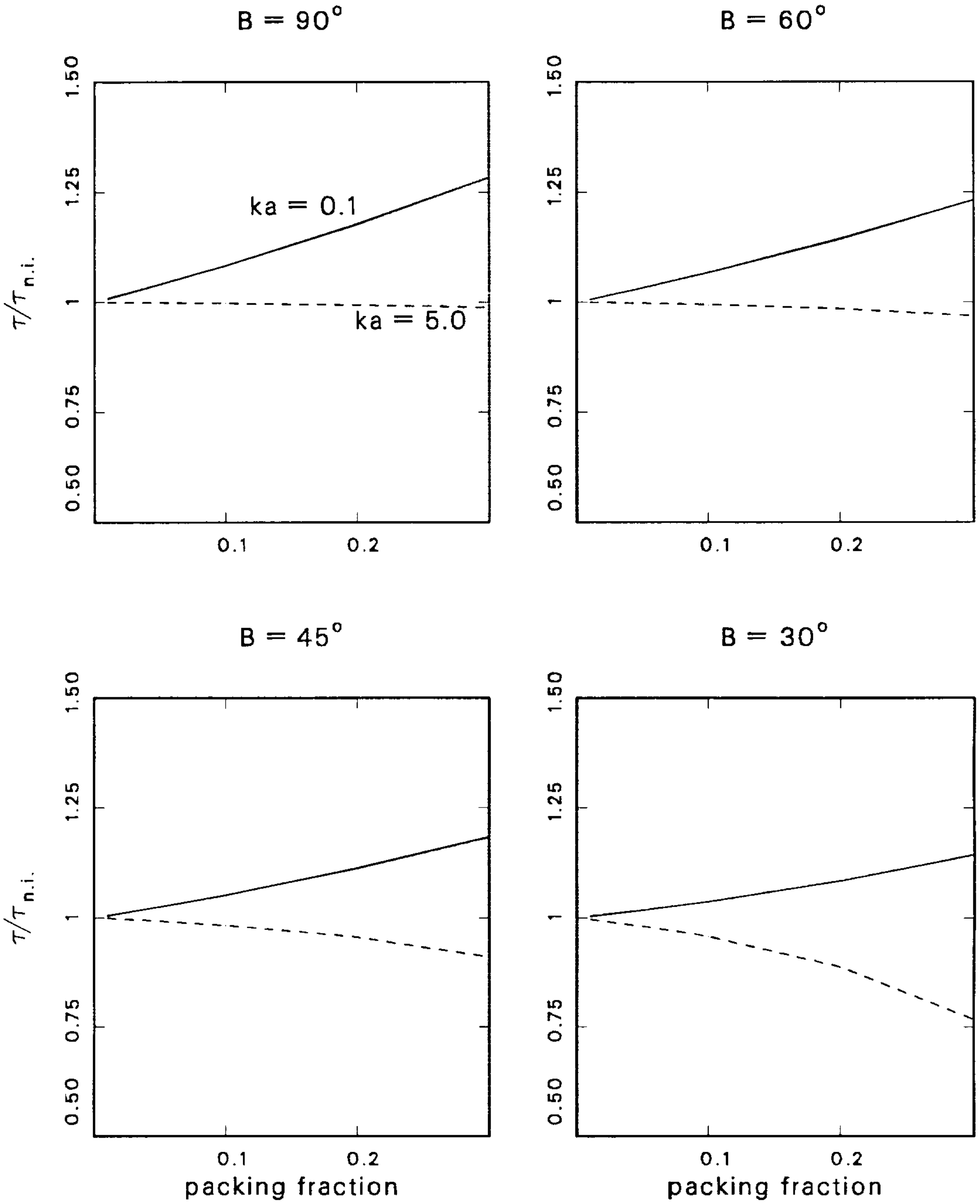

FIG. 73: Variation with packing fraction of the optical depth of a monolayer of identical particles using the pairwise approximation (Eq. 45), normalized by the optical depth assuming non-interacting particles. Packing fraction is varied from 0.01 to 0.30, and incidence angles of 90°, 60°, 45°, and 30° are shown. The integral of Eq. 43 was performed with an increment of 2° in γ and increments of 0.01 and 0.1 in kd for the $ka = 0.1$ and $ka = 5.0$ size particles, respectively.

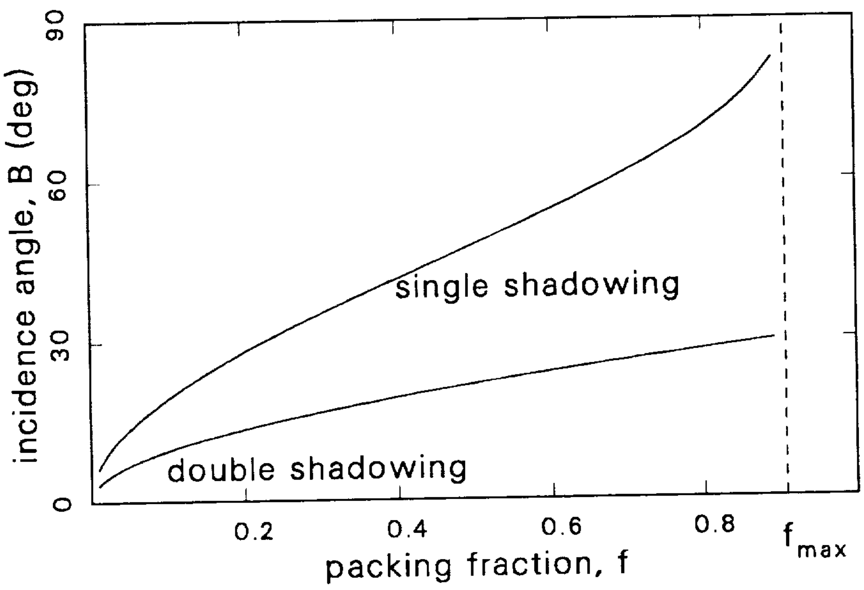

FIG. 74: Relationship between incidence angle and packing fraction f for single- and double-shadowing; a deterministic hexagonal configuration is assumed. For all incidence angles B smaller than those defined by the curves at any given f, shadowing occurs (see Eqs. 47 and 48). Curves terminate at $f \simeq 0.91$, which is the maximum packing fraction $\pi/2\sqrt{3}$ for the assumed configuration.

cause of such a decrease. It is interesting in this case to compare the $ka = 5.0$ curves of Figure 73 to those obtained from simple geometric consideration of the projected fractional area covered by the particles. As we have seen in Section 4.2.2, when coherent interaction effects (including shadowing) are neglected, the relative intensity I/I_i transmitted through a monolayer of large particles is given by

$$\frac{I}{I_i} \simeq \left|1 - \frac{\rho A^{(1)}}{\mu_0}\right|^2,$$

where $A^{(1)}$ is the area of one particle, and $Q_{\rm ext}$ is assumed to be equal to two ($ka \gg 1$). We may modify this to include geometric shadowing by writing

$$\frac{I}{I_i} \simeq \left|1 - \frac{\rho A^{(1)}_{\rm eff}}{\mu_0}\right|^2,$$

where the "effective area" $A^{(1)}_{\rm eff}$ is decreased by the mean fractional area shadowed by other particles. For a situation in which double-shadowing does not occur, $A^{(1)}_{\rm eff}$ is given by:

]

$$A_{\text{eff}}^{(1)} = A^{(1)} - A^{(1)} \left(\int_{2a}^{2a/\sin B} \int_{0}^{2\pi} SF(r,\gamma;a)\rho g(r/2a) r dr d\gamma \right), \tag{49}$$

where $SF(r,\gamma;a)$ is computed from Eq. 34 along with Eq. 42, and $g(r/2a)$ is the radial distribution function discussed above. Note that SF in Eq. 49 corresponds to $-\delta/2$ in the pairwise formulation of Eq. 43. The integral over r is performed over the range $2a \leq r \leq 2a/\sin B$, in which shadowing is possible. Figure 75 compares the result of Eq. 49 to that of the pairwise approximation for $ka = 5$. In all cases, the pairwise formulation shows more pronounced effects of the coherent interactions (deviation from unity) than can be explained by simple geometric shadowing. Figure 36 indicates that this is because, in general, the exact solution for two spheres predicts a somewhat *smaller* extinction cross section than that predicted by Eq. 34; that is, coherent effects are not simply limited to geometric shadowing. The exception to this general rule is for $\alpha = 0$, where the exact solution predicts *larger* extinction than simply one-half of the noninteracting particles value.

Figure 76 shows the phase per unit optical depth of the layer, normalized by the non-interacting result. Once again, the curves for small particles ($ka = 0.1$) show relatively little dependence on the incidence angle, while the curves for large particles ($ka = 5.0$) are strongly dependent upon B. For such large particles, the coherent phase is smaller under the pairwise approximation than under the non-interacting particles assumption. For such particles, we find that the phase is *advanced* by a smaller amount.

5.4 Summary and Discussion

In this chapter, we have investigated the effect of coherent interaction on the extinction behavior of pairs and ensembles of spheres. Results have been compared to those obtained under the "classical" assumption that such coherent effects are negligible.

We began with a study of the problem of two spheres. This simple case is a good starting point, both because of its relative computational simplicity, and, perhaps more importantly, because it allows us to develop a physical intuition about coherent interaction effects and their dependence on size, refractive index, orientation, and particle spacing. This intuition can serve us well in interpreting observations of planetary rings.

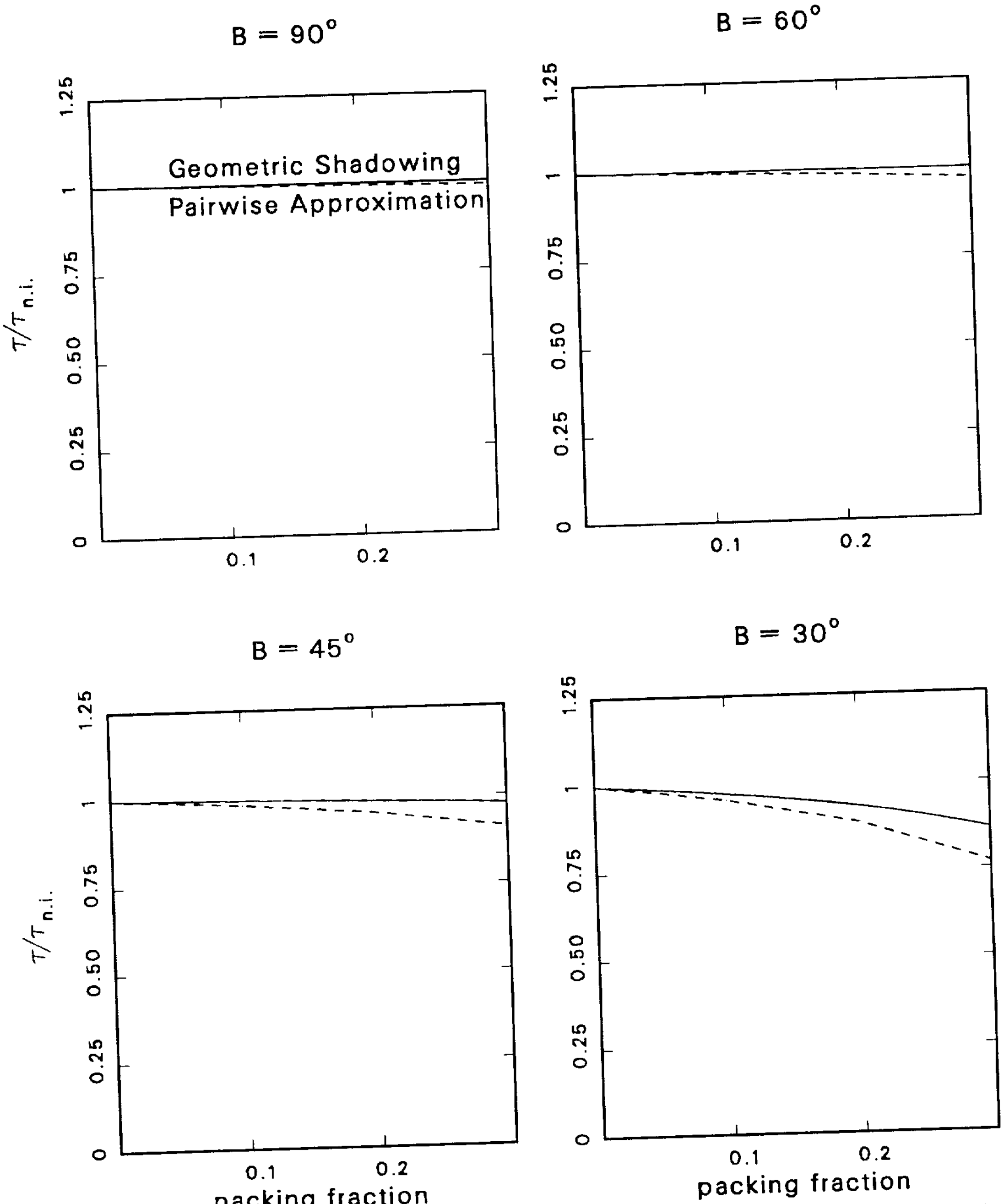

FIG. 75: Comparison of the pairwise-approximation to the geometric shadowing model (Eq. 75) of the optical depth of a monolayer of identical particles, normalized by the non-interacting optical depth. Packing fraction is varied from 0.01 to 0.30, and incidence angles of 90°, 60°, 45°, and 30° are shown. All curves correspond to $ka = 5.0$. Generally good agreement between the two models is apparent; however, the shadowing model persistently predicts a somewhat larger optical depth compared to the pairwise approximation.

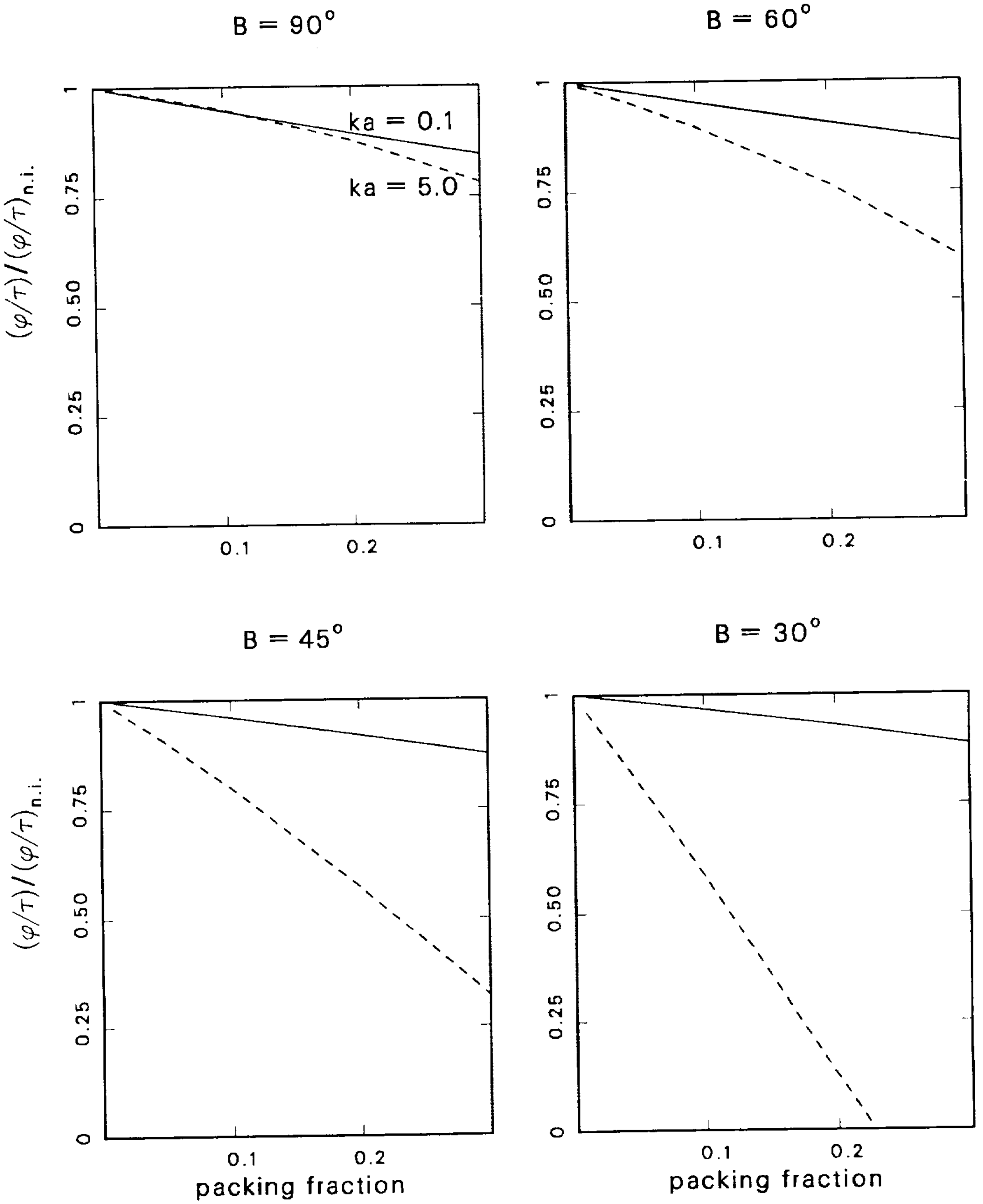

FIG. 76: Variation with packing fraction of the phase delay per unit optical depth of a monolayer of identical particles using the pairwise approximation (Eq. 46), normalized by the phase delay per unit optical depth assuming non-interacting particles. Packing fraction is varied from 0.01 to 0.30, and incidence angles of 90°, 60°, 45°, and 30° are shown. The integral of Eq. 43 was performed with an increment of 2° in γ and increments of 0.01 and 0.1 in kd for the ka = 0.1 and ka = 5.0 size particles, respectively.

5.4.1 Coherent interaction effects

Here we summarize some of the important results obtained from the study of pairs and ensembles of spheres. In the limit of particles small compared to the wavelength, we have found that coherent interaction effects are important for all orientations of the pair relative to the incident wave. The response to an incident wave polarized perpendicular to the plane containing the incidence direction and the particles was found to be completely independent of the pair's orientation; the response to a parallel polarized wave was found to depend strongly on orientation. Overall, the strongest interaction was found to exist when the pair is oriented in the broadside configuration.

An asymptotic model for coherent interactions was formulated solely in terms of the far-field scattering amplitudes of individual particles. For small particles, this model was found to predict some of the observed behavior, for example the lack of dependence on orientation for a perpendicularly-polarized incident field. However, it failed to predict the strong interaction in the broadside configuration. This is presumably because, for dipoles (an accurate model for Rayleigh scatterers), while the far-field response to a parallel-polarized field in the $\alpha = 90^\circ$ direction is very small, there is a maximum in the *near-field* in that direction.

For particles in the resonance region, where the size of the particle is comparable to the wavelength, coherent effects can increase or decrease the extinction by a sizable percentage. Coherent interaction effects are important for all orientation angles, and persist to separations of approximately 10 radii. The asymptotic model was found to describe much of the coherent interaction once the particles were separated by approximately 4 radii. Interestingly, for this size particle, no shadowing, *i.e.*, no persistent decrease in extinction in the endfire configuration, is observed.

For particles large compared to the wavelength, we found that coherent interactions are only significant when the orientation angle α is small. In fact, a simple geometric shadowing model was found to accurately describe the change in Q_{ext} for both touching and slightly separated particles of size $ka \gtrsim 5$. The persistence of the shadow in the $\alpha = 0$ direction was investigated, and both the exact computations and a theoretical consideration of the Fresnel zone size relative to the size of the particle indicated that coherent effects persist until the separation between the particles is $\gtrsim 10a^2/\lambda$.

We also computed the complex extinction for two particles averaged over orientation, as a function of particle separation. We found that, regardless of the size of the particle, average coherent interactions become negligible when the particles are separated by more than about five radii. This implies that "classical" noninteracting particles (radiative transfer) models are valid for volume packing fractions less than about 1%.

We next investigated the validity of a "pairwise-interaction" model developed to characterize the coherent interaction between more than two particles. This model assumes that the most important interactions are those between pairs of particles, and that higher order interactions are negligible. We compared the pairwise approximation to exact computations of the complex extinction for three spheres in four representative arrangements. Sizes up to $ka = 4$ were investigated; this limit was set by the computational complexity of the exact three-sphere problem. We found that the pairwise model was a good approximation to the exact behavior, *except* when the spheres are arranged in the endfire configuration. Further analysis of this particular arrangement indicated that incorporating the concept of shadowing into the pairwise formulation removed much of the discrepancy.

We then computed the extinction of a monolayer of identical particles, using the pairwise formulation. We chose two representative sizes, $ka = 0.1$ and $ka = 5.0$, to represent small and large particles, respectively, and investigated the effect of packing fraction and incidence angle on optical depth and phase. For the small particles, the interaction is relatively independent on the incidence angle, and the optical depth of the layer increases monotonically with increasing packing fraction f over the range $f \leq 0.3$. The phase per unit optical depth decreases slightly with increasing packing fraction, and is similarly insensitive to the incidence angle. For large particles, as one might expect from a geometric shadowing model, the optical depth of the layer is strongly dependent on the incidence angle, decreasing as the incidence angle becomes more oblique. This is presumably due to a fraction of the particles in the layer hiding behind one another, and therefore no longer contributing to the total extinction of the layer. The phase per unit optical depth is also a strong function of incidence angle, decreasing as the incidence angle decreases. The optical depth for $ka = 5$ was also compared to a geometric shadowing model which considers the transmitted intensity to depend on the unshadowed area of particles. The pairwise formulation was found to consistently yield somewhat smaller optical depths, indicating that coherent interaction effects are not limited to simple geometric shadowing effects.

5.4.2 Implications for the Uranian rings

One of the prime reasons for undertaking the study of coherent interactions was the anomalous phase delay behavior of the inner Uranian rings. The idealistic model of a monolayer of identical particles employed here does not appear to suggest that such phase effects result from close packing;

however, a definitive conclusion cannot be drawn until a three-dimensional model incorporating a size distribution of particles is investigated. Results obtained here *do* indicate that coherent interactions can have a significant effect on the optical depth. Relative to the noninteracting case, small particles ($ka \lesssim 2$) increase the optical depth for all incidence angles; large particles ($ka \gtrsim 5$) decrease the optical depth, particularly as incidence angles become more oblique, primarily because of geometric shadowing. Only a limited range of packing fraction, $f \leq 0.3$, was explored, however. These results have implications for interpretation of the Saturn radio occultation data, where the ring opening angle was only 5.9°, as well as for comparison of radio to other Uranian ring occultation data at more oblique incidence angles, as we discuss further below.

As stated in Section 4.4, comparison of integrated optical depths obtained here to those at shorter wavelengths generally supports the conclusion that the Uranian rings are relatively depleted in small particles. However, most of the measurements are noise limited. The best measurements are those of Ring ϵ, and there are some perplexing indications that the integrated optical depth at the much shorter UVS and PPS wavelengths is actually *smaller* than that at radio wavelengths. Specifically, Holberg *et al.* (1987) find that the integrated optical depth is 80–85 km when corrected for the factor of two due to diffraction of the radio waves. This is significantly smaller than the value of ~ 95 km reported here. Lissauer (1989) finds that PPS integrated optical depths are closer to the UVS than to the radio values. Although this is certainly good evidence that there cannot be too many small particles, the fact that the shorter wavelengths show smaller optical depths may well be a clue to some other unmodelled process.

One possibility is that shadowing effects due to incidence angle and wavelength are more important for the UVS and PPS occultations than for radio. The ring opening angle for the radio experiment was 81.5°; for the UVS and PPS observations it was only 27.1° for the σ-Sagitarii occultation and 36.8° for the β-Persei occultation (Colwell *et al.*, 1989). We have seen that, for large particles (and indeed compared to UVS and PPS wavelengths the particles in Ring ϵ are probably very large), optical depth decreases when coherent effects are included. To illustrate, Figure 77 compares, for particles size $ka = 5$, the normalized optical depth as a function of packing fraction for $B = 81.5°$ (radio occultation) and for $B = 27.1°$ (PPS and UVS σ-Sagitarii occultation). For the almost fully-open 81.5° case, there is little coherent interaction for any packing fraction up to 0.3. However, for the more oblique incidence direction of 27.1°, shadowing decreases the optical depth significantly. Although, as we have discussed in Section 4.3, a monolayer is a poor model of Ring ϵ, qualitatively Figure 77 suggests that shadowing effects may be much more important for the more oblique occultations.

Another possibility is that particles in the centimeter size range would appear very large at PPS and UVS wavelengths, but would be in the resonance size range at radio wavelengths. We have seen that these two size ranges affect the extinction in opposite directions, and could result in larger extinction at the longer wavelength, in contrast to the classical noninteracting particles models.

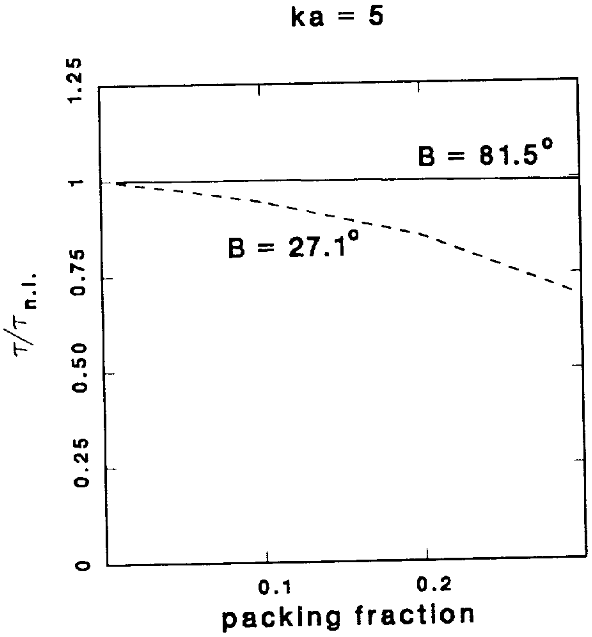

FIG. 77: Comparison of $\tau/\tau_{n.i.}$ for incidence angles of 81.5° and 27.1°, for a monolayer of large particles ($ka = 5$). These incidence angles are the ring opening angles of the radio and the σ-Sagitarii PPS and UVS occultations, respectively. Significant shadowing is observable in the more oblique incidence case; this effect may possibly explain the puzzling observation that integrated optical depths for Ring ϵ appear to be *smaller* for the shorter wavelengths than for the microwave wavelengths discussed in this work.

Chapter 6

Summary and Conclusions

In this work we have shown how data collected during the Voyager 2 radio occultation of the Uranian rings have contributed to a number of areas of study, many of which were not even anticipated in the original Voyager planning. If we recall the expectations for the radio occultation experiment at the time of the Voyager launch, diffraction-reconstruction was not part of the initial plan, in part because the diffraction-limited resolution of about 15 km was thought to be adequate to see all of the important structure of the 70,000 km wide ring of Saturn. Only when the narrow Uranian rings were accidentally discovered in 1977, and when Voyager 1 reached Saturn in 1980, did the concepts of narrow ringlets, density and bending waves, and extremely sharp edges enter the collective consciousness of planetary scientists. Therefore, much of the discussion above could not have been foreseen on the day of the Voyager 2 launch on September 5, 1977. A study of particle sizes in Saturn's rings was expected to be undertaken with the dual wavelength radio data; however, we may again recall that until Voyager 2 actually passed behind the rings of Uranus, it was not known whether the radio signal would be affected by the particles there. The only previously published estimate of particle sizes in the Uranian rings implied typical radii in the micron size range (Pang and Nicholson 1984). Such particles would have been completely invisible to the radio wavelengths. This author was present when the real-time monitors showed the radio signal drop over 20 dB when Voyager passed behind Ring ϵ, and it was certainly exciting to see a leap in the amount of knowledge take place in a split second. It can thus fairly be said that the observations themselves have driven the investigation.

In this chapter we summarize the main results of the work described here, discuss the important limitations of the analyses performed and suggest directions for future contributions to the study of planetary rings using the radio occultation data.

6.1 Observations and Inferences

Application of the radio occultation data to problems of structure and dynamics requires a high-resolution data set with which to work. The original collected data have a resolution on the order of the Fresnel zone size, which is 1–2 km for this experiment. As every Uranian ring with the exception of Ring ϵ is $\sim$ 1–10 km wide, essentially all ring structure is masked by diffraction in the raw data. Fortunately, the coherent nature of the radio source allows for reconstruction of the actual ring transmission through an inverse Fresnel transform operation, which can improve the resolution of the data by almost two orders of magnitude. This technique was initially developed for the almost-circular Saturnian rings (Marouf *et al.*, 1986), and refined here so as to reconstruct high-resolution profiles of the significantly eccentric Uranian rings.

From the high resolution diffraction-reconstructed profiles thus produced, we observe significant radial structure that varies with observation longitude. A number of the rings present dramatically different personae at the two observation longitudes. A wave-like feature has been observed on the inner edge of Ring δ. Many of the observed ring edges are found to be quite sharp, with gradients of optical depth exceeding 1 τ/km, and for most of the rings, the outer edge is significantly sharper than the inner edge, offering a clue to possibly different mechanisms for confinement of the two edges. Using the profiles observed at two widely separated longitudes, we have been able to shed some light on the character of such structure; however, a more complete understanding will require multiple high-resolution observations spread in longitude and time. Unfortunately, the resolution of ground-based occultations is limited by diffraction to a few kilometers, and the UVS and PPS occultations of the entire ring system by the star β-Persei are severely limited by noise. The higher-SNR UVS and PPS occultations by the star σ-Sagitarii resulted in profiles only of Rings δ and ϵ (and the Voyager-discovered Ring 1986U1R) due to the geometry of that occultation.

The sharp edges of many of the rings have led us to search for possible locations of satellites which might exert gravitational torques to simultaneously confine several ring edges (most of which have no known source of confinement). A statistically likely location was found just inside Ring η, which has relatively low-order strong resonances within 1-3 km of the edges of four rings, and may also be responsible for driving the wave-like feature of Ring δ. Unfortunately, the amplitude of perturbations to ring edges due to such a satellite may well be below the detection threshold of current observations.

Significant changes in ring width allow inferences of bounds on the vertical thickness of some of the rings. Observed conservation of integrated optical depth implies that Rings α, γ, δ, and ϵ are not monolayers. (Due to a lack of substantial variation in width, we cannot distinguish between monolayer and many-particle-thick models for the remaining rings.) Further investigation shows that, under the assumptions of the models used, Ring ϵ must be greater than approximately 10 layers thick in the neighborhood of periapse (true anomaly 30°). Similar lines of reasoning indicate that the thickness of Rings α and δ must be at least ~ 4 layers, while Ring γ must be thicker than about 10 layers. Conversion of number of layers to ring thickness requires knowledge of typical particle sizes and typical particle separations, both of which have been investigated here.

In our study of particle sizes, we concentrated on Ring ϵ, due to its relatively low optical depth[1], and the fact that it is wide enough that significant noise reduction via integration can be obtained. For all but Ring ϵ, even a signal-to-noise ratio of over 1500 (32 dB) in a one-second integration time results in 15–40% uncertainty in the estimates of integrated optical depth.

We described three models of the radiowave-ring interaction process which are based on the Mie theory of scattering by coherently non-interacting spheres. If we require the theoretical predictions based on these models to match both the optical depth and phase delay behavior of Ring ϵ, then a lossless refractive index and size distribution exponent $q = 2.75$ results in a relatively broad range of sizes which match the data, as long as $a_{\text{min}} \lesssim 2$ cm and $a_{\text{max}} \gtrsim 150$ cm. Surface mass densities, assuming an ice-like bulk particle density, are $\gtrsim 50$ g-cm^{-2}. If, on the other hand, we allow for the possiblility that the observed phase is of unknown origin, then the observed differential optical depth may imply an "effective" particle size $\gtrsim 70$ cm, with $\sigma \gtrsim 80$ g-cm^{-2}, independent of q.

Given the size information, converting the number of layers into a physical thickness also requires an estimate of the typical separation between particles. If we interpret the results in a self-consistent manner, and require that the layers of the thin-layer model be far enough separated so that coherent interactions are negligible, then the results of Chapter 5 imply that the layers must be separated by ~ 5 particle radii. The minimum physical thickness may therefore be from a few meters, for a less-steep power law exponent ($q \lesssim 2.75$), to a few tens of meters, for $q \gtrsim 3$.

---

[1] Only the fortuitously large ring opening angle (81.5°) for the Uranus occultation allows us to consider an average optical depth of about 1.3 "low"; the small ring opening angle at Saturn (5.9°) resulted in a threshold normal optical depth of ~ 1, beyond which measurements are buried in noise. Most of Ring B and the dense portions of many wave features in Ring A exceeded this threshold optical depth.

The other outer rings (η, γ, and δ) appear to have optical depth and phase delay behavior quite similar to that of Ring ϵ, although the uncertainties are larger due to smaller widths and in some cases higher optical depths. The tenuous companions to Rings η and δ appear to be relatively depleted in particles smaller than $\sim$ 1 cm in size, as the optical depths observed at radio wavelengths are comparable to those at much shorter wavelengths.

Above we have suggested that the surface mass density of Ring ϵ is $\gtrsim$ 50 g-cm^{-2}. This is inconsistent with the surface mass density of $\sim$ 30 g-cm^{-2} implied by the self-gravity theory for uniform ring precession (Goldreich and Tremaine, 1979b). Other results are also inconsistent with predictions of the self-gravity theory. For Rings α, β, and ϵ, empirical eccentricity gradient profiles have been constructed and compared to those obtained from the theory. The theoretically predicted profile variation with longitude does not match the observations, most dramatically for Ring ϵ, but also for Ring β. For Rings α and β, uncertainties in the data preclude meaningful bounds on the surface mass densities, but the self-gravity estimates of $\sigma \sim 2$ g-cm^{-2} seem clearly incompatible with the substantial opacity observed at the 13 cm wavelength. In addition, calculated drag torque due to the extended exosphere of Uranus (Broadfoot *et al.*, 1986) appears to imply very short lifetimes ($\lesssim$ 1000 years) for centimeter and smaller size particles (Goldreich and Porco, 1987).

Confidence in our empirically-derived eccentricity gradient could be greatly increased if high quality profiles of Ring ϵ were available at additional longitudes. The derivation of this gradient profile assumes that the individual particle orbits can be described by Keplerian ellipses, and that these orbits are aligned in the same direction, that is, that the angle of periapse is constant across the ring. The derivation also assumes that individual orbits do not cross. Additional profiles would allow us to test these assumptions directly. Currently work is underway to use all of the Voyager occultation profiles to construct an eccentricity gradient for Ring ϵ, but progress is slowed by the difficulty in assessing the noise in the PPS data.

The self-gravity theory, in its form used for comparison purposes here, assumes that that collisional forces are negligible. The lack of observed apse misalignment for Rings α, β, and ϵ tends to support this assumption (Borderies *et al.*, 1983; French, *et al.*, 1989). In addition, in computing the mass density of streamlines, it is assumed that mass is proportional to optical depth, which requires that the distribution of particle sizes remain constant across the ring, and shadowing to be negligible. Given these caveats, it seems clear that further work is still needed before the apparent discrepency between the dynamical and observational inferences of the eccentricity gradient profiles can be resolved.

One of the most intriguing observations of the Uranian rings is the anomalously large differential phase delay observed for the five inner rings. We showed that Rings 6, 5, 4, α, and β have significantly larger phase delay at 13 cm than do the outer rings, Rings η, γ, δ, and ϵ. The phase delays for the 3.6 cm wavelength are relatively small for all the rings. The only size distribution which provides a match with the observations is a near-monodispersion of nearly lossless particles, of a size which must be within a centimeter or so of the crossing point of the 3.6 and 13 cm extinction curves, a refractive index dependent value. These are overly restrictive conditions and appear unrealistic. The strict single size requirement is also dynamically doubtful for a real planetary ring, where collisional breakup and accretional growth almost surely occur.

6.2 Coherent Interactions

Motivated in part by the anomalous phase behavior of the inner Uranian rings discussed above, we conducted an analysis of the effects of possible coherent electromagnetic interaction between ring particles illuminated by a plane-wave radio source. We began with a study of a pair of particles, and developed a pairwise approximation which we compared to the exact solution for three to five particles. We then extended this approximation to a monolayer of particles. We limited our study to the case of a monolayer due to the difficulties inherent in extending the pairwise approximation to a three-dimensional layer. Although a many-particle-thick layer may be studied as a cascade of monolayers, use of this procedure would require incorporation of coherent *inter*-layer coupling as well. For this reason we explored the simpler case of a monolayer in order to investigate the conditions under which coherent interactions are important and to characterize such interactions. There are certainly indications that the Uranian rings, particularly Ring ϵ, are *not* monolayers; thus our effort here should be regarded as an essential first step towards the more ambitious goal of fully understanding the effects of coherent coupling in more realistic ring models.

In the study of the complex extinction behavior of two particles, we found that, even for touching particles, geometric shadowing is a good model for the exact extinction behavior of particles of size $ka \gtrsim 5$. For such large particles arranged in an endfire configuration, shadowing effects are significant for separations up to $\sim 10a^2/\lambda$. For smaller sizes ($ka \lesssim 1$), coherent interactions are important for all orientations of the particle-pair relative to the incidence direction and are difficult to characterize in terms of a simple physical model, such as shadowing.

We also computed the extinction of a pair of particles averaged over orientation and found that, regardless of the size of the particle, the average coherent interaction becomes negligible beyond a particle separation of about five radii ($d \sim 5a$). This implies that for a random spatial distribution of particles, coherent interactions can be neglected for volume packing fractions less than about 1%, an explicit criterion for the validity of the "classical" model.

To calculate extinction by a collection of coherently-interacting particles, a pairwise-interaction model was developed and tested against exact computations for three or more particles. In general, the approximation was found to agree with the exact computations to within a few percent, except when more than two particles were aligned along the forward direction. This model was extended to a monolayer of identical ring particles, and the extinction behavior as a function of size and incidence angle was investigated. For small particles, coherent effects tend to increase the total extinction, while for large particles the extinction is decreased relative to the non-interacting case. The large particle example is fit approximately by a simple model which considers the reduction in signal intensity to be proportional to the geometric area blocked by the particles; however, the pairwise approximation results in smaller overall extinction than does the geometric shadowing model. In all computational models examined, it has generally been observed that coherent interactions tend to decrease the phase effect relative to the noninteracting case. These results strongly suggest that the Saturn ring observations should be re-examined in view of the considerable shadowing effects expected for a 5.9° ring opening angle.

It is not clear at what point the assumptions implicit in the pairwise-approximation break down. Eventually, when particles become close enough, third-order interactions must become important, and the extinction behavior will diverge from the simple model proposed here. Further work needs to be done to determine when and how this takes place. In the future, results might be extended to consider particle size distributions and alternative vertical arrangements.

6.3 A Look to the Future

In the foreseeable future, we do not expect a great deal of additional data on the detailed structure of the Uranian rings, and the profiles presented here will likely remain one of the best sources of information on these rings for the next several decades. The results described in this work show the Uranian rings to be a rich source of interesting and important dynamical and physical problems. Even though they are much less extensive than the remarkable Saturnian ring system, these narrow rings are by no means simple. The Voyager radio occultation data offer a tantalizing snapshot of the rings at a particular moment of time. So as is usual, observers are left wishing for "one more look" which might offer a few more clues to many of the remaining puzzles. Unfortunately, because of the difficulties inherent in traveling to the outer solar system, no return missions to Uranus are currently planned. From Earth, the flight of Voyager 2 to Uranus took nine years; the continued journey to Neptune took three more. Only a rare alignment of the outer planets allowed such relatively short travel times; without the gravity assist from Jupiter, the flight time to Uranus would have been about 30 years. However, an announcement of opportunity has recently been released by NASA for the Cassini orbiter mission to Saturn. Saturn is something of an "archetype" for planetary rings; it appears to have many of the characteristics of the other three rings systems encompassed in its broad expanse, including narrow, eccentric features, like the ones considered here. So those who look for answers to Uranian ring problems may well find enlightenment when Cassini arrives at Saturn just after the turn of the 21st century. Of course, given the Voyager experience, it would be foolhardy to predict what surprises the Saturnian rings may hold in store for us still.

C-3

Appendix A

Noise Limitations

In the text we have referred to various quantities related to additive thermal noise limitations such as the standard deviation in optical depth σ_τ, the standard deviation in coherent phase delay σ_{ϕ_c}, the optical depth threshold τ_{TH}, and uncertainty intervals for measured values of optical depth τ. This appendix serves to define some of these quantities.

The experiment measures E_c, which is the complex field strength of the coherent received signal. Once corrected for diffraction effects (Marouf *et al.*, 1986), the normal optical depth τ and coherent phase ϕ_c may be calculated from

$$\tau/2\mu_0 + i\phi_c = -\ln(E_c/E_0)^*,$$

where $\mu_0 = \sin(B)$, B is the ring opening angle, E_0 is the value of the field strength in the absence of rings, and * denotes complex conjugate.

Following Marouf *et al.* (1986), the noise power P_N associated with E_c/E_0 is given by

$$P_N = \frac{1}{\mathrm{SNR}_0}\frac{\dot{\rho}}{\Delta\rho},$$

where SNR_0 is the free-space signal-to-noise ratio in a one second integration time (46 and 32 dB for the 3.6 and 13 cm data, respectively), $\dot{\rho}$ is the radial velocity of the ring plane intercept of the radio beam (approximately 8.2 km-sec^{-1} for both ingress and egress here), and $\Delta\rho$ is the resolution of the data in kilometers.

At free space signal levels, the standard deviation of measured normal optical depth is given approximately by

$$\sigma_\tau \simeq \mu_0\sqrt{2P_N}.$$

Denoting by τ_U and τ_L the values of τ corresponding to a 70% confidence interval, respectively, we have

$$\begin{aligned} \tau_L &= \tau - 2\mu_0 \ln(1 + \sqrt{P_N C_\alpha/2}\; e^{\tau/2\mu_0}) \\ \tau_U &= \tau - 2\mu_0 \ln(1 - \sqrt{P_N C_\alpha/2}\; e^{\tau/2\mu_0}), \end{aligned}$$

where $C_\alpha = 2.49$ (Marouf *et al.*, 1986). These limits are given in Table 11 for resolutions of 50 and 200 m for the 3.6 cm signal. Note in particular the asymmetry of the uncertainty interval, and its rapid growth as τ approaches the threshold opacity, τ_{TH}, where

$$\tau_{TH} = -\mu_0 \ln(P_N C_\alpha/2).$$

Values of τ_{TH} for the 3.6 and 13 cm data at several resolutions are given in Table 11; the effect of lower signal-to-noise ratio for the 13 cm data is readily apparent.

The standard deviation of measured coherent phase delay is given by

$$\begin{aligned} \sigma_{\phi_c} &= \sin^{-1}[e^{(\tau-\tau_{TH})/2\mu_0}] && 0 \le \tau \le \tau_{TH} \\ \sigma_{\phi_c} &= \pi && \text{otherwise.} \end{aligned}$$

Uncertainty invervals for both τ and ϕ_c for both wavelengths at 500 m resolution are given in Table 12.

τ	50 m res[a]		200 m res	
	τ_L[b]	τ_U	τ_L	τ_U
0.0	0	0.15	0	0.07
1.0	0.78	1.25	0.89	1.12
2.0	1.64	2.43	1.81	2.20
3.0	2.44	3.78	2.70	3.35
4.0	3.15	5.54	3.53	4.62
4.5	3.45	6.85	3.91	5.34
5.0	3.73	9.46	4.27	6.17
5.5	3.98	∞	4.60	7.20
6.0	4.20	∞	4.90	8.68
6.5	4.39	∞	5.17	12.61
7.0	4.54	∞	5.41	∞

	τ_{TH}[c]		
res (m) λ	50	200	500
3.6 cm	5.2	6.6	7.5
13 cm	2.0	3.4	4.3

TABLE 11: Uncertainty intervals and threshold opacity at 70% confidence level (~1-σ).

[a]: The abbreviation "res" stands for resolution.

[b]: τ_L and τ_U define the lower and upper values of the uncertainty interval centered on indicated τ.

[c]: τ_{TH} is the value of τ larger than which the uncertainty interval includes $\tau = \infty$.

τ	τ_L(3.6 cm)	τ_U(3.6 cm)	τ_L(13 cm)	τ_U(13 cm)	σ_{ϕ_c}(3.6 cm) (cycles)	σ_{ϕ_c}(13 cm) (cycles)
0	0	4.5×10^{-2}	0	0.24	3.6×10^{-3}	1.8×10^{-2}
1.0	0.9	1.1	0.7	1.4	6.0×10^{-3}	3.0×10^{-2}
2.0	1.9	2.1	1.5	2.7	9.9×10^{-3}	5.0×10^{-2}
3.0	2.8	3.2	2.2	4.4	1.6×10^{-2}	8.7×10^{-2}
4.0	3.7	4.4	2.8	7.9	2.7×10^{-2}	0.16
5.0	4.5	5.7	3.3	∞	4.6×10^{-2}	0.5

TABLE 12: 500 m resolution uncertainty intervals (~ 1-σ for τ and ϕ_c).

Appendix B

Dual-wavelength Profiles

Here we present the low resolution (500 m) profiles not specifically discussed in Chapter 4. In each figure, the top panel shows the optical depth profile at both 3.6 (heavy curve) and 13 cm (light curve). The bottom panel shows the phase delay, with increasing phase delay plotted downward. The scales of Figures 78–93 are the same; the scales of Figures 94 and 25 are compressed due to the larger width and optical depth of Ring ϵ. The true anomaly of the observation is noted at the top of each figure.

Note the difference in the phase behavior of the inner rings (6, 5, 4, α, and β) relative to the outer rings (γ, δ, and ϵ). For the inner rings, there is clear phase delay at the 13 cm wavelength, and little phase delay at the 3.6 cm wavelength, while for the outer rings, little phase delay is seen at either wavelength. For example, compare Ring 6 to Ring η. These rings have comparable optical depth, but the phase at 13 cm is delayed by approximatly 0.05 cycles for Ring 6, while there is no detectable phase change associated with Ring η. Similarly, Ring 5 at egress and Ring δ at ingress both have an optical depth of approximately 1.5, but $\phi_c(13 \text{ cm}) \simeq 0.1$ cycles for Ring 5, while there is no detectable phase change associated with Ring δ.

Some of the more optically thick rings (Ring γ, and Ring δ at egress) show detectable phase delay of the 13 cm data; however, given the large opacities, the phase per unit optical depth remains small.

For almost all of the rings, there is no statistically significant difference in optical depth between the two wavelengths. The possible exception is Ring β egress, where a marginal difference ($\sim$ 2-σ) appears to persist over the outer half of the ring. If real, such a difference would indicate the presence of centimeter-sized particles in this portion of the ring.

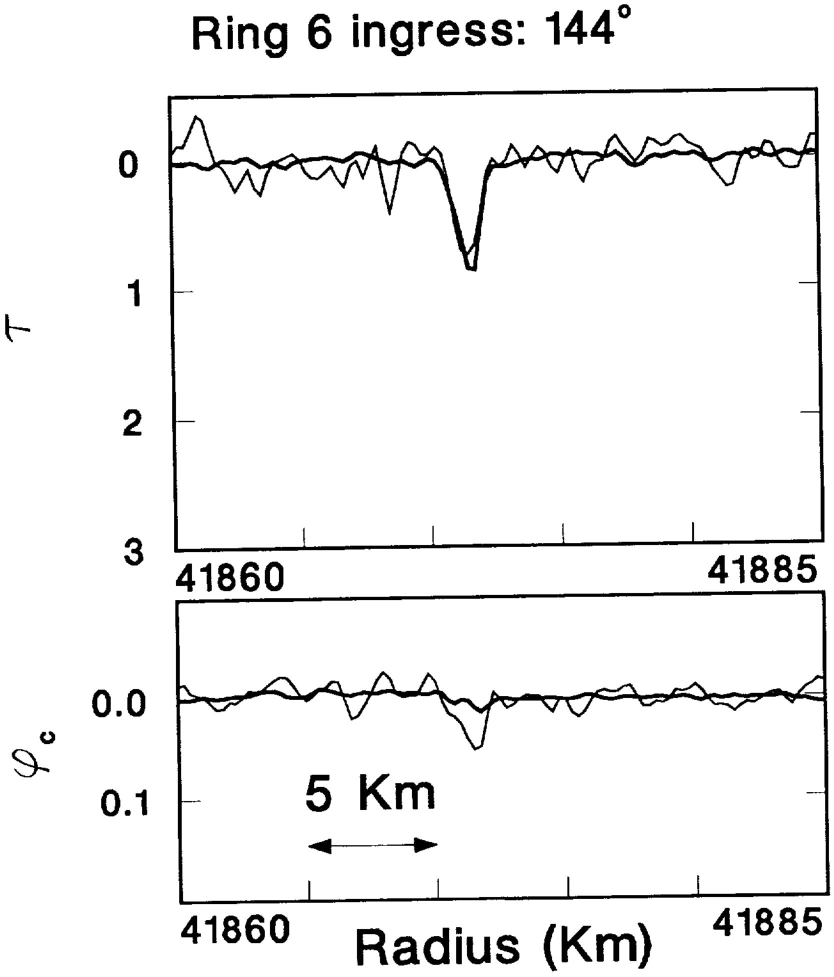

FIG. 78: Opacity and phase profiles of Ring 6 observed at ingress. Angle indicated at top is true anomaly. Heavy curve is for wavelength 3.6 cm, lighter curve for wavelength 13 cm. The 13 cm curve is significantly noiser due to lower transmitter power as well as smaller system gain for the longer wavelength. Within the measurement error, there is no detectable difference in optical depth between the 3.6 and 13 cm wavelengths. There is little effect on the phase at 3.6 cm due to the presence of the ring; there is, however a detectable effect on the 13 cm phase, with the phase retarded in the region of the ring by a maximum value of approximately 0.05 cycles. See Table 7 for quantitative values and confidence intervals.

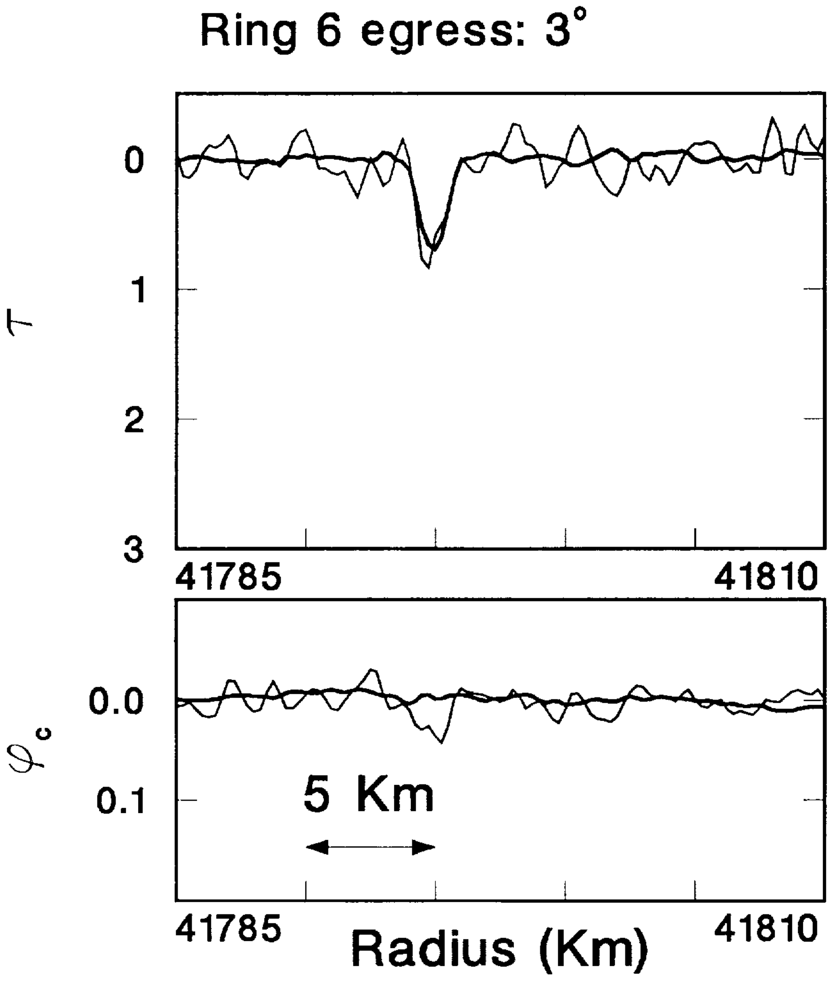

FIG. 79: Opacity and phase profiles of Ring 6 observed at egress. See caption of Figure 78 for details; behavior of this ring is quite similar to that at ingress, with no detectable differential optical depth, and with apparent phase delay at 13 cm.

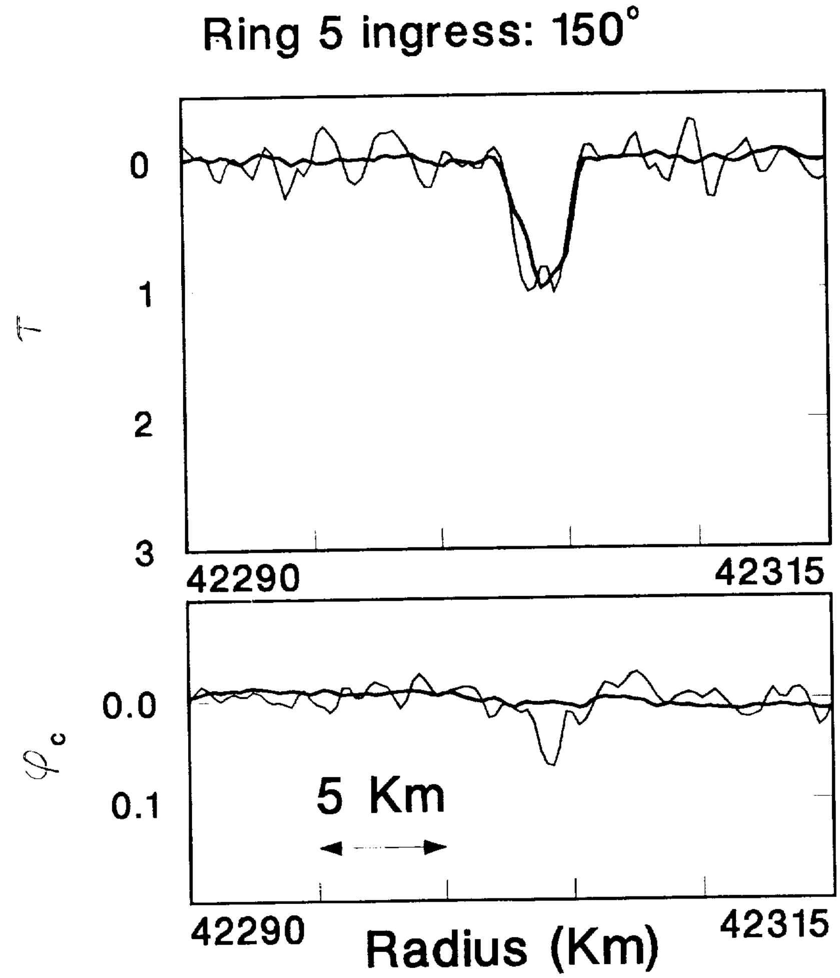

FIG. 80: Opacity and phase profiles of Ring 5 observed at ingress. See caption of Figure 78 for details. Behavior is qualitatively similar to that of Ring 6.

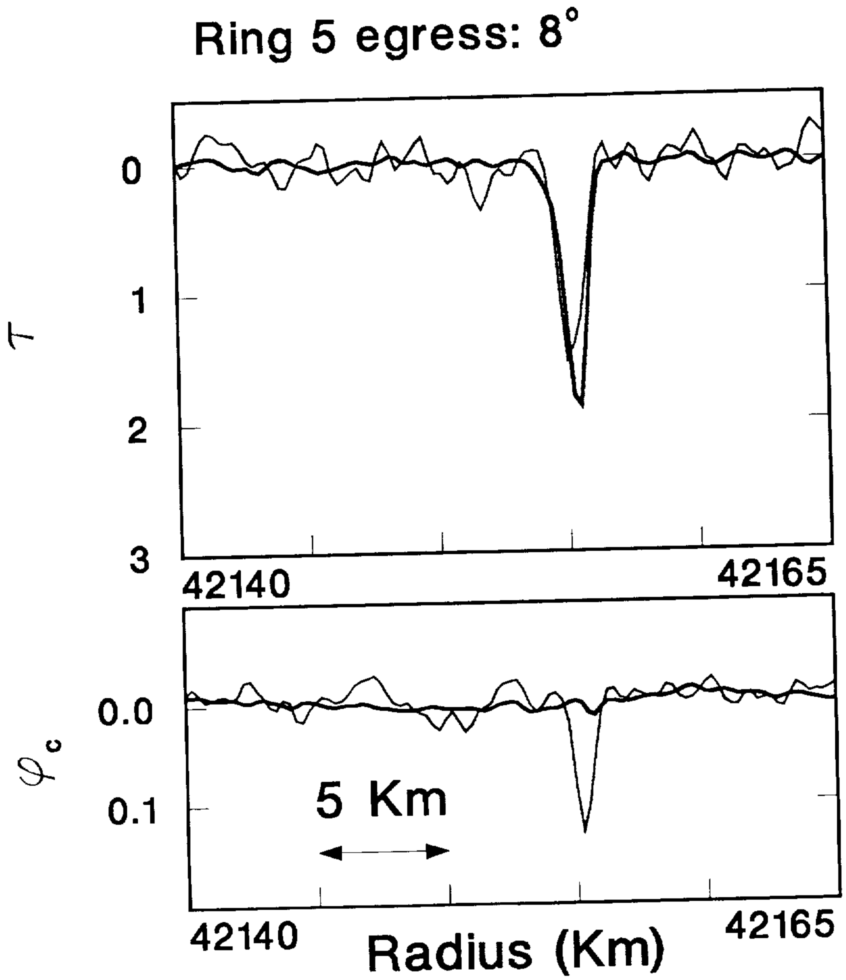

FIG. 81: Opacity and phase profiles of Ring 5 observed at egress. See caption of Figure 78 for details. Behavior is similar to that of Ring 6 as well as to the other observation of Ring 5 (Figure 80); the optical depth of this ring is larger than that of Ring 6, however, and the increased amount of material causes the phase delay at 13 cm to be more apparent.

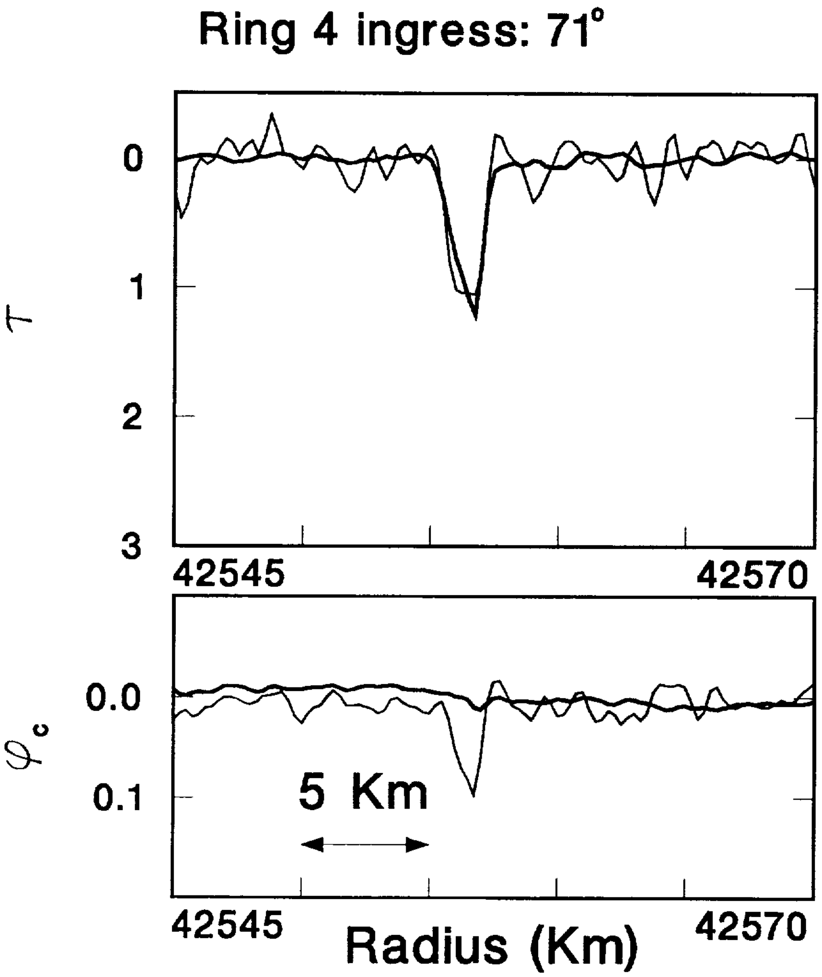

FIG. 82: Opacity and phase profiles of Ring 4 observed at ingress. See caption of Figure 78 for details. Once again, the behavior qualitatively resembles that of Ring 6, with no detectable difference in optical depth between the two wavelengths, but with clear phase delay at 13 cm.

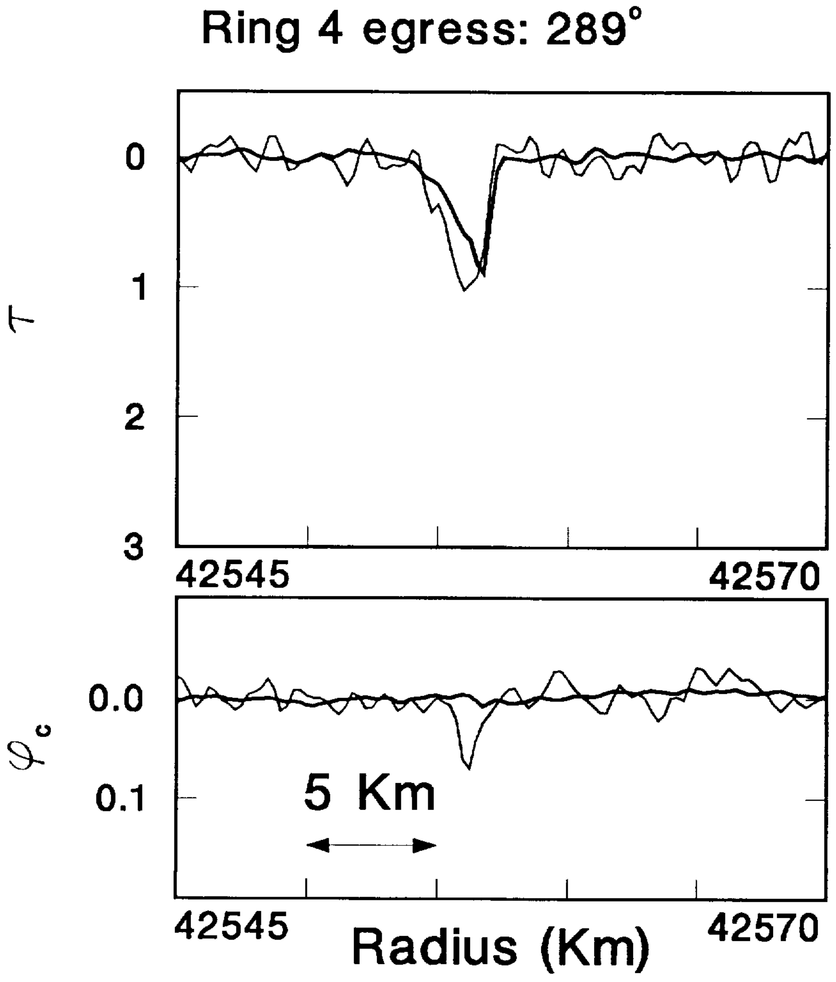

FIG. 83: Opacity and phase profiles of Ring 4 observed at egress. See caption of Figure 78 for details. Behavior is similar to that of this ring at the other observation longitude (Figure 82).

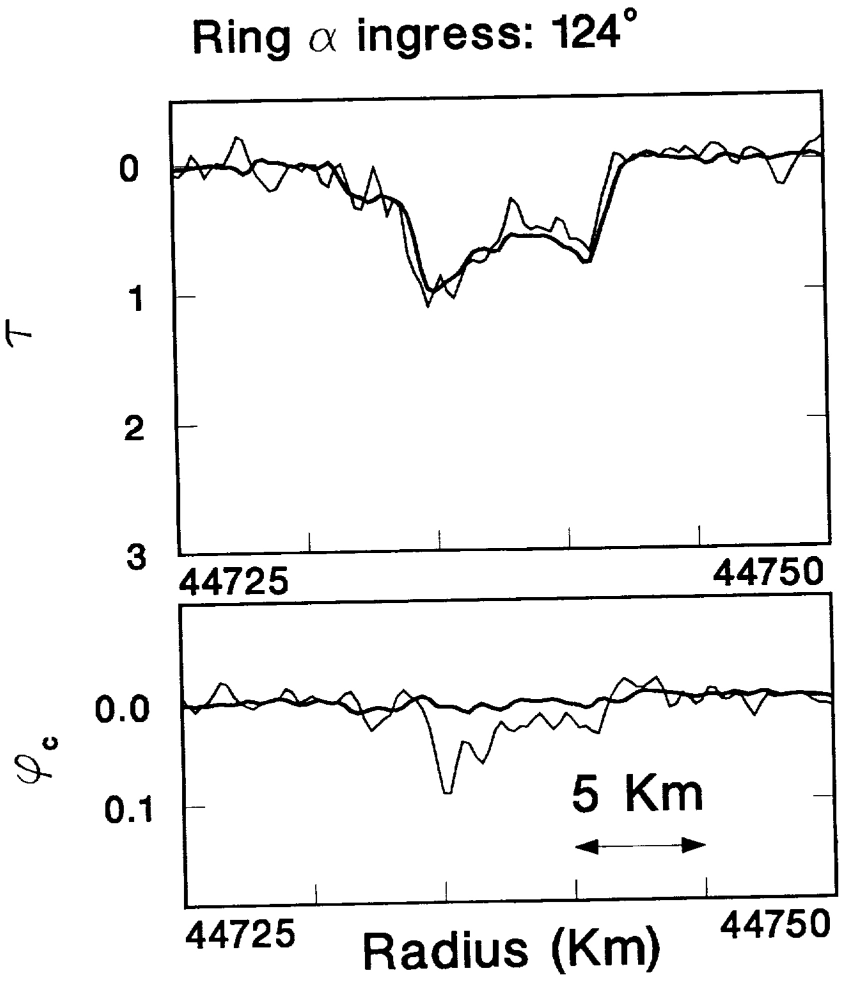

FIG. 84: Opacity and phase profiles of Ring α observed at ingress. See caption of Figure 24 for details.

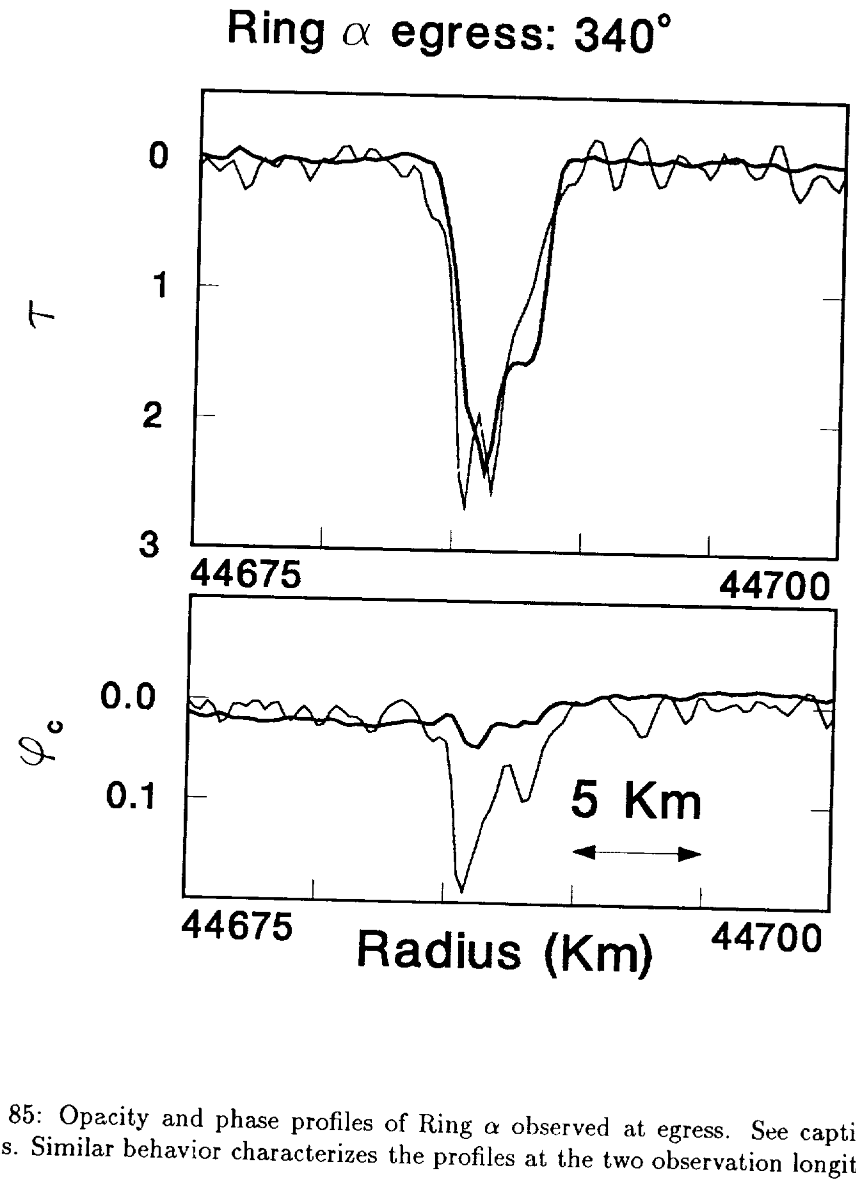

FIG. 85: Opacity and phase profiles of Ring α observed at egress. See caption of Figure 78 for details. Similar behavior characterizes the profiles at the two observation longitudes.

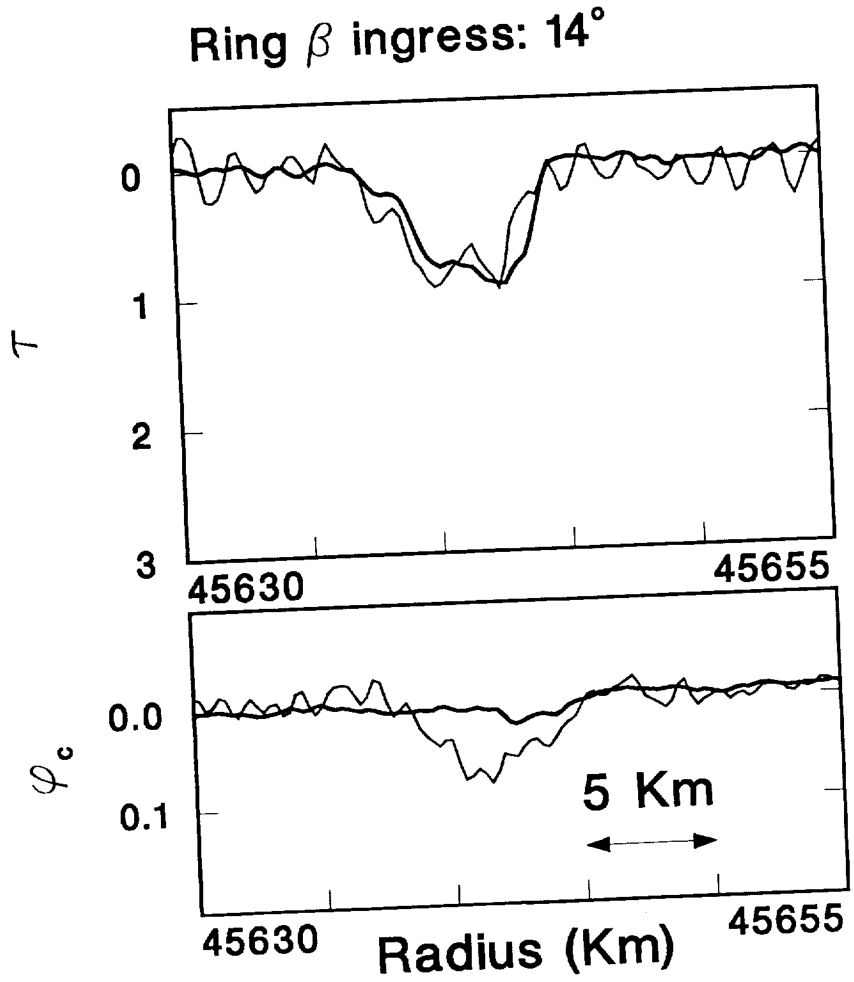

FIG. 86: Opacity and phase profiles of Ring β observed at ingress. See caption of Figure 78 for details. Ring β at this observation longitude, like the other inner rings, shows no significant difference in optical depth between the two wavelengths, but shows significant phase delay at 13 cm, the shape of which closely follows the optical depth profile.

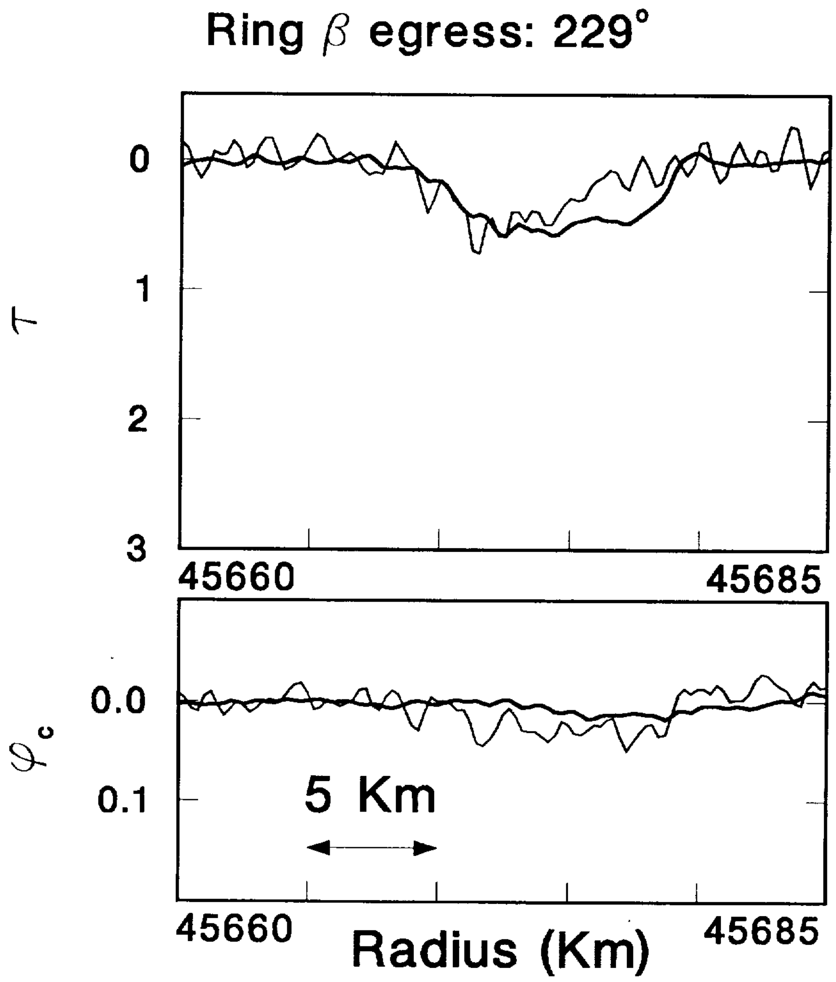

FIG. 87: Opacity and phase profiles of Ring β observed at egress. See caption of Figure 78 for details. This observation of Ring β is the only one of the 18 profiles observed which appears to show a marginally detectable ($\sim$ 2-σ) difference between the 3.6 and 13 cm optical depth profiles, in this case in the outer half of the ring. If real, this may be interpreted as evidence for the presence of particles in the size range of a few to several centimeters. The phase behavior is similar to that of the other rings, but is less apparent due to the small optical depth, and corresponding smaller amount of material present in this ring.

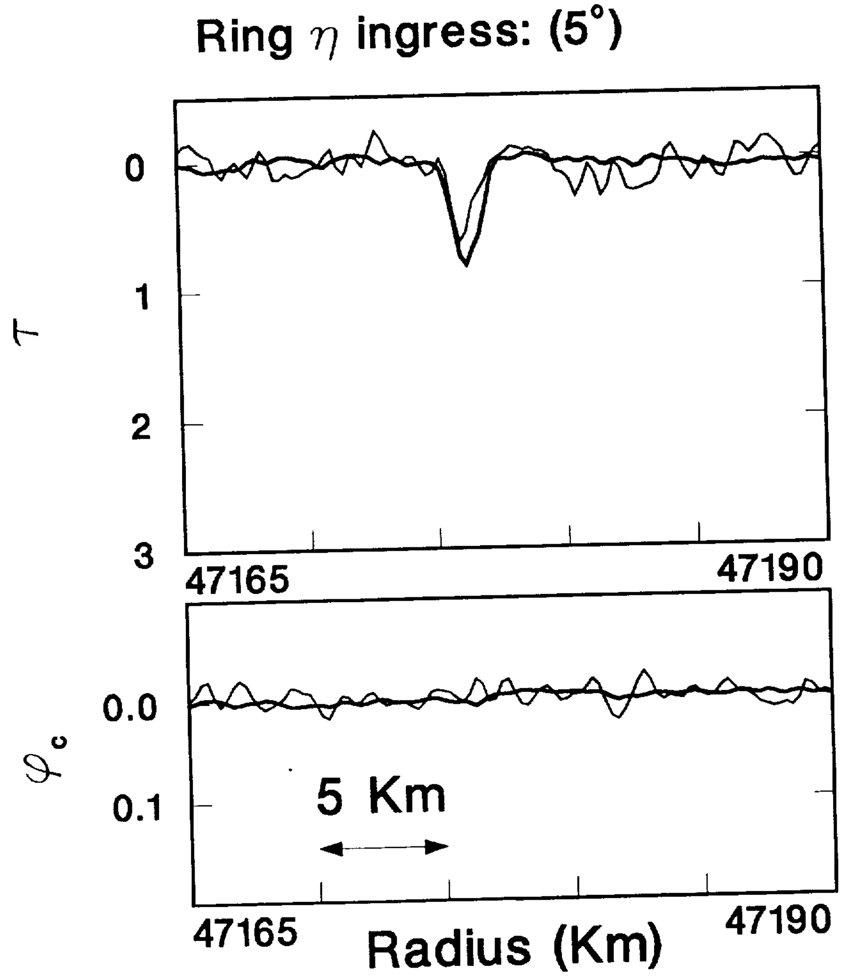

FIG. 88: Opacity and phase profiles of Ring η observed at ingress. True anomaly is enclosed in parentheses to indicate its relative uncertainty for this almost circular ring. See caption of Figure 78 for details. Ring η shows a clear difference in behavior from that of Rings 6–β. Like those rings, it shows no significant differential optical depth; unlike those rings, however, there is also no detectable change in the phase at either wavelength due to the presence of the ring. Similar behavior is observed for all of the outer rings—Ring η through Ring ϵ.

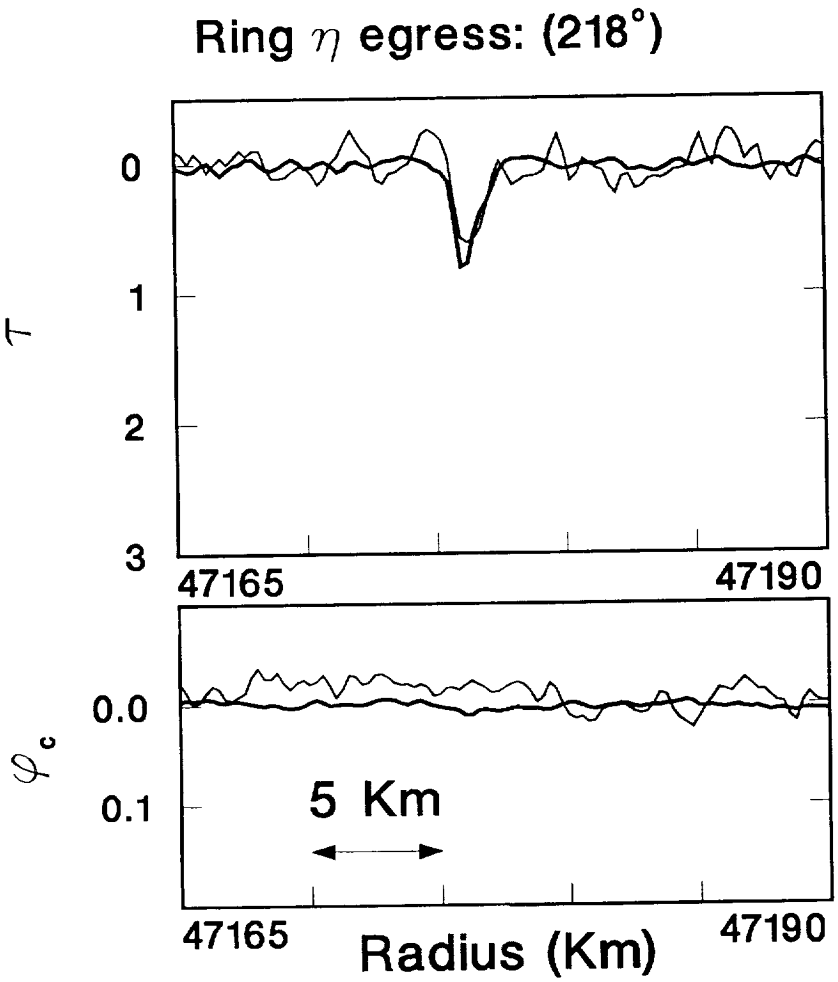

FIG. 89: Opacity and phase profiles of Ring η observed at egress. See caption of Figure 78 for details. There is little detectable difference in optical depth, within the noise limitations, and also no detectable effect on the phase at either wavelength due to the presence of the ring.

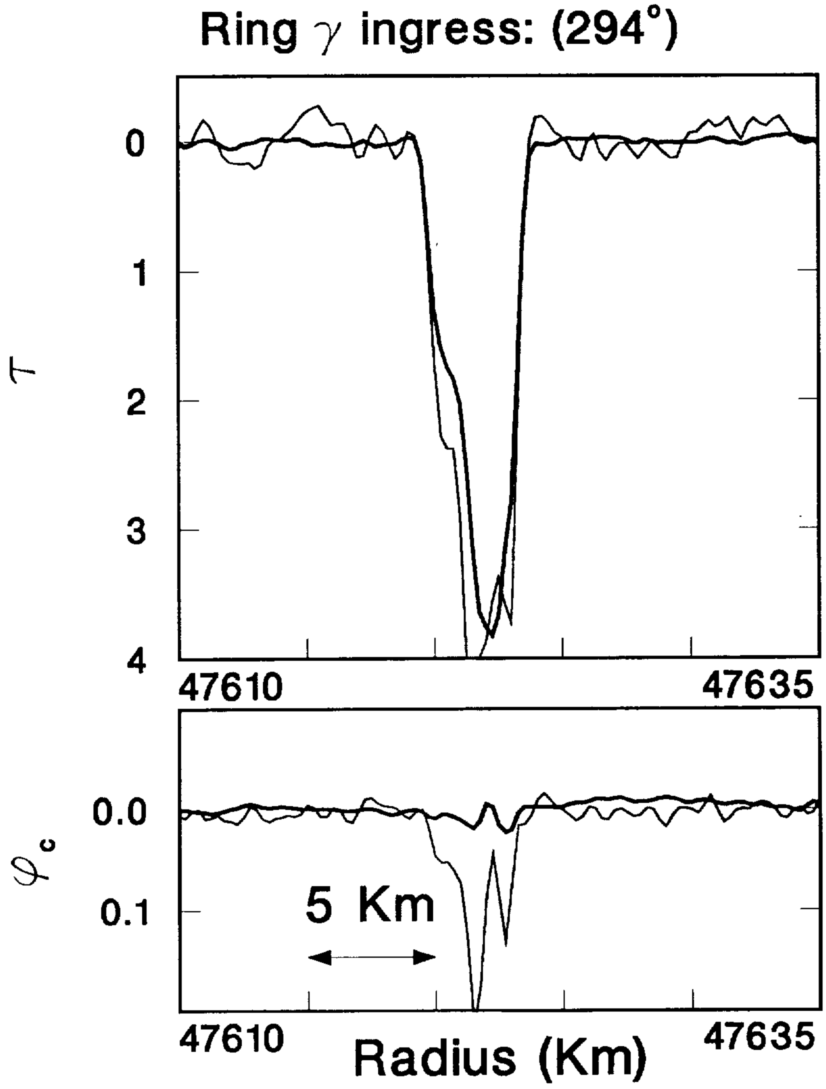

FIG. 90: Opacity and phase profiles of Ring γ observed at ingress. See caption of Figure 78 for details. The optical depths at the two wavelengths are similar; there is noticable phase delay at 13 cm. However, given the large optical depth of this ring, the phase per unit optical depth is much smaller than characteristic values for the inner rings.

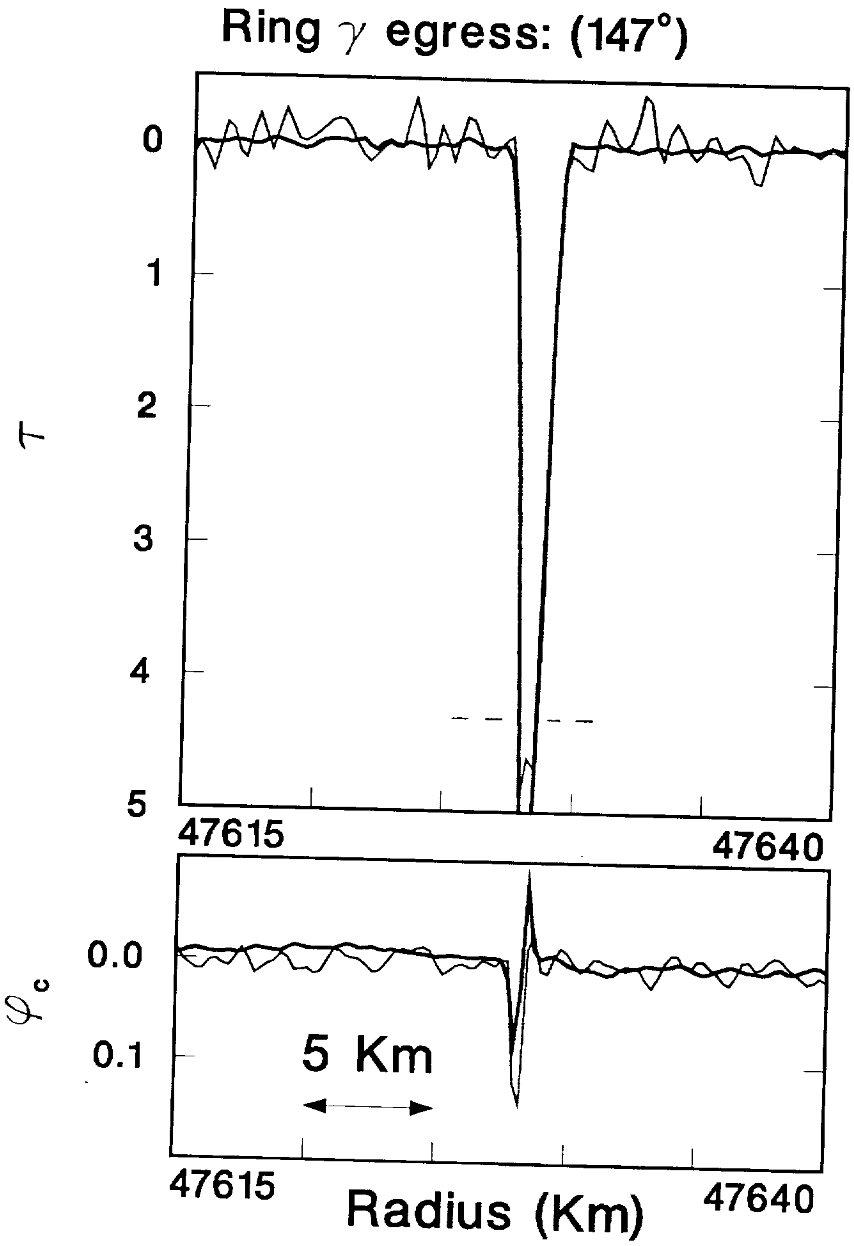

FIG. 91: Opacity and phase profiles of Ring γ observed at egress. See caption of Figure 78 for details. The optical depth at 13 cm appears to be smaller than that at 3.6 cm. However, given the unusually large opacity of the ring, measurements at the 13 cm wavelength in the core of the ring are highly uncertain, and in fact exceeds the 13 cm threshold optical depth (see Table 11 in Appendix A). For this reason, the phase delay measurements in the core of the ring are lost in the noise as well.

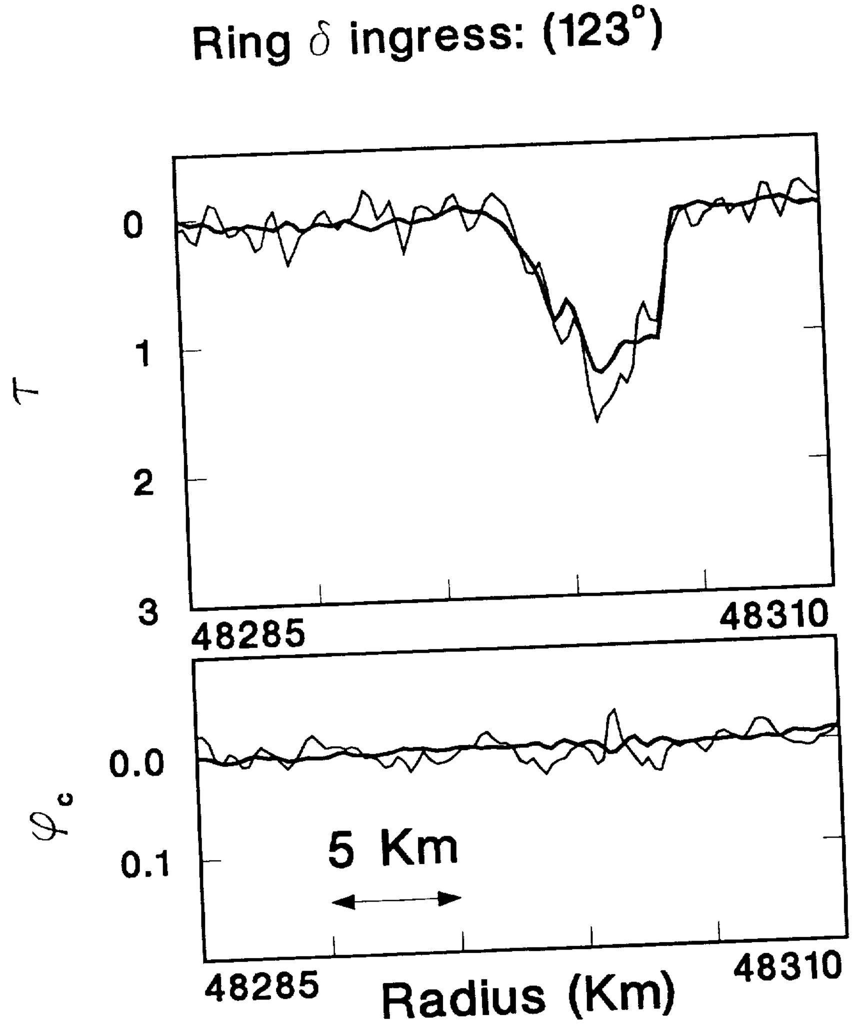

FIG. 92: Opacity and phase profiles of Ring δ observed at ingress. See caption of Figure 78 for details. The optical depth behavior at the two wavelengths is quite similar; little phase delay at either wavelength is evident.

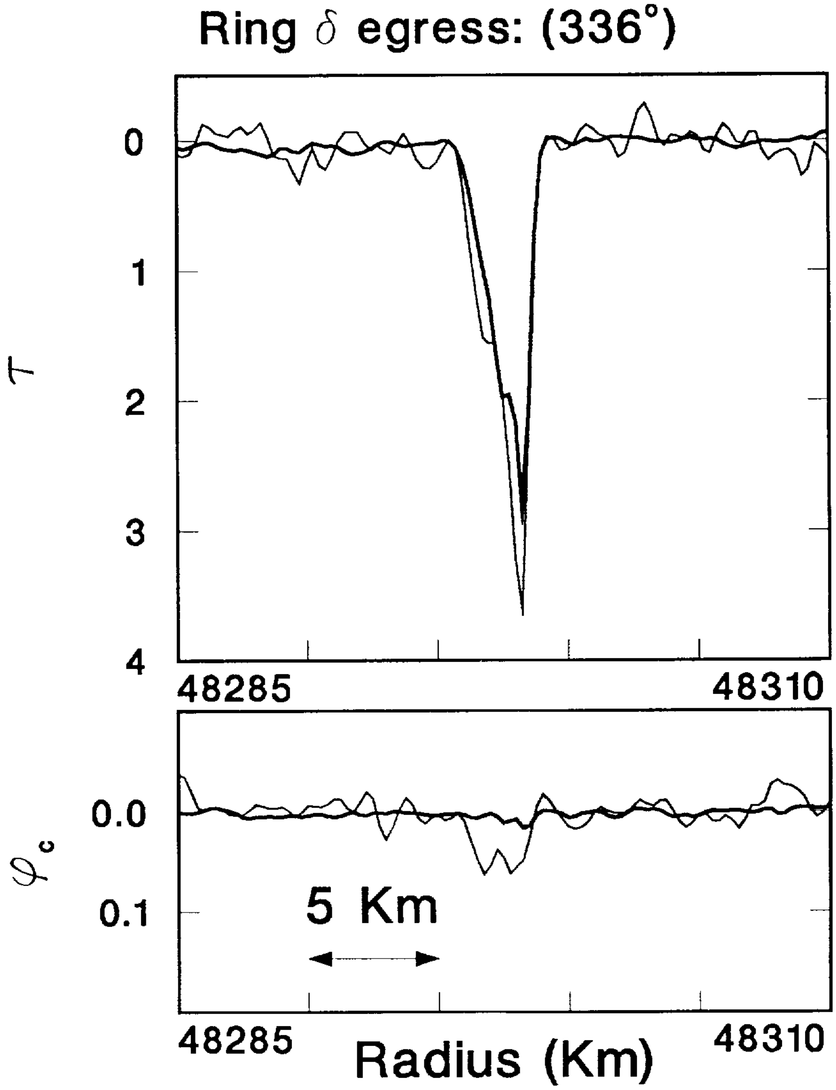

FIG. 93: Opacity and phase profiles of Ring δ observed at egress. See caption of Figure 78 for details. Optical depth at the two wavelengths is similar; the phase delay at 13 cm is small compared to that of the inner rings, given the large optical depth of this ring.

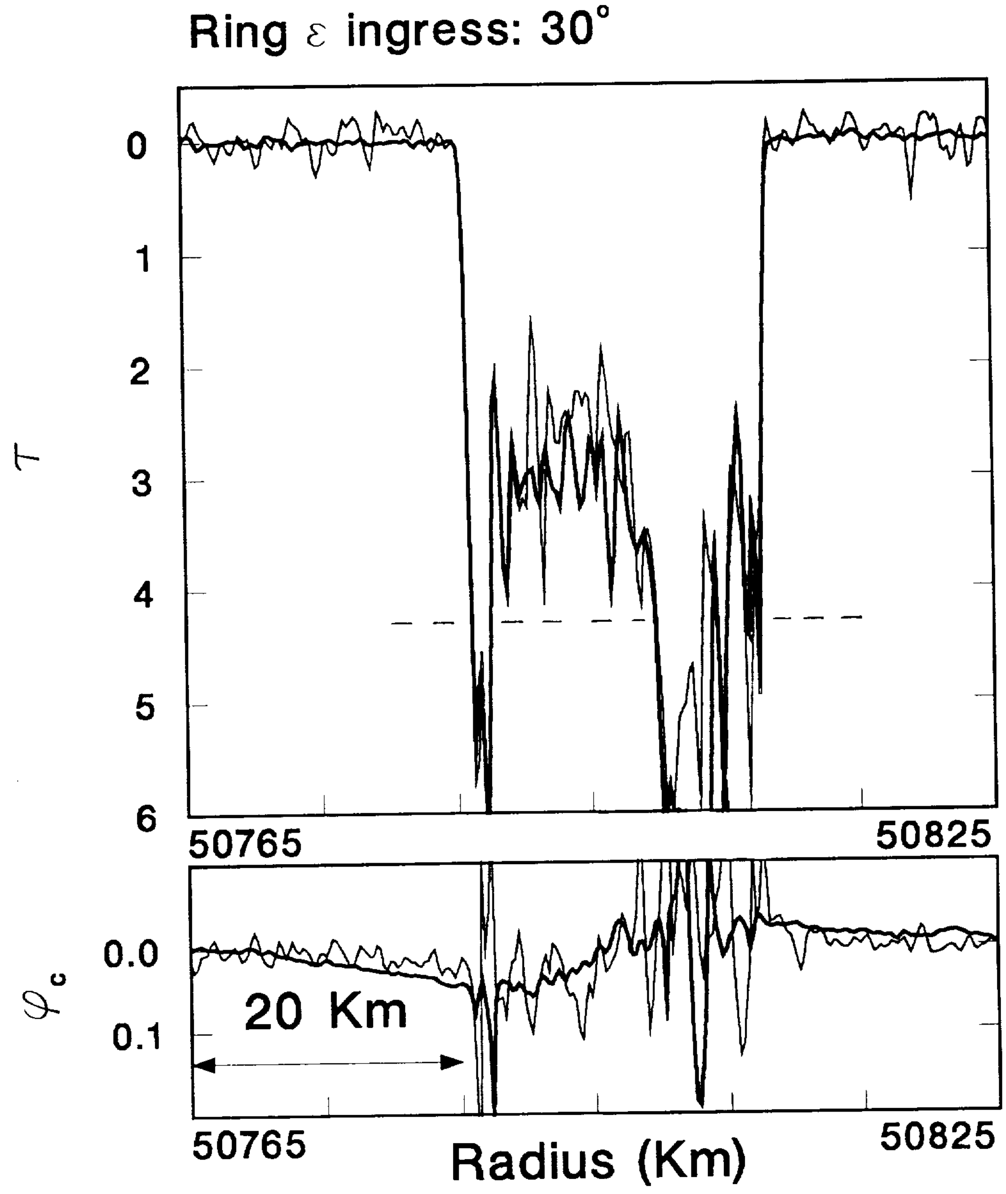

FIG. 94: Opacity and phase profiles of Ring ϵ observed at ingress. See caption of Figure 78 for details. Scales for this figure as well as Figure 25 differ from those of the previous figures. Optical depth at the two wavelengths is quite similar, except in the dense core of the ring (outer one-third), where the 13 cm threshold optical depth (see Appendix A) has been exceeded and measurements can no longer be confidently interpreted. Phase behavior shows no significant differences due to the ring, within the noise limitations; the background fluctuations in phase are due to unmodelled oscillator drift and possibly interplanetary plasma effects.

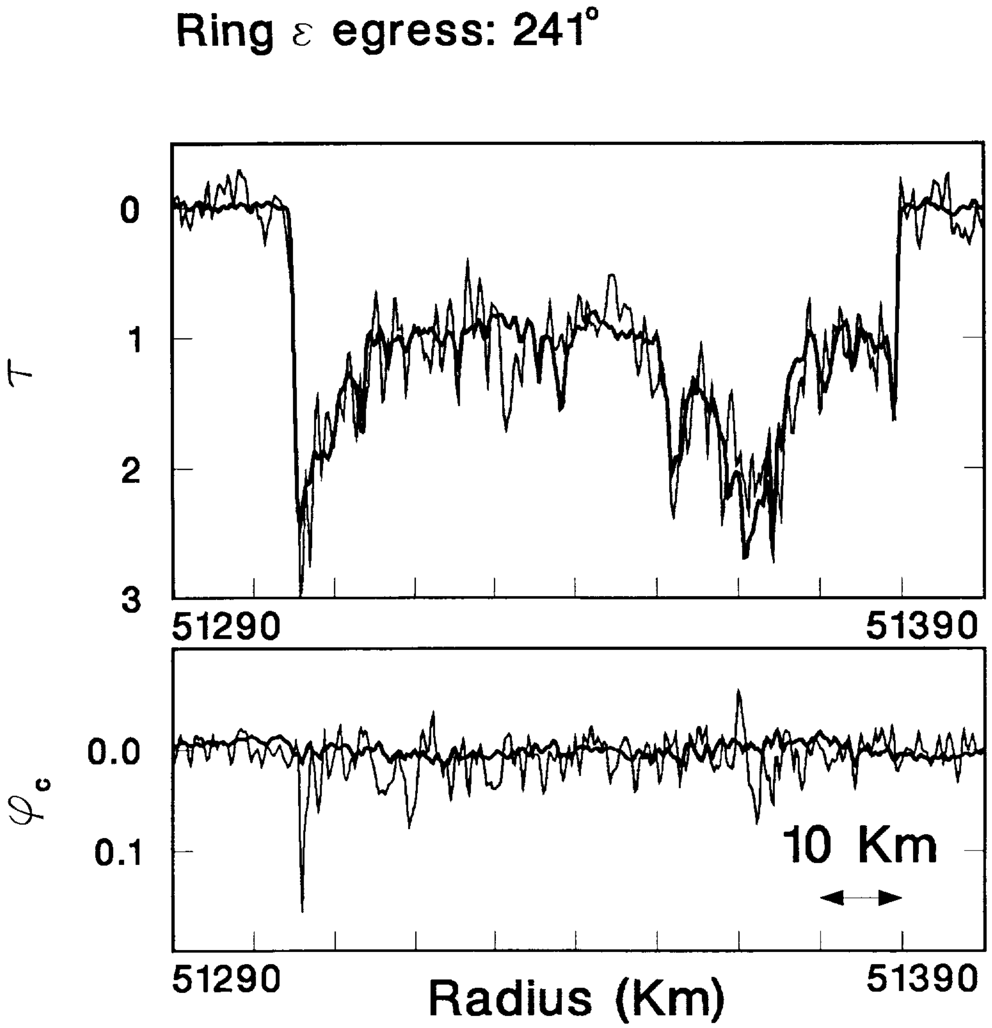

FIG. 95: Opacity and phase profiles of Ring ϵ observed at egress. See caption of Figure 25 for details.

Appendix C

Eccentricity Gradient Profiles

In Chapter 3 we discussed the computation of the eccentricity gradient profile of a ring using two radio occultation profiles. Here we outline the procedure in more detail.

We begin with two profiles of optical depth τ *vs* radius r. The true anomalies of the observations can be computed from the ring orbital parameters given by French *et al.* (1988), along with knowledge of the time of the measurement. We assume that the material distribution in the ring follows non-intersecting Keplerian streamlines of the form

$$r = \frac{a(1 - e^2(a))}{1 + e(a)\cos\theta_p}, \tag{50}$$

where θ_p is the true anomaly, a is the semimajor axis, and $e(a)$ is the eccentricity at a given a. We also assume that the lines of apsides of all streamlines are aligned.

Given the radius r of two points on an eccentric streamline, one can solve for a and e using Eq. 50. We use this method to compute the eccentricity and semimajor axes of the two observed ring edges; for reference, Table 13 lists a and e for the inner and outer edges of Rings α, β, and ϵ.

Ring	e_{inner} ($\times 10^{-4}$)	e_{outer} ($\times 10^{-4}$)	a_{inner} (km)	a_{outer} (km)
α	7.05	7.95	44713.88	44722.15
β	4.10	4.67	45655.44	45664.97
ϵ	75.41	82.93	51120.08	51176.69

TABLE 13: Estimated eccentricities and semimajor axes of the inner and outer edges of Rings α, β, and ϵ.

The eccentricity and semimajor axis of a streamline ***within*** a ring can be computed only if one has a method for isolating individual streamlines. The method we use relies upon the observation that integrated optical depth is approximately conserved in each of the three rings considered (see Table 7). We define streamlines by requiring them to confine equal amounts of integrated optical depth in the two profiles.

Two profiles at a resolution of 500 m are used. For each profile, we have a set of measurements of optical depth τ_i at a set of radii r_i. Small differences in observed integrated opacity (~ 4, 7, and 4% for Rings ϵ, α, and β, respectively; see Table 7) are removed by normalization of both profiles to the same integrated opacity. Using the normalized profiles, we compute a set of values for the cumulative sum

$$\Sigma_i^1 = \sum_{j=1}^{i} \tau_j^1,$$

where τ_j^1 is the optical depth of the j^{th} point in the narrower profile. We define a similar set of values Σ_i^2 for the wider profile. We then interpolate between the pairs (r_i, Σ_i^2) to find radii corresponding to the Σ_i^1 values. This achieved, we now have two radii associated with each streamline, and Eq. 50 is used to compute the corresponding a and e. Subsequently, the eccentricity gradient profile, $q(a) \equiv a\, de(a)/da$, is computed numerically from $e(a)$. Results for Rings α, β, and ϵ are shown in Figure 22.

Once the eccentricity gradient profile is computed, we "propagate" the wider profile to the longitude of the narrower profile for comparison. To do this, we must first associate each measurement of τ with an eccentricity for that streamline. Given the radius, we estimate the semimajor axis of the streamline using

$$a = r\left(\frac{1 + e(a)\cos\theta_p}{1 - e^2(a)}\right).$$

As the eccentricity depends on the semimajor axis, several iterations are necessary to compute a from r. Using the computed eccentricity at that semimajor axis, we determine the amount of stretch or compression due to the eccentricity gradient by finding the ratio of the distance between adjacent streamlines in the original profile relative to that distance in the new profile. Each value of optical depth is multiplied by this ratio to obtain the propagated profile. An example result of this procedure is shown in the upper panel of Figure 23.

References

ACUÑA, M. H., AND N. F. NESS 1976. The complex main magnetic field of Jupiter. *J. Geophys. Res* **81**, 2917-2922.

BOHREN, CRAIG F., AND ARLON J. HUNT 1977. Scattering of electromagnetic waves by a charged sphere. *Can. J. Phys.* **55**, 1930-1935.

BOHREN, CRAIG F., AND DONALD R. HUFFMAN 1983. *Absorption and Scattering of Light by Small Particles.* John Wiley and Sons, New York.

BORDERIES, NICOLE, PETER GOLDREICH, AND SCOTT TREMAINE 1983. The dynamics of elliptical rings *Astron. J.* **88**, 1560-1568.

BORGHESE, F., P. DENTI, R. SAIJA, G. TOSCANO, AND O. I. SINDONI 1984a. Multiple electromagnetic scattering from a cluster of spheres. I. Theory. *Aerosol Science and Technology* **3**, 227-235.

BORGHESE, F., P. DENTI, R. SAIJA, G. TOSCANO, AND O. I. SINDONI 1984b. Macroscopic optical constants of a cloud of randomly oriented nonspherical scatterers. *Il Nuovo Cimento* **81 B**, 29-50.

BROADFOOT, A.L., F. HERBERT, J.B. HOLBERG, D.M. HUNTEN, S. KUMAR, B.R. SANDEL, D.E. SHEMANSKY, G.R. SMITH, R.V. YELLE, D.F. STROBEL, H.W. MOOS, T.M. DONAHUE, S.K. ATREYA, J.L. BERTAUX, J.E. BLAMONT, J.C. MCCONNEL, A.J. DESSLER, S. LINICK AND R. SPRINGER 1986. Ultraviolet spectrometer observations of Uranus. *Science* **233**, 74-79.

BRUNNING, JOHN H., AND YUEN T. LO 1971. Multiple scattering of EM waves by spheres. Parts I and II. *IEEE Trans. Ant. Prop.* **AP-19,** 378-400.

CHAE, DONG GHIE, FRANCIS H. REE, AND TAIKYUE REE 1969. Radial distribution functions and equation of state of the hard-disk fluid. *J. Chem. Phys* **50** 1581-1589.

COLWELL, J. E., L. J. HORN, A. L. LANE, L. W. ESPOSITO, P. A. YANAMANDRA-FISHER, S. H. PILORZ, K. E. SIMMONS, M. D. MORRISON, C. W. HORD, R. M. NELSON, B. D. WALLIS, R. A. WEST, AND B. J. BURATTI 1989. Voyager photopolarimeter observations of Uranian ring occultations. submitted to *Icarus*.

CRUZAN, O. R. 1962. Translational addition theorems for spherical vector wave functions. *Q. Appl. Math* **20,** 33-40.

CUZZI, J. N. 1985. Rings of Uranus: Not so thick, not so black. *Icarus* **63,** 312-316.

CUZZI, J. N., J. J. LISSAUER, L. W. ESPOSITO, J. B. HOLBERG, E. A. MAROUF, G. L. TYLER, AND A. BOISCHOT 1984. "Saturn's rings: Properties and processes." In *Planetary Rings,* edited by R. Greenberg and A. Brahic (University of Arizona, Tucson), pp. 73-199.

DAVE, J. V. 1968. *Subroutines for Computing the Parameters of the Electromagnetic Radiation Scattered by a Sphere.* IBM Palo Alto Scientific Center Report No. 320-3237, Palo Alto Scientific Center, IBM Corporation.

DEAN, CLEON EUGENE 1982. *Electromagnetic Scattering from Two Dielectric Spheres: Mueller Matrix and Extinction Coefficient Calculations.* Dissertation for Degree of Master of Science, Department of Physics, Texas A& M University.

DONES, L., M. R. SHOWALTER, AND J. N. CUZZI 1988. Interparticle shadowing in planetary rings. *BAAS* **20,** p. 858.

ELLIOT, J. L. AND P. D. NICHOLSON 1984. "Rings of Uranus." In *Planetary Rings,* edited by R. Greenberg and A. Brahic (University of Arizona, Tucson), pp. 25-72.

ELLIOT, J. L., R. G. FRENCH, K. J. MEECH, AND J. H. ELIAS 1984. Structure of the Uranian Rings. I. Square-well model and particle-size constraints. *Astron. J.* **89,** 1587-1603.

ELLIOT, J. L., E. W. DUNHAM, AND D. J. MINK 1977. The rings of Uranus. *Nature* **267,** 328-330.

Eshleman, V. R., G. L. Tyler, J. D. Anderson, G. Fjeldbo, G. S. Levy, G. E. Wood, and T. A. Croft 1977. Radio science investigations with Voyager. *Space Sci. Rev.* **21**, 207-232.

Esposito, L. W., N. Borderies, P. Goldreich, J. N. Cuzzi, J. B. Holberg, A. L. Lane, R. B. Pomphrey, R. J. Terrile, J. J. Lissauer, E. A. Marouf, and G. L. Tyler 1983. Eccentric ringlet in the Maxwell Gap at 1.45 Saturn radii: Multi-instrument Voyager observations. *Science* **222**, 57-60.

Freedman A., S. D. Tremaine, and J. L. Elliot 1983. Weak dynamical forcing of the Uranian ring system. *Astron. J.* **88**, 1053-1059.

R. G. French 1987 (October). Personal communication.

French, R. G., J. L. Elliot, and D. A. Allen 1982. Inclination of the Uranian Rings. *Nature* **298**, 827-828.

French, R. G., J. L. Elliot, and S. E. Levine 1986. Structure of the Uranian Rings. II. Ring orbits and widths. *Icarus* **67**, 134-163.

French, R. G., J. L. Elliot, L. M. French, J. A. Kangas, K. J. Meech, M. Ressler, M. W. Buie, J. A. Frogel, J. B. Holberg, J. J. Fuensalida, and M. Joy 1988. Uranian ring orbits from Earth-based and Voyager occultation observations. *Icarus* **73**, 349-378.

French, R. G., P. D. Nicholson, C. Porco, and E. A. Marouf 1989. " Dynamics and structure of the Uranian rings." In *Uranus,* edited by M. S. Matthews, *et al.* (University of Arizona, Tucson), in preparation.

Fuller, Kirk Allison 1987. *Cooperative Electromagnetic Scattering by Ensembles of Spheres.* Ph.D. Dissertation, Department of Physics, Texas A& M University.

Fuller, Kirk 1989. Personal communication.

Fuller, Kirk A., George W. Kattawar, and Ru T. Wang 1986. Electromagnetic scattering from two dielectric spheres: Further comparisons between theory and experiment. *Applied Optics* **25**, 2521-2529.

Goldreich, Peter and Carolyn C. Porco 1987. Shepherding of the Uranian rings. II. Dynamics. *The Astronomical Journal* **93**, 730-737.

REFERENCES

Goldreich, Peter and Scott Tremaine 1979a. Towards a theory for the Uranian rings. *Nature* **277**, 97-99.

Goldreich, Peter and Scott Tremaine 1979b. Precession of the ϵ Ring of Uranus. *The Astronomical Journal* **84**, 1638-1641.

D. L. Gray 1988 (January). Personal communication.

Gresh, Donna L., Paul A. Rosen, G. Leonard Tyler, and Jack J. Lissauer 1986. An analysis of bending waves in Saturn's rings using Voyager radio occultation data. *Icarus* **68**, 481-502.

Gresh, Donna L., Essam A. Marouf, G. Leonard Tyler, Paul A. Rosen, and Richard A. Simpson 1989. Voyager radio occultation by Uranus' rings. I: Observational results. *Icarus* **78**, 131-168.

Grün, E., G. E. Morfill, and D. A. Mendis 1984. "Dust-magnetospheric interactions." In *Planetary Rings,* edited by R. Greenberg and A. Brahic (University of Arizona, Tucson), 275-333.

Hansen, J. P., and I. R. McDonald 1976. *Theory of Simple Liquids.* Academic Press, London.

Hartmann, W. K. 1969. Terrestrial, lunar, and interplanetary rock fragmentation. *Icarus* **10**, 201-213.

Holberg, J. B., P. D. Nicholson, R. G. French, and J. L. Elliot 1987. Stellar occultation probes of the Uranian rings at 0.1 and 2.2μm: A comparison of Voyager UVS and Earth-based results. *Astron. J.* **94**, 178-188.

Hubbard, W. B., A. Brahic, B. Sicardy, L.-R. Elicer, F. Roques, and F. Vilas 1986. Occultation detection of a Neptunian ring-like arc. *Nature* **319**, 636-640.

Jackson, John David 1975. *Classical Electrodynamics.* John Wiley and Sons, New York.

Kangas, J. A. and J. L. Elliot 1987. The wavelength dependence of the optical depth of 1986U1R. *Bull. Amer. Astron. Soc.* **19**, 884.

Kattawar, George W., and Cleon E. Dean 1983. Electromagnetic scattering from two dielectric spheres: Comparison between theory and experiment. *Optics Letters* **8**, 48-50.

KERKER, M. 1969. *The Scattering of Light and Other Electromagnetic Radiation.* Academic, New York.

LANE, A. L., C. W. HORD, R. A. WEST, L. W. ESPOSITO, K. E. SIMMONS, R. M. NELSON, B. D. WALLIS, B. J. BURATTI, L. J. HORN, A. L. GRAPS, W. R. PRYOR 1986. Photometry from Voyager 2: Initial results from the Uranian atmosphere, satellites, and rings. *Science* **233,** 65-70.

LIANG, C., AND Y. T. LO 1967. Scattering by two spheres. *Radio Science* **2,** 1481-1495.

LINDAL, G. F., J. R. LYONS, D. N. SWEETNAM, V. R. ESHLEMAN, D. P. HINSON, AND G. L. TYLER 1987. The atmosphere of Uranus: Results of radio occultation measurements with Voyager 2. *J. Geophy. Res.* **92,** 14987-15001.

J. LISSAUER 1989 (October). Personal communication.

LONGARETTI, PIERRE-YVES 1989. Saturn's main ring particle size distribution: An analytic approach. *Icarus* **81,** 51-73.

MAROUF, ESSAM A. 1975. *The Rings of Saturn: Analysis of a Bistatic-Radar Experiment.* Ph.D. Dissertation, Department of Electrical Engineering, Stanford University.

MAROUF, E. A. AND G. L. TYLER 1982. Microwave edge diffraction by features in Saturn's rings: Observations with Voyager 1. *Science* **217,** 243-245.

MAROUF, E. A., G. L. TYLER, AND V. R. ESHLEMAN 1982. Theory of radio occultation by Saturn's rings. *Icarus* **49,** 161-193.

MAROUF, E. A., G. L. TYLER, H. A. ZEBKER, R. A. SIMPSON, AND V. R. ESHLEMAN 1983. Particle size distributions in Saturn's rings from Voyager 1 radio occultation. *Icarus* **54,** 189-211.

MAROUF, ESSAM A. AND G. LEONARD TYLER 1986. Detection of two satellites in the Cassini division of Saturn's rings. *Nature* **323,** 31-35.

MAROUF, E. A., G. L. TYLER, AND P. A. ROSEN 1986. Profiling Saturn's rings by radio occultation. *Icarus* **68,** 120-166.

MAROUF, E. A., D. L. GRESH, AND G. L. TYLER 1987. Eccentricity gradients of Uranus' ϵ, β, and α rings. *BAAS* **19,** p. 883.

MAROUF, E. A., D. L. GRESH, AND G. L. TYLER 1988. Wave in Ring δ? *BAAS* **20,** p. 845.

MCQUARRIE, DONALD 1976. *Statistical Mechanics.* Harper and Row, New York.

MEI, K. K. 1974. Unimoment method of solving antenna and scattering problems. *IEEE Trans. Ant. Prop.* **AP-22,** 760-766.

MIE, G. 1908. Beitrage zur optik trüber medien speziell kolloidaler metallösungen. *Ann. Phys.* **25,** 377-445.

NICHOLSON, PHILIP D., MAREN L. COOKE, KEITH MATHEWS, JONATHAN H. ELIAS, AND GERARD GILMORE 1989. Stellar occultations by Neptune: Further evidence for incomplete rings. submitted to *Icarus* .

OCKERT, M. E., J. N. CUZZI, C. C. PORCO, AND T. V. JOHNSON 1987. Uranian ring photometry: Results from Voyager 2. *J. Geophys. Res.* **92,** 14969-14978.

OWEN, T., G. E. DANIELSON, A. F. COOK, C. HANSEN, V. L. HALL, AND T. C. DUXBURY 1979. Jupiter's rings. *Nature* **281,** 442-446.

PANG, K. D., AND P. D. NICHOLSON 1984. Composition and size of Uranian ring particles *Lunar Planet. Sci. XV* part 2, 627-628.

PORCO, C. C., J. N. CUZZI, M. E. OCKERT, AND R. J. TERRILE 1987. The color of the Uranian rings. *Icarus* **72,** 69-78.

PORCO, C. C. AND P. GOLDREICH 1987. Shepherding of the Uranian rings. I. Kinematics. *Astron. J.* **93,** 724-729.

RAMO, SIMON, JOHN R. WHINNERY, AND THEODORE VAN DUZER 1965. *Fields and Waves in Communication Electronics.* John Wiley and Sons, New York.

ROSEN, PAUL A., AND JACK J. LISSAUER 1988. The Titan -1:0 nodal bending wave in Saturn's Ring C. *Science* **241,** 690-694.

ROSEN, PAUL ALAN 1989. *Waves in Saturn's Rings Probed by Radio Occultation.* Ph.D. Dissertation, Department of Electrical Engineering, Stanford University.

SHOWALTER, M. R., J. A. BURNS, J. N. CUZZI, AND J. B. POLLACK 1985. Discovery of Jupiter's 'gossamer' ring. *Nature* **316,** 526-528.

SHOWALTER, M. R., J. N. CUZZI, E. A. MAROUF, AND L. W. ESPOSITO 1986. Satellite "wakes" and and the orbit of the Encke gap moonlet. *Icarus* **66,** 297-323.

SHOWALTER, MARK R., JOSEPH A. BURNS, JEFFREY N. CUZZI, AND JAMES B. POLLACK 1987. Jupiter's ring system: New results on structure and particle properties. *Icarus* **69,** 458-498.

SIMPSON, R. A. , G. L. TYLER, AND J. B. HOLBERG 1983. Saturn's pole: Geometric correction based on Voyager UVS and radio occultation. *Astron. J.* **88,** 1531-1536.

SIMPSON, RICHARD A. , G. LEONARD TYLER, ESSAM A. MAROUF, HOWARD A. ZEBKER AND VON R. ESHLEMAN 1984. Saturn's rings: Voyager 1 radio occultation experiment results. *IEEE Trans. Geoscience and Remote Sensing* **GE-22,** 656-665.

SINDONI, O. I., F. BORGHESE, P. DENTI, R. SAIJA, AND G. TOSCANO 1984. Multiple electromagnetic scattering from a cluster of spheres. II. Symmetrization. *Aerosol Science and Technology* **3,** 237-243.

SMITH, BRADFORD A., LAURENCE SODERBLOM, RETA BEEBE, JOSEPH BOYCE, GEOFFERY BRIGGS, ANNE BUNKER, STEWART A. COLLINS, CANDICE J. HANSEN, TORRENCE V. JOHNSON, JIM L. MITCHELL, RICHARD J. TERRILE, MICHAEL CARR, ALLEN F. COOK II, JEFFREY CUZZI, JAMES B. POLLACK, G. EDWARD DANIELSON, ANDREW INGERSOLL, MERTON E. DAVIES, GARRY E. HUNT, HAROLD MASURSKY, EUGENE SHOEMAKER, DAVID MORRISON, TOBIAS OWEN, CARL SAGAN, JOSEPH VEVERKA, ROBERT STROM, VERNER E. SUOMI 1981. Encounter with Saturn: Voyager 1 Imaging science results. *Science* **212,** 163-191.

SMITH, B. A., L. A. SODERBLOM, R. BEEBE, D. BLISS, J. M. BOYCE, A. BRAHIC, G. A. BRIGGS, R. H. BROWN, S. A. COLLINS, A. F. COOK II, S. K. CROFT, J. N. CUZZI, G. E. DANIELSON, M. E. DAVIES, T. E. DOWLING, D. GODFREY, C. J. HANSEN, C. HARRIS, G. E. HUNT, A. P. INGERSOLL, T. V. JOHNSON, R. J. KRAUSS, H. MASURSKY, D. MORRISON, T. OWEN, J. B. PLESCIA, J. B. POLLACK, C. C. PORCO, K. RAGES, C. SAGAN, E. M. SHOEMAKER, L. A. SROMOVSKY, C. STOKER, R. G. STROM, V. E. SUOMI, S. P. SYNNOTT, R. J. TERRILE, P. THOMAS, W. R. THOMPSON, AND J. VEVERKA 1986. Voyager 2 in the Uranian system: Imaging science results. *Science* **233,** 43-64.

SMITH, B. A., *et al.* 1989. Voyager 2 at Neptune: Imaging science results. *Science* **246,** 1422-1449.

STEIN, S. 1961. Addition theorems for spherical wave functions. *Q. Appl. Math* **19,** 15-24.

STRATTON, JULIUS ADAMS 1941. *Electromagnetic Theory.* McGraw-Hill, New York.

TRINKS, W. 1933. Zur Vielfachstreuung an kleinen Kugeln. *Ann. Phys. Dtsch* **22,** 561.

TYLER, G. L. 1987. Radio propagation experiments in the outer solar system with Voyager. *Proc. IEEE* **75,** 1404-1431.

TYLER, G. L., E. A. MAROUF, AND G. E. WOOD 1981. Radio occultation of Jupiter's ring: Bounds on optical depth and particle size and a comparison with infrared and optical results. *JGR* **86,** 8699-8703.

TYLER, G. L., V. R. ESHLEMAN, J. D. ANDERSON, G. S. LEVY, G. F. LINDAL, G. E. WOOD, AND T. A. CROFT 1981. Radio science investigation of the Saturn System with Voyager 1: Preliminary results. *Science* **212,** 201-206.

TYLER, G. L., E. A. MAROUF, R. A. SIMPSON, H. A. ZEBKER, AND V. R. ESHLEMAN 1983. The microwave opacity of Saturn's rings at wavelengths of 3.6 and 13 cm from Voyager 1 radio occultation. *Icarus* **54,** 160-188.

TYLER, G. L., D. N. SWEETNAM, J. D. ANDERSON, J. K. CAMPBELL, V. R. ESHLEMAN, D. P. HINSON, G. S. LEVY, G. F. LINDAL, E. A. MAROUF, AND R. A. SIMPSON 1986. Voyager 2 radio science observations of the Uranian system: Atmosphere, rings, and satellites. *Science* **223,** 79-84.

VAN ALLEN, R. E., R. J. CESARONE, AND D. L. GRAY 1982. Voyager Uranus-Neptune navigation planning document. PD618-125 vol 1, chapter 4. 1 October 1982. Jet Propulsion Laboratory, Pasadena, California.

VAN DE HULST 1981. *Light Scattering by Small Particles.* Dover, New York.

WANG, R. T. 1979. "Extinction signatures of non-spherical/non-isotropic particles." In *Light Scattering by Irregularly Sphaped Particles,* edited by Donald W. Schuerman (Plenum Press, New York), pp. 255-272.

WANG, R. T., J. M. GREENBERG, AND D. W. SHUERMAN 1981. Experimental results of dependent light scattering by two spheres. *Opt. Lett.* **6**, 543-545.

WEIDENSCHILLING, STUART J., CLARK R. CHAPMAN, DONALD R. DAVIS, AND RICHARD GREENBERG 1984. "Ring particles: Collisional interactions and physical nature." In *Planetary Rings,* edited by R. Greenberg and A. Brahic (University of Arizona, Tucson), 367-415.

ZEBKER, H. A., G. L. TYLER, AND E. A. MAROUF 1983. On obtaining the forward phase functions of Saturn ring features from radio occultation observations. *Icarus* **56**, 209-228.

ZEBKER, H. A. AND G. L. TYLER 1984. Thickness of Saturn's rings inferred from Voyager 1 observations of microwave scatter. *Science* **223**, 396-398.

ZEBKER, HOWARD A., ESSAM A. MAROUF, AND G. LEONARD TYLER 1985. Saturn's rings: Particle size distributions for thin layer models. *Icarus* **64**, 531-548.